

Copyright
by
Atsuko Nitta
2000

**EVALUATION OF MODE IDENTIFICATION
TECHNIQUES IN TWO KEY WHITE DWARF
PULSATORS**

by

ATSUKO NITTA, B.S., M.A.

DISSERTATION

Presented to the Faculty of the Graduate School of

The University of Texas at Austin

in Partial Fulfillment

of the Requirements

for the Degree of

DOCTOR OF PHILOSOPHY

THE UNIVERSITY OF TEXAS AT AUSTIN

December 2000

**EVALUATION OF MODE IDENTIFICATION
TECHNIQUES IN TWO KEY WHITE DWARF
PULSATORS**

APPROVED BY
DISSERTATION COMMITTEE:

Supervisor: _____

To my family.

Acknowledgements

My thesis would not have been completed without many people's help, understanding, patience, encouragement and guidance.

I would like to thank Don and Kepler for everything they have done. Throughout the many difficult times as a graduate student, they have always been there, helped and guided me, through the ordeal of trying to become an astronomer. They have been the most wonderful supervisors anyone can have. From the very first time I entered the lab, looking for a project to work on, Ed and Don along with Kepler, whom I met a few months after joining the lab, have been great mentors — showing what it is to be a good scientist by setting excellent examples of different styles of scientists. I would also like to thank Rob for being an understanding and very encouraging committee member offering much good advice. Jim also has shown much interest and support whenever I needed some.

My husband Scot had to do an awful lot of reading and correcting the grammar in this thesis. Without him, this thesis would have been quite unreadable and hence a disaster (and instead of writing this, I would have left school without a thesis probably). He has always been quite understanding and helpful from when I first walked into the lab. He has taught me many skills necessary to become an astronomer and taught me to have high standards for research.

My other professional brothers and sisters: Mikemon (thank you for your phone call after the closed door session) who was my professional twin brother (meaning we both started working in the lab around the same time) answered many many questions and continue to do so. I still call Mikemon when I read a theoretical paper and don't understand it. Antonio is another one who has been bugged by me whenever I had questions, especially on doing CCD high speed photometry. Judi looks after me when I go to meetings. She makes sure I don't pass out before I give a talk. Paul has given me numerous email help, especially when I was learning about white dwarf models. He has always been patient, kind and helpful. Chris is always so energetic, brilliant and kind. The "oldest brothers" Steve and Matt has always taken care of the junior students from Texas. Todd is the one who gave me many good reviews on white dwarf stars and the WET when I first started working in the lab. Travis and Anjum have taught me new things as well as how little I knew and how much more I need to learn. They have also supported me so much, especially during the last months in graduate school while I was writing my thesis and being difficult. With all these professional siblings and Don, Ed and Kepler as professional parents, I am sure we are one of the best professional families in the world. My WET colleagues all over the world have also been wonderful people to work with. I have learned so much and enjoyed their friendship. For example, Gerald and I have had many talks over coffee, both scientific and personal, and Michel Breger paid for my first observing run. Chris Koen and I enjoyed many conversations on how strange American culture is over lunch in the lab and bombarded Mikemon with questions. I look forward to doing more

work with them in the future.

My colleagues at Apache Point Observatory (Ellyne, Jeff, Dan, Steph, Bruce) have also been very patient and understanding. Without their support, I would not have been able to finish my degree. They have protected me and have done extra work for me while I was finishing my thesis. They are great friends and wonderful colleagues.

Everybody at McDonald Observatory and the Astronomy department at UT helped me in many ways and many times. Mark Cornell probably is one of the most important people at the observatory making sure all computers run the way they do. I have heard people say we don't know how much we owe to him until we leave and go to other institutions. Dave Doss, Marian Freuh, Doug Otoupal, Jerry Martin, Earl Green, Ed Dutchover, Darin Crook, and many others have helped me out countless times when I had telescope/instrument problems. The chief chef at the observatory Robert has often cooked us spectacular dinners (especially when it was cloudy and the observers were tense) and his crew baked my favorite Mexican wedding cookies whenever I was there. The engineers (David Boyd, Fred Harvey), machinists (Jimmy Welborn, George Barczak) were always very kind and helped me at many occasions. Elizabeth Korves, the graduate student coordinator in the astronomy department, has helped many graduate students navigate through all the paperwork. Especially since I left Austin before I graduated, she was a valuable resource and help in getting things done such as reserving a room for the defense to getting the signature papers from the right people. Bev Wills

was always few rooms down the hall late at night. I have often hopped down to her room to ask questions. She gave me moral support through my years in graduate school.

Many thanks to Karen Winget for having a wonderful dinner and party after the defense. She has been very supportive and understanding as she saw me go through the ordeal of graduate school. We have had many chats and laughs together.

I would also like to thank Prof. Akio Sugamoto, my supervisor when I was in Japan. He was the first person who taught me about the joy of research in science. Without him, I would not have gone to graduate school and definitely not have come to Texas. He has always supported me and welcomed me every year when I went to see him at Ocha dai.

My friends from Toho Girls' High School and my college classmates never laughed (not at least in public) at my ambition to come to the United States to study or to become an astronomer. They have cheered, supported and encouraged me when I was feeling down and I am very very grateful to have such wonderful friends. I also would like to thank friends (especially Yuriko, Joanne and Divas who cooked many dinners) I met in Austin for their support and the wonderful time we spent together.

My family (Papa, Mama, Akira, Hitoshi, grandparents, uncles, aunts, cousins) have all been very supportive and very understanding all my life. Without their continuous support, I would not have become who I am. I thank you all very much.

Preface

I used “we” throughout this thesis. This is because I would not have been able to do any of the work without the help and guidance of my committee members especially Don, Kepler and Ed, along with the other students and collaborators around the globe.

Chapter 2 and 3 are written so that it can be submitted to a journal later. Thus there is some repetition in the background materials in these chapters.

EVALUATION OF MODE IDENTIFICATION TECHNIQUES IN TWO KEY WHITE DWARF PULSATORS

Publication No. _____

Atsuko Nitta, Ph.D.
The University of Texas at Austin, 2000

Supervisor: D.E. Winget, S.O. Kepler

The success of asteroseismology lies in the correct identification of the normal modes of oscillation. The Whole Earth Telescope (WET) identified the normal modes of a helium white dwarf pulsator, GD358, by analyzing the period distribution of the pulsation modes. Another way to identify modes is by comparing pulsation amplitudes in the UV to the optical. To cross-calibrate the two mode identification methods, we observed GD358 in August, 1996 with the Hubble Space Telescope (HST) to obtain the UV data while observing nearly simultaneously from the ground. During our observations, GD358 went through a very drastic amplitude modulation in a time scale of hours. These short time scale amplitude changes made the direct UV to optical amplitude determinations difficult. We successfully eliminate the possibility that the 423s mode, the dominant mode at the time of these observations, is an $\ell = 3$ or 4 g-mode pulsation, but we cannot unambiguously decide if it is an $\ell = 1$ or 2.

Theoretical calculations indicate that the massive pulsating DA white dwarf BPM 37093 has a crystallized interior (Winget et al. 1997; Kanaan

1996; Montgomery 1998). Crystallization was predicted theoretically 40 years ago (Kirshnitz 1960; Abrisokov 1961; Salpeter 1961) although uncertainties in the nature and extent of crystallization, as well as its associated effects, are the largest sources of uncertainty in calculating the ages of the coolest white dwarf stars—important chronometers of the galactic disk. The WET observed BPM 37093 in April 1998 and again in April 1999, simultaneously with the HST, in hopes of using both the period distribution and the amplitude comparison method to identify the ℓ value of the modes and measure the first crystallized mass-fraction of a stellar interior. Here we also rule out the possibility of the observed modes being $\ell = 3$ and higher and demonstrate that not all the observed modes are $\ell = 1$. If all the observed modes are $\ell = 2$, then we conclude that the crystallization mass fraction is between 0 – 80%, depending mainly on the surface H layer.

In the end, we evaluate the amplitude comparison method and address advantages and problems using this method compared to other mode identification methods.

Table of Contents

Acknowledgements	v
Preface	ix
Abstract	x
Table of Tables	xv
List of Figures	xvi
Chapter 1. Overview	1
1.1 Overview	1
1.1.1 White Dwarf Stars	1
1.1.2 Asteroseismology of White Dwarf Stars	4
1.1.3 Goal of this Project	6
Chapter 2. Toward a Calibration of Two Different Mode Identification Methods	8
2.1 White Dwarf Stars	8
2.2 Asteroseismology	10
2.3 Mode Identification Techniques	11
2.3.1 The Period Distribution Method using the WET	13
2.3.2 The Mode Identification of GD358 by the Period Distribution Method	15
2.3.3 The Limb Darkening Method	20
2.3.4 Obtaining the Lightcurve and Fourier Transform Ratios	25
2.3.5 Other Works on the Limb Darkening Method	39
2.3.6 Mode Identification Using the Radial Velocity and Flux Amplitude Ratio	42
2.3.7 Mode Identification Using Harmonics and the Linear Combination Modes	42

2.4	GD358 HST Observations	44
2.4.1	The Zeroth Order Reflection	44
2.4.2	The UV Observations	51
2.5	The Ground-based Optical Observation of GD358	70
2.6	GD358 Fourier Transform	74
2.6.1	Optical Fourier Transform	74
2.6.2	UV Fourier Transform	76
2.7	Mode Identification of GD358	84
2.7.1	Fourier Transform Ratios	84
2.7.2	Lightcurve Ratios	88
2.7.3	Amplitude Ratios	96
2.7.4	ℓ Identification	98
Chapter 3. Asteroseismology of a Massive DAV BPM37093		107
3.1	Introduction	107
3.2	Observation of BPM37093	116
3.2.1	The UV Data	116
3.2.2	The Ground-Based Optical Data taken with the WET	125
3.3	Fourier Transform	130
3.4	Amplitude Modulation	136
3.5	Application of The Period Distribution Method to BPM37093	142
3.6	Application of the Limb Darkening Method	152
3.6.1	Mode Identification using Amplitude Ratios	152
3.6.2	Mode Identification using the Fourier Transform Ratio	158
3.6.3	Contamination Sources	163
3.6.4	Summary	166
Chapter 4. Summary & Conclusions		168
4.1	Summary & Conclusions	168
4.1.1	GD358 & Its Drastic Amplitude Changes	169
4.1.2	BPM37093 Observations	171
4.1.3	Mode Identification Methods	174
4.1.4	Does the Limb Darkening Method Work?	179

4.1.5	Asteroseismology with the limb darkening method	182
4.2	The New Simultaneous HST & WET Observations of GD358 in May–June, 2000	184
Appendix A. Amplitude Changes in GD358		190
A.1	Changes in the Dominant Mode	190
A.2	Amplitude Estimates of the 423s Mode During the HST Observation	195
Bibliography		202
Vita		208

Table of Tables

2.1	Physical Parameters of GD358 from the Period Distribution Method	22
2.2	Physical Parameters of GD358 from Different Models	57
2.3	Journal of Optical Observations for GD358 in August, 1996 . . .	70
3.1	Journal of Optical Observations of BPM37093	127
3.2	Periods Observed in 1998 and 1999 WET runs	148
4.1	Estimated Crystallization Mass Fraction and Various Physical Parameters	175
4.2	Estimated Number of Orbits Necessary to Achieve 1 and 2σ Detection	186
A.1	Journal of Observations for September 1996 and April 1997 . . .	195

List of Figures

2.1	GD358 Fourier Transform from WET run in 1994	18
2.2	Fine Structure Splitting due to Rotation and Magnetic Field . .	19
2.3	Amplitude ratio vs. Wavelength using Koester's 25,000K DB model.	21
2.4	$\ell = 1$ models for 21000K to 29000K with $\log g = 8.0$	28
2.5	$\ell = 2$ models for 21000K to 29000K with $\log g = 8.0$	29
2.6	$\ell = 1$ models for $\log g = 7.5$ to 8.5 with $T_{\text{eff}} = 22000\text{K}$	30
2.7	$\ell = 1$ models for $\log g = 7.5$ to 8.5 with $T_{\text{eff}} = 23000\text{K}$	31
2.8	$\ell = 1$ models for $\log g = 7.5$ to 8.5 with $T_{\text{eff}} = 24000\text{K}$	32
2.9	$\ell = 1$ models for $\log g = 7.5$ to 8.5 with $T_{\text{eff}} = 25000\text{K}$	33
2.10	$\ell = 1$ models for $\log g = 7.5$ to 8.5 with $T_{\text{eff}} = 26000\text{K}$	34
2.11	$\ell = 1$ models for $\log g = 7.5$ to 8.5 with $T_{\text{eff}} = 27000\text{K}$	35
2.12	$\ell = 1$ models for $\log g = 7.5$ to 8.5 with $T_{\text{eff}} = 28000\text{K}$	36
2.13	$\ell = 1$ models for $\log g = 7.5$ to 8.5 with $T_{\text{eff}} = 29000\text{K}$	37
2.14	$\ell = 2$ models for $\log g = 7.5$ to 8.5 with $T_{\text{eff}} = 26000\text{K}$	38
2.15	Pixel vs. Count rate	46
2.16	Fourier Transform Before and After the Removal of HST's Orbit Effect	48
2.17	Zeroth Order Lightcurve Before and After the HST's Orbit Ef- fect Removal	49
2.18	Final Zeroth Order Lightcurve	50
2.19	zeroth Order Band Pass	52
2.20	DB Model Spectra with $\log g = 8.0$	53
2.21	The Various DB Model Spectra with zeroth Order Bandpass . .	54
2.22	Time Averaged Spectrum of GD358 using Parallax Distance . .	58
2.23	Time Averaged Spectrum of GD358 using Seismological Distance	59
2.24	Time Averaged Spectrum of GD358 using Seismological Distance	60
2.25	Ratio of GD358 Observed UV spectrum and Koester's Model Spectrum	62

2.26	Ratio of GD358 data spectrum and $\log g = 7.75$ Model Spectrum	63
2.27	Ratio of GD358 data spectrum and $\log g = 7.5$ Model Spectrum	64
2.28	Ratio of GD358 data spectrum and $\log g = 8.25$ Model Spectrum	65
2.29	Ratio of GD358 data spectrum and $\log g = 8.5$ Model Spectrum	66
2.30	The Values of sc^2 for Various GD358 Models	67
2.31	UV Lightcurve Before and After the HST's Orbit Effect Removal	68
2.32	Total UV Lightcurve	69
2.33	Optical lightcurve of GD358 in August 1996	71
2.34	Optical lightcurve of GD358 in August 1996	72
2.35	Fourier Transform of GD358 now and then	75
2.36	Running Fourier Transform of GD358 (Part 1)	77
2.37	Running Fourier Transform of GD358 (Part2)	78
2.38	GD358 UV Fourier transforms (Part 1)	80
2.39	GD358 UV Fourier Transforms (Part 2)	81
2.40	GD358 UV Fourier Transforms (Part 3)	82
2.41	GD358 UV Fourier Transforms (Part 4)	83
2.42	Models with different Normalization	85
2.43	Fourier Transform Ratios	87
2.44	Lightcurve and Fourier Transform Ratios	90
2.45	423 s mode Phase across the Wavelength	91
2.46	Fourier Transform of Residual Lightcurves (Part 1)	92
2.47	Fourier Transform of the Residual Lightcurves (Part 2)	93
2.48	Fourier Transform of the Residual Lightcurves (Part 3)	94
2.49	Fourier Transform of the Residual Lightcurve (Part 4)	95
2.50	Amplitude Ratios for 423, 464 and 770s Modes in GD358	97
2.51	Lightcurve, Fourier Transform, and Amplitude Ratios	99
2.52	Data vs. 25500K, $\log g=8.0$ DB model	100
2.53	Simulated Fourier Transform Ratios (case1)	102
2.54	Simulated Fourier Transform Ratios (case2)	103
2.55	Simulated Fourier Transform Ratios (case3)	104
3.1	The Masses and Temperature of DAVs	109
3.2	Amplitude ratio vs. Wavelength using Koester's DA model.	111

3.3	$\ell = 1$ Model Calculations for Different $\log g$	112
3.4	$\ell = 2$ Model Calculations for Different $\log g$	113
3.5	$\ell = 1$ Model Calculations for Different T_{eff}	114
3.6	$\ell = 2$ Model Calculations for Different T_{eff}	115
3.7	BPM37093 time-averaged spectrum.	118
3.8	Observed BPM37093 HST Spectrum and the Model Spectrum .	119
3.9	Observed BPM37093 HST and IUE spectra	120
3.10	Observed BPM37093 HST spectrum divided by the Model Spec- tra	122
3.11	The Lightcurves in the UV gathered by HST (visit 1)	123
3.12	The Lightcurves in the UV gathered by HST (visit 2).	124
3.13	The Lightcurve of Optical data of BPM37093 gathered by the WET (Part1)	128
3.14	The Lightcurve of Optical data of BPM37093 gathered by the WET (Part2)	129
3.15	The Fourier transforms of BPM37093 in the UV and the optical.	132
3.16	Window of BPM37093 in UV and optical	133
3.17	The Fourier Transforms of BPM37093 from 1999 WET run . . .	134
3.18	The Fourier Transforms of BPM37093 (1999 and 1998)	135
3.19	The Running Fourier Transform (part1)	137
3.20	The Running Fourier Transform (part 2)	138
3.21	The Running Window	139
3.22	The Amplitude Modulation during the WET run.	141
3.23	Period Spacing Diagram of BPM37093	149
3.24	Relative (UV to optical) Phases of 4 Periodicities vs. Wavelength for BPM37093	153
3.25	BPM37093's UV/OPT amplitude ratios over wavelength (inde- pendent data points only)	156
3.26	BPM37093's UV/OPT Amplitude Ratios over Wavelength using the Running Lightcurves	157
3.27	The UV to optical Fourier Transform Ratio over UV wavelength for 4 independent Measurements	159
3.28	The UV to optical Fourier Transform Ratio over UV wavelength for 31 Measurements	160
3.29	The Amplitudes of BPM37093's Observed Modes in the UV (es- timated using 4 independent running lightcurves)	161

3.30	The Amplitudes of BPM37093's Observed Modes in the UV (estimated using the 31 running lightcurves)	162
3.31	The Observed, Model and Residual Spectra of BPM37093	165
3.32	The Fourier Transform Ratio and Pulsation Amplitude Ratio of BPM37093	167
4.1	Amplitude ratio vs. Wavelength using Koester's 25,000K DB model.	187
4.2	Amplitude ratio vs. Wavelength using Koester's 11,520K, $\log g = 8.75$ DA model.	188
A.1	Optical lightcurve of GD358 in August 1996	191
A.2	Fourier Transforms of GD358 on the 1st and 2nd day of the Optical Observation	192
A.3	Fourier Transform of an-0034 Before and After Prewhitening . .	193
A.4	GD358 Fourier Transforms at 3 Different Times	196
A.5	GD358 Lightcurves over Time	197
A.6	Amplitude Modulation of 423s Mode	200
A.7	423s mode Amplitude Ratio w/ Different Amplitude Estimates .	201

Chapter 1

Overview

1.1 Overview

1.1.1 White Dwarf Stars

Stars like our sun shine by burning hydrogen in their cores. Eventually, they will run out of fuel to burn and will, after undergoing poorly understood transformations, become white dwarf stars. The stars with initial masses less than $8 - 10M_{\odot}$ ¹ are thought to end up as white dwarf stars (Romanshin & Angel 1980; Weidemann & Koester 1983; Reimers & Koester 1994; Jefferies 1997). This amounts to about 98% of all stars ever formed². As the end point of stellar evolution, the structure of the white dwarf stars provides constraints on the evolution prior to the white dwarf stage. A star's life between its young stage of burning hydrogen in the core (we call these stars, like our sun, main sequence stars), and its ending white dwarf stage is much more complicated than either endpoint, involving burning successively heavy elements in the core, multiple element burning in the star's envelope, and the loss of significant amount of its total mass. It is therefore a great help to be able to constrain what can happen between these two endpoints by learning as much as we can about them.

¹ M_{\odot} stands for the mass of the sun or $2 \times 10^{33}\text{g}$.

²Here we are considering all stars that have nuclear burning in their cores.

The mass distribution of white dwarf stars is very narrow, independent of their surface chemical compositions; their average mass is around $0.6 \pm 0.1 M_{\odot}$ ³. What makes the white dwarf stars have such similar masses despite the wide mass range of their progenitors is not yet understood. But this similarity results in a great advantage in that the white dwarf stars form a very homogeneous class of stars and our discoveries about one white dwarf star are likely applied to other white dwarf stars as well (Robinson 1979; Winget 1986; Bergeron et al. 1995).

White dwarf stars shine by releasing their residual thermal energy from the time when there was nuclear burning inside them and contraction that followed the nuclear burning phase. That is, they are hot objects which give off energy in the form of light, causing them to cool. So, as the white dwarf stars become older, they become both dimmer and cooler. The simple relationship between their temperatures and ages makes them great chronometers and the white dwarf stars have been used to put a limit on the age of our galactic disk of about 9 billion years (Winget et al. 1997; Liebert, Dahn, & Monet 1988; Oswalt et al. 1996; Leggett, Ruiz & Bergeron 1996). Since the oldest (therefore the dimmest) white dwarf stars are still bright enough to be detected by our telescopes on Earth, the cut-off luminosity after which we no longer find any more white dwarf stars is an indicator of how long the galaxy has been around. There simply has not been enough time since the the birth of our galaxy for white dwarf stars to cool and dim past a certain point⁴. By combining this

³The average mass of H atmosphere white dwarf stars (DAs) is $0.59 \pm 0.13 M_{\odot}$ (Bergeron et al. 1995), and for He I dominated white dwarf stars (DBs), $0.585 \pm 0.063 M_{\odot}$ (Beauchamp et al. 1996).

⁴Currently, the known coolest white dwarf star is about $T_{\text{eff}} = 3500\text{K}$.

lower limit of the age of the galactic disk with a theoretical estimate on how long it took from the birth of the universe until galaxies were formed, we can then place a lower limit to the age of the universe (Winget et al. 1987). Current models with this technique estimate this age to be about 11 billion years (Leggett, Bergeron, Ruiz 1998). With many new large telescopes being built and wide field surveys to support them, we will soon be able to increase the number of the known white dwarf stars in both the galactic disk and in the galactic halo. We will therefore also be able to measure the halo age using the white dwarf stars and better understand the process of galaxy formation.

To use white dwarf stars as reliable chronometers, it is important that we understand both their internal structures and how they cool. One process we especially need to better understand is the process of crystallization inside the cores of the coolest and most massive white dwarf stars. Theory predicts that when the white dwarf stars age and become cool enough, the interior will crystallize (Kirshnitz 1960; Abrosikov 1961; Salpeter 1961). Currently the largest source of uncertainties for the white dwarf age estimate (about 1 to 2 billion years) comes from the crystallization process and its associated effects. Release of latent heat is expected in the process of crystallization and depending on the amount and how the heat is released, this can slow the brightness change of white dwarf stars with age. Since our understanding of how the crystallization occurs in the interior of white dwarf stars is uncertain, it adds uncertainties to age estimate of the white dwarf stars. Despite its importance, crystallization inside white dwarf stars have never been directly tested until Kanaan et al. (1992), discovered a massive pulsating white dwarf star BPM37093. Due to its high mass, this star should be substantially crystallized; due to its pulsations,

it should be able to reveal the nature of crystallization to us. In this work, we attempt to constrain the crystallization mass fraction of BPM37093 via the technique of asteroseismology.

As white dwarf stars evolve (and cool), they pulsate in nonradial g-modes when they are in certain temperature ranges called the *instability strips*. Similar to the geologist who studies the structure of the Earth by studying how the waves generated by earthquakes propagate through the Earth’s interior, we can study the structure of the white dwarf stars by studying their g-mode pulsations. We call the normal mode analysis of stars *asteroseismology*. Unlike many objects which we can take apart and see how they are made of, we cannot open up a star to study its interior. We must be less direct. Asteroseismology gives us an unique opportunity to study stellar interiors. Since pulsating white dwarf stars are otherwise normal white dwarf stars, and because they form a very homogeneous group, what we learn from the pulsating white dwarf stars should be applicable to both the pulsating and the non-pulsating white dwarf stars.

1.1.2 Asteroseismology of White Dwarf Stars

The first step in asteroseismology is to match observed pulsation mode periods to those predicted by our best theoretical models. To do this, each observed mode must be labelled by three integers, the radial overtone number k which is the number of pulsation nodes in the radial direction, the spherical harmonic index ℓ which is the total number of surface nodal lines, and the azimuthal quantum number m which is the number of surface nodal lines crossing a line of latitude. The models we use to predict the star’s pulsation periods depend

on such parameters as total mass, effective temperature, chemical composition, envelope masses and core masses. By changing the physical parameters of the model, we get different sets of normal modes. Different sets of stellar parameters can give similar sets of periodicities, but with different sets of (k, ℓ, m) . We must therefore have very accurate mode identifications for asteroseismology to succeed. In particular, the ℓ value is often the most critical identification to have correct.

There are currently four different methods to identify pulsation modes, but we will concentrate our work on what we call *the period distribution method* and *the limb darkening method*. We will not discuss on the third method since it is not as easily applicable to all white dwarf stars⁵. The period distribution method has seen large successes with pulsating white dwarf stars showing many periodicities such as GD358 (Winget et al. 1994) and PG1159–035 (Winget et al. 1991), but has been less successful with stars with only few periodicities. The limb darkening method was first applied by Robinson et al. (1995) and requires data in both the ultraviolet (UV) and optical wavelengths. This method relies on the differences in pulsation amplitude between the optical and the UV, due to limb darkening and geometric cancellation, to identify the modes. It has only been applied to stars after the launch of the Hubble Space Telescope (HST) since the HST is currently the only satellite that can provide us with the UV data we need. Since this method does not rely on the number of modes observed in the star, we can identify the modes for stars with only one

⁵There has been only one star, G117–B15A, studied by the third method probably because it relies on the assumption of mechanism producing the harmonics and the linear combination modes and the method is also not applicable to all white dwarf stars (e.g. we cannot apply this method to white dwarf pulsators which show no harmonics or linear combination modes such as BPM37093.).

pulsation period.

Taking the same idea a bit farther, Clemens, van Kerkwijk & Wu (2000) used not only the continuum but also the observed line profile variations in the DAV pulsator, G29–38, to identify ℓ values of its modes. They also found the amplitude of the radial velocity variation to the light variation is an ℓ indicator. This technique requires time series line profile spectra, and therefore requires a large telescope — the 10m Keck telescope in this case. As more large size telescopes are built and time is easier to obtain, this technique might become more popular in the future.

The forth mode identification method uses the amplitude of the linear combination modes, modes whose frequencies are the sum or difference of the normal modes, and harmonics to identify the ℓ value of the parent modes (Brassard, Fontaine & Wesemael 1995). The theoretical amplitudes come from a theory of how the linear combination modes and the harmonics arise and hence, this theory must be correct in order to correctly identify modes. This group, however, reports reasonable results for at least one star, G117–B15A.

1.1.3 Goal of this Project

In this thesis, we will evaluate two mode identification methods by applying the limb darkening method to GD358 and comparing the results to those of the period distribution method as found in Winget et al. (1994) and Bradley & Winget (1994). Since the number of pulsating white dwarf stars to which we can apply the limb darkening method is larger than those we can apply the period distribution method, it is important we check the consistency of these different methods.

We will also discuss the coordinated ground-based network of telescopes and HST observations of BPM37093. BPM37093 is currently the only star we know that offers us a chance to estimate the crystallization mass fraction inside the star. BPM37093 does not have enough observed pulsation modes to apply the period distribution method. We have to use the HST UV data and the limb darkening method to identify the modes. Also, because of its scientific importance, we decided that we should do everything we can, i.e. attempt to apply both mode identification methods if possible, to identify the modes.

Chapter 2

Toward a Calibration of Two Different Mode Identification Methods

2.1 White Dwarf Stars

Given enough time, we believe $\approx 98\%$ of all stars (stars with initial masses less than about $8 - 10M_{\odot}$ according to Romashin & Angel 1980; Weidemann & Koester 1983; Reimers & Koester 1994; Jefferies 1997) will become white dwarf stars (Weidemann 1990; Kepler & Bradley 1995 and references therein). White dwarf stars therefore contain information about the history of the majority of stars in the galaxy.

White dwarf stars come in two flavors: 75% of the white dwarf stars have H atmosphere (DAs) and the rest are the H-deficient non-DAs, including the DBs, whose atmospheres are dominated by HeI lines (McCook & Sion 1999). In contrast with the masses of their main-sequence progenitors, the mass distribution of the white dwarf stars is amazingly narrow. Recent results show the average mass of the DAs to be $0.59 \pm 0.13M_{\odot}$ (Bergeron et al. 1995), and for the DBs, $0.585 \pm 0.063M_{\odot}$ (Beauchamp et al. 1996). That different chemical composition white dwarf stars have the same mean mass is very striking, and why we see such a narrow mass range is not yet clear. The great advantages of this uniformity, however, is that what we learn from one white dwarf star is

likely to be applicable to the others.

The high surface gravity of white dwarf stars (typically $\log g = 8.0$ for $0.6M_{\odot}$ white dwarf stars) makes them chemically stratified due to diffusion of the heavy elements that produces chemically pure surface layers. Their high gravity coupled with their normally slow rotation, on the order of days (Winget et al. 1991; Winget et al. 1994; Koester et al. 1998), means we can assume they are spherically symmetric to a very good approximation. As most white dwarf stars no longer have any nuclear energy source, their evolution is characterized almost entirely by cooling. Thus, there is a simple relationship between the age of a white dwarf star and its luminosity and temperature: the older a white dwarf star is, the dimmer and cooler it is. Their stratified layers, spherical symmetry and relatively simple energetics make them easy to model compared to their main sequence progenitors, for example.

The reward we get from a deeper understanding of white dwarf stars is huge. The internal structure of white dwarf stars gives us a boundary condition to their prior evolution. The structure of white dwarf stars at different temperatures gives us clues about the physics of matter under extreme conditions (the core is electron degenerate, for example). By determining accurate ages of the white dwarf stars, we can measure the lower limit to the age of the galactic disk. Although the white dwarf stars are intrinsically dim due to their small size, 2249 white dwarf stars have been spectroscopically identified (McCook & Sion 1999) and the development of new instruments, larger telescopes and surveys such as the Sloan Digital Sky Survey (York et al. 2000) will increase the number of white dwarf stars by a factor of 10 to 100 in the future. With this increased sample, we expect to observe a statistically significant number

of white dwarf stars in the galactic halo. These halo white dwarf stars can tell us the age of the halo independent of the ages derived by other methods.

In the next section, we describe how we extract information from the pulsating white dwarf stars and learn about their internal structures using the technique of asteroseismology.

2.2 Asteroseismology

Asteroseismology is the study of pulsating stars through normal mode analysis. Since we cannot directly observe below the stellar photosphere, asteroseismology is one of the most effective ways to study the stellar interior. It has the potential of teaching us the total stellar mass, the core composition, the mass and composition of any stratified layers, the rotation rate, and the nature and size of a magnetic field, for example. The theoretical models we use to derive the above quantities also compute the absolute luminosity of the model. By comparing this with the star's apparent luminosity, we can derive the distance to the star —a distance measurement independent of trigonometric parallax.

Asteroseismological analysis is done in three main steps: (1) observe as many pulsation modes as possible; (2) identify the modes with radial overtone number k , spherical harmonics index, or degree, ℓ and azimuthal quantum number m ; (3) compare the identified observed modes with numerical models. The parameters of the model with the best match to the observed modes are interpreted as the star's physical parameters. The more modes detected and identified, the more accurately we can derive the physical parameters. Detecting pulsation modes is by no means easy, but the required observational techniques are well understood. It is mode identification (determining k , ℓ , and

m for each mode) that is the main difficulty in asteroseismology. Despite extensive observations of several pulsating white dwarf stars, the pulsation modes have only been unambiguously identified for GD358 and PG1159-035. In this chapter, we test the validity of a mode identification technique by comparing its results with the earlier results on GD358.

2.3 Mode Identification Techniques

The pulsation frequencies we observe in the white dwarf pulsators are believed to be nonradial g-modes. There are several lines of evidence which supports this assertion. First, the periods we observe in the pulsating white dwarf stars (100 to 1000s) corresponds to the expected range of periods for nonradial g-mode pulsations (McGraw 1979; Winget et al. 1982; Robinson, Kepler & Nather 1982). Second, Robinson, Kepler & Nather (1982) calculated the phases and amplitudes of nonradial g-modes as a function of wavelengths. Their calculations predicted that pulsation mode phases should be constant across all wavelengths and this has indeed been observationally confirmed. They also calculated how the amplitude of g-mode pulsations would change with respect to wavelength¹ and again observationally confirmed their predictions. When only the DAs were known to pulsate, Winget (1981) predicted that the DBs should also pulsate in nonradial g-modes but at a higher temperature than the DAVs and confirmed this by discovering the first pulsating DB white dwarf star (DBV), GD358 (Winget et al. 1982). The asteroseismological analysis of PG115-035 and GD358 showed very good match between observation and

¹The behavior of the amplitude at different wavelengths is one way to identify the pulsation modes as discussed later in this section.

nonradial g-mode pulsation theory (Winget et al. 1991; Winget et al. 1994). Kepler (1984) showed the pulsations are not r-modes, which also have similar period range. These evidence strongly supports that the pulsations observed in white dwarf pulsators are nonradial g-modes.

Since the white dwarf stars have high surface gravities ($\log g = 8.0$ for a typical $0.6M_{\odot}$ white dwarf) and relatively slow rotation (Kepler 1984; Kepler, Robinson & Nather 1983; Pilachowski & Milkey 1987; Winget et al. 1991; Winget et al. 1994; Koester et al. 1998), these nonradial g-modes can be described by the spherical harmonics $Y_{\ell m}(\theta, \phi)$, and the radial overtone number k . Each mode is labeled by three integers: the spherical harmonic index, ℓ , which counts the number of nodal lines wrapping around the surface of the star; the azimuthal quantum number, m , which is the number of nodal lines that cross the poles; and the radial overtone number, k , the number of nodes in the radial direction. In order to extract accurate information about stellar interiors via asteroseismology, correct identification of these three integers, especially the ℓ value, is crucial.

Ever since the birth of the Whole Earth Telescope (Nather et al. 1990) in 1987, the mode identification method for pulsating white dwarf stars has been dominated by the method we will hereafter call the “*period distribution method*” (Winget et al. 1991; Winget et al. 1994). Robinson et al. (1995), on the other hand, successfully demonstrated another method which we will call the “*limb darkening method*”. Each method has been used individually, but they have not been tested or calibrated against each other. In this chapter, we compare these two methods by applying the limb darkening method to GD358, the prototype of the DBVs, whose modes were successfully identified by the

Whole Earth Telescope (Winget et al. 1994) using the period distribution method. First, we will briefly describe how both methods work.

2.3.1 The Period Distribution Method using the WET

One way to identify and label pulsation modes is by analyzing patterns in the period and frequency distribution of the modes. This technique has been successfully applied by the Whole Earth Telescope (WET) using their extensive data sets. The WET is a network of telescopes — a dozen or so, spread across different longitudes in both the Northern and Southern hemispheres — and astronomers around the world who are interested in studying pulsating white dwarf stars and other variable stars. By spacing the participating observatories around the globe, the WET strives to ensure at least one site in the network is always in darkness, observing the target variable. The WET typically observes a star for about 2 weeks, gathering long, ideally continuous, lightcurves. Fourier transform of the lightcurves are used to look for periodicities in the lightcurves.

In an ideal world where we have an infinite, uninterrupted lightcurve, a pulsation will show up as a single peak in the Fourier transform. But if there are gaps in the data (a lightcurve from a single telescope taken over many nights, for instance, will have a periodic gap due to the daily sunrise), then the Fourier transform will show not a single peak corresponding to a single pulsation, but also many alias peaks surrounding the pulsation peak, with the spacing between the peaks corresponding to one cycle per day, the interval between gaps in the lightcurve. In cases where there are many pulsation periods closely spaced, we end up with a forest of peaks in the Fourier transform and it is very difficult to determine which peaks correspond to the pulsations of the star, and which

peaks are just aliases due to gaps in the lightcurves.

To solve this problem, Ed Nather and his collaborators organized a network of telescopes around the globe to observe a target 24 hours a day, for up to weeks, to beat down the forest of confusing aliases. This is the WET. Besides eliminating the alias peaks, the WET produces high resolution, high S/N data which enable detections of low amplitude modes and resolves modes closely spaced in frequency.

According to pulsation theory (see for example Bradley, Winget & Wood 1993; Winget et al. 1991; Kawaler & Bradley 1994), the average period difference between consecutive k and fixed ℓ and m modes tell us the total mass of the star. Pulsation modes with the same k and ℓ , but different m , have the same frequency unless stellar rotation and/or a magnetic field breaks up its azimuthal symmetry. In the case of rotation, the symmetry-breaking of an $\ell = 1$ mode will result in a equally spaced triplet of modes, with peaks corresponding to $m = 0, \pm 1$ in the Fourier transform. The separation between the triplets is determined by the speed of the rotation. By observing this fine structure splitting caused by stellar rotation and accurately measuring the period spacing between consecutive radial overtone k modes, we identify the ℓ and m values of the modes. This is what we have called the *period distribution method*. It is a very powerful technique when there are many modes present in the star, such as those observed in GD358 as well as PG1159-035 (a hot, $T_{\text{eff}} = 140000\text{K}$, H-deficient white dwarf star [Winget et al. 1991; Winget et al. 1994]), but it is less effective in stars in which we do not observe large numbers of detectable modes. In the next section, we summarize how this method was applied to GD358 to identify its observed modes.

2.3.2 The Mode Identification of GD358 by the Period Distribution Method

As an example of how mode identification is done using the period distribution method, we briefly summarize the previous WET results of GD358. The details of how this star was solved is given in Winget et al. (1994) and Bradley & Winget (1994).

Period Spacings

In the asymptotic limit of large k , a nonradial g-mode's pulsation period is,

$$P_{k\ell} = C \times \frac{k}{\sqrt{\ell(\ell+1)}} + \text{constant} \quad (2.1)$$

where C is a constant that depends on the structure, mainly on the total mass, of the star (Winget et al. 1991; Bradley 1993). This relation leads us to a constant period spacing between consecutive k and fixed ℓ modes, $\Delta P = C/\sqrt{\ell(\ell+1)}$. As the constant C depends on the total stellar mass, a measurement of the period spacing give us an estimate of the total stellar mass.

We have yet to observe strictly uniform period spacings in a white dwarf star, though. This is because white dwarf stars are not chemically homogeneous from the center to the surface. For a $0.6M_{\odot}$ DB white dwarf star, for example, we believe there is a core made of C and O and a nearly pure He envelope on top of it. The chemical transition zone between He and C can sometimes influence the position of the radial nodes of the normal pulsation modes. Compared to the modes without a node at the transition zone, the modes with nodes at the transition zone have smaller kinetic energies (Winget, Van Horn, & Hansen 1981). Because it takes less energy to oscillate when a node is at the chemical

transition zone, when there is a node close to the transition zone, it moves towards the transition zone. This shifting of a node affects the mode’s period. A mode whose period has been affected in this manner is called a “trapped mode”. Thus, the period spacings will not be precisely uniform. The average period spacing will still give us a good estimate of the total stellar mass, but the details of the observed non-uniform period spacings will reveal the details of the nonhomogenieties in the star’s interior — in this example, the size and location of the He envelope of the star.

In 1990 and again in 1994, the WET observed GD358 for about 11 days. Winget et al. (1994) identified about 180 periodicities in the Fourier transform. Figure 2.1 shows the Fourier transform of the 1994 WET run which shows slightly different amplitudes, but nearly identical frequencies, as those observed in 1990. In the frequency region where the largest peaks are ($1000\mu\text{Hz}$ to $2400\mu\text{Hz}$), they saw a series of triplet peaks. The spacings between one triplet to the next were close to being equal in period and consistent with the theory of equal period spacing between consecutive radial overtone modes of a given ℓ . The spacings within each triplet were also similar to each other. These observations imply the observed modes are of the same ℓ . The deviations from equal period spacing were accounted for by the fact that the star is not entirely homogeneous, i.e. it’s a typically stratified white dwarf star. But what is the ℓ value of the observed modes? Bradley & Winget (1994) found, by assuming all observed modes are $\ell = 1$, the best fit model to the deviations from uniform period spacing gave a He layer mass of $\log M_{\text{He}}/M_{\star} = -5.7^{+0.18}_{-0.30}$, while the average period spacing gave a total stellar mass of $0.61 \pm 0.03 M_{\odot}$. If all modes observed were assumed to be $\ell = 2$, then the best match to the observed

period spacing resulted in a model with a luminosity, and hence distance, wildly inconsistent with prior parallax measurement on this star. Thus they concluded the modes must be $\ell = 1$.

Fine Structure Splitting

As already described, normal modes with the same ℓ and k have a $2\ell + 1$ m-degeneracy unless the azimuthal symmetry is broken. In the case of stellar rotation breaking the symmetry, the size of the splitting gives us the rotation rate of the star, and should be constant for all modes with same ℓ if the star is rotating as a solid body. In the case of differential rotation, the splitting will be different from one k to another reflecting the rotation rate at different parts in the star.

A magnetic field is another effect that can break the azimuthal symmetry. Since the magnetic field will force any displacement of material that crosses over the magnetic field line back to its place, it acts as an additional restoring force to the pulsation modes. It has been shown [See for example, Montgomery (1994) for a nice derivation] that this causes the frequencies of the mode to be shifted proportionally to the square of m , thus $m = 1$ and $m = -1$ will shift their frequencies the same amount. Combining the two effects, the stellar rotation and a magnetic field, a triplet of modes will still be seen, but with unequal splitting between components even in first order. In Figure 2.2 we show graphically how first order stellar rotation and magnetic fields both affect the triplet splittings.

Observed triplets do not always indicate the modes are $\ell = 1$. The star's inclination can systematically change the observed amplitudes of modes

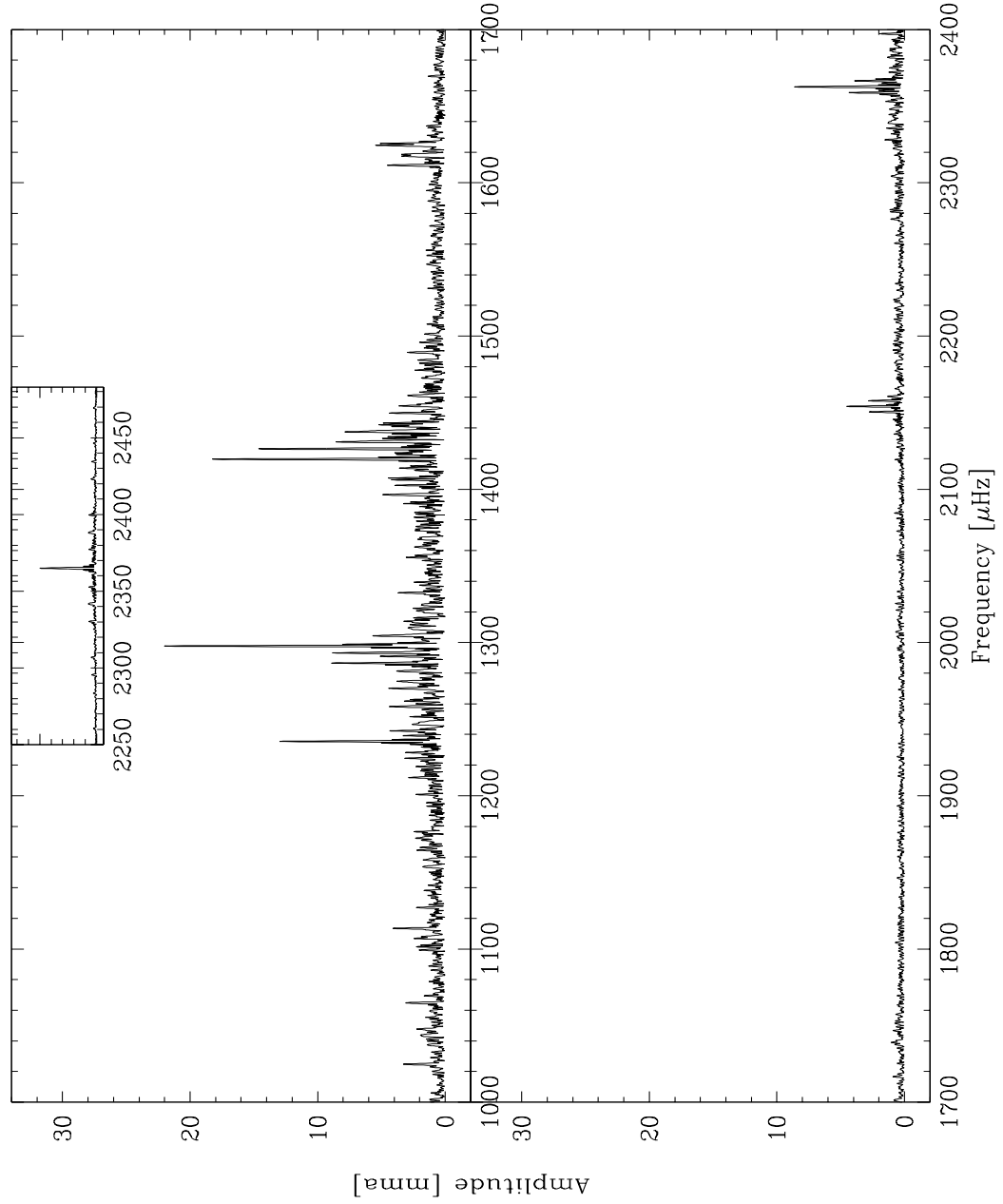


Figure 2.1: GD358 Fourier Transform from the WET run in 1994. Although the amplitudes of the modes are slightly different from the 1990 WET Fourier transform, the same period spacing and triplet structures are observed here. Inside the small box on the top shows the Fourier transform of a sinusoid sampled the same way the data was sampled during the 1994 WET run.

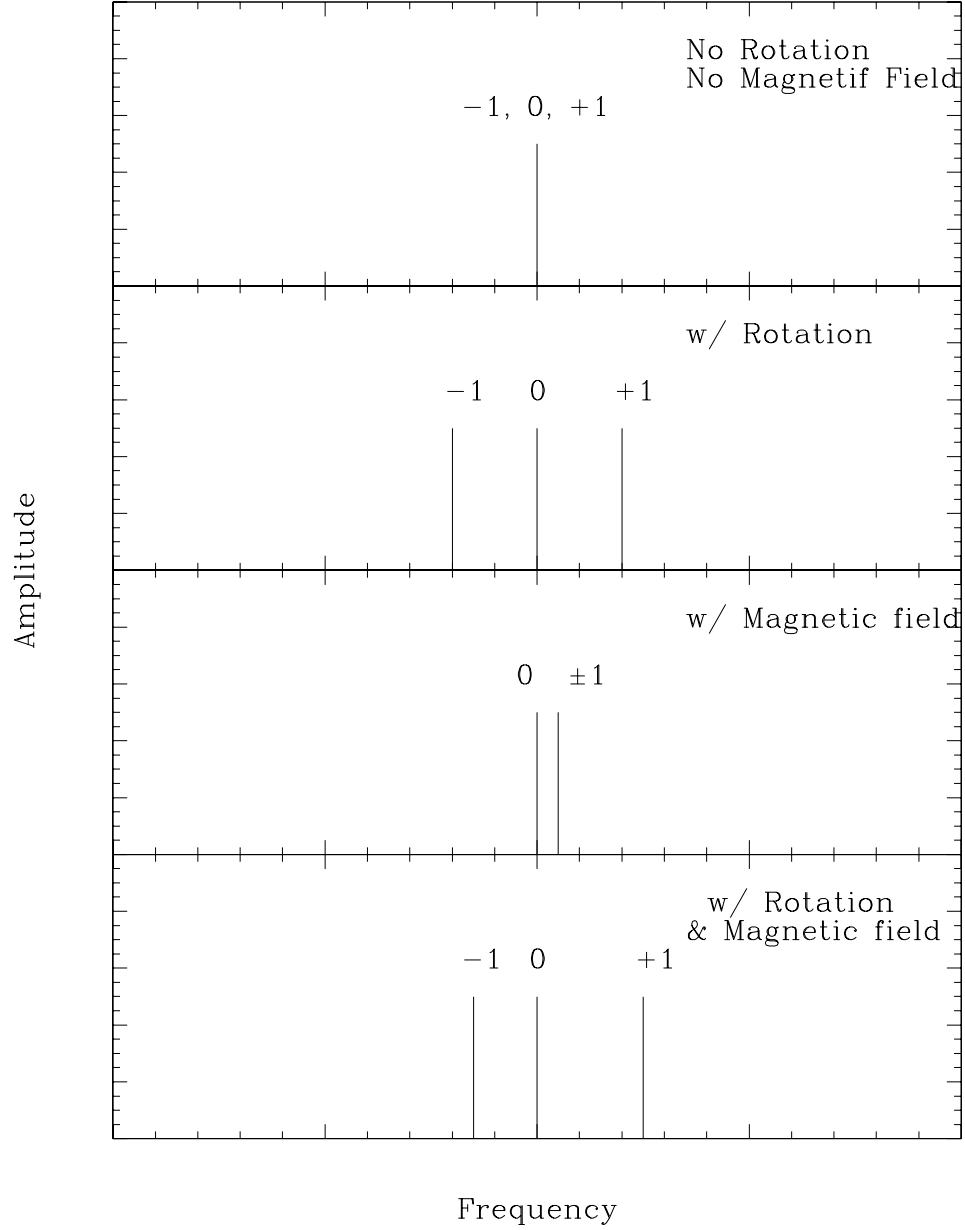


Figure 2.2: Fine structure splitting due to rotation and magnetic field. Assume we have a $\ell = 1$ mode. On top we show when there is nothing to break the azimuthal symmetry. The second panel shows how the rotation affects the frequencies of different m modes. The triplet is equally spaced here. In the third panel, we show how the magnetic field affects the frequencies. As the splitting is proportional to the square of m , $m = \pm 1$ have same frequencies. The fourth panel shows the triplet when there are both rotation and magnetic field. The splitting becomes unequally spaced.

with certain m values to become too small to be observed. For example, it is possible to have only 3 out of the 5 possible different m modes of an $\ell = 2$ pulsation show up in the Fourier transform. In the case of GD358, the period spacing indicated that the observed modes are all $\ell = 1$, and the fine structure triplets can be explained by stellar rotation and magnetic field breaking the symmetry of $\ell = 1$ modes. Note, however, that in PG1159-035 (Winget et al. 1991), we observed $\ell = 1$ modes with 3 peaks and $\ell = 2$ modes with 5 peaks in the Fourier transform, exactly as theory predicts. Moreover, the ratio of the fine structure splitting of the $\ell = 1$ and the $\ell = 2$ modes also agreed well with the asymptotic theory (Winget et al. 1991).

The observed GD358 triplet spacings between the $m = 0$ and $m = 1$ modes were consistently larger for all k 's than those between the $m = 0$ to $m = -1$ modes. These differences can be an indication of the presence of a magnetic field and detailed calculations indicated that if so, the magnetic field strength is $1300 \pm 300\text{G}$. See Montgomery (1993) for detailed calculations of the effect of magnetic fields on the pulsation frequencies of white dwarf stars.

From Winget et al. (1994), the best fit model to the WET 1990 observations gives physical parameters of GD358 as shown in Table 2.1. The table represents one of the best cases of what asteroseismology can achieve with accurate mode identification.

2.3.3 The Limb Darkening Method

Robinson et al. (1995) developed a mode identification method we call “*the limb darkening method*” and applied it to G117-B15A, a DAV. The nonradial g-modes cause bright and dim patches on the stellar surface (which can be

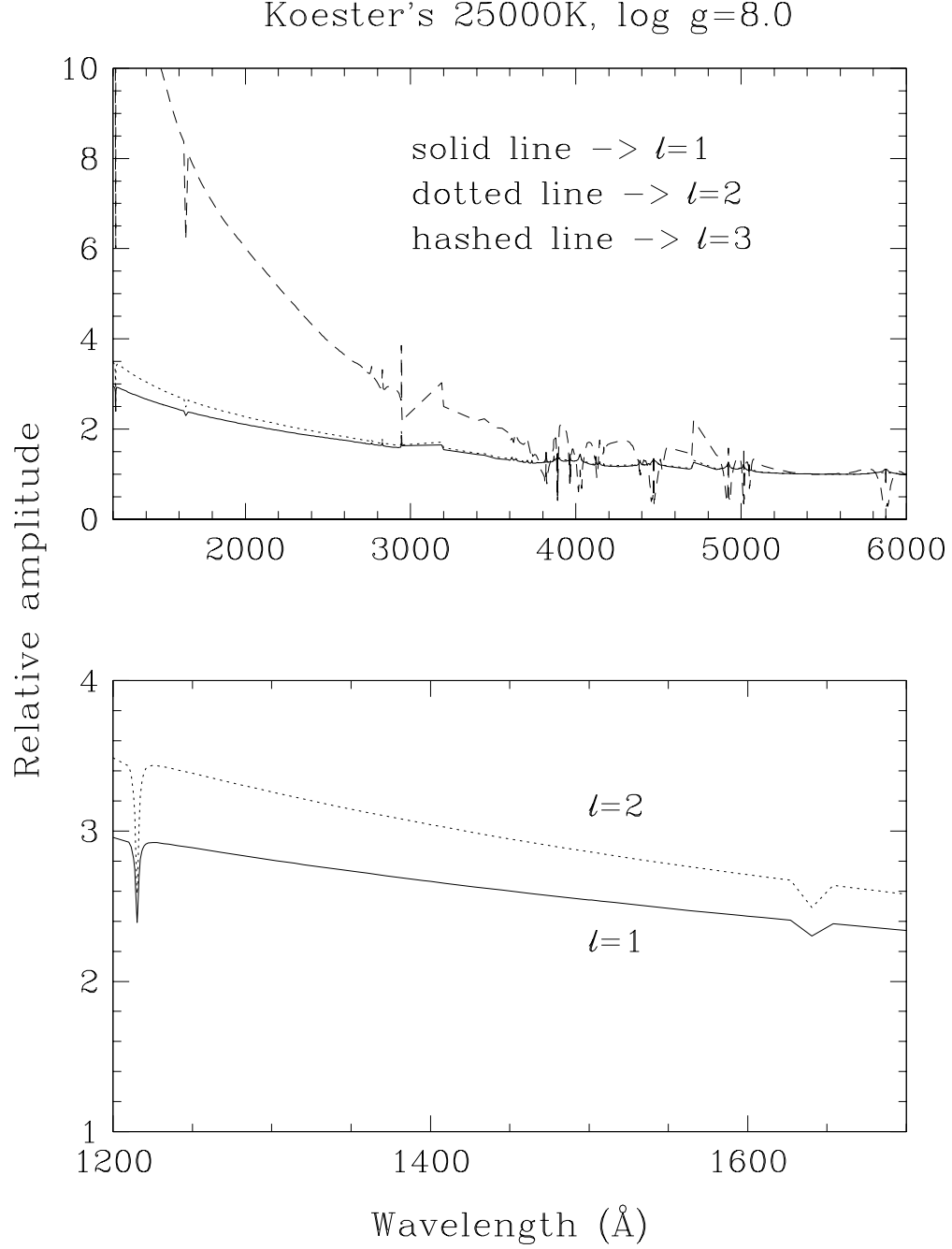


Figure 2.3: DB model calculations of the pulsation amplitude at each wavelength compared to that at 5500 Å. Different ℓ -value modes have different wavelength dependences. The model plotted has parameters of $T_{\text{eff}} = 25000\text{K}$ and $\log g = 8.0$. The amplitudes have been normalized at 5500 Å.

Physical Parameters	Values
$T_{\text{eff}}(\text{k})$	$24000 \pm 1000\text{K}$
$\log g$	8.0 ± 0.1
M/M_{\odot}	0.61 ± 0.034
$\log(L/L_{\odot})$	$-1.30^{+0.09}_{-0.12}$
Distance	$42 \pm 3 \text{ pc}$
$\log M_{\text{He}}/M_{\star}$	$-5.70^{+0.18}_{-0.30}$
Chemical transition zone thickness	$\approx 8 \text{ pressure scale heights}$
Magnetic Field Strength	$1300 \pm 300\text{G}$
Rotation	$0.89 - 1.6 \text{ days}$

Table 2.1: Physical parameters derived from the best fit model to GD358's 1990 WET data using the period distribution method.

described by the spherical harmonics) which change over time. The lightcurves we observe are the integrated fluxes over the stellar disk changing vs. time. Thus, there is always a geometric cancellation effect between the bright and dim patches that plays a role in determining the observed pulsation amplitudes.

There is (at least) one additional effect which changes the observed pulsation mode amplitudes: limb darkening. Photons coming from the stellar limb have a thicker envelope to travel through than do the photons coming from the center of the disk and short wavelength photons tend to be absorbed more often as they travel to the star's surface than do the longer wavelength photons. These two effects result in fewer photons getting out from the limb of the disk while the stellar disk itself appears smaller in the UV than it does in the optical. The first effect is simply limb darkening, but the second effect causes the amount of limb darkening to be a function of wavelength.

Now combining geometric cancellation with limb darkening is where we begin to see the use of all this. As the effective disk size becomes smaller with

wavelength, geometric cancellation is less effective and pulsation amplitudes in the UV become larger than those in the optical. How large the differences are depends on the geometry of the bright and dim patches, i.e. the ℓ values. Thus, modes with different ℓ s have different amplitudes in the UV compared to those in the optical. Figure 2.3 show the results of theoretical calculations using Detlev Koester's model atmospheres described in Finley, Koester, & Allard (1997). The model displayed has an effective temperature $T_{\text{eff}} = 25000\text{K}$ and the logarithm of its surface gravity $\log g = 8.0$. (The same model describing the time averaged UV continuum is in Figure 2.22 to 2.24 later in this chapter.) The pulsation amplitudes have been normalized by the amplitude at 5500\AA . Regardless of a pulsation mode's amplitude, period, or the inclination of its pulsation axis to the line of sight, for a given temperature and surface gravity of the model, the amplitude ratio $\text{Amp}(\lambda_1)/\text{Amp}(\lambda_2)$ is a function only of the mode's ℓ value. Thus we can determine the ℓ value of a pulsation mode simply by measuring the mode's amplitude at two different wavelengths. To maximize the discernible differences, we would be wise to choose one wavelength in the UV and one in the optical. This is the essence of the limb darkening method. The greatest advantage of the limb darkening technique is that the number of pulsation modes observed is not important; we can determine the ℓ value even for a star with a single mode. In the traditional WET approach, we need to observe many modes in order to discern the telltale patterns of equal frequency splittings and equal period spacings. Since most white dwarf pulsators are not observed to have the hundreds of modes as observed in PG1159-035 and GD358, the limb darkening technique may be our best hope of mode identification for most white dwarf pulsators.

Figure 2.3 implies equation 2.2 below which illustrates other notable effects besides the ℓ -dependent amplitude ratio. If all the modes observed in a star are of the same ℓ value, the ratio of the lightcurves obtained at different wavelengths, as well as the ratio of the pulsation spectra (the Fourier transform), should also be ℓ -dependent. The relative amplitude, r_ℓ , defined in the following equation,

$$\frac{Amp(\lambda_1)}{Amp(\lambda_2)} = r_\ell \quad (2.2)$$

can be rewritten to,

$$Amp(\lambda_1) = r_\ell \times Amp(\lambda_2) \quad (2.3)$$

where

$Amp(\lambda_1)$: amplitude of a mode at wavelength λ_1 and

$Amp(\lambda_2)$: amplitude of a mode at wavelength λ_2 .

For the nonradial g-mode pulsations of the variable white dwarf stars, the phases of the pulsation modes are expected to be constant over wavelength because the light variations are caused only by the effect of a changing temperature on the surface of the star; geometric distortion from the pulsations is negligible (Robinson, Kepler & Nather 1982). If the star only pulsates in one ℓ , equation 2.3 tells us that when a lightcurve shows a peak at a given time in one wavelength, the lightcurve in another wavelength will also show a peak simultaneously. In other words, equation 2.4 holds for all points in the lightcurves:

$$\delta I(\lambda_1)_i = r_\ell \times \delta I(\lambda_2)_i \quad (2.4)$$

and also,

$$FT(\lambda_1)_i = r_\ell \times FT(\lambda_2)_i \quad (2.5)$$

where

$\delta I(\lambda_1)_i$: The value of i^{th} point in lightcurve at wavelength λ_1

$\delta I(\lambda_2)_i$: The value of i^{th} point in lightcurve at wavelength λ_2

$FT(\lambda_1)_i$: The value of i^{th} point in Fourier transform at wavelength λ_1

$FT(\lambda_2)_i$: The value of i^{th} point in Fourier transform at wavelength λ_2

Since λ_1 and λ_2 can be any wavelength, we will use λ_1 to be somewhere in the UV where we can observe with the Hubble Space Telescope (HST) (from roughly 1100 Å to 2600 Å) and $\lambda_2 = 5500\text{Å}$, the optical wavelength used in our model calculation and close to the observed wavelength from the ground. The calculated r_ℓ is close to unity when there is not much difference between λ_1 and λ_2 , but for $\lambda_1 = 1200\text{Å}$ and $\lambda_2 = 5500\text{Å}$, for example, it is expected to be close to 3.0 for an $\ell = 1$ mode and around 3.5 for an $\ell = 2$ mode in a typical DBV model with $T_{\text{eff}} = 25000\text{K}$ and $\log g = 8.0$.

To summarize, the limb darkening method can give us the following information: (1) the ℓ value of each individual mode by plotting the mode's amplitude ratio vs. wavelength. and/or (2) the ℓ value dominating the total lightcurve using the ratios of the Fourier transforms and lightcurves at different wavelengths. The method uses the assumption that the observed pulsation mode can be described by nonradial modes whose surface brightness are described by the spherical harmonics.

2.3.4 Obtaining the Lightcurve and Fourier Transform Ratios

As we discuss in a later section, the reduced lightcurves are in relative fractional intensities and thus the mean brightness level is set to 0. Calculating point by

point lightcurve ratios can therefore result in some of the ratios diverging. The Fourier transform ratios suffer similarly since at least in theory, at frequencies where there are no periodicities in the lightcurves, the amplitudes in the Fourier transforms are 0. In reality, the noise in the data will result in non-zero values throughout the frequency range of our interest. In order to avoid getting divergence problems while calculating the lightcurve ratios however, we had to use the following method. The notations are the same as used earlier in this section (e.g. r_ℓ : the lightcurve ratio). We first define χ^2 as follows.

$$\chi^2 = \sum_i \{\delta I(\lambda_1)_i - r_\ell \times \delta I(\lambda_2)_i\}^2 \quad (2.6)$$

We are looking for the r_ℓ that will minimize χ^2 . This can be done by obtaining an r_ℓ that will satisfy,

$$\frac{\partial \chi^2}{\partial r_\ell} = 0 \quad (2.7)$$

Solving equation 2.7 for r_ℓ , we get

$$r_\ell = \frac{\sum_i \delta I(\lambda_1)_i \times \delta I(\lambda_2)_i}{\sum_i \delta I(\lambda_2)_i^2} \quad (2.8)$$

Similarly, for the Fourier transform ratios,

$$r_\ell = \frac{\sum_i FT(\lambda_1)_i \times FT(\lambda_2)_i}{\sum_i FT(\lambda_2)_i^2} \quad (2.9)$$

We therefore calculated all our lightcurve and Fourier transform ratios using equations 2.8 and 2.9, avoiding the possibly messy point-by-point divisions.

Koester's Models

Detlev Koester has provided us with a grid of DB models with surface gravities of $\log g = 7.50, 7.75, 8.00, 8.25$, and 8.50 . At each surface gravity, there are models with effective temperatures ranging from $T_{\text{eff}} = 20500\text{K}$ to 29500K

at intervals of 500K. We will use this model grid to match our observations. Ideally, we would solve for the effective temperature, surface gravity and ℓ value solely from the amplitude ratio. But we find the situation much simpler than this when we compare the models. The differences in the $\ell = 1$ models between $T_{\text{eff}} = 29000\text{K}$ and $T_{\text{eff}} = 24000\text{K}$ with $\log g = 8.0$, for instance, are so small that it would not be possible to distinguish them from each other with current observational accuracies (Figure 2.4). Also, varying the surface gravity from $\log g = 7.5$ to 8.25 has little effect on the calculated ratios for models with temperature higher than $T_{\text{eff}} = 25500\text{K}$. Figures 2.6 to 2.13 show $\ell = 1$ modes from models with different surface gravities, for effective temperatures of 22000K to 29000K in 1000K steps. For T_{eff} higher than 25500K , the calculated ratios are essentially insensitive to the surface gravity. We see a similar trend for the theoretical $\ell = 2$ modes (Figure 2.14). These results implies that we can identify the mode without the knowledge of T_{eff} and $\log g$ as long as the star has $T_{\text{eff}} \geq 25500\text{K}$, or as long as it has $T_{\text{eff}} \geq 25000\text{K}$ and $\log g \leq 8.25$ as anticipated for GD358 based on the optical spectra of Beauchamp et al. (1999) and high resolution UV spectra of Provencal et al. (2000). Once the modes are identified, we can compare the data and the model's normal mode periods to find out which model has the periods of the modes observed as what ℓ values. The best fit model found this way will give us physical parameters, including T_{eff} and $\log g$, which are identified as the star's.

We note that we have an independent way to constrain T_{eff} and $\log g$ from our data. As we will describe in the next section, the UV data come in the form of time series spectra. By summing the individual spectra over time, we obtain a high quality UV spectrum (Figure 2.22) which can be used

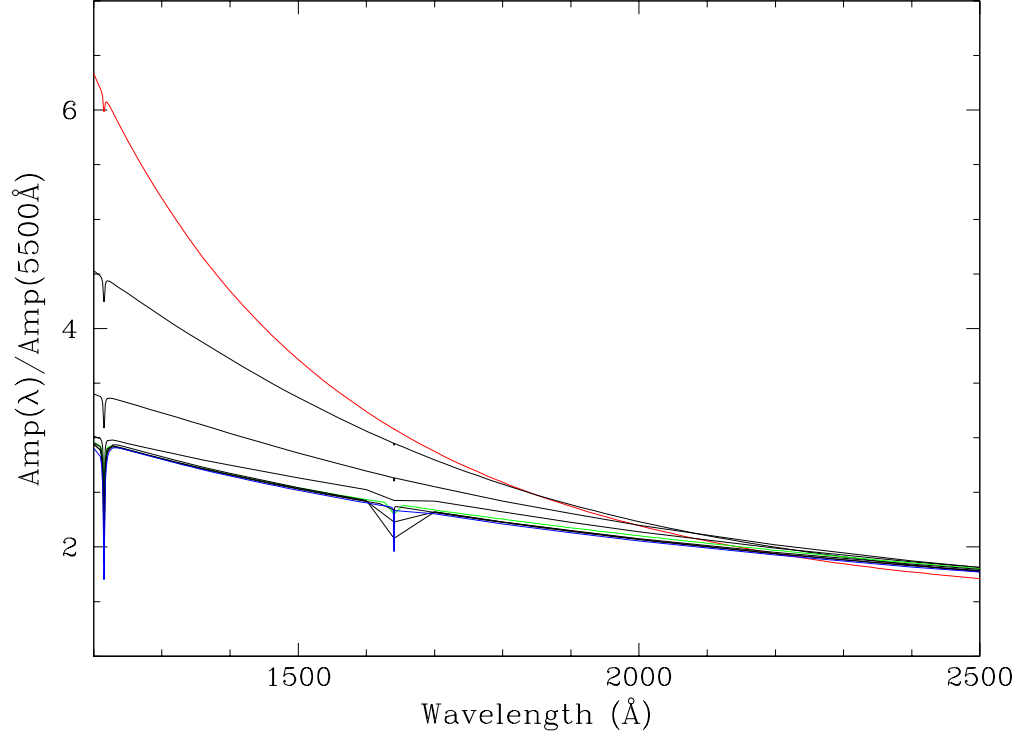


Figure 2.4: The amplitude ratios for $\ell = 1$ DB models with T_{eff} ranging from 21000K to 29000K in 1000K increments with $\log g = 8.0$. The 21000K model is in red, the 25000K model is in green and the 29000K model is in blue. It requires extremely accurate amplitude measurements to observationally tell the difference between the 24000K and 29000K models.

to determine T_{eff} and $\log g$ of the star. It will be interesting to compare these T_{eff} and $\log g$ to those obtained by other methods.

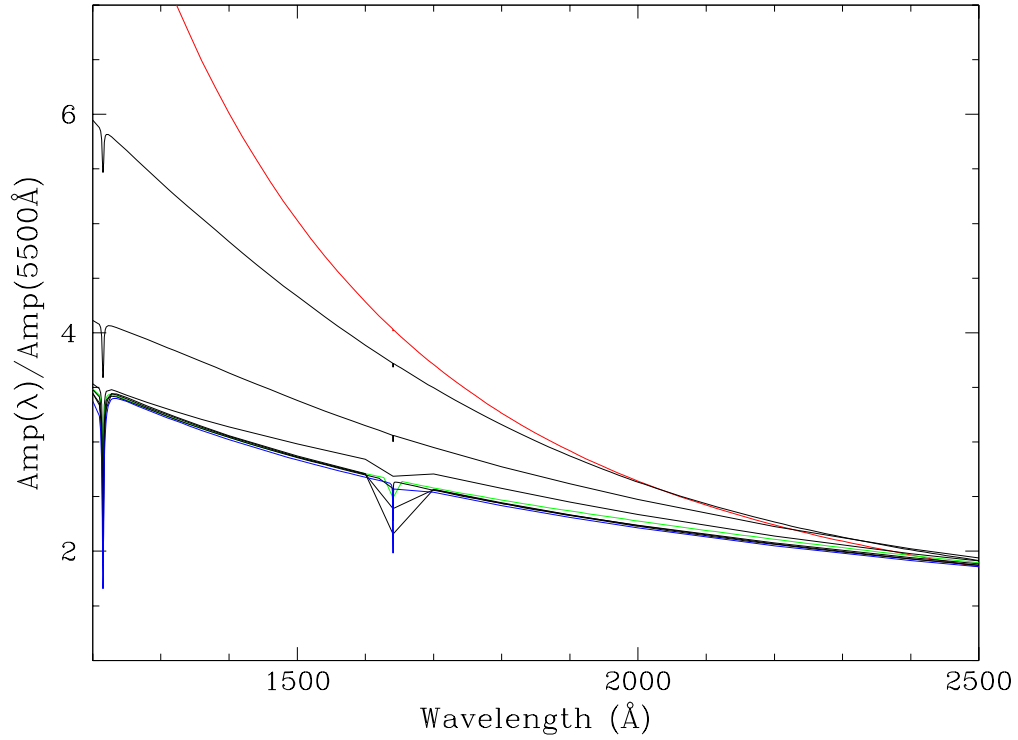


Figure 2.5: The amplitude ratios for $\ell = 2$ DB model with T_{eff} ranging from 21000K to 29000K in 1000K increments with $\log g = 8.0$. The 21000K model is in red, the 25000K model is in green and the 29000K model is in blue. It requires extremely accurate amplitude measurements to observationally tell the difference between the 24000K and 29000K models.

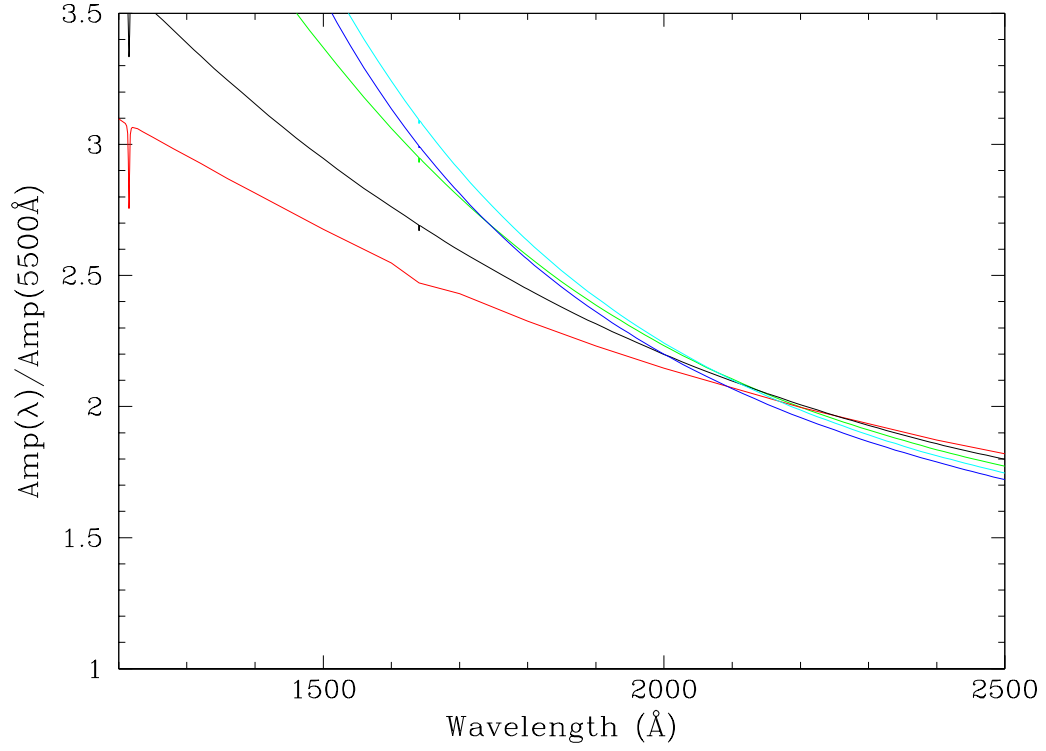


Figure 2.6: The amplitude ratios for $\ell = 1$ DB model with surface gravities ranging from $\log g = 7.5$ (red), 7.75 (black), 8.00 (green), 8.25 (cyan), and 8.50 (blue). All models have $T_{\text{eff}} = 22000\text{K}$.

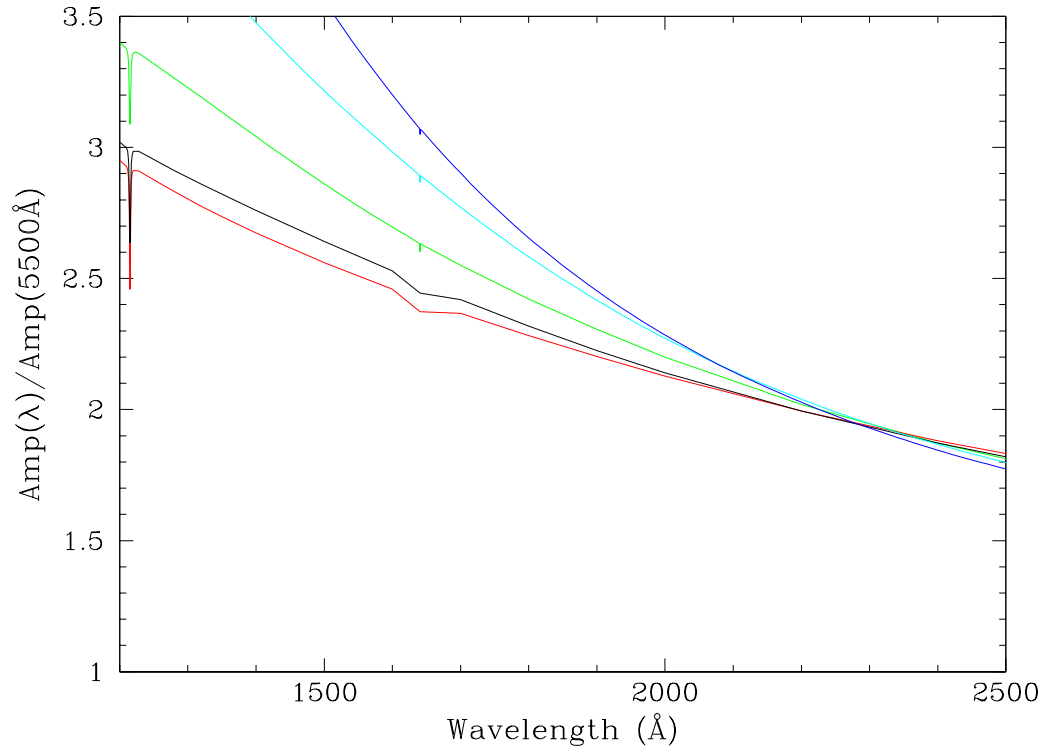


Figure 2.7: The amplitude ratios for a $\ell = 1$ DB models with surface gravities ranging from $\log g = 7.5$ (red), 7.75 (black), 8.00 (green), 8.25 (cyan), and 8.50 (blue). All models have $T_{\text{eff}} = 23000\text{K}$.

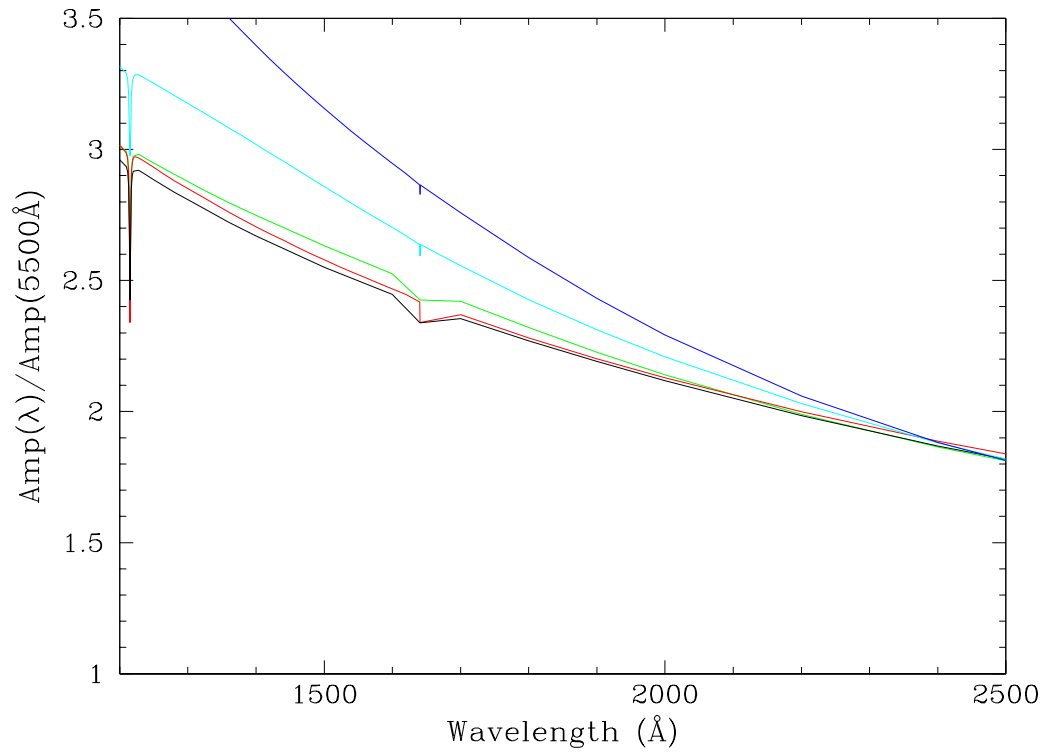


Figure 2.8: The amplitude ratios for a $\ell = 1$ DB models with surface gravities ranging from $\log g = 7.5$ (red), 7.75 (black), 8.00 (green), 8.25 (cyan), and 8.50 (blue). All models have $T_{\text{eff}} = 24000\text{K}$.

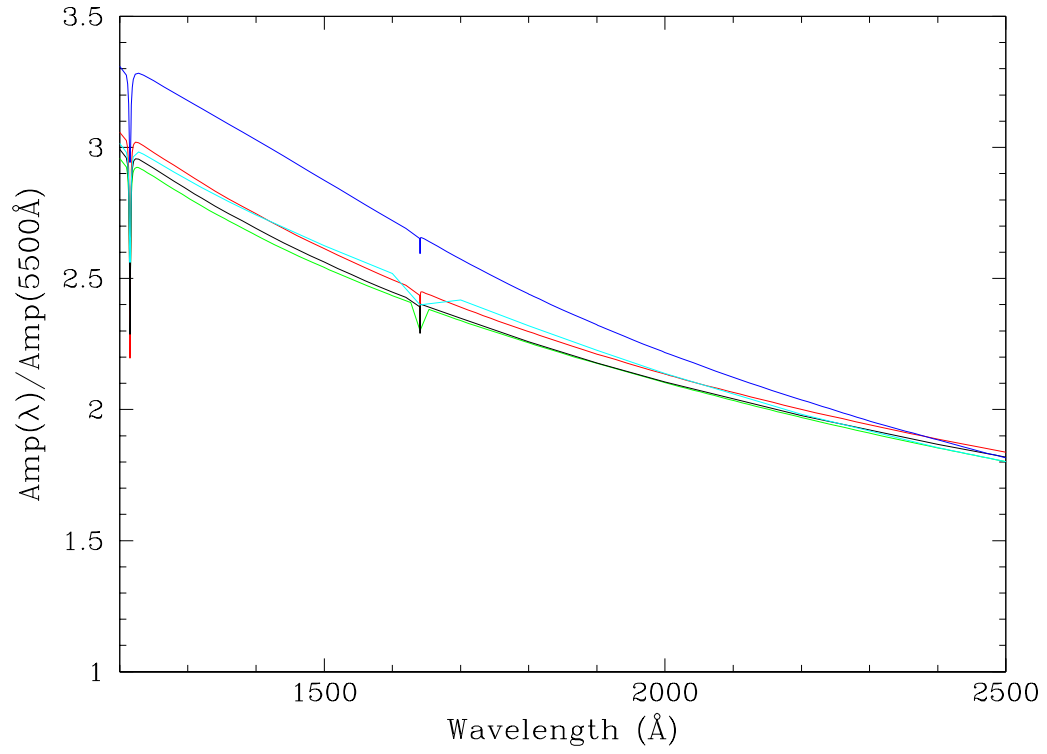


Figure 2.9: The amplitude ratios for a $\ell = 1$ DB models with surface gravities ranging from $\log g = 7.5$ (red), 7.75 (black), 8.00 (green), 8.25 (cyan), and 8.50 (blue). All models have $T_{\text{eff}} = 25000\text{K}$.

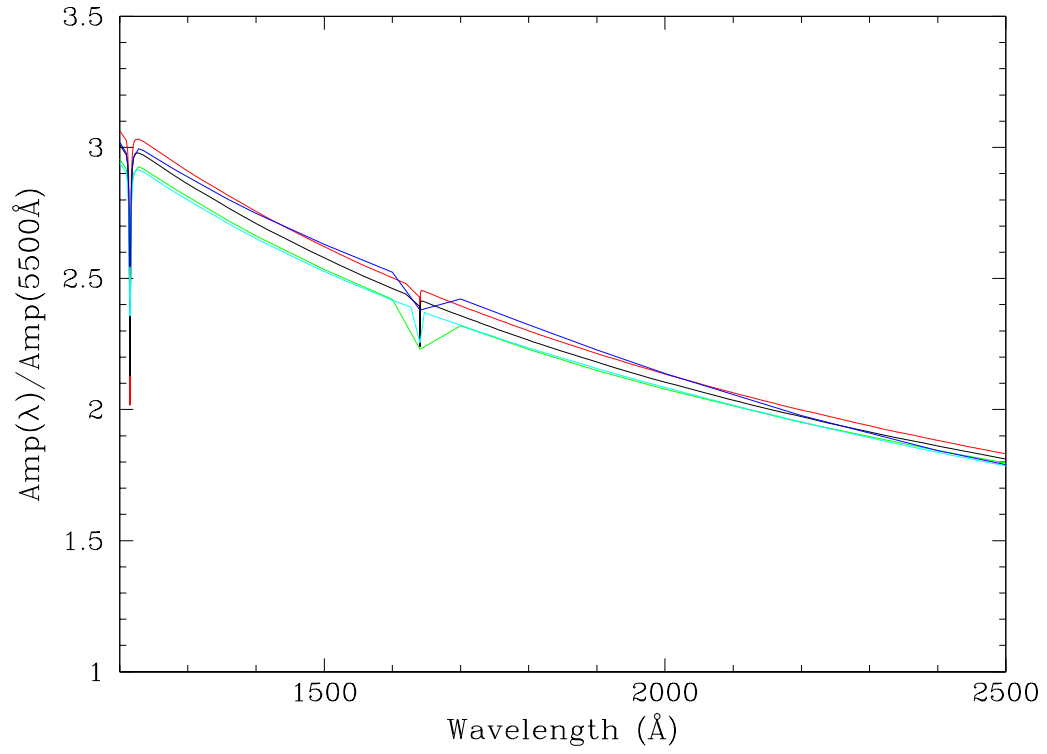


Figure 2.10: The amplitude ratios for a $\ell = 1$ DB models with surface gravities ranging from $\log g = 7.5$ (red), 7.75 (black), 8.00 (green), 8.25 (cyan), and 8.50 (blue). All models have $T_{\text{eff}} = 26000\text{K}$.

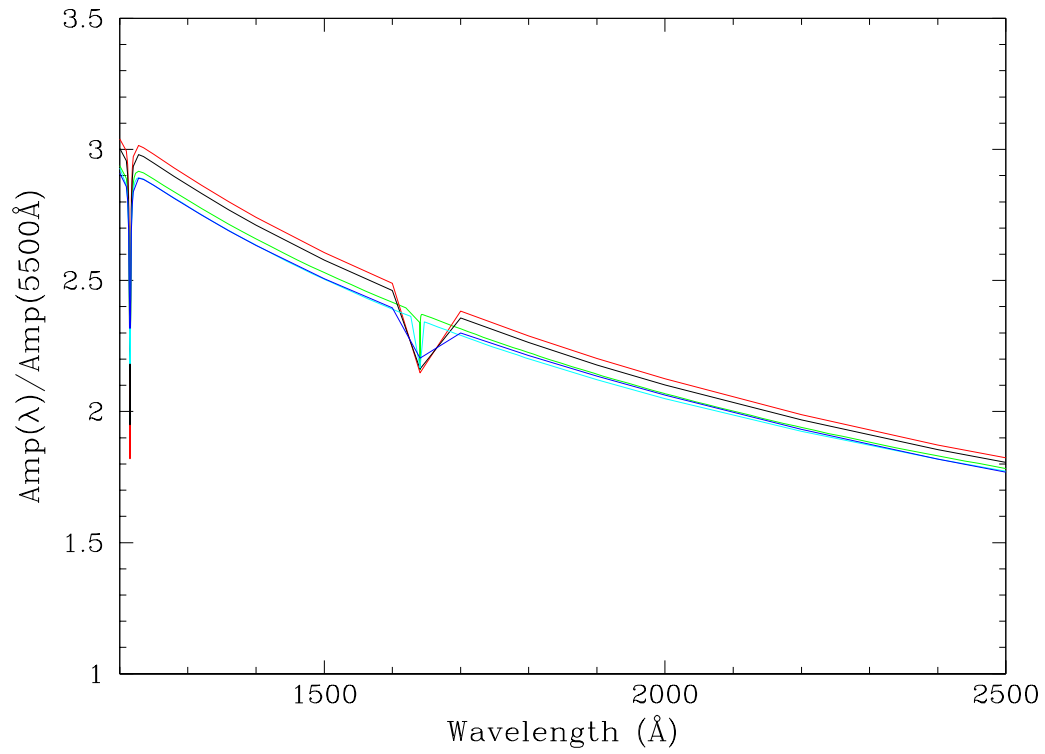


Figure 2.11: The amplitude ratios for a $\ell = 1$ DB models with surface gravities ranging from $\log g = 7.5$ (red), 7.75 (black), 8.00 (green), 8.25 (cyan), and 8.50 (blue). All models have $T_{\text{eff}} = 27000\text{K}$.

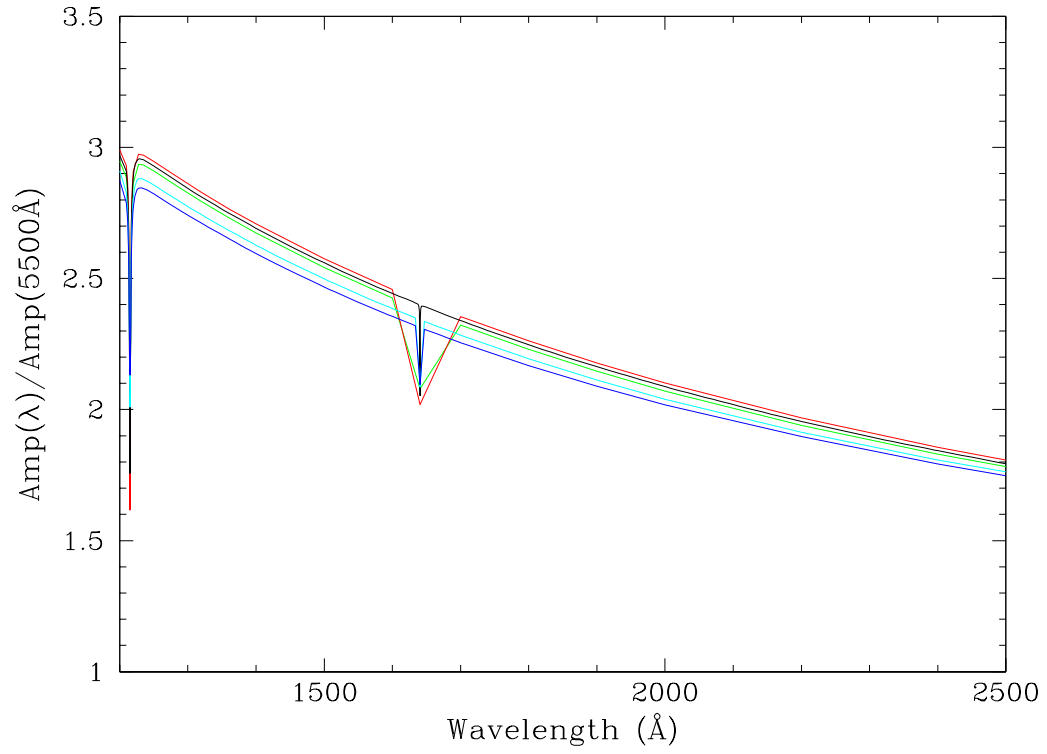


Figure 2.12: The amplitude ratios for a $\ell = 1$ DB models with surface gravities ranging from $\log g = 7.5$ (red), 7.75 (black), 8.00 (green), 8.25 (cyan), and 8.50 (blue). All models have $T_{\text{eff}} = 28000\text{K}$.

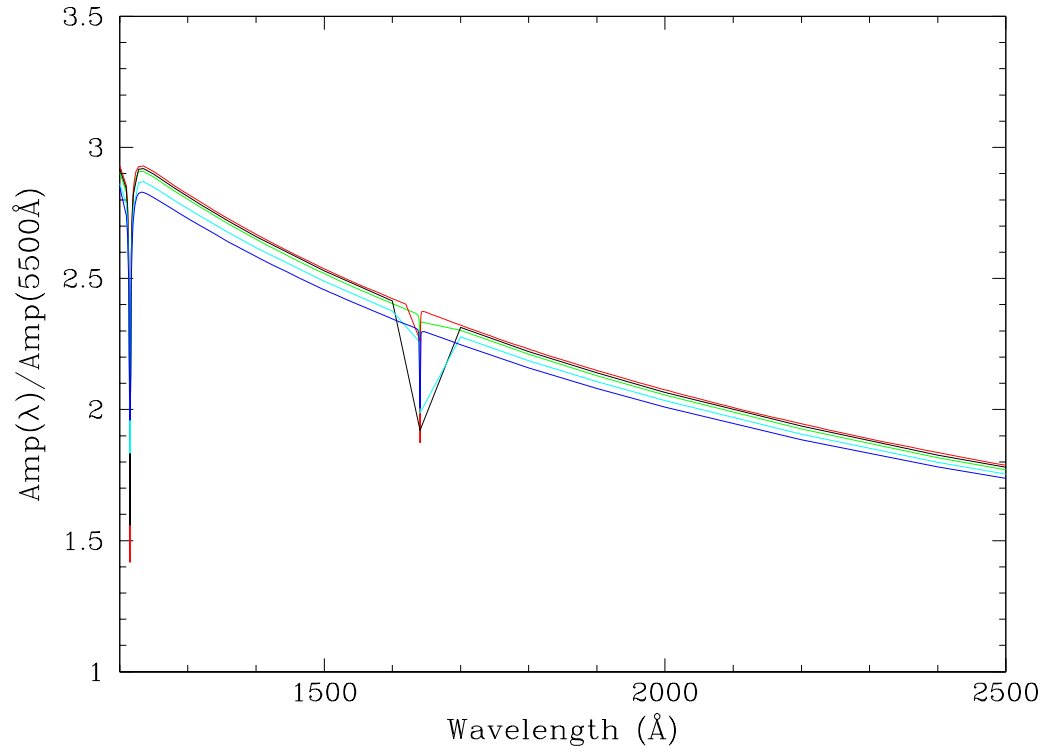


Figure 2.13: The amplitude ratios for a $\ell = 1$ DB models with surface gravities ranging from $\log g = 7.5$ (red), 7.75 (black), 8.00 (green), 8.25 (cyan), and 8.50 (blue). All models have $T_{\text{eff}} = 29000\text{K}$.

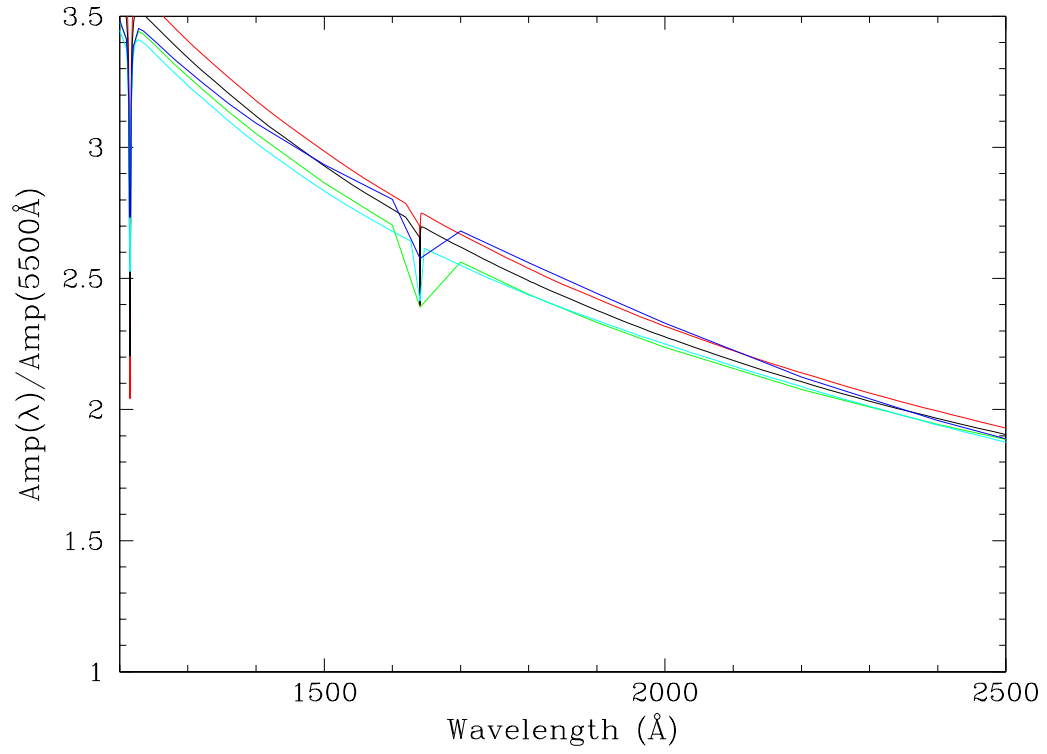


Figure 2.14: The amplitude ratios for a $\ell = 2$ DB models with surface gravities ranging from $\log g = 7.5$ (red), 7.75 (black), 8.00 (green), 8.25 (cyan), and 8.50 (blue). All models have $T_{\text{eff}} = 26000\text{K}$.

2.3.5 Other Works on the Limb Darkening Method

Here we briefly describe other people’s work using the limb darkening method and new model calculations.

Applying the Limb Darkening Method to Other Pulsators — by Kepler et al. (2000)

Kepler et al. (submitted to ApJ, 2000) present successful mode identifications for three white dwarf pulsators (a DBV, PG1351+489 and two hot DAVs, G226-29 and G185-32) with the limb darkening method. They used the HST to obtain time series spectroscopic data using a similar setup to our GD358 UV observations as discussed in the following sections. They also used models provided by Koester, similar to ours (again, we will talk about this in the following sections). The pulsation mode’s phases are expected to be constant over wavelength according to the calculations by Robinson, Kepler & Nather (1982) and Kepler et al. (2000) confirm this for G226-29 and PG1351+489, but four out of the eight modes observed in G185-32 had phase differences between the UV and the zeroth order data with effective wavelength of 3400Å (we discuss the zeroth order data in Section 2.4.). Despite the phase shifts, though, the ℓ -values of these modes were identified without any problems. They did have one periodicity they were not able to identify, a mode which showed very little wavelength dependence, but this mode did not have any phase shift. They concluded this periodicity is not a g-mode, but a periodicity perhaps due to a binary companion.

New Model Calculations by Ising & Koester (2000)

Ising & Koester (2000) show that when nonlinear effects are taken into account, the theoretical amplitude ratio vs. wavelength curves can change significantly depending on the pulsation amplitudes. In particular, they found that for some models, amplitude ratio vs. wavelength curves (chromatic amplitude ratio curves) of an $\ell = 3$ mode can become similar to those of $\ell = 1$ and $\ell = 2$ modes. If so, the mode identification using the limb darkening method may not be as easy as one might think based on the earlier model calculations (see Figures 2.3 for an example). In their work, they also found that including the effects of the pulsations on limb darkening resulted in large changes to some of the theoretical chromatic amplitude curves. We don't have more details about their calculations, so we will use them only as a warning flag.

Applying the Limb Darkening Method Using the Time Series Optical Spectrum — by Clemens, van Kerkwijk & Wu (2000) and van Kerkwijk, Clemens & Wu (2000)

Clemens, van Kerkwijk & Wu (2000:hereafter, CvKW) applied the limb darkening method to the large amplitude DA pulsator, G29–38. Instead of gathering the UV data using the HST and comparing the UV pulsation amplitudes with the optical amplitudes as Kepler et al. (2000) and we did, they examined both the amplitude in the continuum and the line profile variations of the observed absorption lines in their time series spectra taken with the 10m Keck telescope. Although their data are only in the optical, because of the data's high signal to noise, they were able to apply the limb darkening method without relying on having observations over a large wavelength range. They found that the models can match their observations, both the amplitudes in the continuum and the

line profile variations, qualitatively, but not quantitatively. They identified five $\ell = 1$ modes and one $\ell = 2$ mode from the quantitative observed differences in the line profile variations.

The differences between CvKW's observations and the models were systematic. They found that the chromatic amplitudes of the pulsation modes in G29–38 were steeper than the theoretical curves. They also saw phase shifts in their data with the blue photons arriving earlier than the red photons. The linear models currently cannot reproduce these puzzling observations.

Another thing CvKW and the companion paper van Kerkwijk, Clemens & Wu (2000:hereafter vKCW) measured, which had never been measured before, is the relative phases between the maximum radial velocity and the maximum flux of a pulsation. In the adiabatic case, the relative phase between the velocity and the flux is 90 degrees, but their observations showed that for all observed g-modes, the phase differences were less than 90 degrees, i.e. nonadiabatic processes are important.

The limb darkening method using the high signal to noise optical time series spectra must also be checked for consistency, similar in our effort with GD358 and the HST and the optical observations which is the theme of this chapter. They have since acquired data on GD358 again using the 10m Keck telescope, but have not yet finished their analysis. It is important to find out if the GD358 observations will be consistent with their G29–38 results, since the results from the G29–38 observations come from one mode behaving quantitatively very differently from other five modes, instead of the observations matching the models.

2.3.6 Mode Identification Using the Radial Velocity and Flux Amplitude Ratio

One of the newest discoveries of CvKW and vKCW is that the ratio between the observed velocity and flux amplitudes is itself an ℓ indicator. Their high signal to noise time series spectra allowed them to measure the line of sight velocity variations due to pulsations. When the amplitude of the velocity variations were compared to the amplitude of the flux variations, they found that the mode that was identified as an $\ell = 2$ mode from the line profile variations also had the largest velocity to flux amplitude ratio. This also needs to be checked for consistency, along with the line profile variations mentioned in the last section, with their new GD358 observations.

If we are to routinely use the velocity-to-flux amplitude ratios for ℓ identifications, the measurements will have to be made by large telescopes such as the Keck 10m telescopes. Since there are many new large telescopes being built and coming into operation around the world, this might actually become a practical approach to identifying modes in the near future.

2.3.7 Mode Identification Using Harmonics and the Linear Combination Modes

There is another mode identification method we will not be testing in this thesis. It has not been applied widely as the two methods already described, but here we summarize it briefly. Some pulsating white dwarf stars show periodicities corresponding to sums and differences of the nonradial g-modes “linear combination modes” as well as periodicities corresponding to integer numbers times the nonradial g-mode period (harmonic modes). Brassard, Fontaine & Wesemael (1995) showed that the amplitudes of the harmonics and linear com-

bination modes can tell us the ℓ values of the parent nonradial g-mode.

Robinson, Kepler & Nather (1982) showed that nonradial g-mode pulsations in white dwarf stars manifest themselves as temperature variations on the surface. Assuming the flux of the pulsating white dwarf stars respond linearly and instantaneously to the temperature variations on the surface, Brassard, Fontaine & Wesemael (1995) derived analytical expressions on how the amplitudes of the harmonics and linear combination modes depend on “parent” modes’ ℓ and m values (equations 63 to 66 in their paper). Their expressions are valid for low amplitude pulsators only and if their mechanism of how the linear combination modes arise is correct, their expressions are useful in identifying observed pulsation modes. This method has the advantage that it does not require coordinated HST and ground based observations nor the full resolving power of the WET, however it can (currently) only be applied to low-amplitude stars which have these combination modes. Yanqin Wu (1998) has a different explanation as to why the linear combination modes exist which seem to work in at least some instances, so we obviously need further work and testing on these ideas.

2.4 GD358 HST Observations

In 1996, we used the HST to gather the UV data from space and organized a 3-site campaign to gather optical data simultaneously. We used the now de-commissioned Faint Object Spectrograph (FOS) on-board the HST with the G160L grating in “RAPID readout mode” to take UV time-series spectra of GD358. We integrated for 10s per spectrum and chose the G160L grating because it gave us the lowest spectral resolution ($\approx 2\text{\AA}/\text{pixel}$), and the bluest and longest spectral range (1200 to 2500 \AA) available. As seen earlier in Figure 2.3, the pulsation amplitude, lightcurve and Fourier transform ratios have strong ℓ dependence in the UV, and the G160L grating provided us with the best wavelength region for this project.

2.4.1 The Zeroth Order Reflection

Bill Welsh, then at University of Texas at Austin, first pointed out to us that when using the FOS with the G160L grating, the undispersed (zeroth order) light also falls on an area of the detector not normally used to acquire data (Welsh et al. 1998; Eracleous & Horne 1996). In the final reduction files from the HST data reduction pipeline, however, the zeroth order data do not show up. Instead they are in the intermediate reduction files, files with extensions c4h and c4d for example. In Figure 2.15, we show a sample spectrum plotted as count rate vs. pixel number taken from one of the intermediate reduction files. The large peak around pixel 630 (corresponding to $\approx 3400\text{\AA}$) is the undispersed zeroth order data while the small wiggles beyond pixel 1300 ($\approx 1100\text{\AA}$) are the UV first order spectra. This zeroth order data have much larger signal than the UV data and are acquired simultaneously with the UV data. Quite

coincidentally, this is just the kind of simultaneous data we need for our analysis as we will discuss later.

Artifacts Due to the HST's Orbit

Figure 2.16 shows the Fourier transform of the zeroth order and UV lightcurves. Each lightcurve was formed by integrating the flux over the entire observed wavelength region. This gives us the brightness of the star in each bandpass sampled every 10s. We then divided each lightcurve by the mean brightness level and subtracted 1 to represent the light variation in the fractional intensity. We use the unit *mi* for fractional intensity which stands for *modulation intensity*. The units of Fourier transforms of lightcurves in *mi* are *modulation amplitude*, abbreviated as *ma*, or *modulation power* abbreviated as *mp*. *mp* is defined as $mp = ma^2$. In Figure 2.16, the vertical unit is in “mma” which is mili-modulation amplitude or 1/1000 of 1ma. In the transform, there is a striking peak around $185\mu\text{Hz}$ corresponding to the HST's 90 min orbit. Kepler et al. (2000) saw similar effect in their data and attributed to the target drifting slightly inside the aperture and some light being lost, which results in modulation of the observed intensity. Welsh et al. (1998) who also saw change in the count rate in their FOS data at the latter half of each orbit concluded that this was caused by the image motion problem due to inadequate shielding of the FOS from the Earth's magnetic field. Whichever is the cause of the problem, in order to remove this effect, we used a nonlinear least square fitting program to fit the period, amplitude, and phase of a simulated sinusoidal HST orbit to the lightcurve. We then subtracted the sine curve from the lightcurve and recalculated the Fourier transform. Figure 2.17 shows the lightcurve before

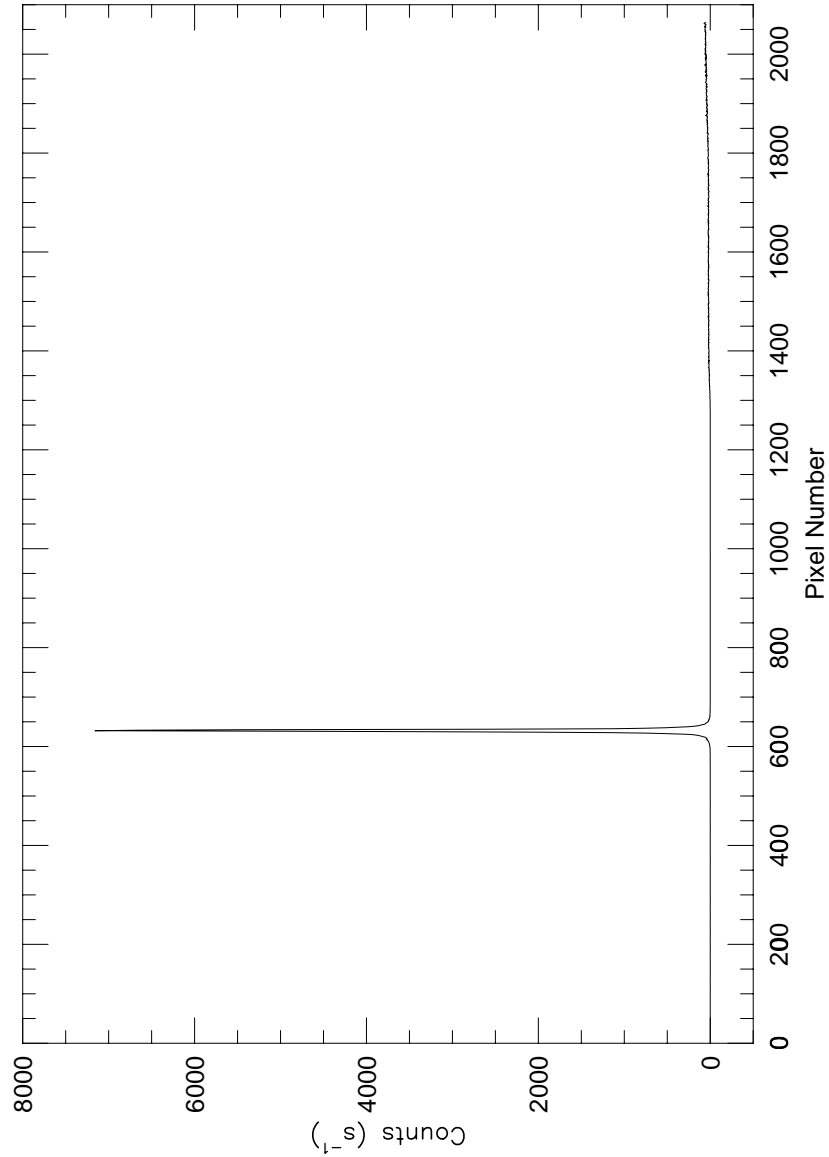


Figure 2.15: Counts vs. pixel number for the FOS, highlighting the bonus zeroth order light. The FOS, when using the G160L grating, puts the first order spectrum from pixel 1300 and beyond. Around pixel 630 ($\approx 3400\text{\AA}$, see later section for the effective wavelength of the zeroth order data), there is a large spike caused in the undispersed (zeroth order) light falling on the detector. The actual UV spectra are the wiggles at pixel 1300 ($\approx 1100\text{\AA}$) and beyond.

(black) and after (blue) the orbital effect was removed. We have also shown the simulated orbital modulation as the red curve.

Figure 2.18 shows just the final reduced lightcurve (the same lightcurve as the blue curve in Figure 2.17.). The large gaps come from the low-earth orbit of the HST which causes the target to be occulted by the Earth during roughly half of the 90 min orbit. The large gap in the bottom panel is caused by the HST passing through the Southern Atlantic Anomaly (SAA) region². As there are high rates of energetic particles in this region which can cause damage to the memory boards on the HST, no data are taken when the HST is in the SAA region. The small gaps come from the on-board data transfer to the data recorder. We wish we could have had the data transfer occur during the time the target was occulted, but we had no control over when this took place. We were granted 8 orbits for this project, but due to the observational constraints, i.e. to coordinate the ground based observation with the HST observation, we had to give up one orbit. About one quarter of the first orbit was spent carefully centering the target in the aperture (the so-called “peak-up” procedure) and hence the lightcurve from the first orbit is shorter than the others.

The Effective Wavelength of the Zeroth Order Data

The measured bandpass of the FOS zeroth order light obtained on the ground, before it went into space, is shown in Figure 2.19. It is very broad, with an effective wavelength around 3400Å. The bandpass was never measured while the FOS was in space, but a loss of sensitivity in the blue is suspected due to

²Energetic particles from the sun which are not shielded by the van Allen’s belt reach the Earth in this region.

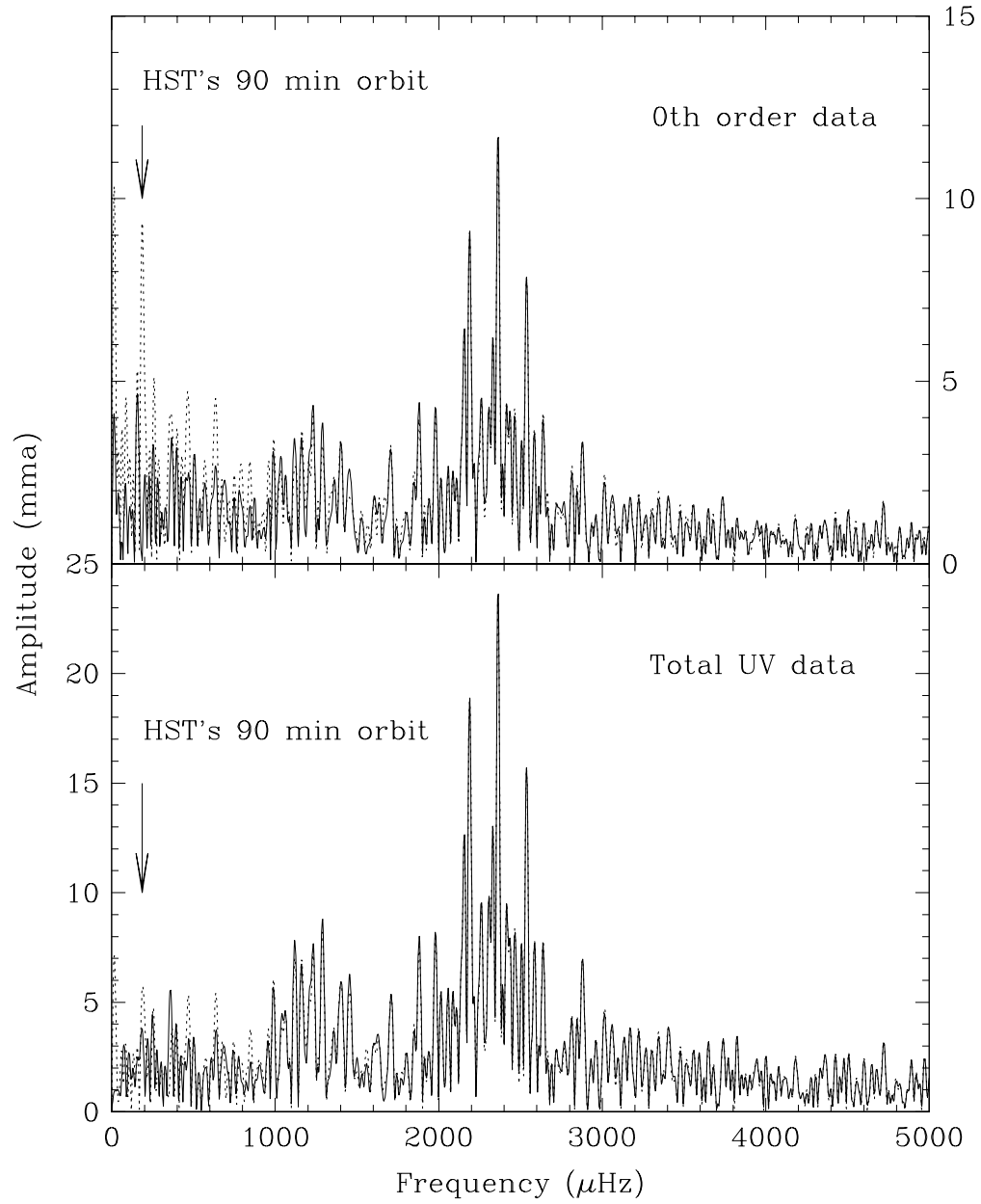


Figure 2.16: The Fourier transform of the UV and zeroth order data before (dotted lines) and after (solid lines) the removal of the HST's orbital effect.

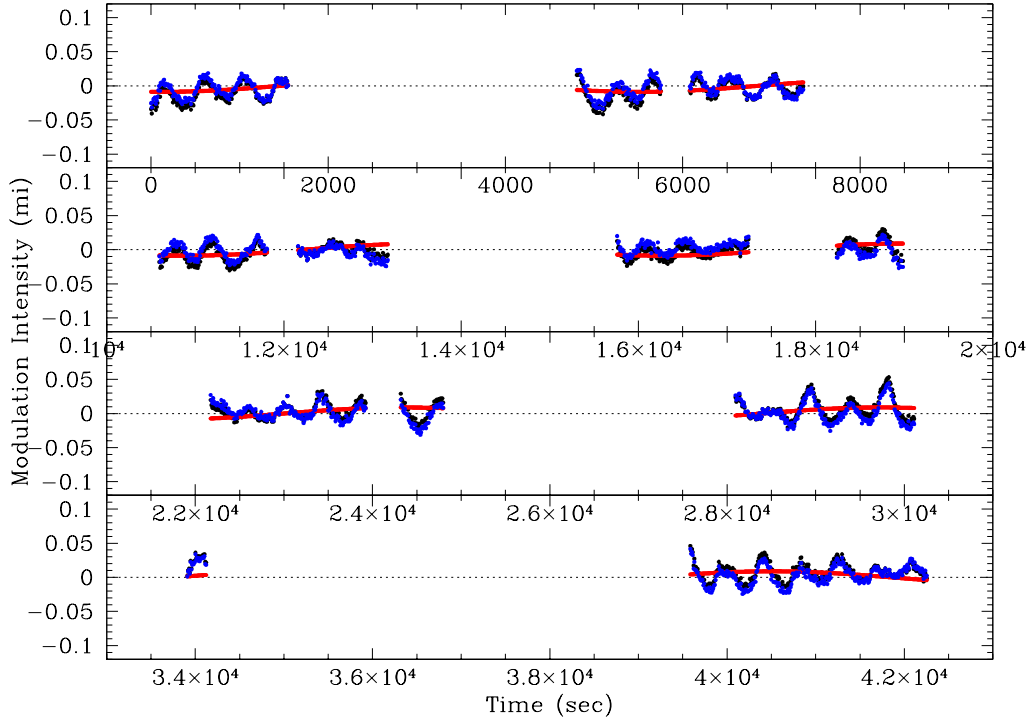


Figure 2.17: The zeroth order HST lightcurve. The black points show the original lightcurve, the red is our fit to the HST's orbit, and the blue curve is the lightcurve with the orbital modulation removed. The differences before and after the orbit removal are so small that it is hard to distinguish between the black and blue curves in this figure.

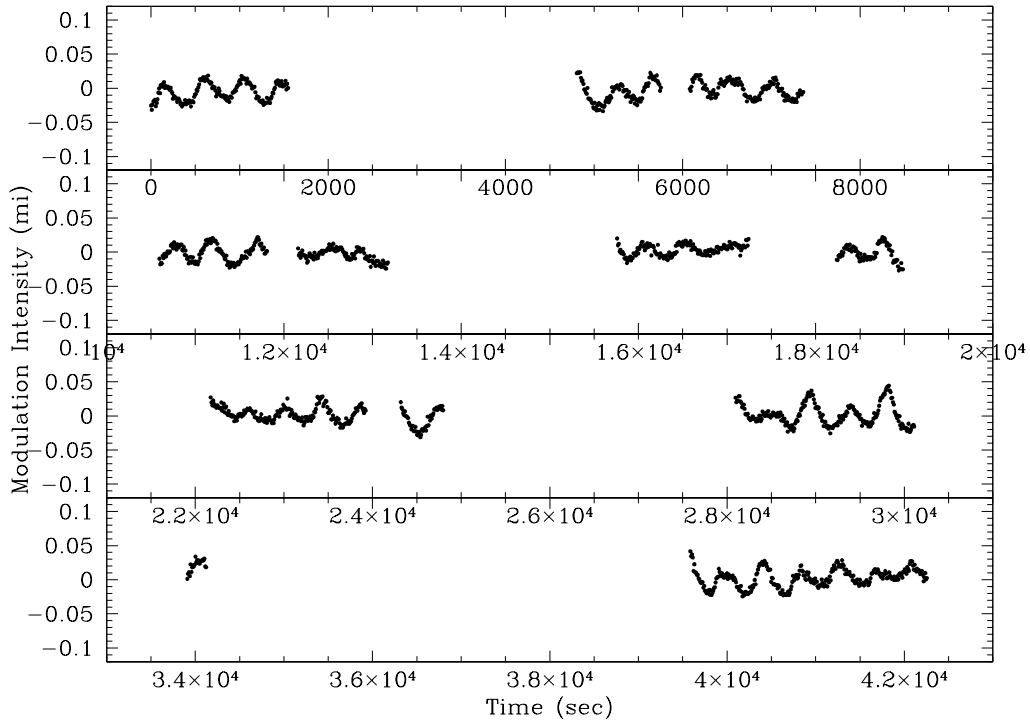


Figure 2.18: The final reduced zeroth order lightcurve. The larger gaps in the lightcurve come from the HST's low-earth orbit, resulting in the target being occulted by the Earth. The smaller gaps come from the data being recorded.

de-gassing within the instrument. When convolved with DB model spectra as shown in Figure 2.20, the effective wavelength goes from 2700Å for a 21000K, $\log g = 8.0$ model, to 2430Å for a 29000K, $\log g = 8.0$ model (see Figure 2.21). The model spectra show a peculiar jump around 3200Å which is due to a lack of resolution in the models we used. This discontinuity has an effect on our estimates, but one which we deem is small enough to ignore. If de-gassing did occur, however, the convolved spectra in Figure 2.21 are not valid, and we can only guess the effective wavelength. Welsh et al. (1998) used 3400Å for the zeroth order wavelength and so did Kepler et al. (2000) for their analysis on other pulsating white dwarf stars exactly the same as ours. We will therefore take 3400Å as the valid effective wavelength for our data as well.

The zeroth order data are especially important to us. We are interested in simultaneous lightcurves at different wavelengths and the zeroth order data give us a U-like lightcurve we can compare with the simultaneous first order UV data. We tried to obtain a simultaneous optical lightcurve from the ground (next section), but due to poor weather, we were unsuccessful. With the fast amplitude modulation we observed in GD358 as we later discuss, the importance of simultaneous data with the UV data became very important, and the existence of the zeroth order lightcurve, then, was vital to the success of our project.

2.4.2 The UV Observations

The Time Averaged UV Spectrum

The HST data were reduced using the standard HST data reduction pipeline (“calfos” inside the STSDAS package in IRAF). The pipeline converts the data

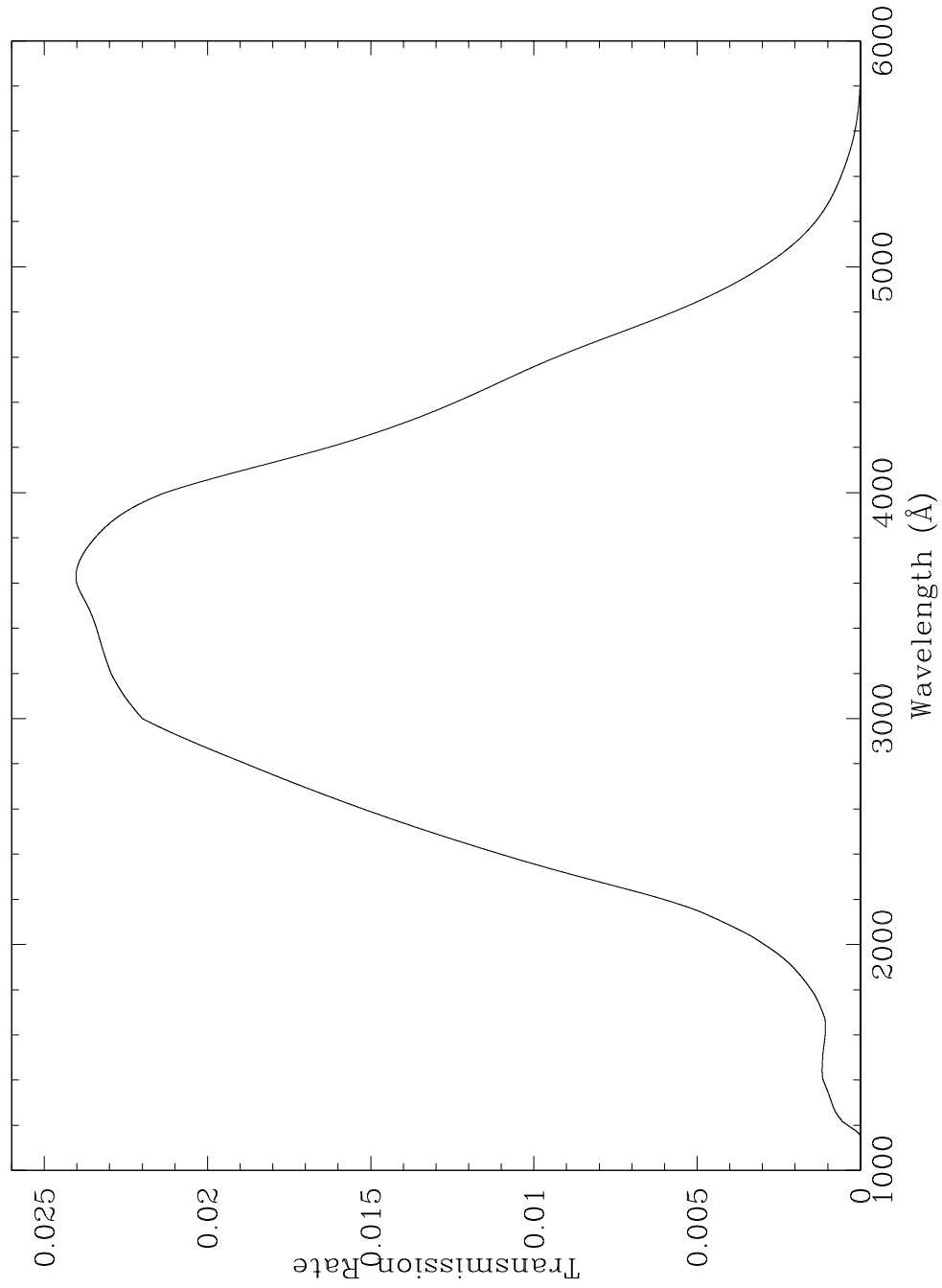


Figure 2.19: The zeroth order bandpass of the FOS as measured on Earth. The bandpass was never measured while in space. There might have been some leakage of gas, and consequent loss of sensitivity, at the shorter wavelength region.

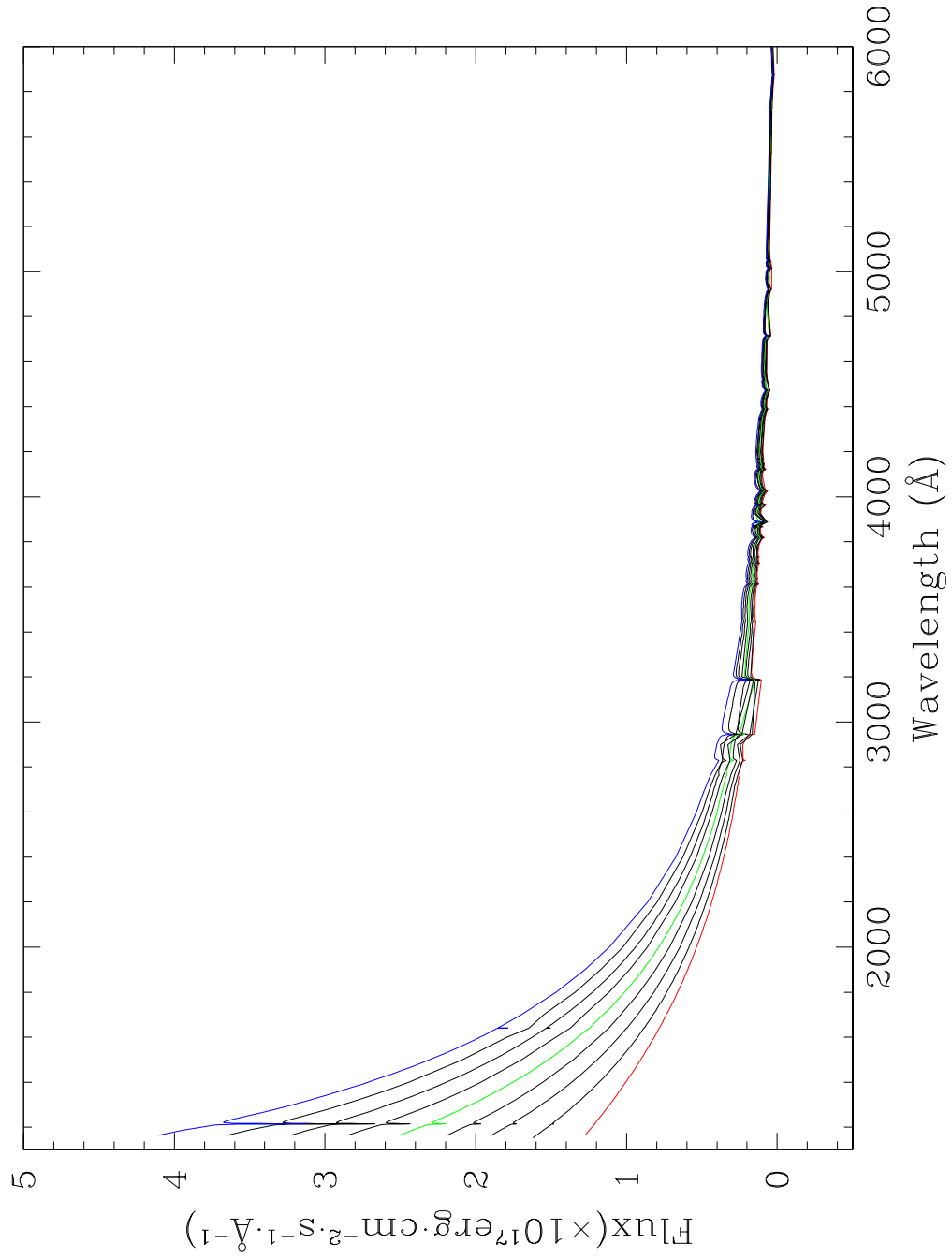


Figure 2.20: Various DB model spectra with $\log g = 8.0$ and different effective temperatures (from 21000K to 29000K). The jumps around 3200 \AA are from a lack of resolution in the model spectra.

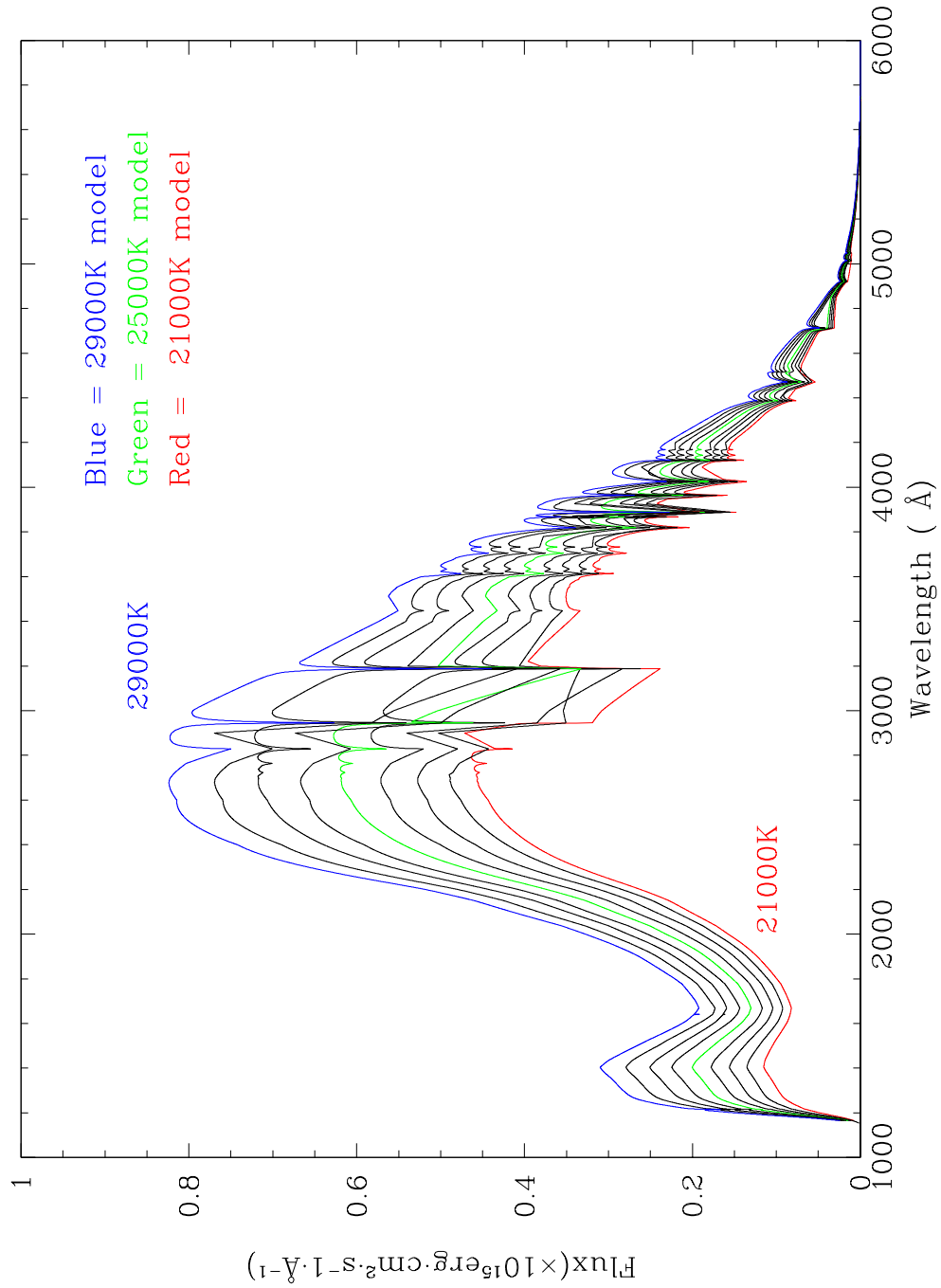


Figure 2.21: The various DB model spectra from Figure 2.20 after being convolved with the zeroth order FOS bandpass from Figure 2.19. The effective temperature of the DB models range from 21000K to 29000K. All models have $\log g = 8.0$. Again, the discontinuities around 3200 \AA are an artifact of the DB models used here.

from raw counts to count rates with corrections for dead diodes, geomagnetic-induced image motion, and deadtime. It also does a scattered light subtraction, flat field correction, sky subtraction, and finally, wavelength and flux calibrations.

Figures 2.22 and 2.23 show the time averaged UV spectrum taken by the HST along with Koester’s model spectra for a DB with $\log g = 8.0$ with different temperatures (same as Figure 2.20). The distance to GD358 has been observationally determined by parallax (36 ± 4 pc from van Altena, Lee & Hoffleit 1995) and by asteroseismology (42 ± 3 pc from Bradley & Winget 1994). Figure 2.22 assumes the parallax distance of 36 pc and the radius of the white dwarf as $0.00128R_{\odot}$ which we use from Bradley & Winget (1994). The radius estimate comes from the apparent luminosity, parallax distance and an effective temperature of 24000K which was a common temperature arrived at by several different groups (Koester, Weidemann, & Vauclair 1983; Koester et al. 1985; Liebert et al. 1986; Thejl, Vennes, & Shipman 1991). Figure 2.23 assumes the asteroseismological distance of 42 pc and corresponding radius of $0.00127R_{\odot}$. The agreement in Figure 2.22 between the 25,000K DB model and the observations is quite good, although the match is less impressive in the short wavelength region (less than 1500\AA). At these shorter wavelengths, the observational scatter increases, due at least in part to scattered light contamination within the FOS, a known problem (Koester 1999, private communication). On the other hand, the agreement between the observations and models assuming the asteroseismological distance (Figure 2.23) is not nearly as good. We have tried fitting the spectrum using other surface gravity models keeping the distance at 42 pc, but still could not find any good agreements. Although the

error bars of the two distance measurements overlap with each other, our data clearly favor the smaller value. If we take the distance as 32 pc, a value still allowed by the parallax measurement at the low end of the allowed range, we find the agreement between the data and models change, favoring a different T_{eff} and $\log g$. If we change the radius of the model white dwarf, the fit again will change. Koester has independently fit our UV spectrum with a model grid different (improved slightly compared to ours) from the one he previously provided us and has concluded he can best fit the data with a $T_{\text{eff}} = 23700\text{K}$, $\log g = 8.0$ model. As they are received by us, the models calculate the star's absolute flux. In order to compare the model to the observed, apparent flux, we must therefore normalize the model spectra. We use the model flux, along with the distance, the radius of the white dwarf model and assuming no interstellar absorption (Provencal et al. 2000) to estimate the observable, apparent flux. Koester, on the other hand, used the observed V magnitude to normalize the models, adjusting his models until the V magnitudes matched observations. We will show later that depending on how one normalizes, the fit changes substantially. This is quite unsettling, but we believe we have found a method which finds the best possible fit.

Different atmospheric models, for example a pure He atmosphere vs. a He atmosphere with trace amounts of H, change the fit. Table 2.2 shows the list of the models Koester fit the data with along with a few other temperature estimates done independently by others. Provencal et al. (2000) used high resolution spectra obtained in the UV to determine the GD358 temperature, while Beauchamp et al.'s (1999) optical spectroscopic temperature is based on an observed HeII line. All the estimates, including ours, are consistent with

Model or the Name of the Group	T_{eff}	logg	Comments
Our Fit (no H)	25500	8.0	Fitting UV continuum by deviation A
Koester (no H)	24560 ± 80	8.0	V=13.65 used for normalization
	24090 ± 620	7.50	V=13.50 used for normalization
	24000 ± 210	7.75	V=13.50 used for normalization
	23929 ± 610	8.00	V=13.50 used for normalization
Koester (w/ 1.0^{-6}H)	24750 ± 500	7.5	V=13.50 used for normalization
	25000 ± 900	8.0	V=13.50 used for normalization
	25150 ± 440	8.25	V=13.50 used for normalization
Provencal	27000 ± 1000	8.0	Using C lines in UV
Beauchamp (no H)	24900	7.91	Fitting He lines in the optical
Beauchamp (w/ 1.0^{-5}H)	24700	7.92	Fitting He lines in the optical

Table 2.2: Different models and methods result in different T_{eff} and $\log g$ estimate for GD358. Although our models were provided by Koester, as we use a different fitting technique than his, we decided to call it “our fit” in this table.

each other. Koester and Beauchamp also calculated DB models with a small amount of atmospheric H, small enough that it is not detectable, and show that it can alter the temperature³. The models we use do not have any H.

Clearly, the choice of how we normalize the models changes the fit to the observations. As we could not decide a priori which method is best, we

³Provencal et al. (2000) placed a limit of H in GD358 as significantly lower than $\log M_{\text{H}}/M_{\text{He}} = -5$. Koester’s models are within this constraint and Beauchamp’s models give us the range of T_{eff} for GD358 using his models.

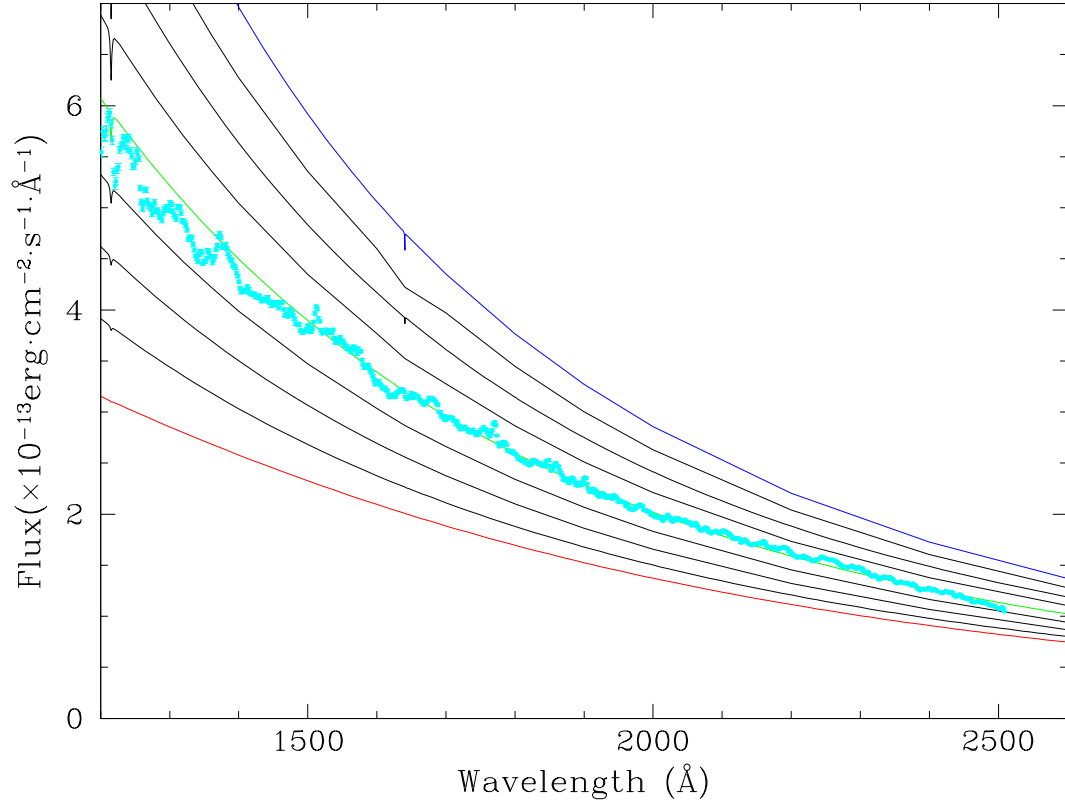


Figure 2.22: Observed and model spectra of GD358. The light blue dots are the time averaged first order spectrum of GD358 taken by the HST. All models have $\log g = 8.0$, but different effective temperatures, from 21000K to 29000K in 1000K increments. The red curve is the 21000K model, the green curve is the 25000K model and the dark blue curve is the 29000K model. The distance to GD358 is assumed to be 36 pc, the parallax distance from van Altena, Lee, and Hoffleit (1995)

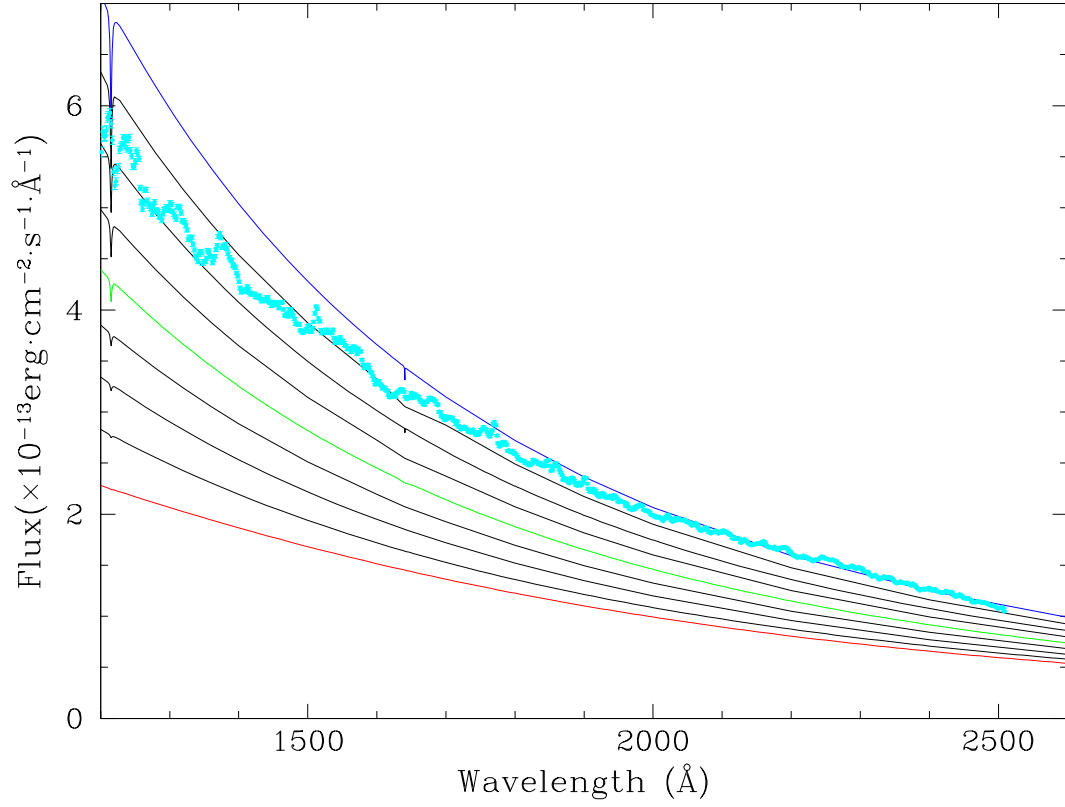


Figure 2.23: Observed and model spectra of GD358. The light blue dots are the time averaged first order spectrum of GD358 taken by the HST. All models have $\log g = 8.0$, but different effective temperatures, from 21000K to 29000K in 1000K increments. The red curve is the 21000K model, the green curve is the 25000K model and the dark blue curve is the 29000K model. The distance to GD358 is assumed to be 42 pc, the asteroseismological distance from Bradley & Winget (1994).

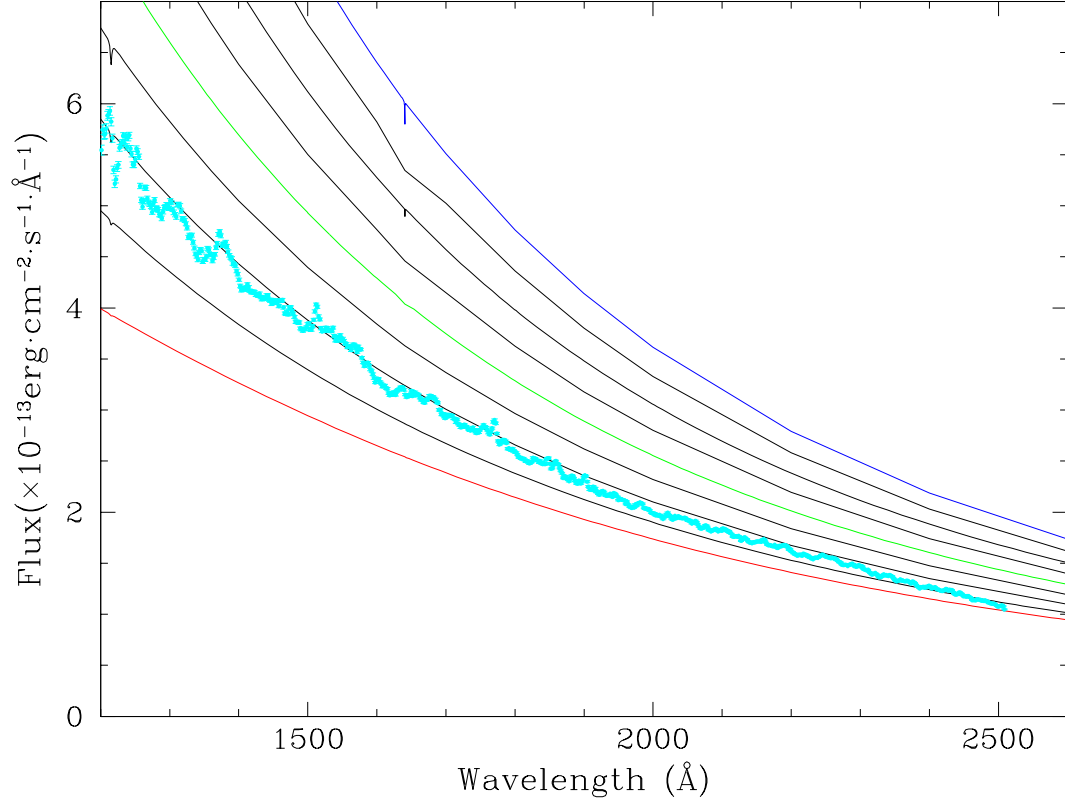


Figure 2.24: Observed and model spectra of GD358. The light blue dots are the time averaged first order spectrum of GD358 taken by the HST. All models have $\log g = 8.0$, but different effective temperatures, from 21000K to 29000K in 1000K increments. The red curve is the 21000K model, the green curve is the 25000K model and the dark blue curve is the 29000K model. The distance to GD358 is assumed to be 32 pc, the lowest parallax distance allowed by the error bar of van Altena, Lee, & Hoffleit (1995)

decided to test quantitatively how well each model fits the data. We divided the observed spectrum by an un-normalized model spectra. The best fit model will give us a straight, flat, line ignoring noise in the data. Figures 2.25 to 2.29 show the results of the divisions. In each figure, the models have temperatures ranging from 21000K to 29000K in 1000K increments. We actually calculated the ratio for models with 500K increments, but for clarity, do not include them in the figures. The dotted lines in each figure show the average value of the ratio of the observed spectrum to the model spectrum for each model. In order to determine which model is the best fit, we summed the square of the differences of the ratio at each wavelength from the average ratio and call this quantity “sc2”. The smallest value of sc2 tells us that the spectrum ratio is the closest to a flat line, and is hence the best fit model. The values of sc2 for all models are shown in Figure 2.30. From this plot, we conclude that the best fit models have a range of T_{eff} between 25500K and 26500K. As we discussed in the previous section, in this temperature range, the calculated ratio of UV to optical mode amplitude do not show significant changes with gravity. Therefore, we will use a $\log g = 8.0$, $T_{\text{eff}} = 25500\text{K}$ model to compare with our observation.

The UV Lightcurves

Using the STSDAS package in IRAF, we integrated the time-series spectra to 50Å bins and created 26 different UV lightcurves from 1100Å to 2500Å. We also created a single UV lightcurve integrating light over the entire observed UV bandpass. The HST’s orbital effect was removed the same way we did for the zeroth order data. Similar to Figure 2.17 of the zeroth order lightcurve, Figure 2.31 shows the single UV lightcurve both before and after the removal

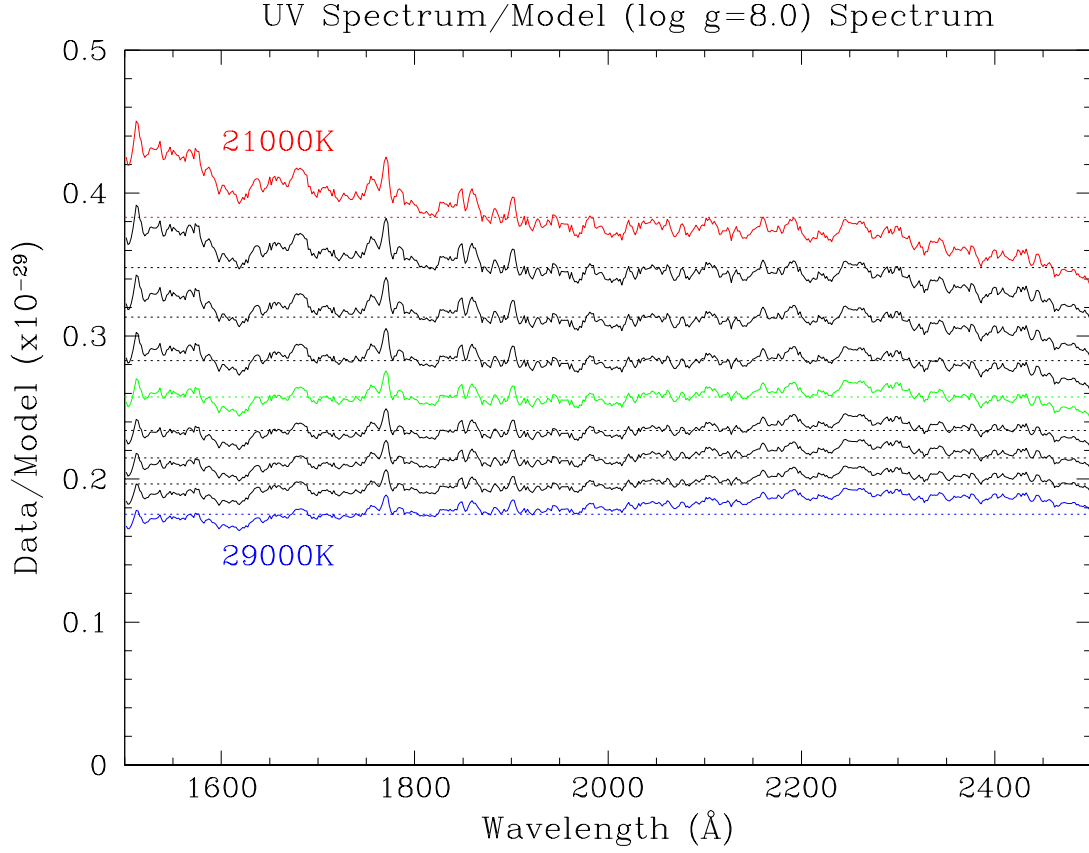


Figure 2.25: The observed GD358 UV spectrum divided by Koester's model spectra (no H) with $\log g = 8.0$ at various temperatures. The red curve shows the results of observed spectrum divided by the 21000K model, the green shows the observed spectrum divided by the 25000K model and the blue shows the observed spectrum divided by the 29000K model. The best fit model should result in a straight, flat line. The dotted lines are the average value of the observed spectrum divided by the model.

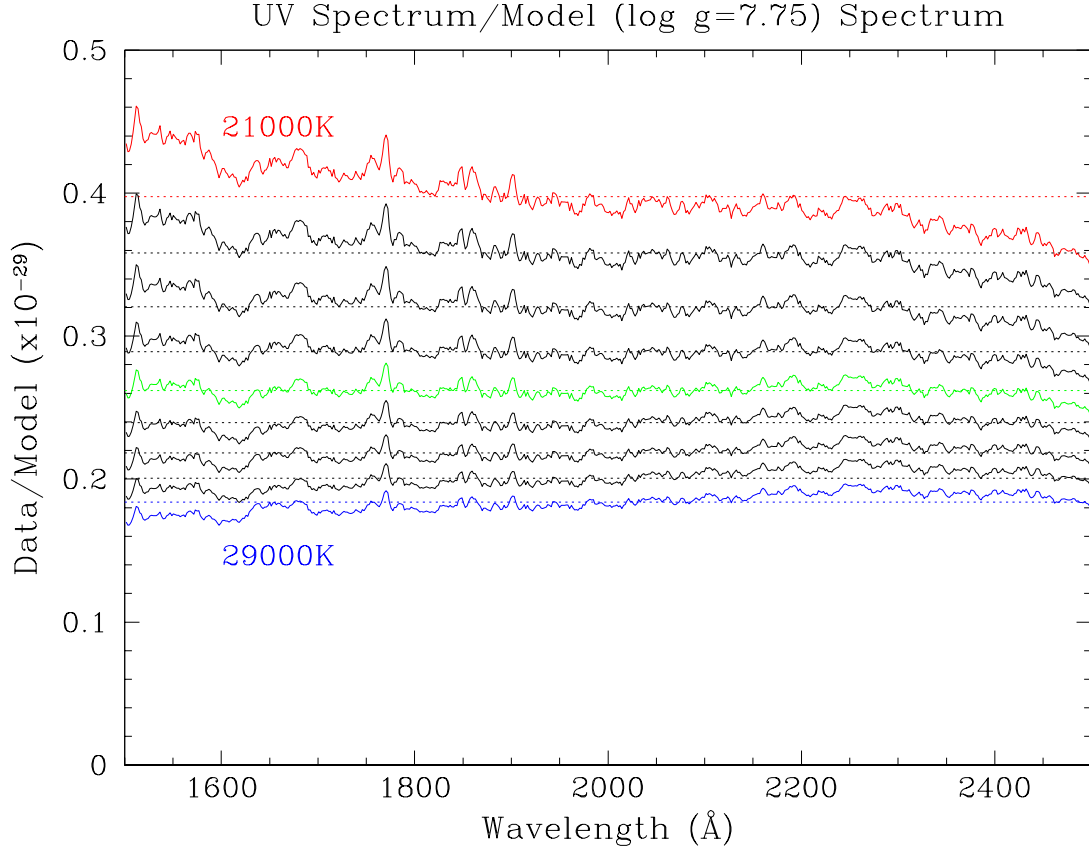


Figure 2.26: The observed GD358 UV spectrum divided by Koester's model spectra with $\log g = 7.75$ at various temperature. The red curve shows the results of observed spectrum divided by the 21000K model, the green shows the observed spectrum divided by the 25000K model and the blue shows the observed spectrum divided by the 29000K model. The best fit model should result in a straight, flat line. The dotted lines are the average value of the observed spectrum divided by the model.

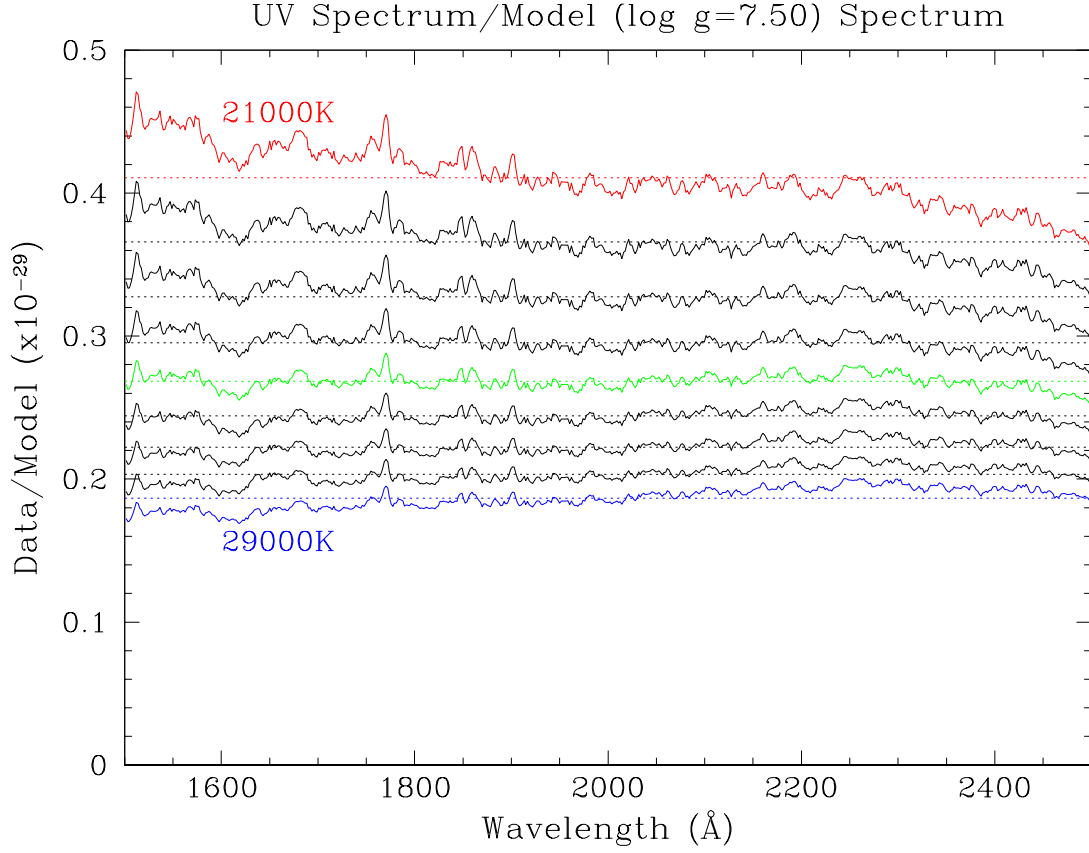


Figure 2.27: The observed GD358 UV spectrum divided by Koester's model spectra with $\log g = 7.5$ at various temperature. The red curve shows the results of observed spectrum divided by the 21000K model, the green shows the observed spectrum divided by the 25000K model and the blue shows the observed spectrum divided by the 29000K model. The best fit model should result in a straight, flat line. The dotted lines are the average value of the observed spectrum divided by the model.

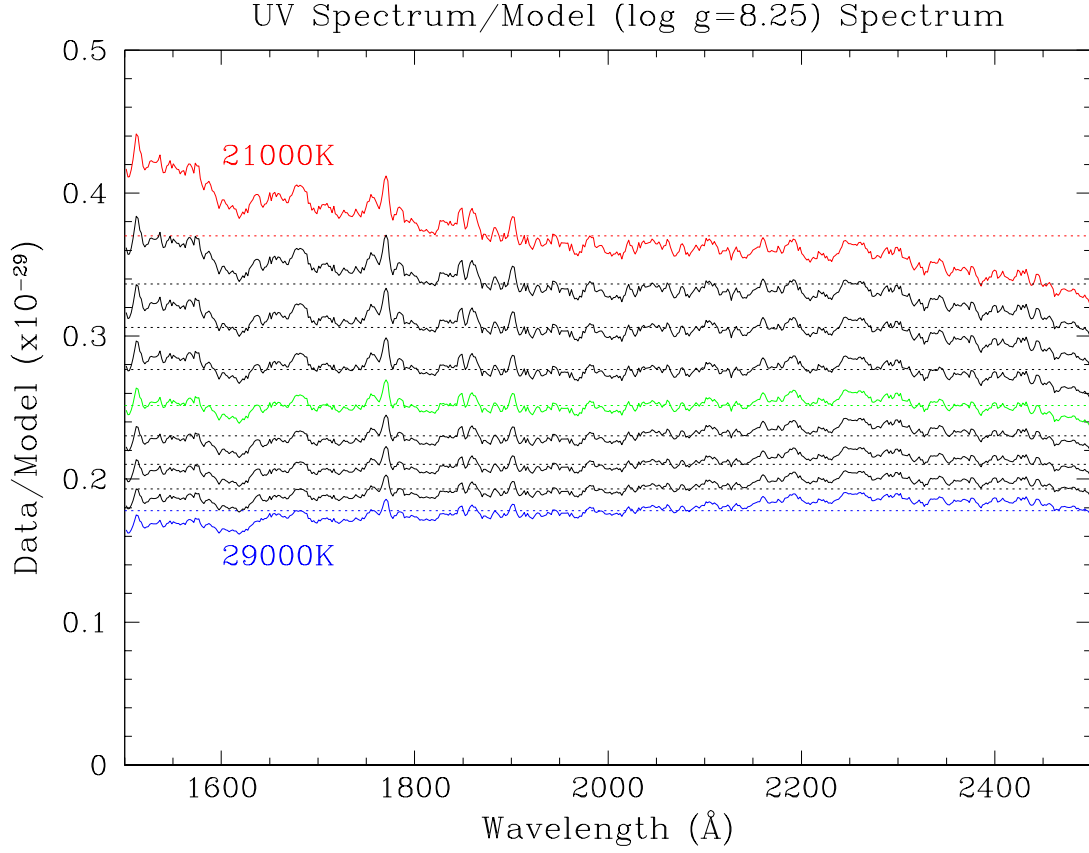


Figure 2.28: The observed GD358 UV spectrum divided by Koester's model spectra with $\log g = 8.25$ at various temperature. The red curve shows the results of observed spectrum divided by the 21000K model, the green shows the observed spectrum divided by the 25000K model and the blue shows the observed spectrum divided by the 29000K model. The best fit model should result in a straight, flat line. The dotted lines are the average value of the observed spectrum divided by the model.

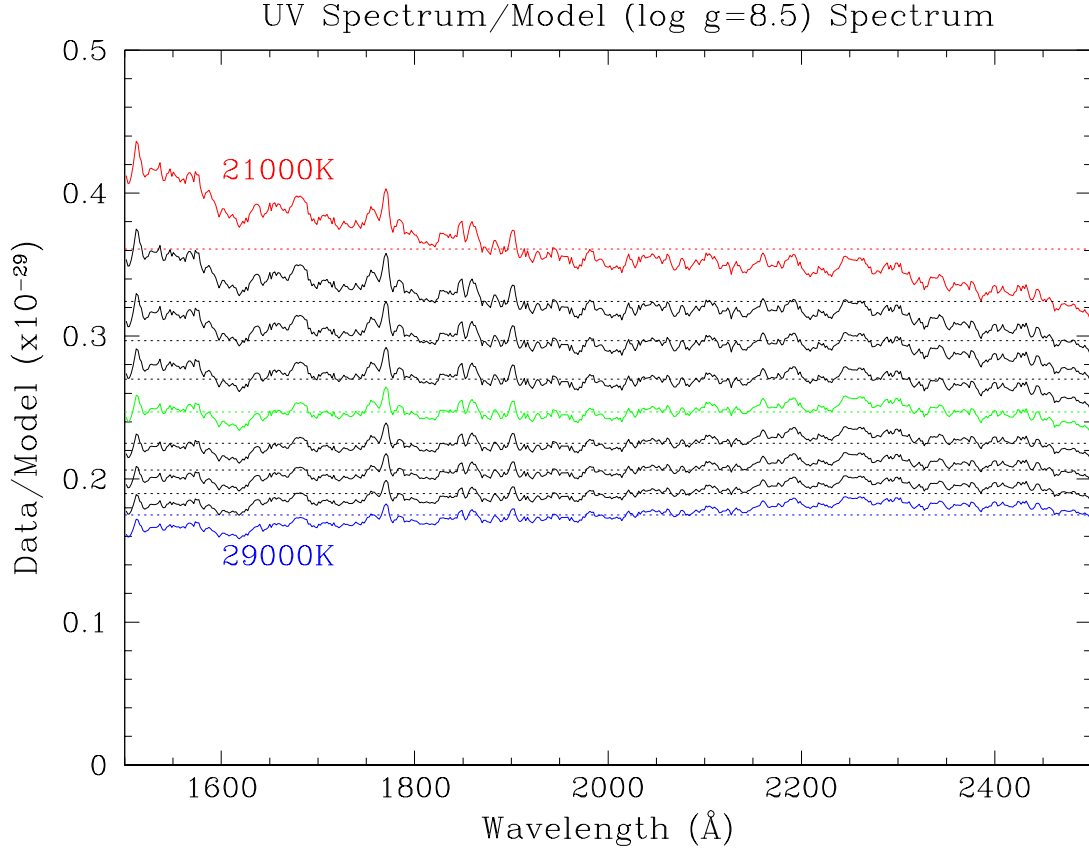


Figure 2.29: The observed GD358 UV spectrum divided by Koester's model spectra with $\log g = 8.5$ at various temperature. The red curve shows the results of observed spectrum divided by the 21000K model, the green shows the observed spectrum divided by the 25000K model and the blue shows the observed spectrum divided by the 29000K model. The best fit model should result in a straight, flat line. The dotted lines are the average value of the observed spectrum divided by the model.

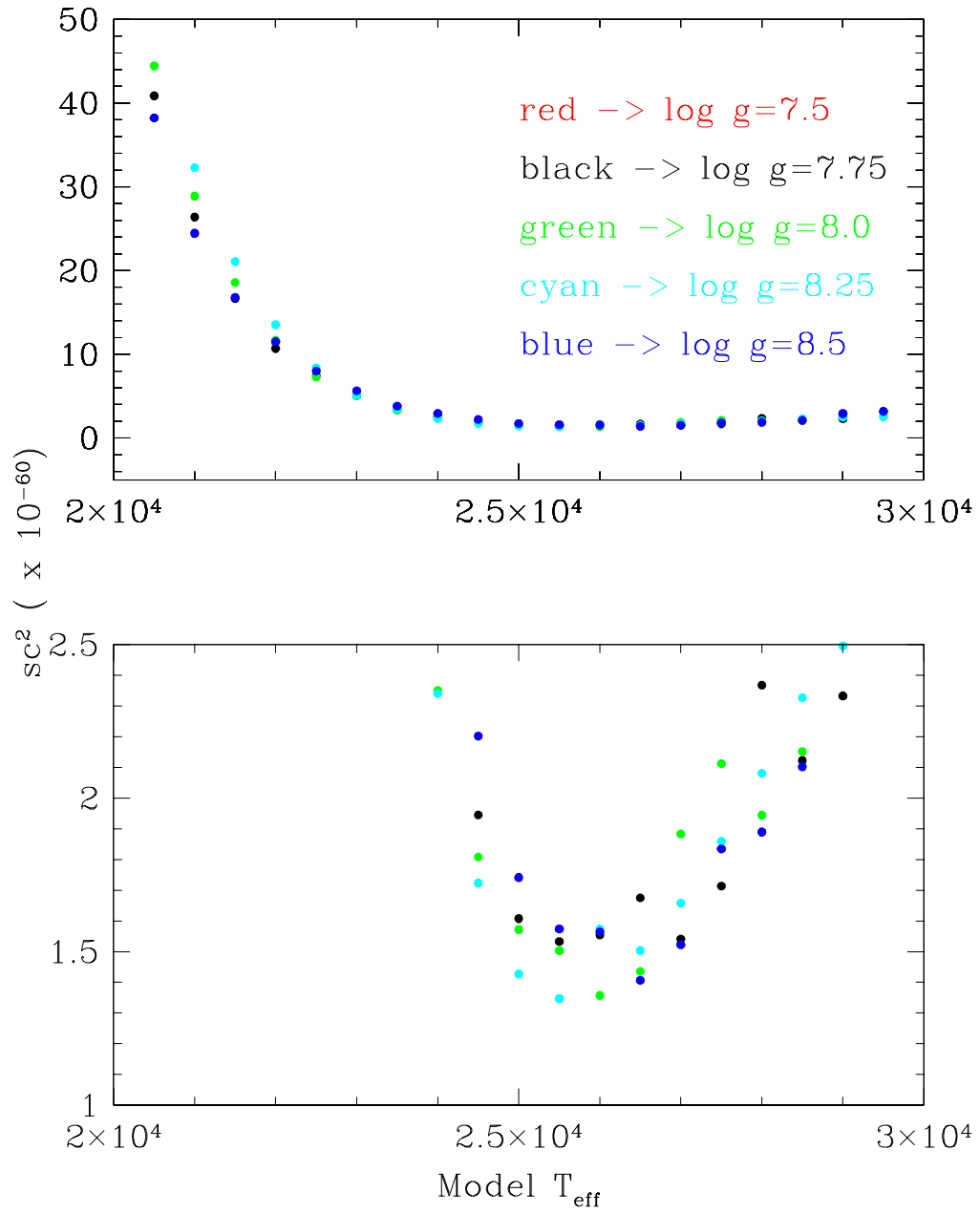


Figure 2.30: The values of sc^2 for various GD358 Models. The bottom panel is an enlarged region of the upper panel.

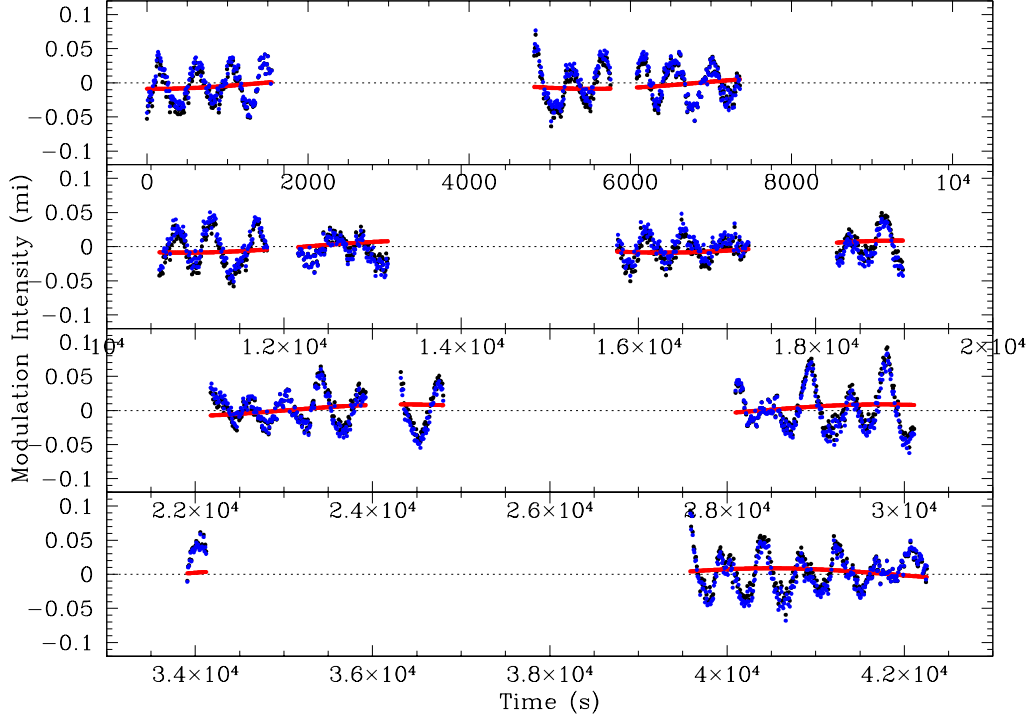


Figure 2.31: The summed UV lightcurve. The black shows the original lightcurve, the red is our fit to the HST's orbit, and the blue curve is the lightcurve with the orbital modulation removed. The differences between the black and blue lightcurves are so small that it is hardly distinguishable in this figure.

of orbital effect.

Figure 2.32 shows the final reduced lightcurve (the blue lightcurve in Figure 2.31). As both the zeroth order and UV data were taken simultaneously, they both suffer exactly the same way from the orbital effects and the data transfer interruptions, as can easily be seen by examining Figures 2.31 and 2.17.

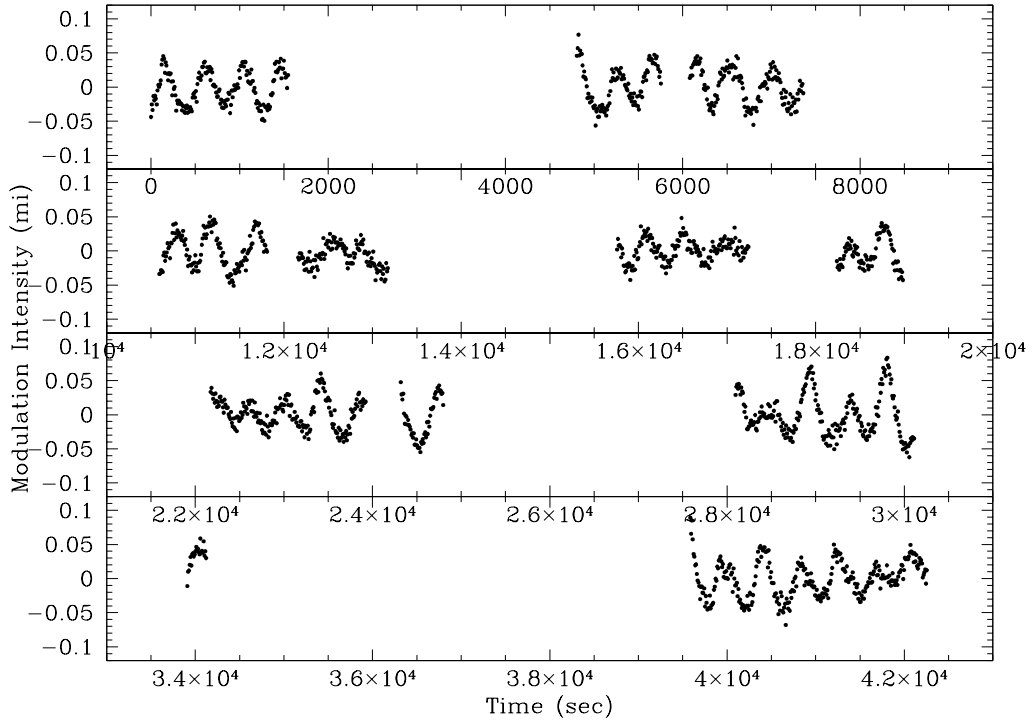


Figure 2.32: Total UV lightcurve. The data were binned over the entire observed UV range. The gaps in the lightcurve come from the HST's low orbit resulting in the target occulted by the Earth (the larger gaps) and the data being recorded (smaller gaps).

Telescope	Run	Date (UT)	Time(UT)	Length (s)
Suhora 60-cm	suh-55	1996 Aug 10	23:28:00	8890
McDonald 82-inch	an-0034	1996 Aug 12	2:46:20	18970
Suhora 60-cm	suh-56	1996 Aug 12	20:26:40	14730
McDonald 82-inch	an-0036	1996 Aug 13	3:06:30	13840
Suhora 60-cm	suh-57	1996 Aug 13	19:12:10	22050
McDonald 82-inch	an-0038	1996 Aug 14	3:14:10	12920
BAO 85cm	bao-0026	1996 Aug 14	13:10:00	13610
Suhora 60-cm	suh-58	1996 Aug 14	23:19:10	5370
McDonald 82-inch	an-0040	1996 Aug 15	3:04:30	15780
McDonald 36-inch	an-0041	1996 Aug 16	2:54:00	15700
BAO 85cm	bao-0027	1996 Aug 16	13:01:50	1250
BAO 85cm	bao-0028	1996 Aug 16	13:42:30	9330
McDonald 36-inch	an-0042	1996 Aug 17	5:01:50	6420
McDonald 36-inch	an-0043	1996 Aug 18	4:05:30	3930
Suhora 60-cm	suh-59	1996 Aug 18	21:02:10	13010
McDonald 36-inch	an-0042	1996 Aug 18	4:05:30	3930
McDonald 36-inch	an-0043	1996 Aug 19	2:44:40	2100
McDonald 36-inch	an-0044	1996 Aug 19	2:44:40	2100
McDonald 36-inch	an-0044	1996 Aug 19	3:47:00	4250
McDonald 36-inch	an-0045	1996 Aug 19	3:47:00	4250
McDonald 36-inch	an-0046	1996 Aug 19	4:58:30	7160
Suhora 60-cm	suh-60	1996 Aug 19	20:28:00	15290
Suhora 60-cm	suh-61	1996 Aug 20	21:04:00	10670

Table 2.3: Journal of ground-based observation for GD358 in August, 1996

2.5 The Ground-based Optical Observation of GD358

To obtain the optical lightcurves, we had three sites on the Earth observing GD358 around the time of the HST observation: Beijing Astronomical Observatory (BAO) in China, Mt.Suhora Observatory in Poland and McDonald Observatory in the USA. The journal of observations is in Table 2.3.

Figures 2.33 and 2.34 show the 11-day lightcurve observed by the three sites. Each panel corresponds to one day. In the bottom panel of Figure 2.34,

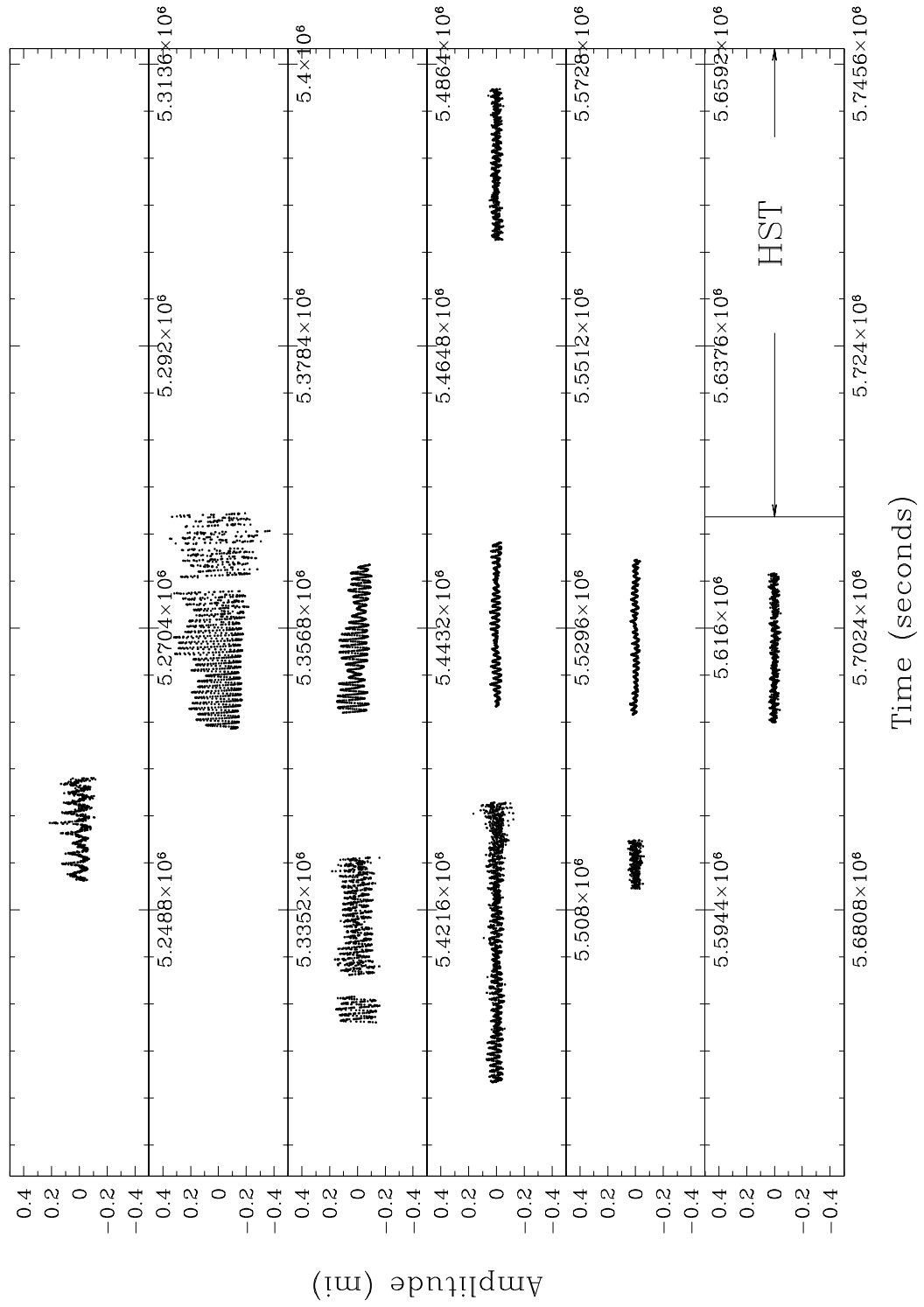


Figure 2.33: First half of the ground-based optical lightcurve of GD358. Each panel is one day long.

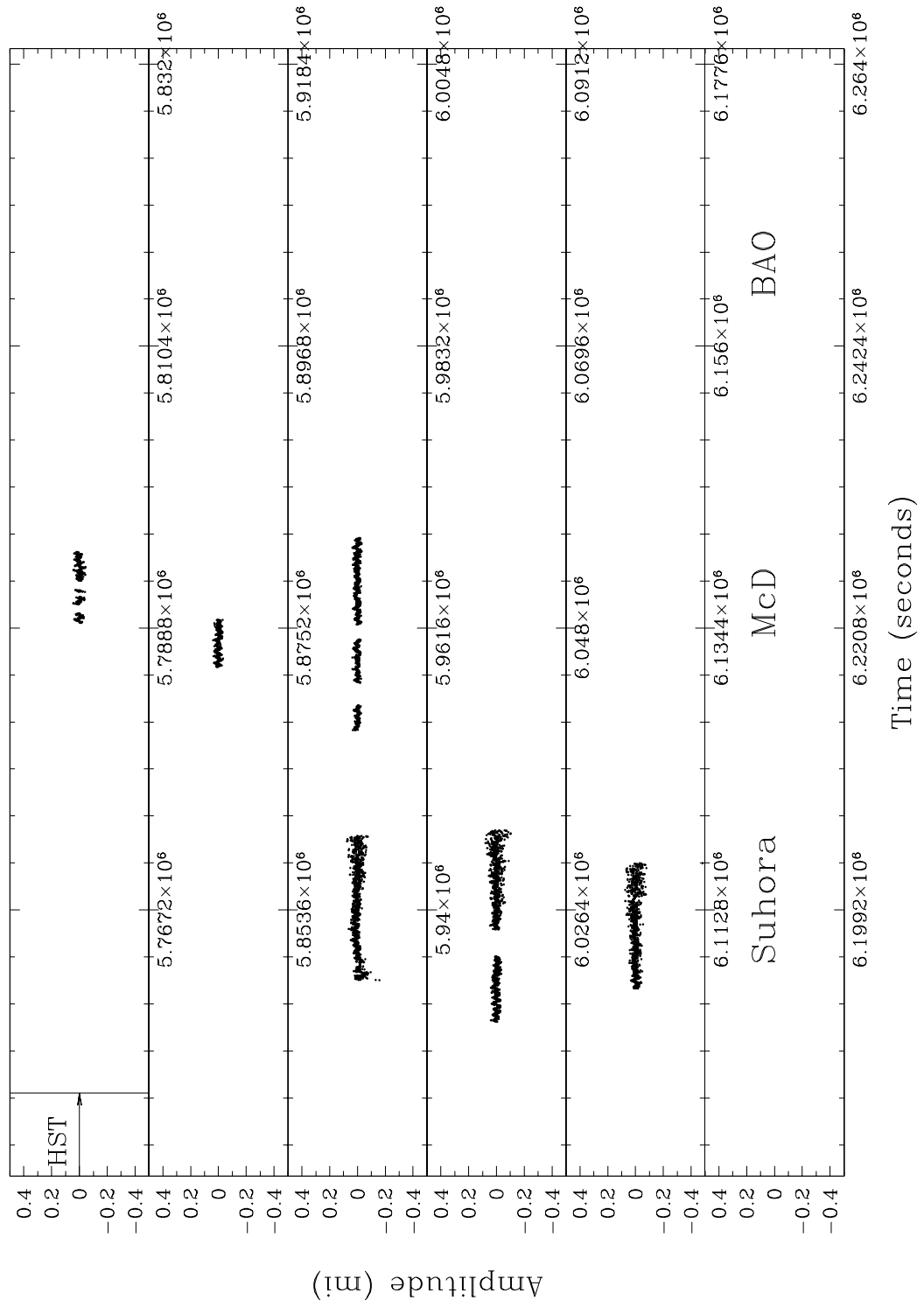


Figure 2.34: Second half of the ground-based optical lightcurve of GD358. Each panel is one day long.

we labeled which observatory observed at which time of the day. We have also labeled when the HST observations took place. As you can see, we have no simultaneous data from the ground and the HST due to the poor weather. This was most unfortunate as we need the optical data along with the UV data from the HST in order to identify the pulsation modes using the limb darkening method. Normally, having data close in time, but not simultaneous with the HST data would have been OK since the amplitude of GD358's pulsations have generally been observed to be fairly stable with time. As a quick glance at Figure 2.33 will immediately show, however, this time, GD358's pulsation amplitudes were far from stable. These large amplitude changes are quite interesting, but totally destroy the possibility of applying the limb darkening mode identification method without additional, really simultaneous, observations with the HST's UV lightcurves. Had it not been for the zeroth order HST lightcurves, we would not have been able to continue. Instead though, we can use the ground data to explore the amplitude changes as desired, and the zeroth order data to proceed in our quest for mode identification in GD358.

2.6 GD358 Fourier Transform

2.6.1 Optical Fourier Transform

As we mentioned earlier, we observed the largest and fastest pulsation amplitude changes ever observed in GD358 during our ground-based observation. Although the changes are quite exciting from the standpoint of pulsation theory, they introduced many obstacles in our path to calibrating the limb darkening method.

Figure 2.33 clearly shows the differing amplitudes and shapes of the lightcurves throughout our observations. In fact, the amplitude changes were so drastic, neither the lightcurve nor its Fourier transform appeared anything like those we had previously seen. To illustrate the differences, Figure 2.35 shows three different Fourier transforms of GD358: May 1994 WET run, the optical data we took in August 1996, and the near-simultaneous HST UV data we have already described in the previous section (see Figure 2.33, 2.34 and 2.32 for the lightcurves). The “windows” shown in this figure are a visualization of how well we sampled the pulsations. We simulate a lightcurve consisting of a single sinusoid sampled in the same time sequence as our data. The Fourier transform of this lightcurve is what we call the window. If the lightcurve were uninterrupted and infinitely long, the window would look like a single peak (delta function). The non-continuous nature of more typical data will reveal itself in the window as additional “alias” peaks surrounding the main peak. Thus, a single sinusoidal oscillation will show up not as a single peak, but as a group of peaks in the Fourier transform.

The 423s mode which was only the 10th highest amplitude mode in previous observations by Winget et al. (1994) and Nather et al. (1995) grew

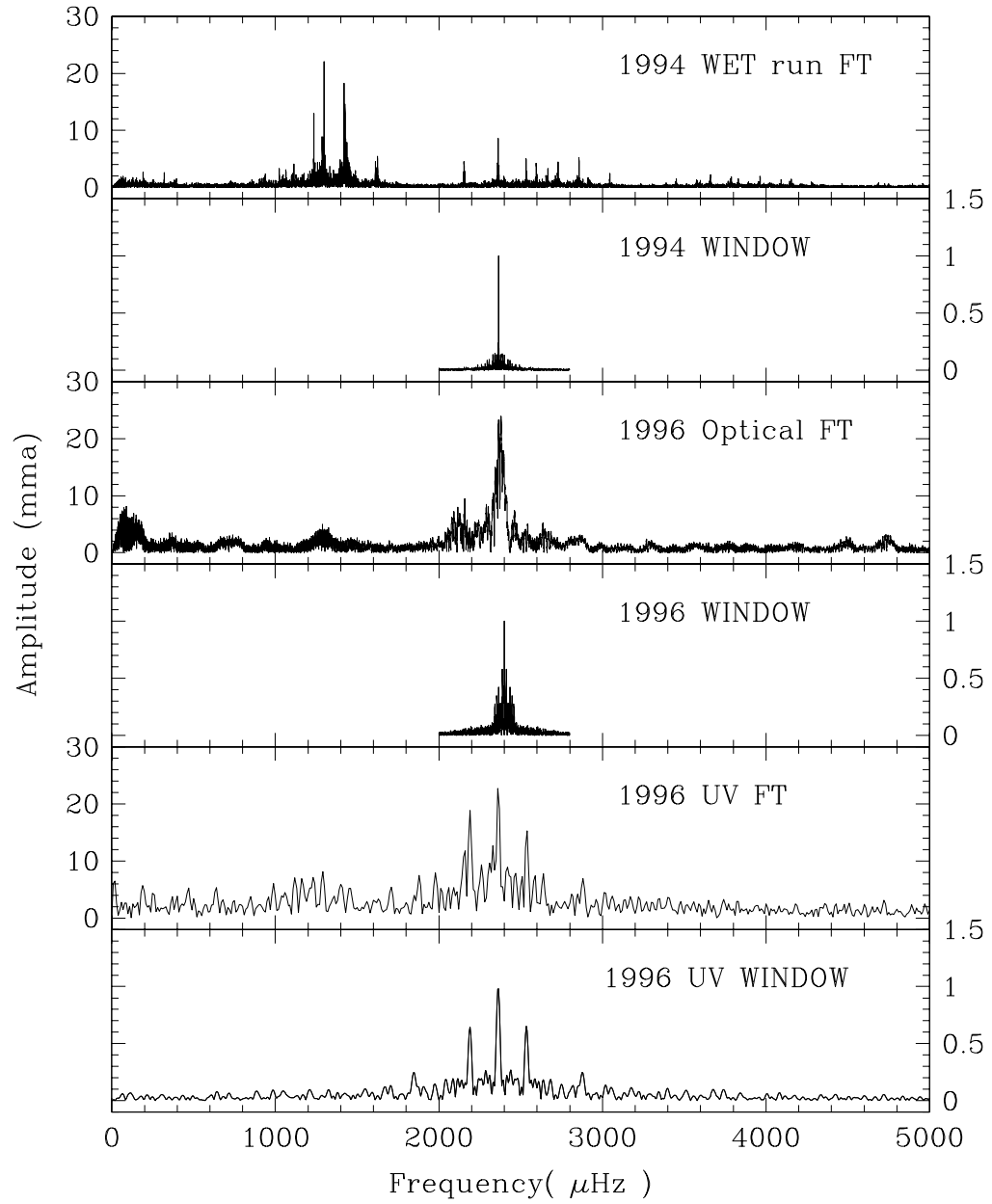


Figure 2.35: Different Fourier transforms of GD358. The top two panels show the Fourier transform and window from the WET run in 1994. The middle two panels show the optical data from August, 1996 and the bottom two panels show the UV data from August 1996.

to become the dominant mode in an August 1996 data set. As its amplitude peaked, there was little additional power in the star's other modes. GD358's amplitude modulation was not limited to this one mode. Throughout August, many of the mode amplitudes were not stable. We show the Fourier transform of individual optical runs in Figures 2.36 and 2.37. Although the resolution of each transform is not very good, they do illustrate how drastically the amplitudes changed over timescales of hours and days. In Figure 2.36, all but the last panel have the same vertical scale. The bottom two panels show the Fourier transform of the run suh-57, but at two different scales since the amplitudes are getting too small to be clearly seen in the larger vertical scale. All the panels in Figure 2.37 have the same vertical scale as the bottom panel of Figure 2.36. Some of the observed amplitude changes are probably due to beating between closely spaced frequencies. For instance, the 423s ($2363\mu\text{Hz}$) mode and the 464s ($2454\mu\text{Hz}$) mode have a beat period of about 1.3 hrs.

All large changes we see, however, cannot be explained entirely by beating. The frequency range where we see most of the pulsation power is different from suh-55 and the rest of the data. The suh-60 data set shows a hint of the power around $1200\mu\text{Hz}$. To concentrate on identifying the pulsation modes using the limb darkening method, we will now put aside the amplitude modulation (see Appendix for additional information on it).

2.6.2 UV Fourier Transform

We show the 26 UV Fourier transforms created from the 26 lightcurves described in the previous section in Figures 2.38 to 2.41. Each panel is labeled by the mid-wavelength of the wavelength range used to create the lightcurve.

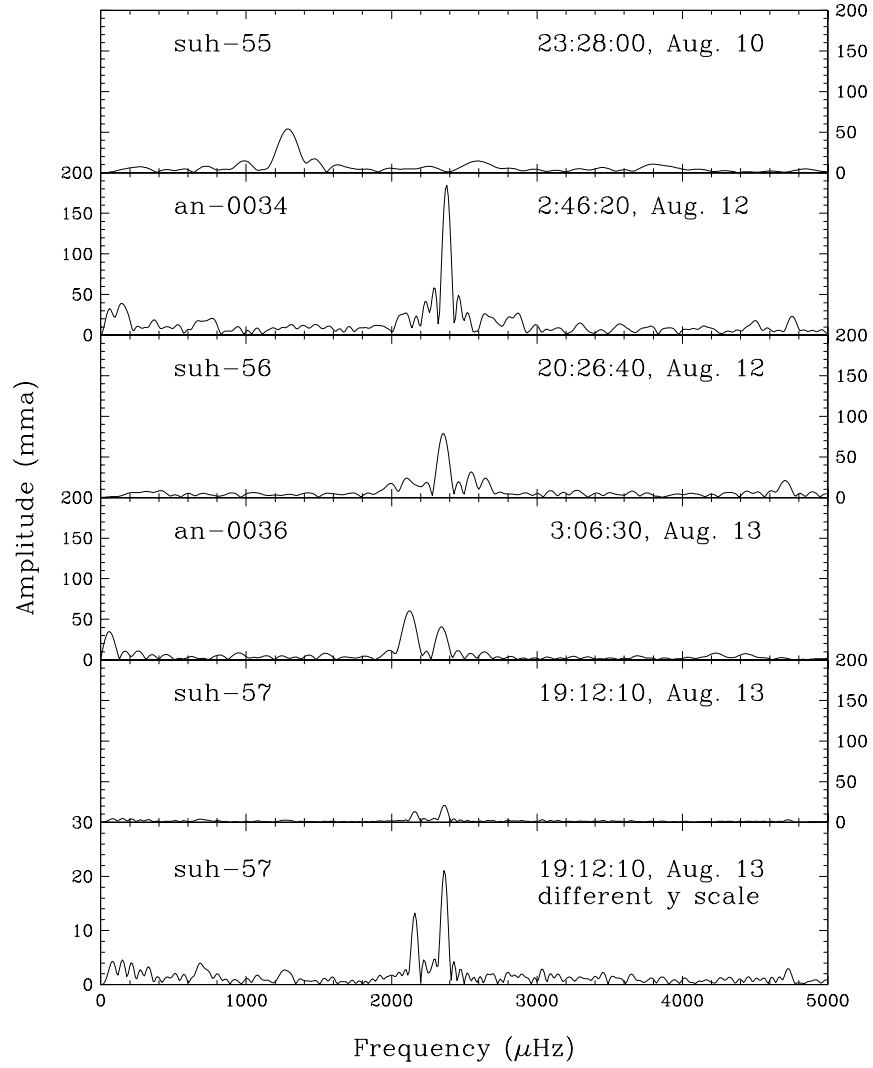


Figure 2.36: Running optical Fourier transform of GD358 in August, 1996. Note that except for the bottom panel, the vertical scales are all the same. The Fourier transform of suh-57 is shown twice in 2 different vertical scales. By the time suh-57 was taken, the amplitudes of the modes were getting quite small compared to those in an-0034. The amplitudes continued to change throughout August.

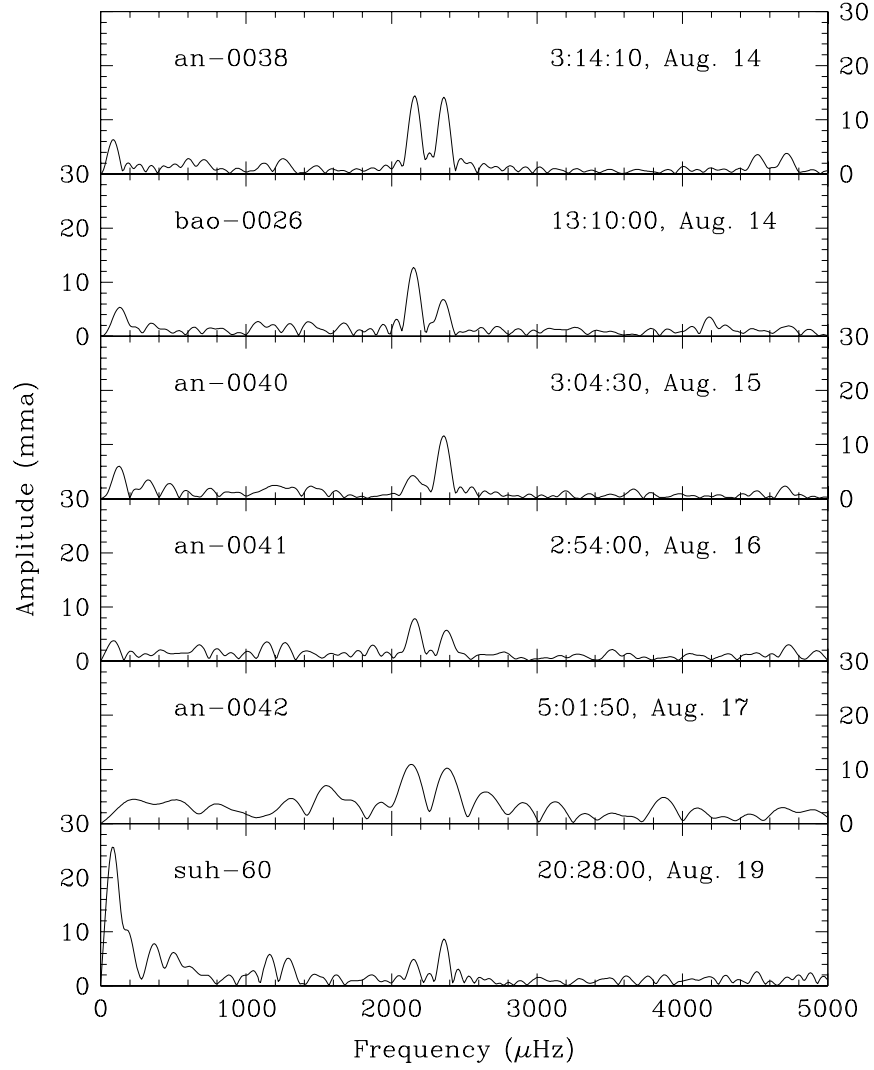


Figure 2.37: Continued running optical Fourier transform of GD358 in August, 1996. The vertical scales are the same in each panel and identical to that used in the bottom panel of Figure 2.36. The normally dominant 770s ($1427\mu\text{Hz}$) and 700s ($1298\mu\text{Hz}$) modes, as seen in Winget et al. (1994) and Nather et al. (1995), are barely present.

Although we cannot resolve each individual pulsation mode in the individual power spectra, we can still see how the amplitudes of the pulsations change with wavelength: the shorter wavelength data have larger amplitude.

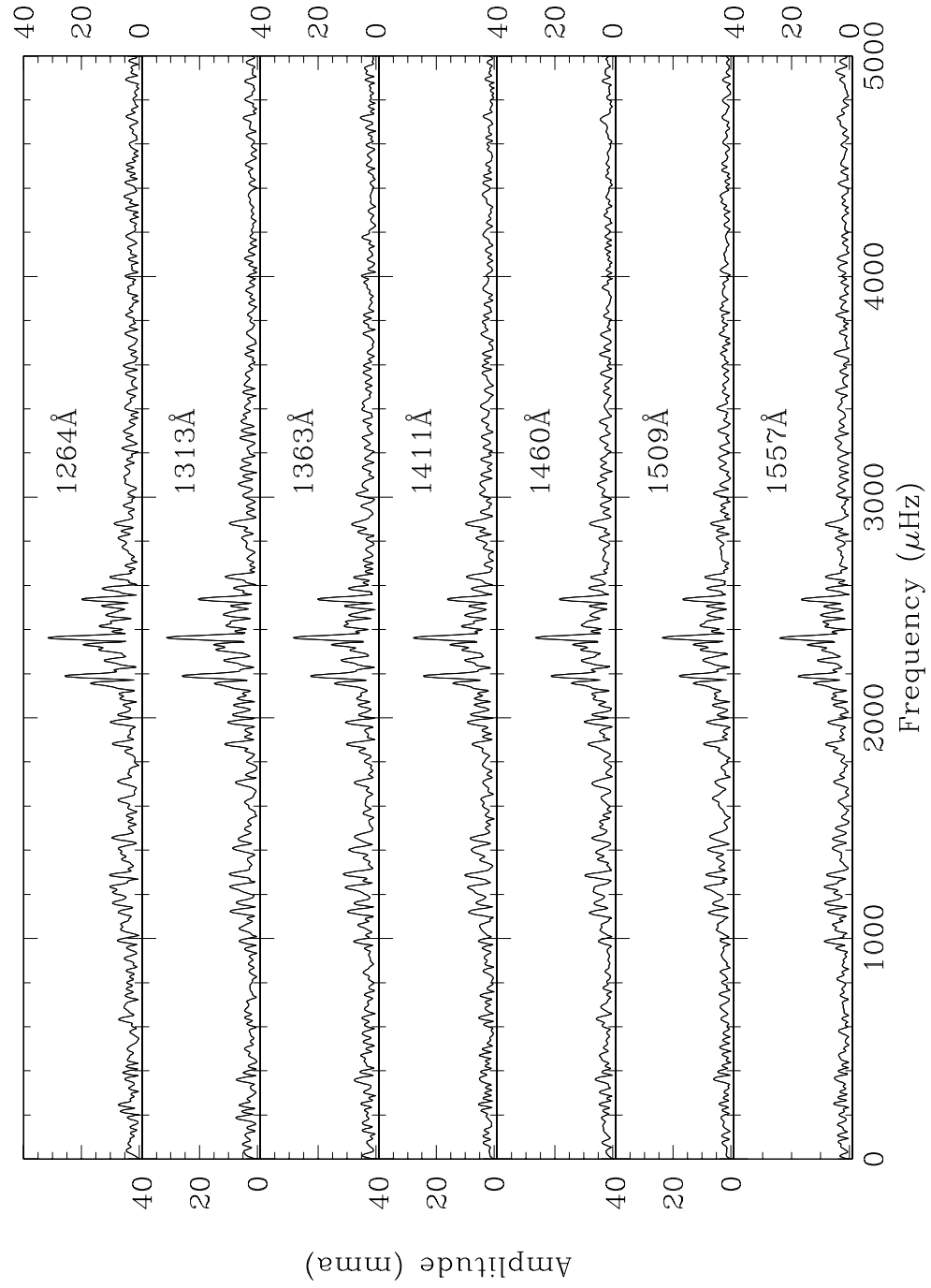


Figure 2.38: GD358 UV Fourier Transforms in the UV (Part 1). Each panel is labeled by the mid-wavelength of the wavelength range used to created the lightcurve which produced the Fourier transform.

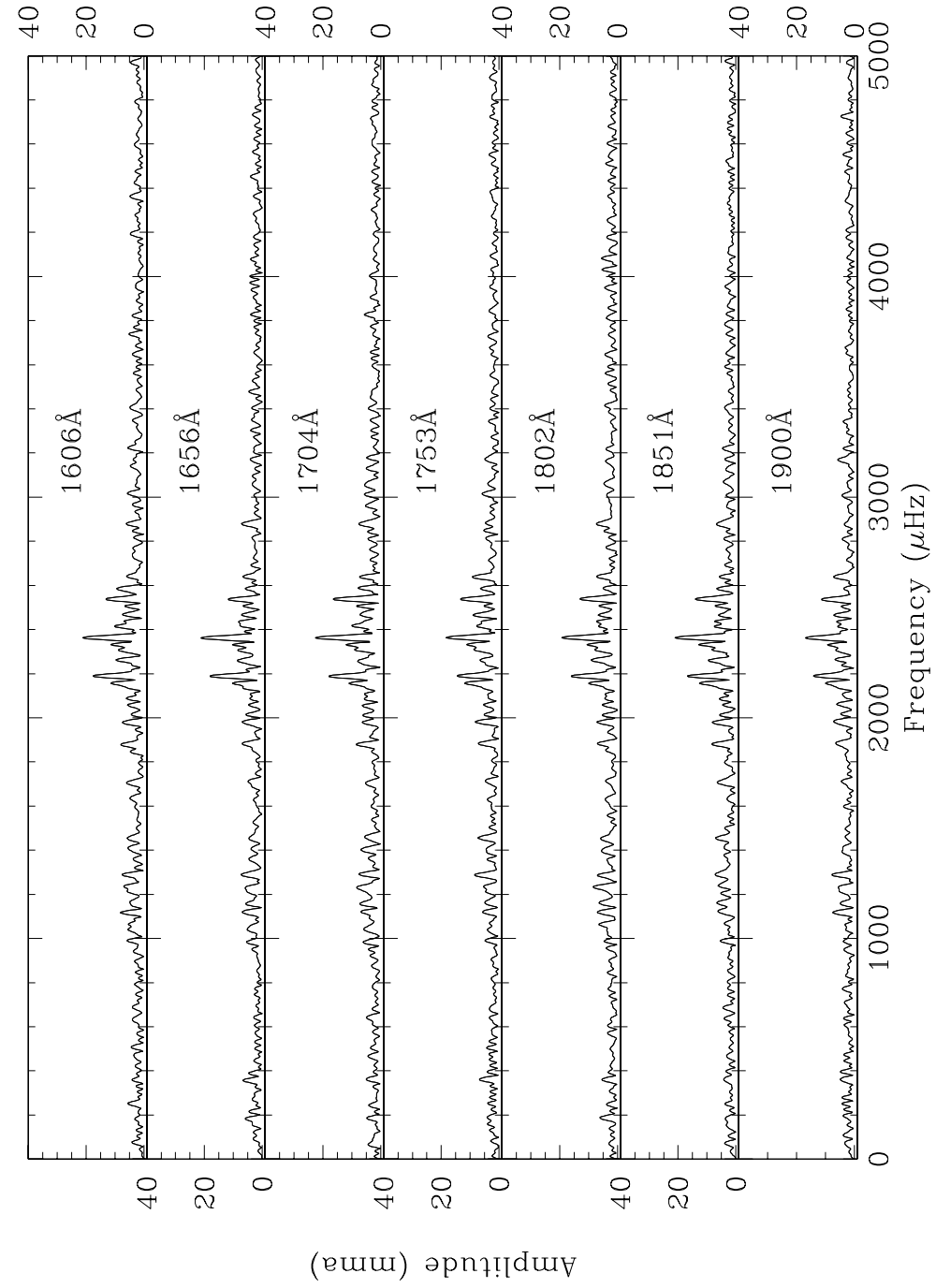


Figure 2.39: GD358 UV Fourier Transforms in the UV (Part 2). Each panel is labeled by the mid-wavelength of the wavelength range used to created the lightcurve which produced the Fourier transform.

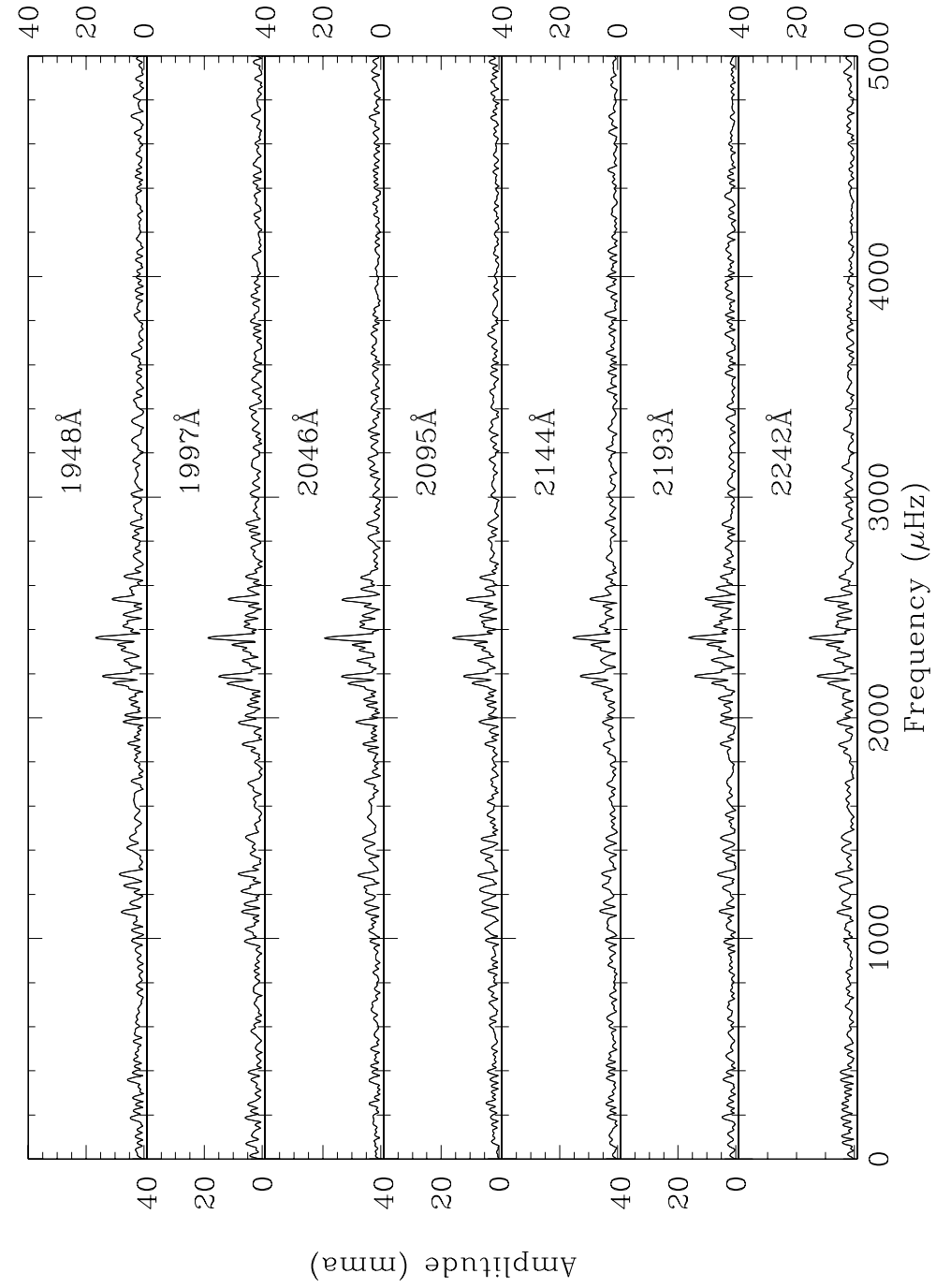


Figure 2.40: GD358 UV Fourier Transforms in the UV (Part 3). Each panel is labeled by the mid-wavelength of the wavelength range used to created the lightcurve which produced the Fourier transform.

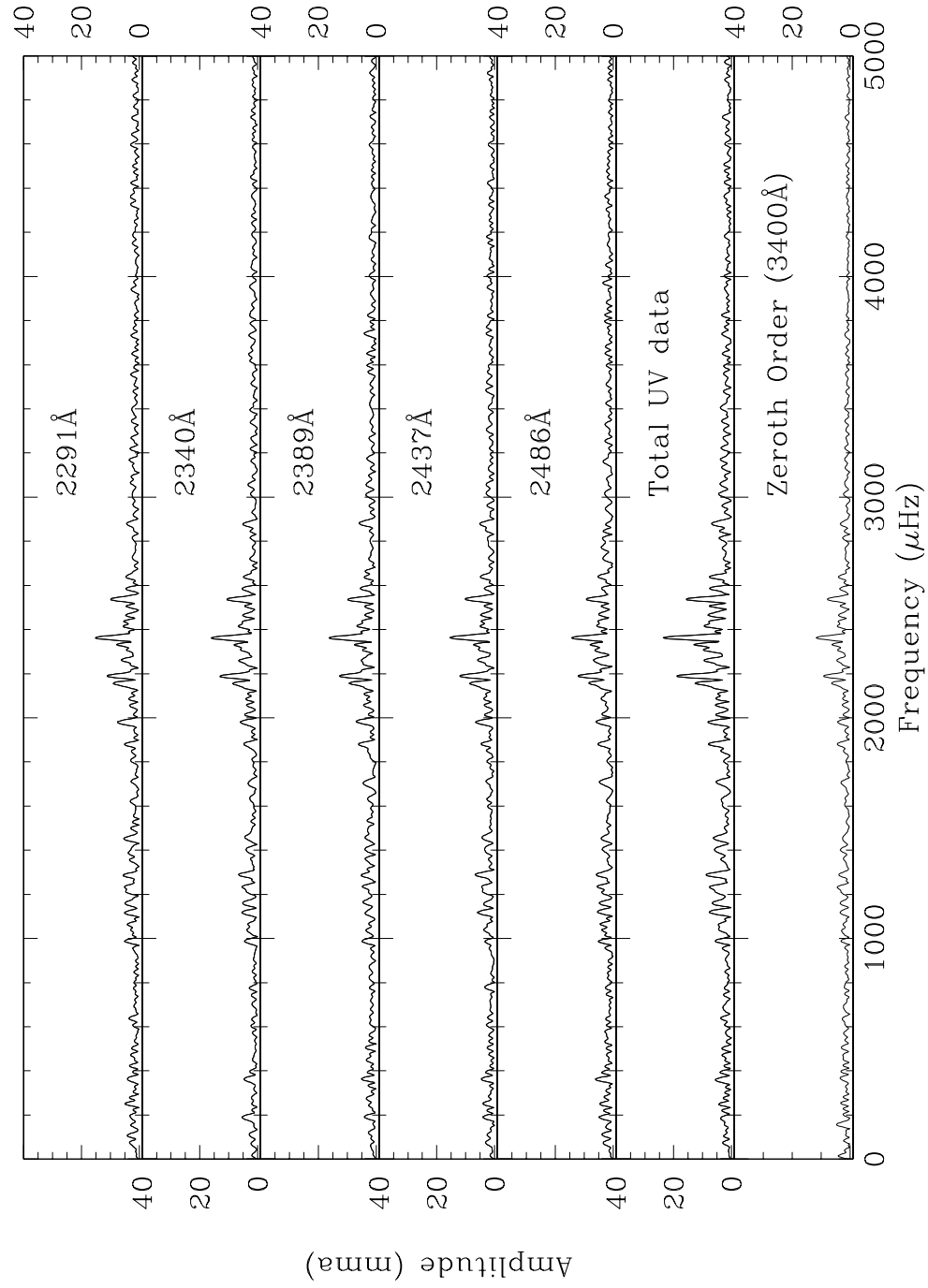


Figure 2.41: GD358 UV Fourier Transforms in the UV (Part 4). Each panel is labeled by the mid-wavelength of the wavelength range used to created the lightcurve which produced the Fourier transform.

2.7 Mode Identification of GD358

We will use the Fourier transform ratio, the lightcurve ratio, and the amplitude ratio of our data on GD358 to attempt mode identification. The first two ratios can tell us, at least in principle, if the data consist of more than one ℓ or not, while the last approach can tell us the ℓ value of each individual mode.

2.7.1 Fourier Transform Ratios

GD358's pulsation spectrum was changing during the HST observations (Figures 2.36 and 2.37). This makes analysis using the ground-based optical data impossible to compare directly with the HST UV data. We therefore decided to use the simultaneous HST zeroth order data as a comparison base instead. Although this solves the simultaneity problem, using the zeroth order data does have its drawbacks. Its shorter effective wavelength (3400Å compared to 4200Å for our optical data) is unfortunate as it makes it harder to distinguish between different models. Figure 2.42 shows how the model calculations change by taking a ratio between data in the UV with data either at 4220Å or at the zeroth order (3400Å) wavelength. Still, the simultaneous nature of the zeroth order data is critical and we have no choice but to accept the compromise in wavelength coverage.

Figure 2.43 shows the ratio of each of the UV Fourier transforms (discussed in the previous section) with the zeroth order data Fourier transform. Also plotted is the 25500K, $\log g = 8.0$ DB model calculated using Koester's model atmosphere. The Fourier transform ratio tells us that the models observed in GD358 are not $\ell = 3$, but either $\ell = 1$ or $\ell = 2$. It is difficult to decide if the modes are $\ell = 1$ or $\ell = 2$ as the ratios at shorter wavelengths

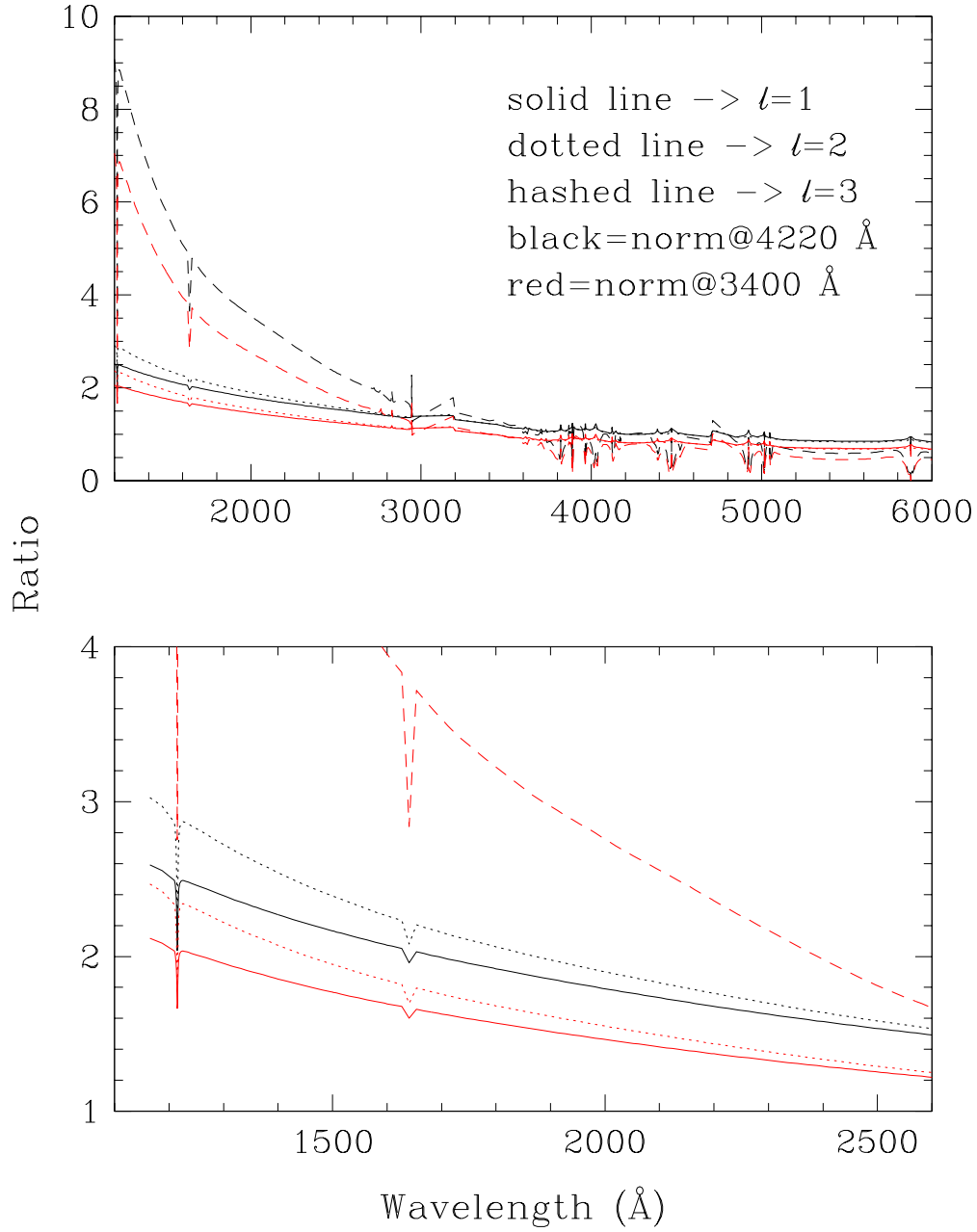


Figure 2.42: DB model amplitude ratio vs. wavelength as a function of ℓ and normalization wavelength. The black lines are normalized at 4220Å, while the red lines are normalized at 3400Å. The $\ell = 1$ calculations are in solid lines, $\ell = 2$, dotted lines and $\ell = 3$ in hashed lines. The bottom panel shows the wavelength region our HST data cover. The difference between the $\ell = 1$ and $\ell = 2$ lines normalized at 3400Å is smaller than that for the 4220Å lines, making it harder to distinguish different ℓ modes with the shorter wavelength normalization.

favor $\ell = 2$ while at longer wavelengths, they prefer $\ell = 1$. This disparity can not be due to having a mixture of $\ell = 1$ and $\ell = 2$ modes present in the star as such a mixture would show a more uniform disagreement across wavelength rather than the non-uniform one we are seeing here. (Section 2.7.4 treats this issue more directly.) As we discussed in the Section 2.4.2, we know our atmosphere models agree well with data when we compared the UV continuum spectrum (Figure 2.25). As Fontaine et al. (1996) pointed out in their reanalysis of G117-B15A HST data taken by Robinson et al. (1995) using their model atmosphere models, the models that describes the continuum come from the total emergent flux where the amplitude ratios are computed using the local flux and how they change with temperature (i.e. temperature derivative of the local flux). Therefore, getting a good fitting continuum does not ensure we will get a good fit with for the amplitude ratios.

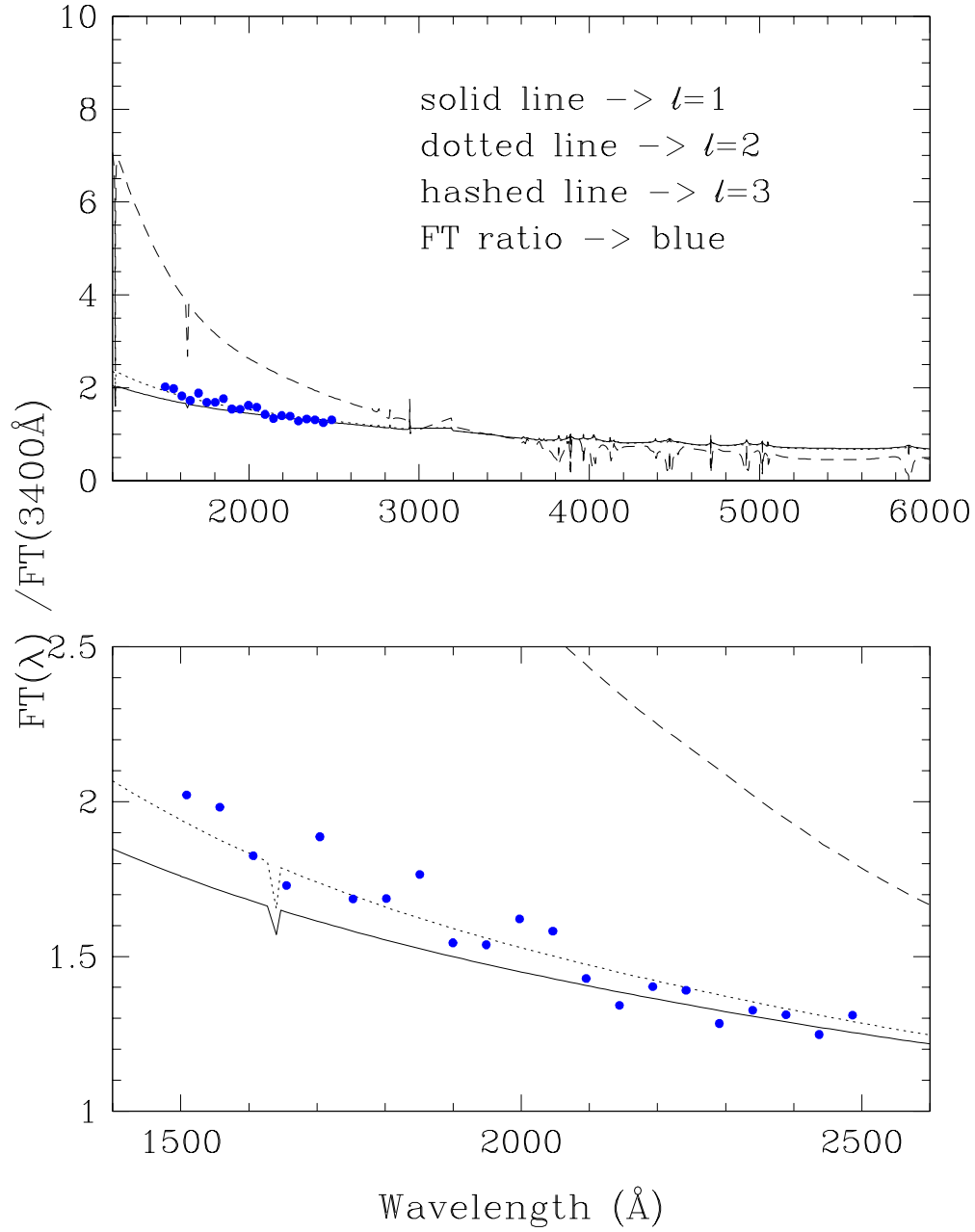


Figure 2.43: Observed vs. model GD358 Fourier transform ratios. The Fourier transform ratios (dots) are shown along with the DB model calculated using Koester's model atmosphere with an effective temperature 25500K and $\log g = 8.0$. The solid line shows the $\ell = 1$ calculation, the dotted line, the $\ell = 2$ calculation and the hashed line shows the $\ell = 3$ calculation. The observed ratios tells us that the observed modes are not $\ell = 3$ modes, but it is hard to tell if they are $\ell = 1$ or 2 as they seem to have different trends at different wavelength region: the shorter wavelength ratios prefer $\ell = 2$ while the longer wavelength ratios prefer $\ell = 1$.

2.7.2 Lightcurve Ratios

We show the results of the lightcurve ratios in Figure 2.44. All the data points are lower than both the model calculations and the Fourier transform ratios. We first thought perhaps the phases of the 423s mode in the UV lightcurves are different from the zeroth order lightcurve by either a mistake in the data reduction process or some unknown physical processes inside GD358. Robinson, Kepler and Nather (1982) showed that nonradial g-modes have constant phases at different wavelengths, so this phase explanation shouldn't be correct, but we should check.

After observing the large amplitude modulation in GD358's lightcurves, it was not hard for us to imagine other unusual things happening inside the star. Although differences in phases can result in the lightcurve ratios being different from the Fourier transform ratios, it is hard to imagine how to get the lightcurve ratios to be consistently smaller than the Fourier transform ratios at all wavelengths. Figure 2.45 shows the 423s mode's phase vs. wavelength. The phases were estimated using the linear least squares fitting technique and the error bars in the figure are the formal errors. We confirmed that as expected, the phases are consistent within the error bars. This result rules out phase playing a role in the lightcurve ratios being consistently lower than the Fourier transform ratios.

The only explanation we currently have is that the lightcurve ratio is more sensitive to noise in the data than are the Fourier transform ratios. For example, if noise moves a pulsation peak a few seconds later in one lightcurve than in another, there will be a large difference in these two curves' ratio. Such effects should cancel out and just increase the noise band as we evalu-

ate the lightcurve ratios at all points in the lightcurves, but perhaps they do not for some unknown reasons. We suspect that the differences between the Fourier transform ratio and the lightcurve ratio tells us the level of noise in the lightcurves and therefore we do not use the lightcurve ratios any further in our analysis.

Fourier Transform of the Residual Lightcurve

In order to verify that a lightcurve at one wavelength really can be expressed as some constant times a lightcurve of a different wavelength, we constructed a set of residual lightcurves $RLC(\lambda_1)$ such that:

$$RLC(\lambda_1) = \delta I(\lambda_1) - r_{lc} \times \delta I(\lambda_2) \quad (2.10)$$

where

$RLC(\lambda_1)$: Residual lightcurve at wavelength λ_1

$\delta I(\lambda_1)$: Lightcurve at wavelength λ_1

$\delta I(\lambda_2)$: Lightcurve at wavelength λ_2

r_{lc} : Lightcurve ratio of data at λ_1 (UV wavelength) and λ_2 (zeroth order data) obtained observationally

Figures 2.46 through 2.49 show the Fourier transforms of the residual lightcurves. In each figure, the Fourier transforms of the original lightcurves are shown in black, while the residual lightcurves' Fourier transforms are shown in red. The residual lightcurve Fourier transforms show very little significant power at the frequencies in the normal lightcurve Fourier transforms, thus indicating that Equation 2.10 indeed does hold true for our data.

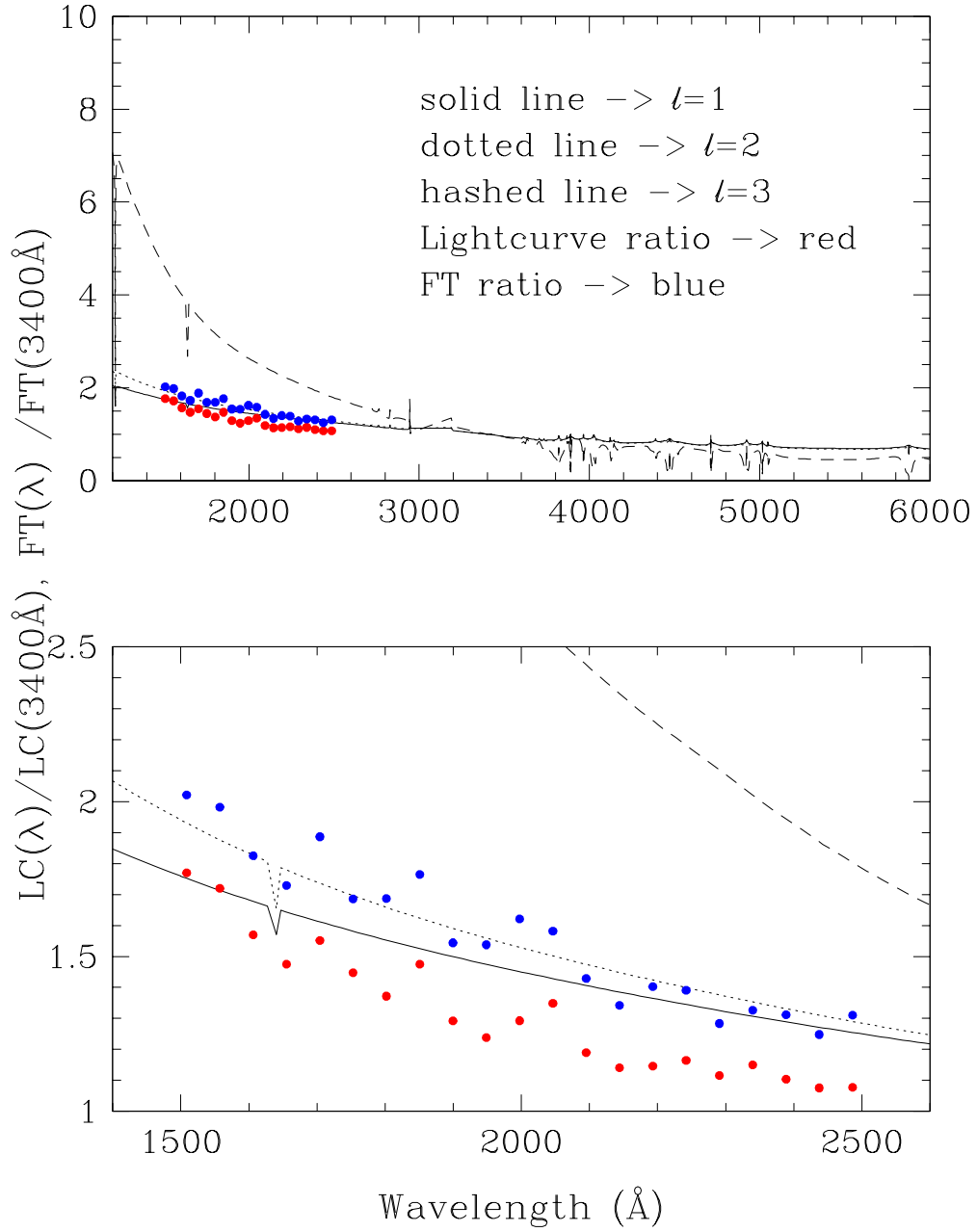


Figure 2.44: The observed and model GD358 lightcurve and Fourier transform ratios. The observed lightcurve ratios is shown in red and the Fourier transform ratios in black. The lightcurve ratios is always smaller than the Fourier transform ratios. We believe this is due to the increased sensitivity to noise in the lightcurve ratios.

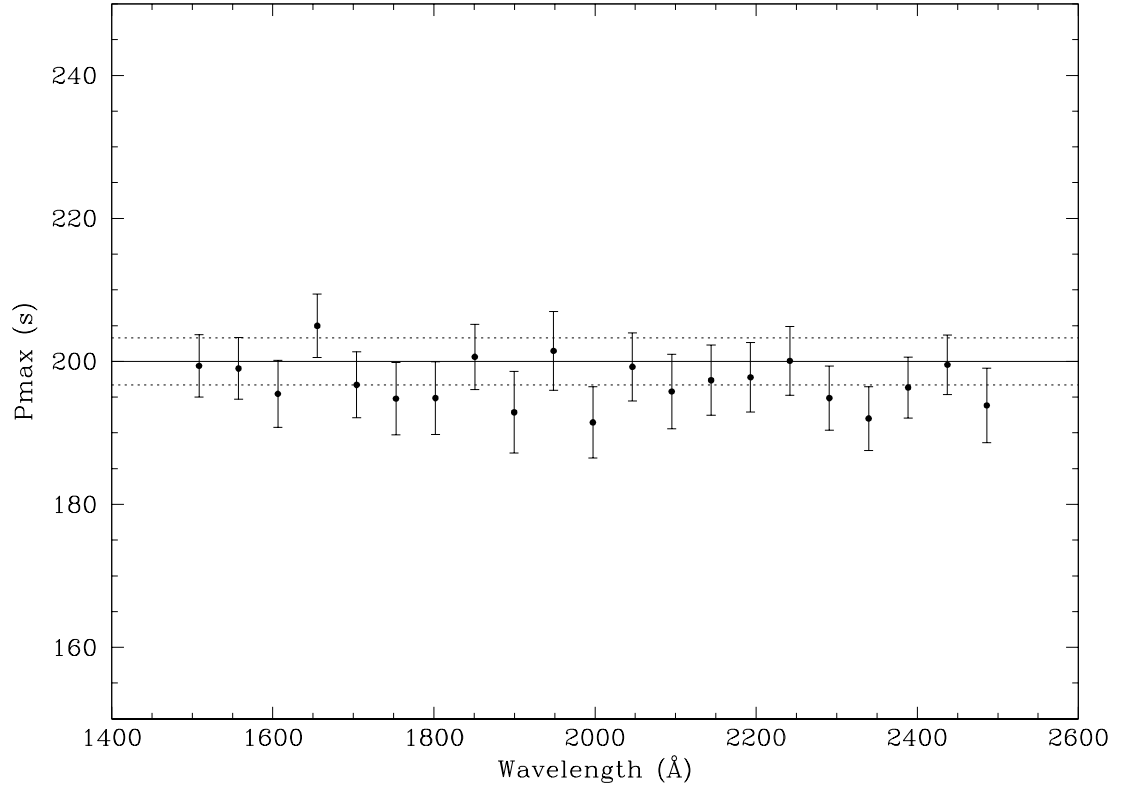


Figure 2.45: The phase of the 423s mode in GD358 vs. wavelength. The solid line shows the phase measured in the zeroth order lightcurves and the dotted lines show the formal error. Within the error bars, the phase at all wavelengths is constant, as expected from standard first order g-mode pulsation theory (Robinson, Kepler, & Nather 1982).

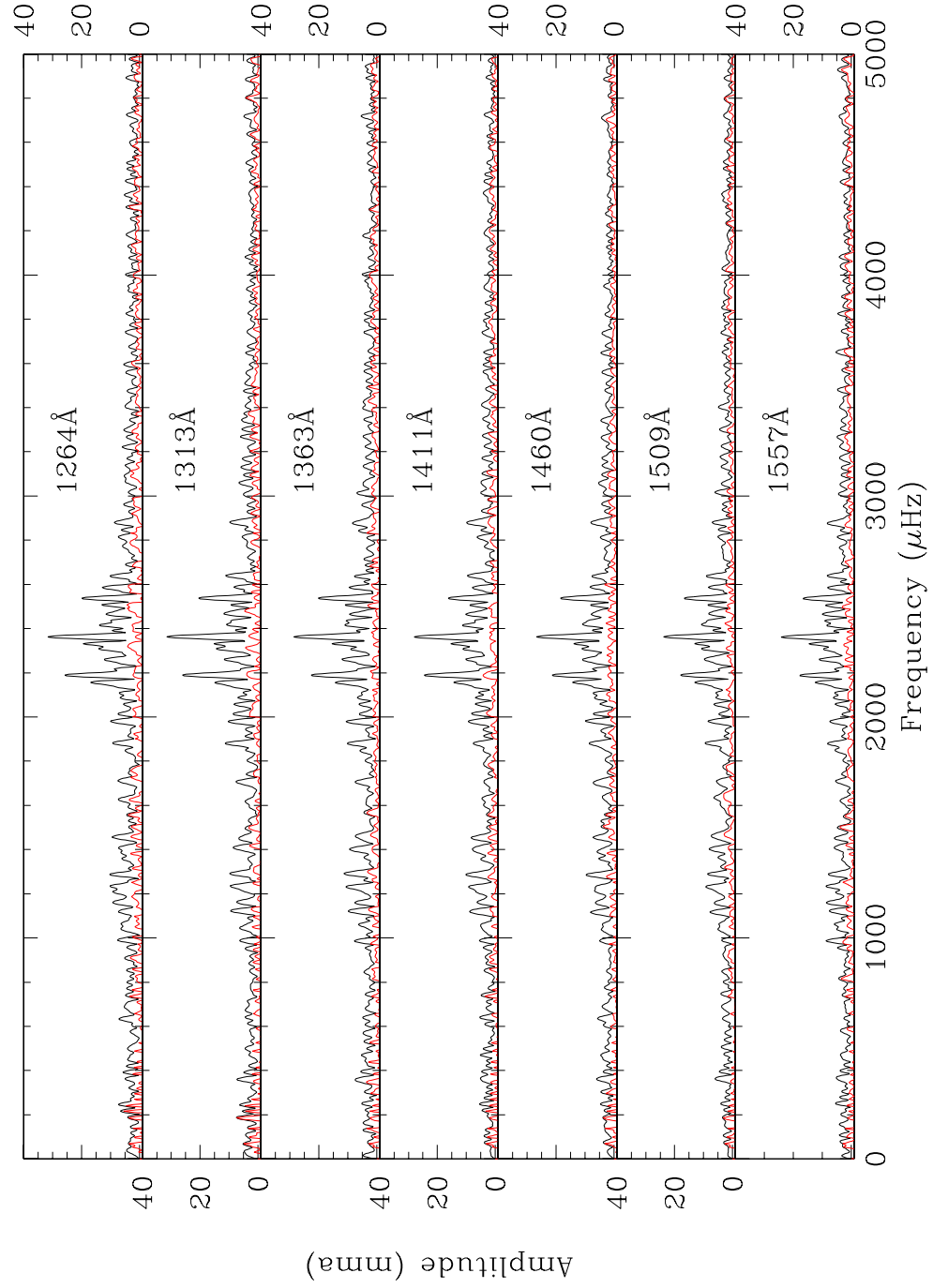


Figure 2.46: Fourier transforms of normal and residual UV lightcurves. Each panel is labeled by the wavelength we used to create the UV lightcurve. The Fourier transforms of the residual lightcurves are shown in red, and the original Fourier transforms in black. There is almost no remaining pulsation power in the residual lightcurve Fourier transforms.

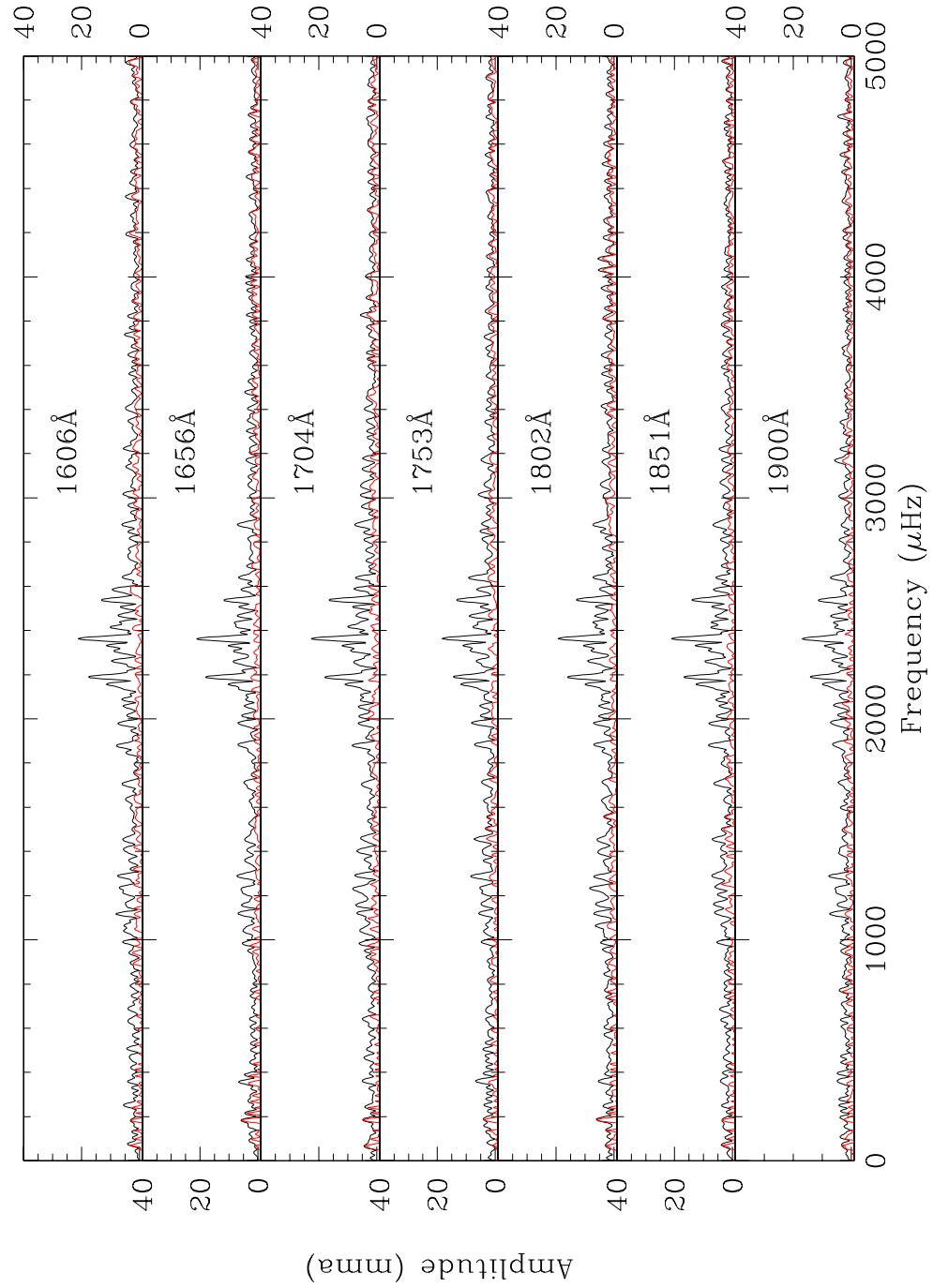


Figure 2.47: Fourier transforms of normal and residual UV lightcurves. Each panel is labeled by the wavelength we used to create the UV lightcurve. The Fourier transforms of the residual lightcurves are shown in red, and the original Fourier transforms in black. There is almost no remaining pulsation power in the residual lightcurve Fourier transforms.

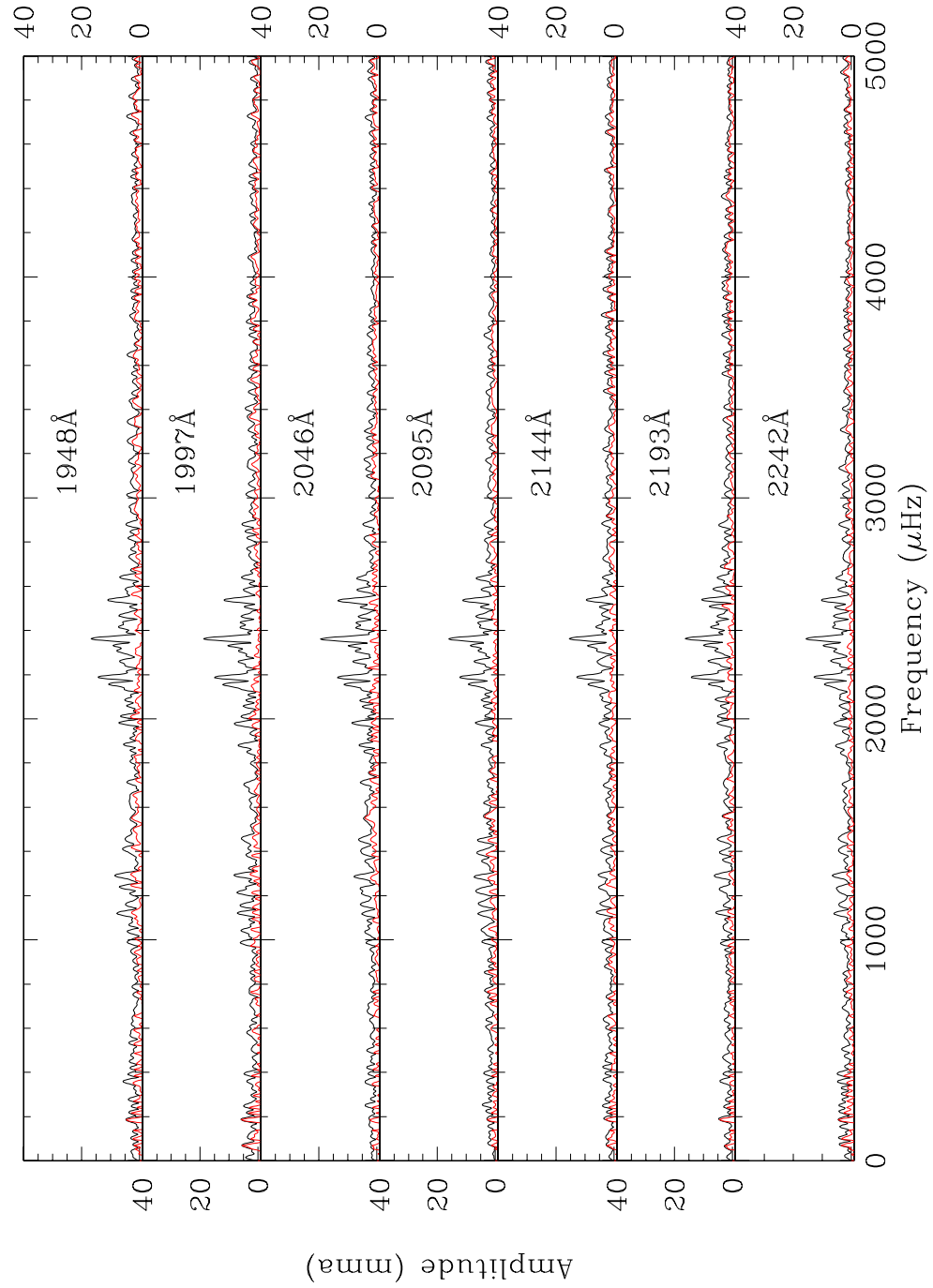


Figure 2.48: Fourier transforms of normal and residual UV lightcurves. Each panel is labeled by the wavelength we used to create the UV lightcurve. The Fourier transforms of the residual lightcurves are shown in red, and the original Fourier transforms in black. There is almost no remaining pulsation power in the residual lightcurve Fourier transforms.

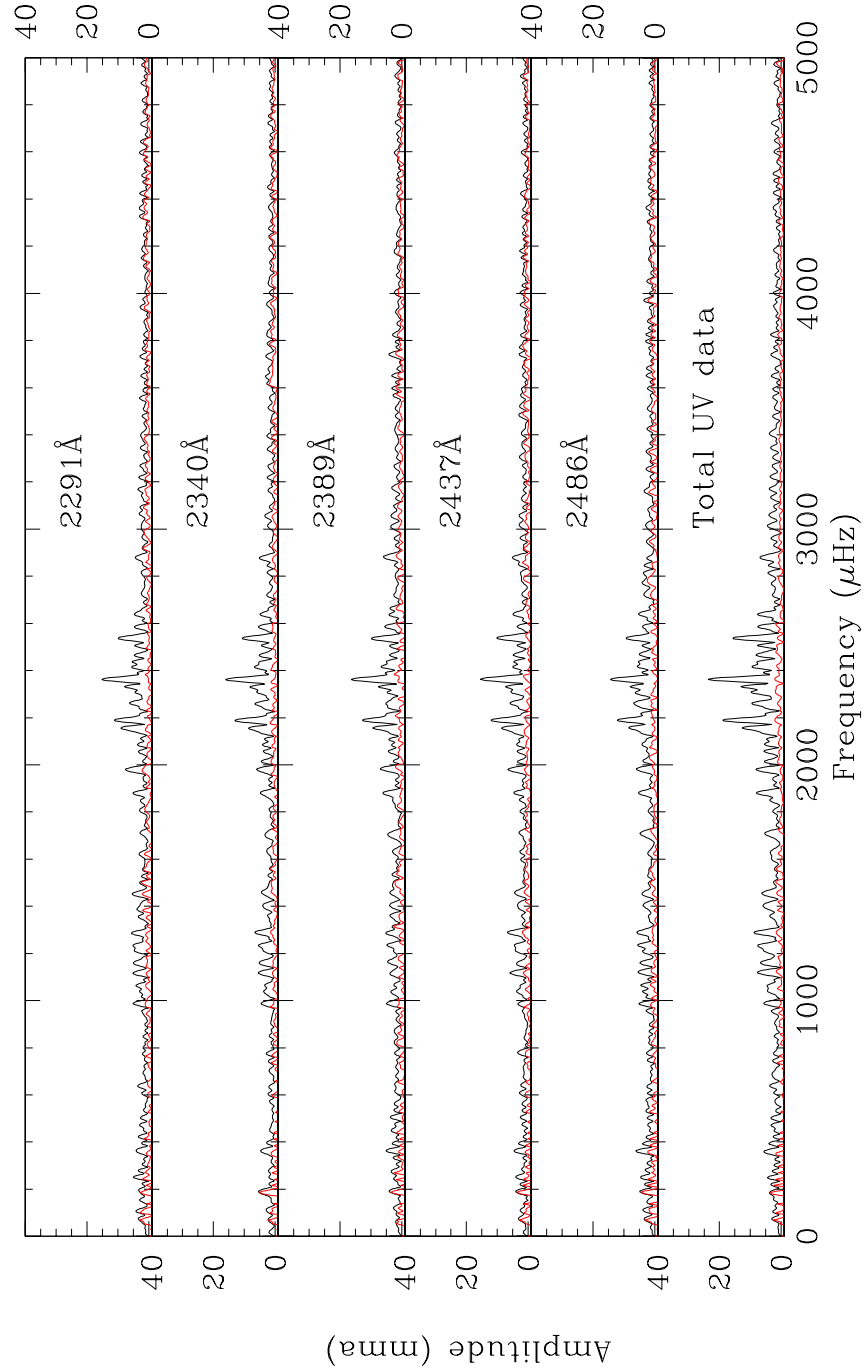


Figure 2.49: Fourier transforms of normal and residual UV lightcurves. Each panel is labeled by the wavelength we used to create the UV lightcurve. The Fourier transforms of the residual lightcurves are shown in red, and the original Fourier transforms in black. There is almost no remaining pulsation power in the residual lightcurve Fourier transforms.

2.7.3 Amplitude Ratios

The Fourier transforms of the zeroth order and the UV data show that there is more than one mode present in our observations of GD358. There are peaks around 423s, 464s and 770s. Since the zeroth order data have a better signal to noise ratio than do the UV data, we determined the periods for each mode from the zeroth order data using a nonlinear least squares fitting program. To determine the amplitudes in the UV lightcurves, we used a linear least squares fitting program, fitting only the amplitude of each mode with the period and phase fixed to those of the zeroth order data. Figure 2.50 shows the corresponding amplitude ratios between the UV and the zeroth order data for each mode.

The error bars are the formal errors estimated using the least squares fitting program. The 423s mode has the smallest error bars while the 770s mode has the largest, not surprising considering their relative amplitudes (11.04mma for 423s mode and 3.49mma for 770s mode). It is clear that we can exclude the possibility of any of the three modes being $\ell = 3$. All modes are consistent with being $\ell = 1$, but the error bars are large compared to the differences between $\ell = 1$ and $\ell = 2$ models, however. The size of the error bars and the small differences between the theoretical $\ell = 1$ and $\ell = 2$ curves make it difficult to identify the ℓ -value unambiguously. The size of the uncertainties are determined by the length and the continuity of the lightcurves used to estimate the amplitudes. The UV and the zeroth order lightcurves suffer in both. The HST is not designed to take continuous data and also impossible to get many orbits of observing time for one star. The small differences in the models come from using the zeroth order data whose effective wavelength (3400Å) is much

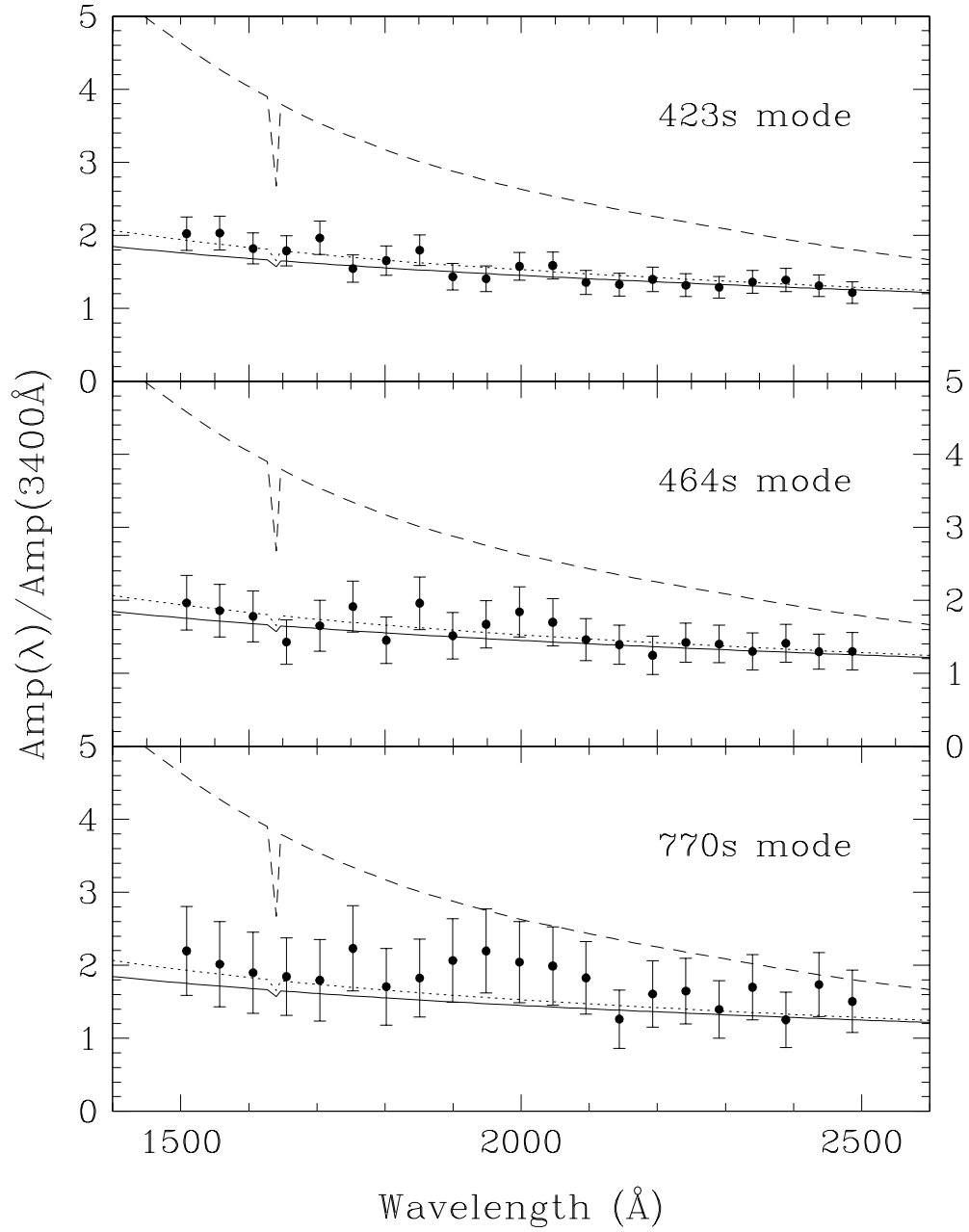


Figure 2.50: The amplitude ratio for 423, 464 and 770s modes in GD358. The error bars on the 464s and 770s modes are much bigger than those of the 423s mode because the 423s mode had significant larger amplitude than the other two modes. The solid line is the theoretical $\ell = 1$ amplitude ratio curve, the dotted line is theoretical $\ell = 2$ amplitude ratio curve and the hashed line is the theoretical $\ell = 3$ amplitude ratio curve.

shorter than the optical data (4200Å) which we originally planned to use. This resulted in the theoretical amplitude ratio curves of $\ell = 1$ and 2 to have smaller differences in the UV than we expected.

2.7.4 ℓ Identification

We summarize all three of our calculated ratios in Figure 2.51 and 2.52 where we also show DB model calculation with $T_{\text{eff}} = 25500\text{K}$, $\log g = 8.0$ and $\ell = 1, 2$ and 3. First, it is easy to notice the agreement between the Fourier transform ratio and the 423s mode amplitude ratios. We originally thought this meant whatever the ℓ value the 423s mode is, the other modes present in the data must be the same. Unfortunately, however, the Fourier transform ratio is dependent on the amplitudes of the modes, thus it is being dominated by the 423s mode and is less sensitive to the ℓ value of the 464s and 770s modes. We illustrate this in the following simulations. In the simulations we used DA models instead of DB models. This is because we noticed the amplitude dependency of the Fourier transform ratio while we were studying a DAV called BPM37093 which we will discuss in the next chapter. Although DA models and DB models have quantitatively different ℓ vs. wavelength dependences, they are the same qualitatively: at shorter wavelengths, the amplitude ratios for both $\ell = 1$ and $\ell = 2$ become larger and the $\ell = 2$ modes have larger amplitude in the UV than $\ell = 1$ mode. The conclusions derived from these simulations are similar for the DAs and the DB models.

Case 1

Assume only two modes are present in the optical lightcurve with one mode being $\ell = 1$ and another being $\ell = 2$. Assume the amplitude of $\ell = 2$

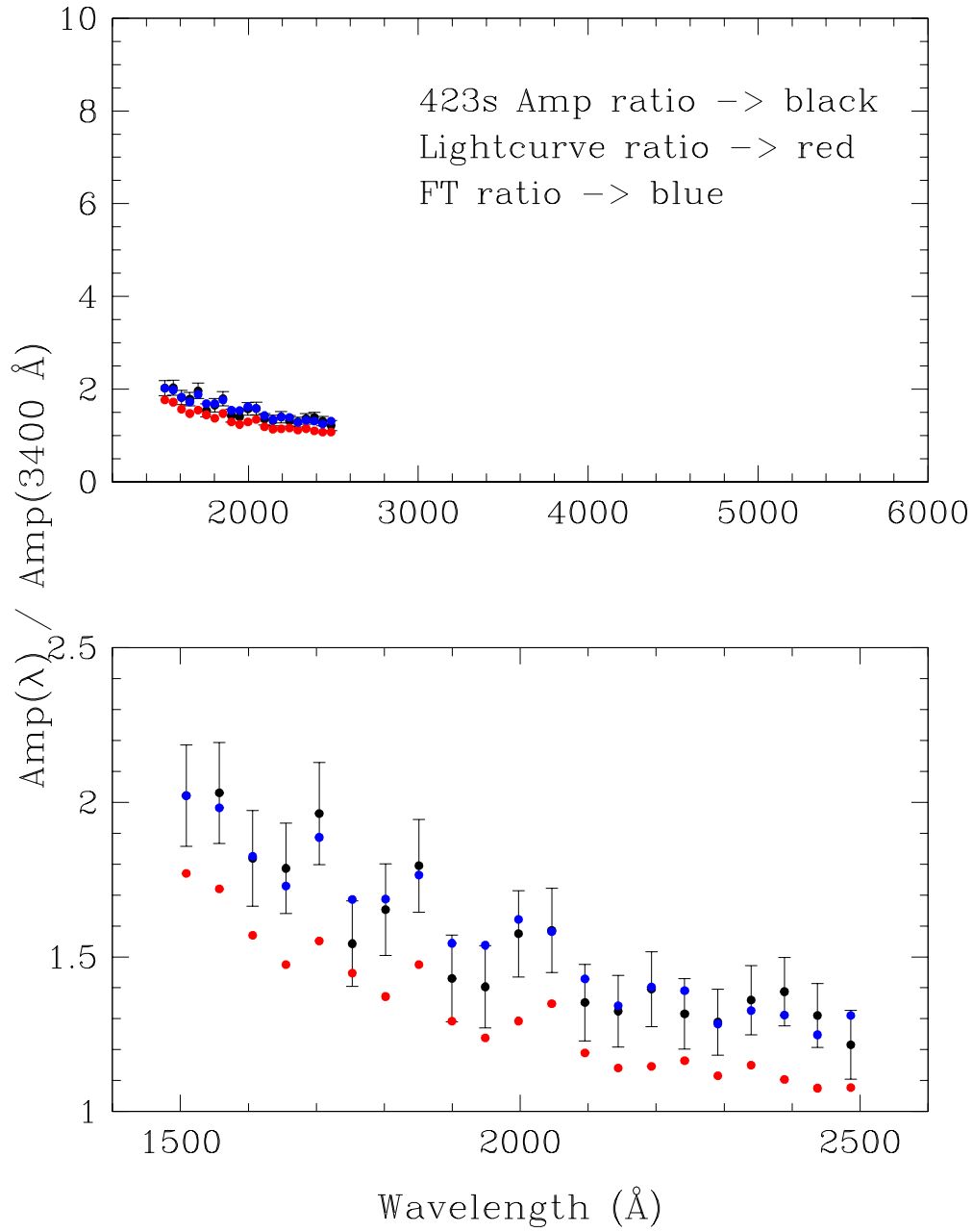


Figure 2.51: All three observed GD358 ratios. The ratio of of lightcurve is in red, the Fourier transform ratio is in blue and the 423s amplitude ratio is in black. The Fourier transform ratio and the amplitude ratio are in good agreement with each other, but the lightcurve ratio is always lower than the other two.

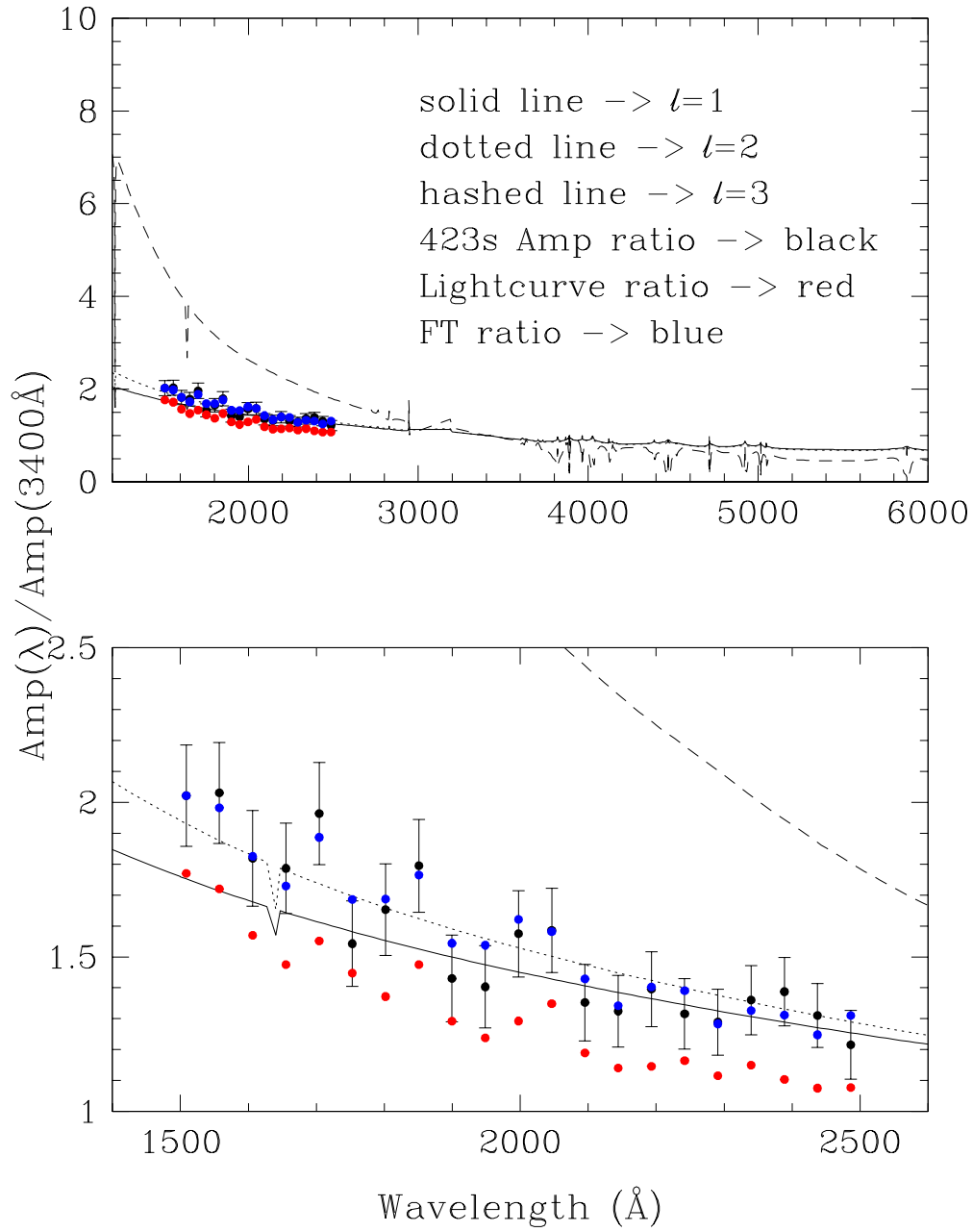


Figure 2.52: The data in Figure 2.51 along with theoretical models. The lightcurve ratio is in red, the Fourier transform ratio is in blue and the 423s amplitude ratio is in black. The lines represent the 25500K, $\log g = 8.0$ DB model calculated using Koester's model atmosphere. The data definitely exclude $\ell = 3$, but whether they prefer $\ell = 1$ or $\ell = 2$ can only be shown by computing s^2 as discussed in the text.

mode is twice that of the $\ell = 1$ mode. Fixing the optical amplitude, we calculated the UV amplitude using the model amplitude ratios, then calculated the Fourier transform of the simulated lightcurves and took the ratios as we did for the real GD358 data. Figure 2.53 shows the resulting Fourier transform ratio along with the theoretical $\ell = 1$ and $\ell = 2$ calculations used to construct the UV lightcurves. The Fourier transform ratio looks much more similar to the $\ell = 2$ curve than the $\ell = 1$ curve. The amplitudes of the modes act like weights and the Fourier transform ratio is a weighted average of the ℓ values of the modes. This conclusion is enforced in our two remaining simulations as well.

Case 2

This is a similar simulation as in Case 1, but now both modes have identical amplitudes. The resulting Fourier transform ratio (Figure 2.54) comes out right in the middle between the $\ell = 1$ and $\ell = 2$ models, exactly as expected with two modes of different ℓ with identical weights.

Case 3

This is also similar to Case 1, but now the $\ell = 1$ mode has twice the amplitude of the $\ell = 2$ mode. The resulting Fourier transform ratio (Figure 2.55) comes out closer to the $\ell = 1$ model calculation, again as expected given the higher $\ell = 1$ weight.

These three simulations show that it is not a surprise that the Fourier transform ratios come out very similar to the 423s mode amplitude ratios (Figure 2.43). As the 423s mode had the largest observed amplitude, the Fourier transform ratio is expected to reflect primarily the amplitude ratio of the 423s mode. Therefore we cannot conclude that the other modes, at 464s whose am-

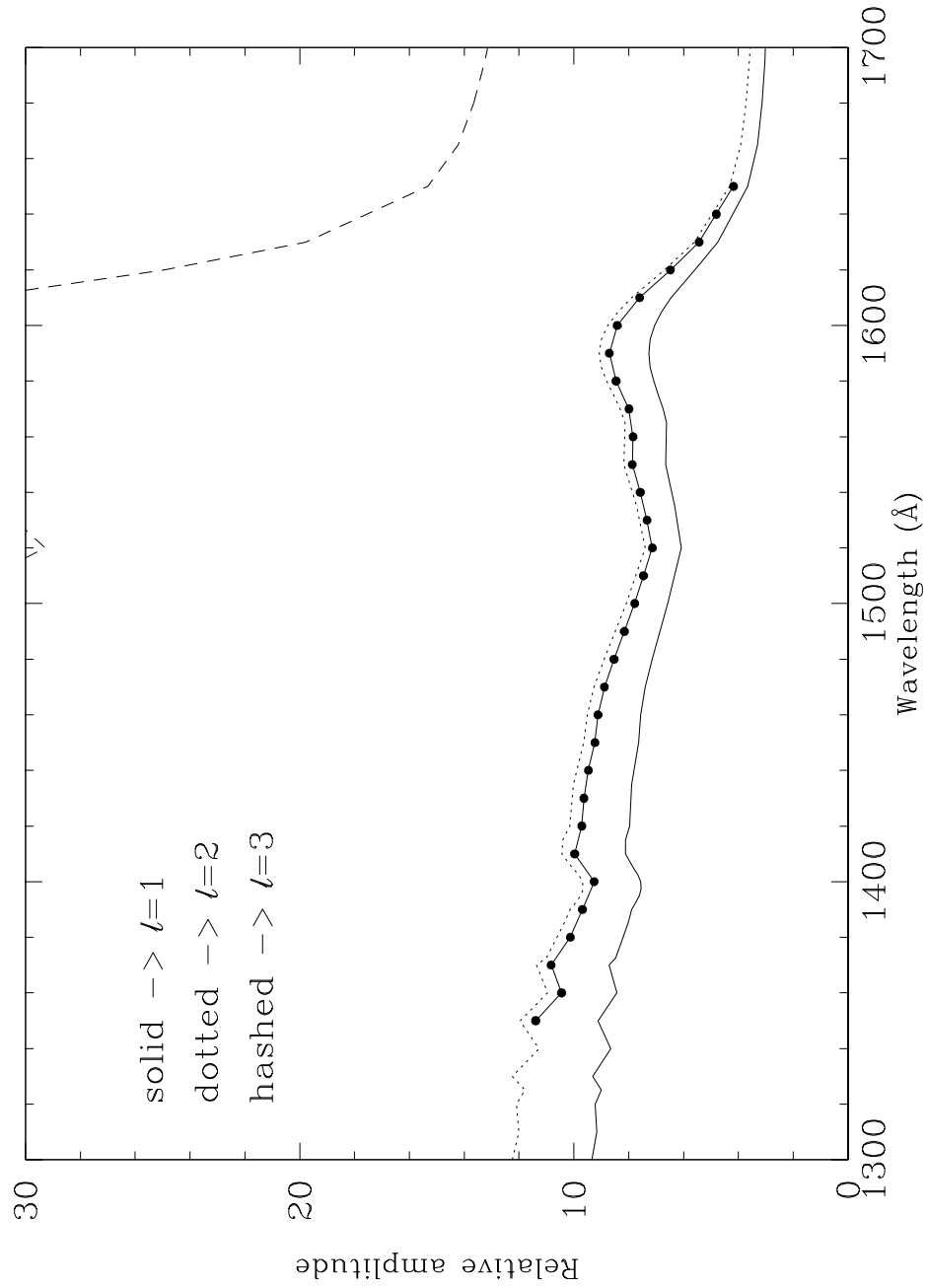


Figure 2.53: A simulated Fourier transform ratio (dots) is shown with DA model based on Koester's model atmosphere with an effective temperature of 11750K and $\log g = 8.75$. The solid line shows the $\ell = 1$ calculation, the dotted line the $\ell = 2$ calculation and the hashed line shows the $\ell = 3$ calculation. The simulated optical amplitude was set to be 2:1 for the two modes.

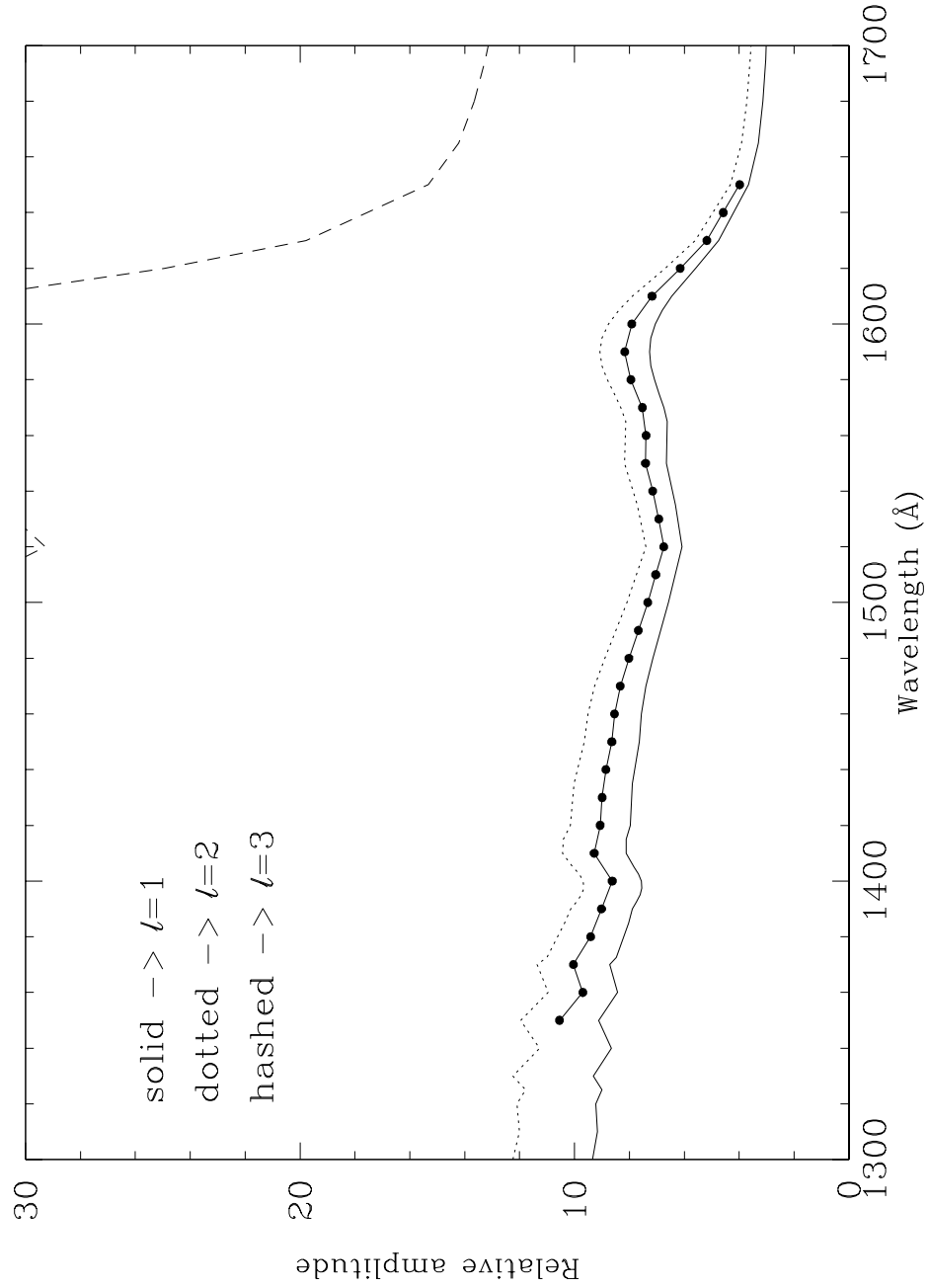


Figure 2.54: A simulated Fourier transform ratio (dots) is shown with DA model calculated using Koester's model atmosphere with an effective temperature of 11750K and $\log g = 8.75$. The solid line shows the $\ell = 1$ calculation, the dotted line the $\ell = 2$ calculation and the hashed line shows the $\ell = 3$ calculation. The simulated optical amplitude was set to be 1:1 for the two modes.

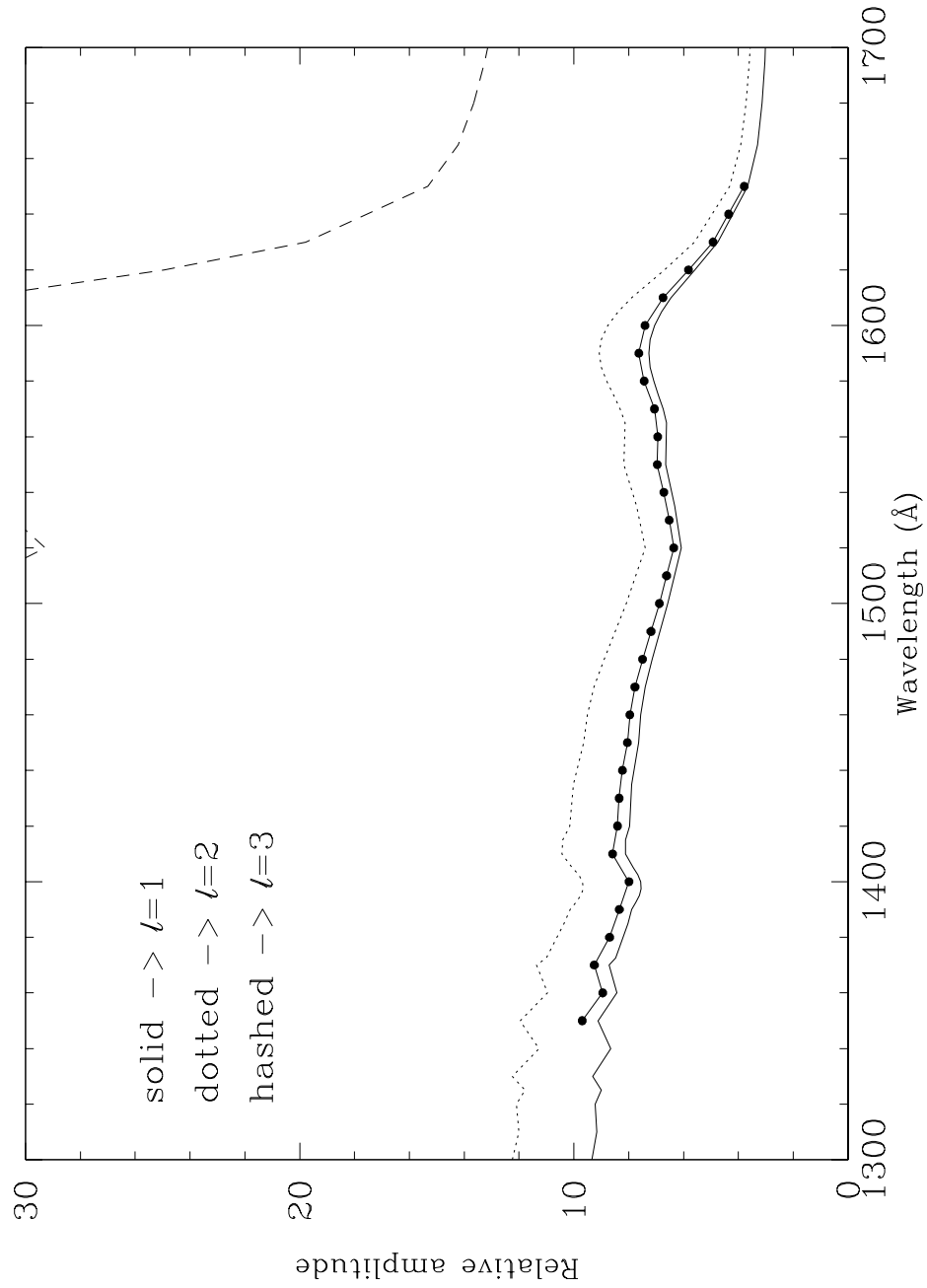


Figure 2.55: A simulated Fourier transform ratio (dots) is shown with DA model using Koester's model atmosphere with an effective temperature of 11750K and $\log g = 8.75$. The solid line shows the $\ell = 1$ calculation, the dotted line the $\ell = 2$ calculation and the hashed line shows the $\ell = 3$ calculation. The simulated optical amplitude was set to be 1:2 for the two modes.

plitude is half and 770s whose amplitude is 1/3 of the 423s mode amplitude, are the same ℓ as the 423s mode.

Summary

The data taken by the HST showed constant phase vs. wavelength as expected from linear g-mode oscillation as calculated by Robinson, Kepler & Nather (1982). The mode identification via the period distribution method assigned $\ell = 1$ for the 423s mode (Winget et al. 1994). We have shown that the limb darkening method gives us either $\ell = 1$ or 2. This is consistent with the period distribution method, but we need better amplitude measurements to conclusively determine the modes' ℓ values without any doubt.

Could we possibly have both $\ell = 1$ and $\ell = 2$ modes present (this is called “accidental degeneracy”) at similar period? If so, this could add confusion to the ℓ determination by the limb darkening method because the UV amplitude could be dominated by the $\ell = 2$ mode and the optical by the $\ell = 1$ mode. The best fit model from Bradley & Winget (1994) does not have any $\ell = 2$ mode around 423s. The closest is $\ell = 2$, $k = 15$ and $k = 16$ modes whose periods are 414.5s and 433.6s respectively (Montgomery, 2000 private communication). Therefore, if Bradley & Winget’s (1994) results are correct, it is very unlikely that we have accidental degeneracy. In other words, there should not be two different ℓ values to assign for the 423s mode.

We plan to solve this dilemma of getting better ℓ identification by observing GD358 again with the HST for 10 orbits in May–June, 2000. We have organized a WET campaign to observe from ground to ensure simultaneous

optical data this time⁴. The long timebase (about 2 weeks) coverage by the WET ensures better period determinations as well as better optical amplitude determinations which are essential to successful mode identification using the limb darkening method. We hopefully can conclusively test the consistency of the limb darkening method with the period distribution method with these observations. The analysis of the spring 2000 data is not included in this thesis. For now, we can say that the limb darkening method discussed here are consistent with all mode being $\ell = 1$ and agree with the results from the period distribution method (Winget et al. 1994).

⁴The HST no longer has FOS on-board and the instrument we used in spring 2000 does not take simultaneous zeroth order data with the UV data.

Chapter 3

Asteroseismology of a Massive DAV BPM37093

3.1 Introduction

Crystallization of the interiors of white dwarfs was predicted theoretically 40 years ago (Abrisokov 1960; Kirshnitz 1960; Salpeter 1961), but in spite of its importance in astrophysics, we have no direct observational evidence to test the theory. Uncertainties in the nature and extent of crystallization, as well as its associated effects, are the largest sources of uncertainties in calculating the ages of the coolest white dwarf stars—important chronometers for the galactic disk. Nature kindly provided us with a cosmic lab to test the theory of crystallization in stellar interiors when Kanaan et al. (1992) discovered that BPM37093 is a massive hydrogen atmosphere white dwarf pulsator (DAV). The star’s high mass is unique amongst known DAVs. Figure 1 in Montgomery & Winget (1999), reproduced here in Figure 3.1, shows mass vs. T_{eff} (taken from Bergeron et al. 1995) for the known DAVs. According to Bergeron et al. (1995), BPM37093 has a mass of $M = 1.09 \pm 0.05 M_{\odot}$. Koester & Allard’s (2000) estimates using IUE spectra are $T_{\text{eff}} = 11520 \pm 110\text{K}$ and $\log g = 8.67 \pm 0.14$ corresponding to $M = 1.03 \pm 0.08 M_{\odot}$. Either mass estimate makes BPM37093 the most massive white dwarf pulsator we currently

know. Theoretical calculations by Winget et al. (1997) show that this massive DAV should have a crystallized core. The non-radial g-modes we observe in the pulsating white dwarf stars involve predominantly horizontal motions of material. In the models, the crystallized part of the stellar interior cannot easily sustain shear motions, and so it excludes non-radial g-modes. Thus, the modes have all their nodes in the non-crystallized part of the model, resulting in modes with longer periods and larger period spacing than they would have in otherwise identical non-crystallized models. Detailed calculations by Montgomery and his collaborators suggest that we should be able to observe this effect (Winget et al. 1997; Montgomery 1998; Montgomery & Winget 1999). If we find observational evidence of crystallization inside BPM37093, it will be the first such discovery. The solid lines in Figure 3.1 show the theoretical calculations (Winget et al. 1997; Montgomery 1998; Montgomery & Winget 1999) of the mass fraction of crystallization assuming a pure oxygen core. Theoretical evolutionary models suggests BPM37093 has an interior close to 90% crystallized. For a pure C core model, BPM37093 should have crystallization mass fraction of 50%, and for mixture of C and O, the crystallization mass fraction are expected to be between 50 to 90%, depending on the mixture.

To use BPM37093's pulsation modes to explore the extent of its crystallized core, we must be able to identify the pulsation modes. Considering the scientific importance of detecting crystallization in a stellar interior, we organized simultaneous WET and HST observations of BPM37093 in April 1999. These data combined then should allow us identify the ℓ values of the observed modes. During the WET run, the number of periodicities we observed in BPM37093 was small — about four or so. With so few modes, it

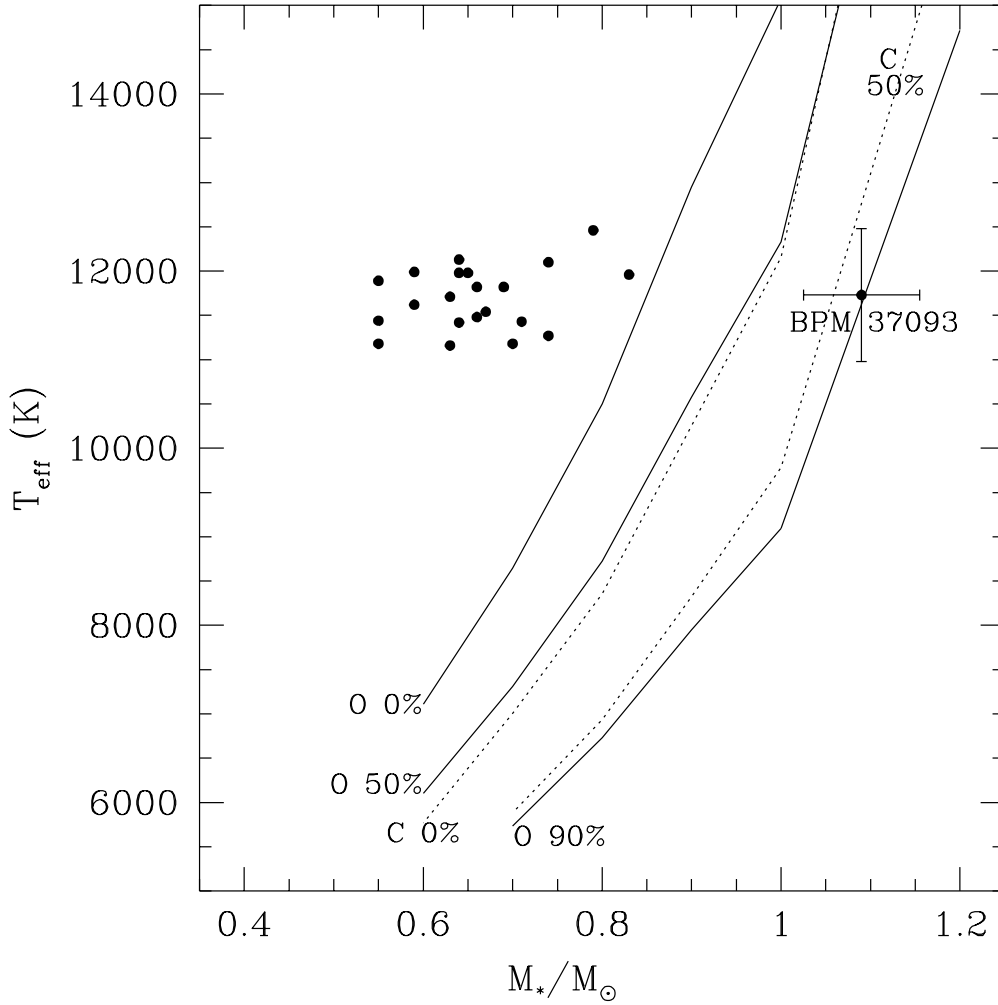


Figure 3.1: The masses and effective temperature of the known DAVs along with theoretical crystallized mass fraction: this figure was provided by Mike Montgomery. This is a similar to Figure 1 in Montgomery & Winget (1999). The dots represent the known DAVs. The masses and effective temperatures of the stars were taken from Bergeron et al. (1995). BPM 37093 is by far the most massive of the known DAVs. The solid lines are the calculated constant crystallization mass fraction assuming a pure oxygen core. The dotted lines are those for a pure carbon core. If BPM 37093 has a pure oxygen core, it should be close to 90% crystallized. Montgomery (1998) and Montgomery & Winget (1999) show that for a mixture of carbon and oxygen, it should be at least 50% crystallized.

is impossible to apply the period distribution method and get a unique mode identification using the WET data alone. We thus concentrate on the limb darkening method. Figure 3.2 shows the model calculation of the wavelength dependence of the pulsation mode amplitude ratio, normalized at 5500Å. The model has $T_{\text{eff}} = 11500\text{K}$ and $\log g = 8.75$ which are similar to the physical parameters determined by Koester using IUE spectra (Koester & Allard 2000).

The DA Models

As in the case for GD358, Koester provided us with DA model atmospheres to be used for this project. Figures 3.3 to 3.6 show the surface gravity and T_{eff} dependence on the calculated amplitude ratio. The models have parameters ranging from $T_{\text{eff}} = 10000\text{K}$ to 14750K in 250K increments, and $\log g = 7.50$ to 8.75 in 0.25 increments. As we did for the DB models, we examine the gravity and temperature dependence of the theoretical amplitude ratios. In Figure 3.3 and Figure 3.4, we note that the models show only very small differences between different surface gravities above $\log g = 8.0$. Therefore, although we do not have a model grid precisely with Koester & Allard's calculated $\log g$ of BPM37093 ($\log g = 8.67$), the model grid with $\log g = 8.75$ are precise enough and there is no need to interpolate the models to produce a $\log g = 8.67$ model. In Figures 3.5 and 3.6, we show the calculated amplitude ratio for $\ell = 1$ and $\ell = 2$ for a fixed $\log g = 8.75$ with various effective temperatures. The calculated amplitude ratios for $\ell = 1$ show that the differences between models with $T_{\text{eff}} = 11500\text{K}$ to 12500K are small, and we would not be able to distinguish them observationally. Similar conclusions holds for the $\ell = 2$ calculations. Therefore we find our model grid is quite adequate for our work.

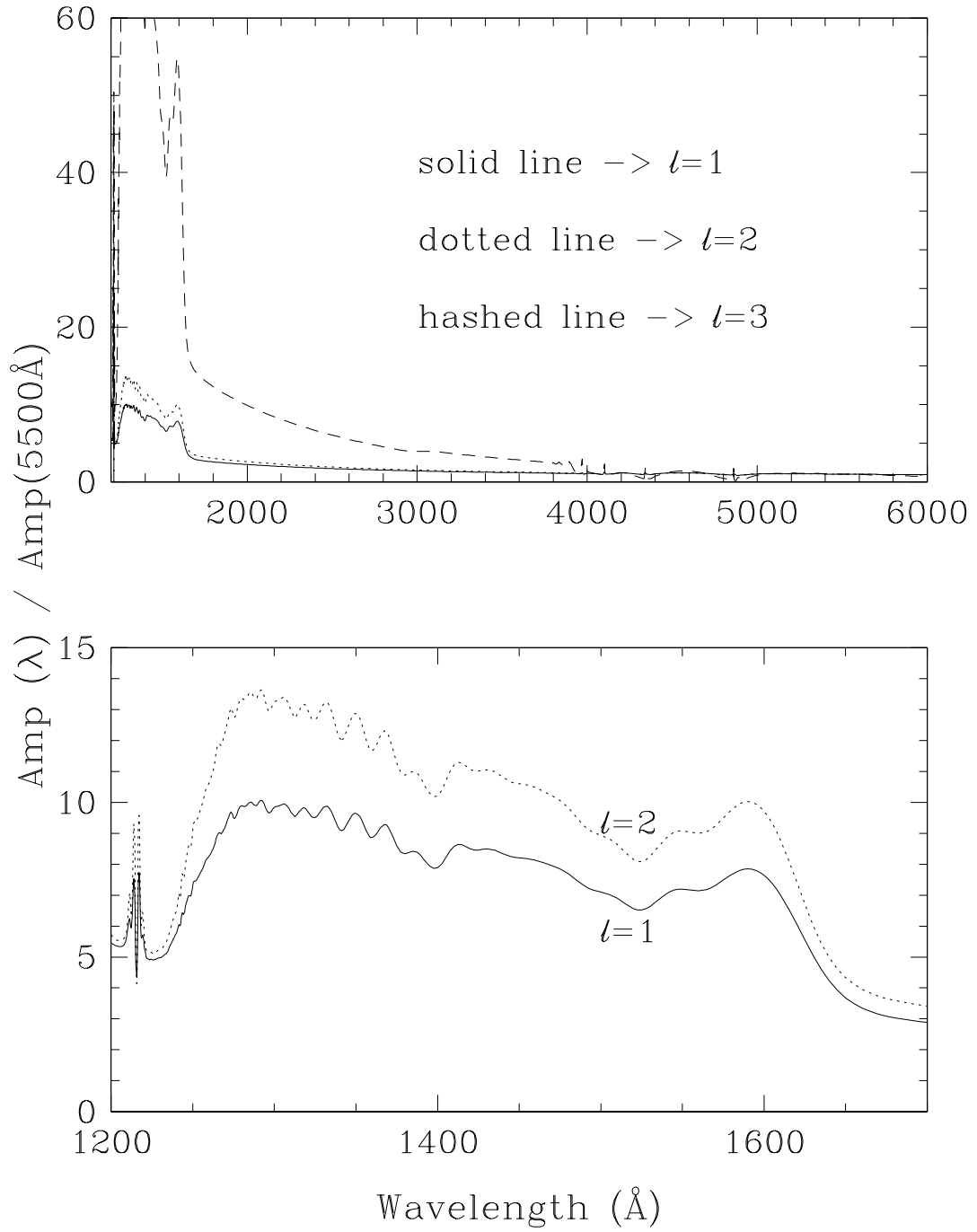


Figure 3.2: Calculation of the amplitude ratios vs. wavelength for different values of ℓ for Koester's 11500K, $\log g = 8.75$ model. The amplitude ratios are normalized at 5500Å.

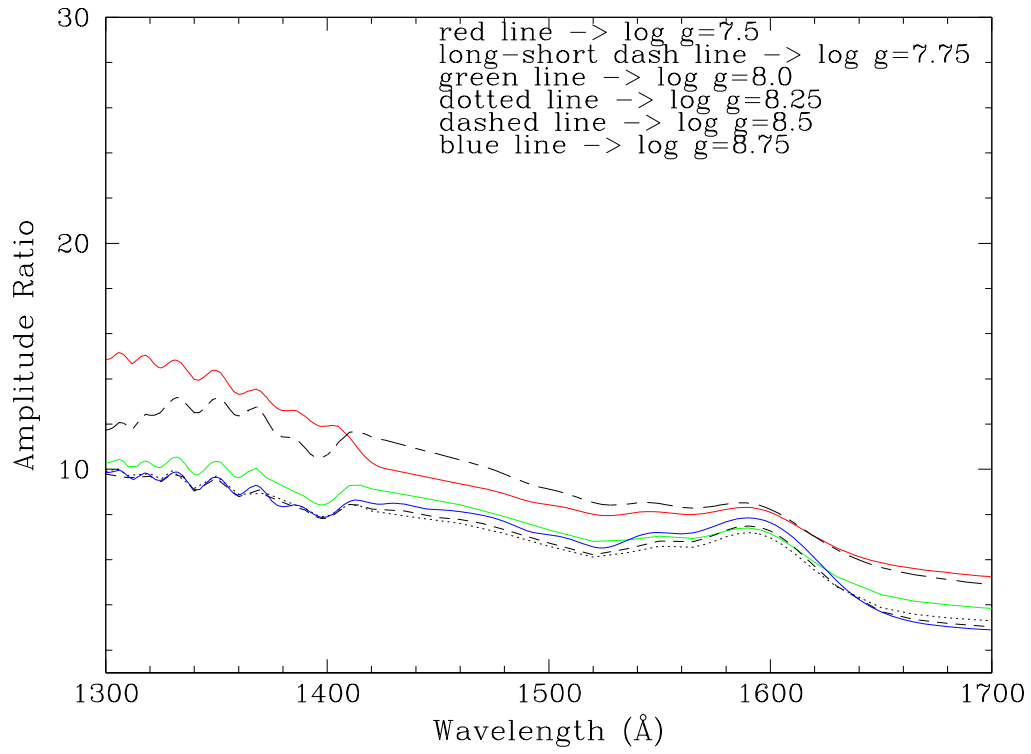


Figure 3.3: $\ell = 1$ model calculations for different $\log g$ and fixed $T_{\text{eff}} = 11500\text{K}$. The differences between $\log g = 8.0$ to $\log g = 8.75$ are not large enough for us to distinguish observationally.

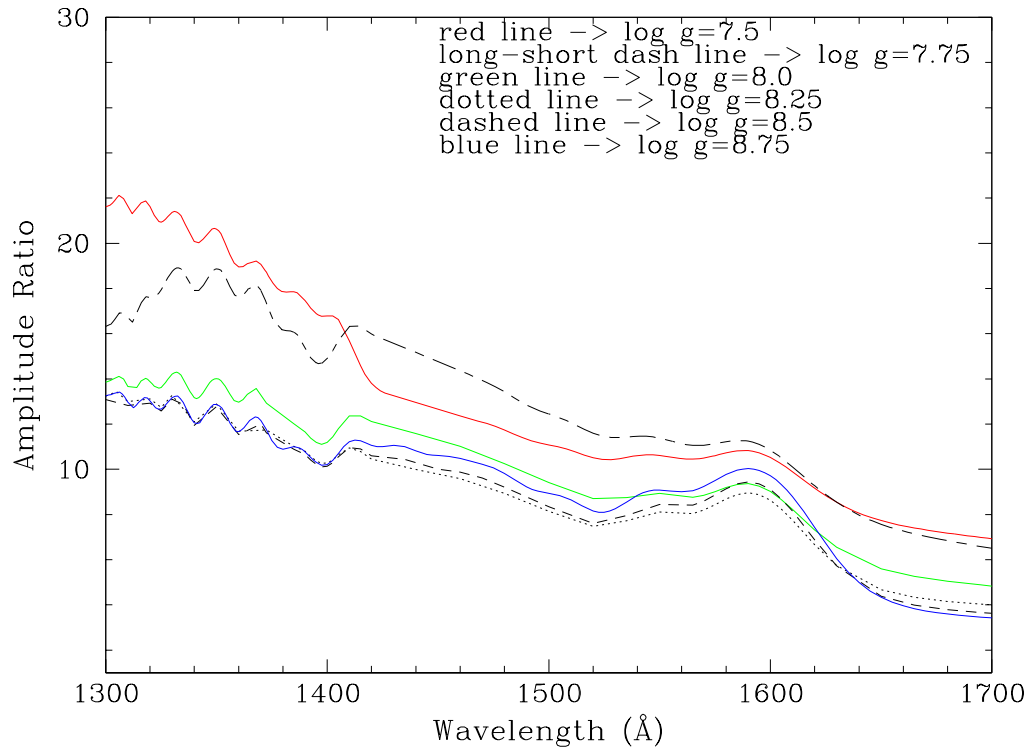


Figure 3.4: $\ell = 2$ model calculations for different $\log g$ and fixed $T_{\text{eff}} = 11500\text{K}$. The differences between $\log g = 8.0$ to $\log g = 8.75$ are not large enough for us to distinguish observationally.

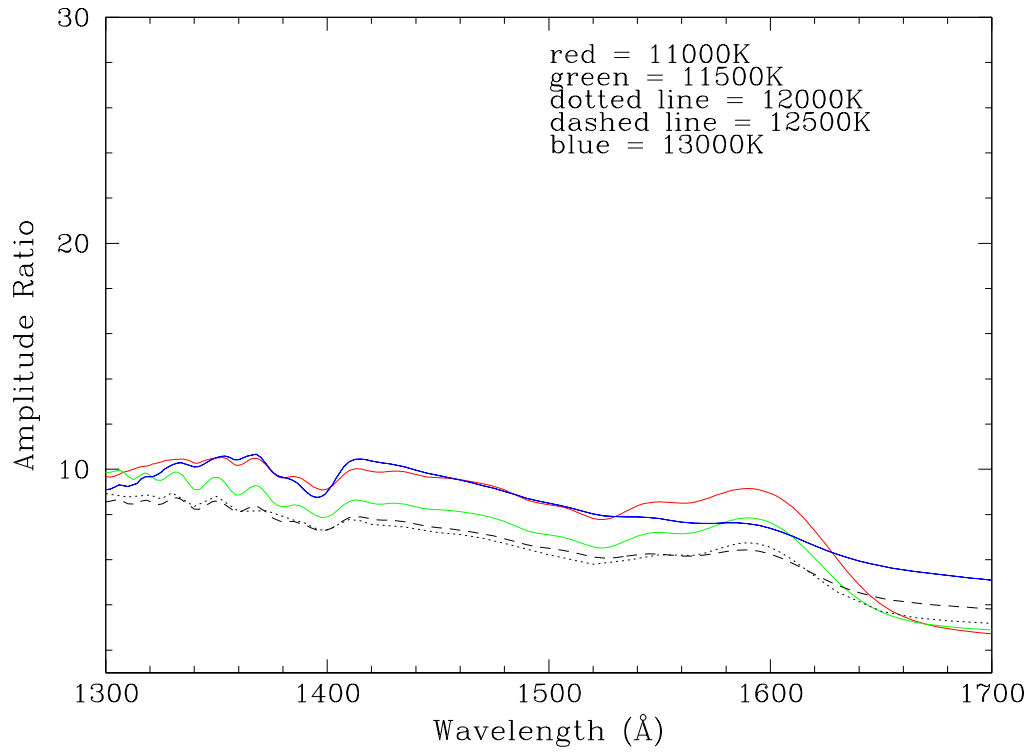


Figure 3.5: $\ell = 1$ model calculations for different T_{eff} with fixed $\log g = 8.75$. The differences in temperatures are not large enough for us to distinguish observationally.

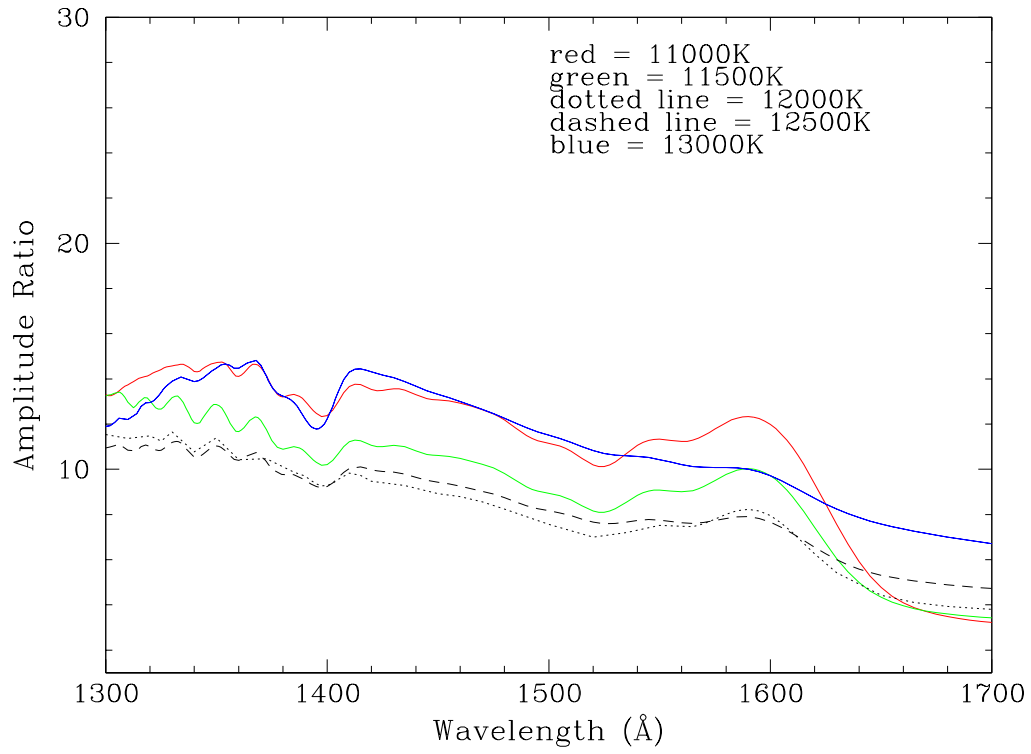


Figure 3.6: $\ell = 2$ model calculations for different T_{eff} with fixed $\log g = 8.75$. The differences in temperatures are not large enough for us to distinguish observationally.

3.2 Observation of BPM37093

3.2.1 The UV Data

To gather time series UV observations of BPM37093, we used the Space Telescope Imaging Spectrograph (STIS) on board the HST with the FUV-MAMA detector, G140L grating, and the so called “ 52×0.5 ” slit aperture in TIME-TAG mode. This setup records the position and arrival time of the photons as they hit the detector. For our observations, we choose the G140L grating because its wavelength sensitivity (1150-1700 Å) matched most closely with the wavelength region sensitive for measuring ℓ -values, as seen from the model calculations in Figure 3.2. We used the 52×0.5 slit ($25'' \times 0.5''$ projected on the detector) to get as much light as possible from the star and as little light as possible from the sky while minimizing the effect of target movements in the aperture and still have the Space Telescope Science Institute (STScI) supported calibration frames. The point spread function of MAMA detector has a very steep peak with extended low level wings. At $0.37''$ from the center of the stellar image, there is less than 0.01% of the flux compared to the center. Thus, the 52×0.5 aperture allows most of the light from the star to be detected. The next larger supported aperture, 52×2.0 which is $26'' \times 2.0''$ projected on the detector, would have resulted in larger sky/background noise. The next smaller aperture (52×0.2) would have resulted in a loss of star light from our target. We were awarded 8 orbits¹ for this project. We used one orbit as a “rehearsal” a month before the scientific observation to check the accuracy of our the coordinates and proper motion. We then split the 7 remaining orbits

¹We originally were awarded 16 orbits and the observations were carried out in April 1998. But due to a proper motion translation error, our observations failed. We were allowed to retry the observations in 1999, and were granted 8 new orbits.

into two visits: one 3-orbit observation and one 4-orbit observation. Our instrument setup was not allowed to be used for more than 4 continuous orbits due to a fear of filling up the data recorder on board the HST and saturating the detector. It is also required that any two visits must be separated by at least one day. The HST observations were successfully carried out from April 13, 21:30:12 UT to April 14 01:44:37 and from April 14, 20:06:51 UT to April 15, 01:58:51 UT.

After we acquired the data, we used the standard data reduction pipeline — the “CALSTIS” task in the STSDAS reduction package in IRAF. The data reduction process includes dark count correction, flat field correction, wavelength calibration, background subtraction, and conversion from count rate to flux.

Figure 3.7 shows the time-averaged spectrum of BPM37093. Detlev Koester (private communication) used this spectrum and determined a mass and temperature estimate of BPM37093 consistent with his earlier results from IUE data (Koester & Allard 2000). We show their model spectrum along with our HST spectrum and the IUE spectrum in Figures 3.8 and 3.9. Our HST spectrum is consistent with the IUE spectrum, but is much less noisy. The model fits the IUE spectrum quite well, but it does not describe the better signal to noise HST spectrum quite as well.

We attempted to obtain our own temperature and mass estimates for BPM37093 by dividing the observed spectrum with a model spectrum grid, much as we did for GD358. The model which produces a straight line, or closest to a straight line, indicates the best fit model in our grid. Unfortunately, this method worked very poorly. Figure 3.10 show the ratios of the observed spec-

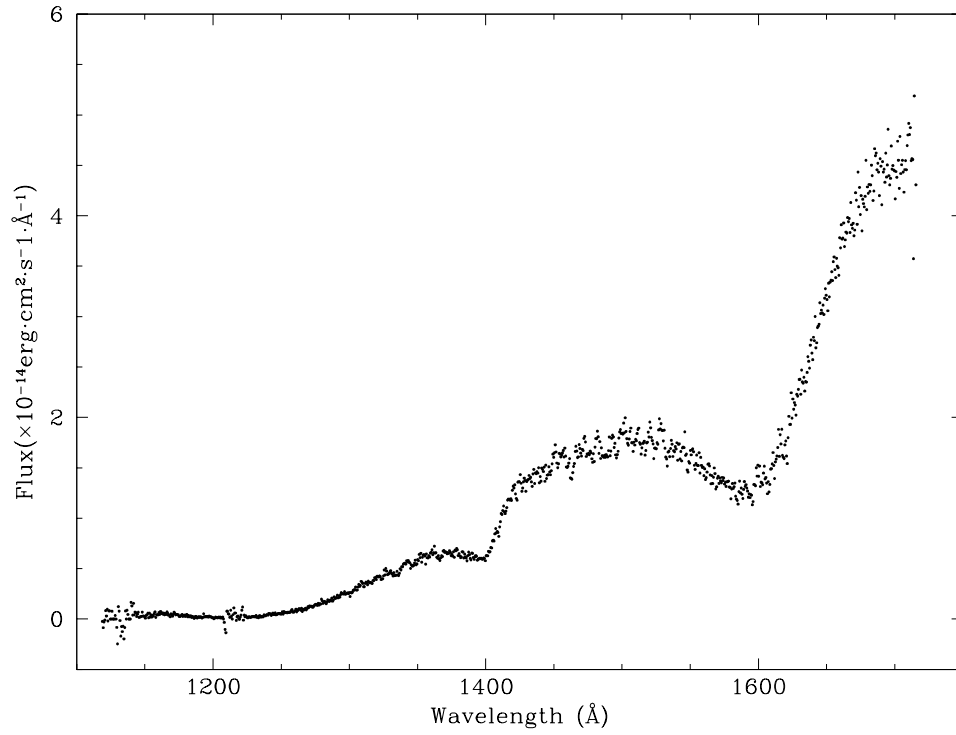


Figure 3.7: BPM37093 time-averaged spectrum. Note the 1400Å and 1600Å quasi molecular (H_2 for 1600Å and H_2^+ for 1400Å feature) features. The scatter around 1200 to 1250Å comes from the imperfect removal of geocoronal lines during data reduction.

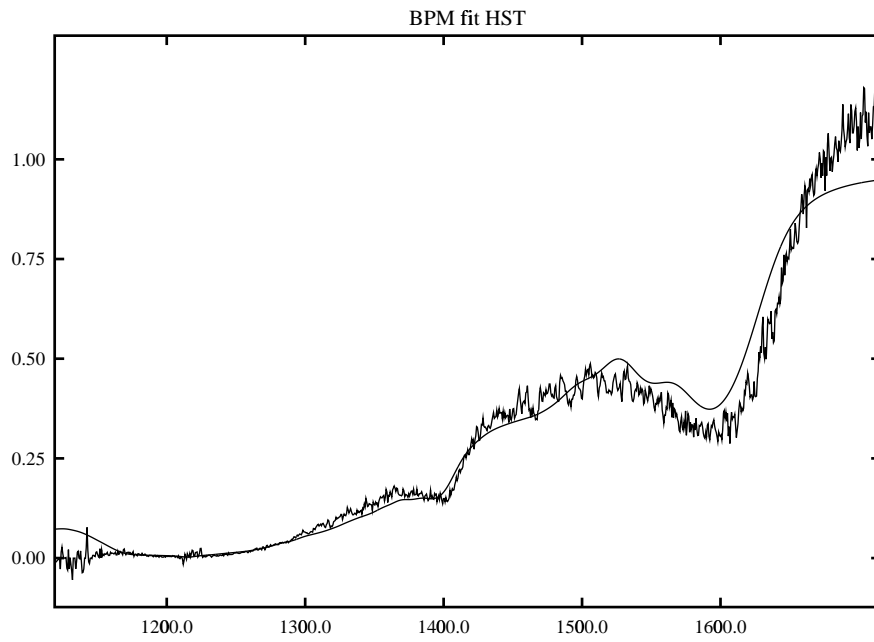


Figure 3.8: Observed BPM37093 HST spectrum and Koester's model spectrum (smooth line). The x-axis is wavelength in \AA and the y-axis is linear scale in flux but the numbers are arbitrary. This figure was created by Detlev Koester. The model has $T_{\text{eff}} = 11520\text{K}$ and $\log g = 8.67$. The fit is not as good for wavelengths longer than 1500\AA .

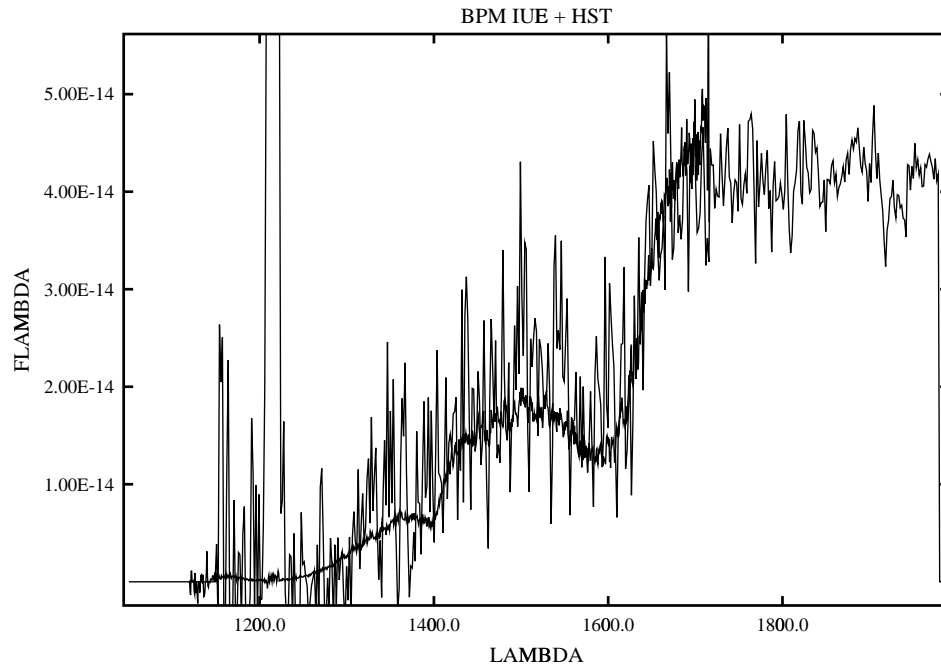


Figure 3.9: Observed BPM37093 HST spectrum and the noisier IUE spectra. This figure was created by Detlev Koester. The x-axis is wavelength in \AA and the y-axis is flux in $\text{erg} \cdot \text{s}^{-1} \cdot \text{cm}^{-1} \cdot \text{\AA}^{-1}$. The HST spectrum is consistent with the IUE spectrum, but the IUE spectrum is much noisier than the HST spectrum.

trum to the model spectra with various temperatures and $\log g = 8.75$. These figures indicate that we have problems fitting the spectrum of BPM37093: the models must not be quite complete. We know from Kepler, Robinson & Nather (2000) who have successfully applied the limb darkening method to two other, but less massive, DAVs (G226-29 and G185-32) that one can obtain ℓ identifications using Koester’s models for DAVs. As BPM37093 has an unusually high mass, it is possible that the model has some physics missing that is needed to describe BPM37093. We already discussed in the previous section how the calculated amplitude ratios are insensitive to T_{eff} and $\log g$ around the expected parameter space of BPM37093. Therefore, the imperfect fit of the continuum might not be critical in obtaining the ℓ identifications.

As the observed photons are time-tagged, we can bin the data into any time interval of our choice. We used 80s bins to obtain time series spectra. Since BPM37093’s pulsation modes have periods longer than 500s, using an 80s sampling time does not compromise our capability to measure the pulsation periods accurately. To transform the time series spectra into lightcurves, we simply integrated the flux into 100Å bins. As one can see in the integrated spectrum (Figure 3.7), there is not much flux in the 1200 — 1300Å range. Since the *calstis* routine that corrects the data for geocoronal lines is not perfect, some of the data points have negative flux and we therefore decided not to use the flux below 1300Å in our mode identification analysis. We integrated the flux from 1300—1400Å, 1310—1410Å, 1320—1420Å and so on up to 1600—1700Å. This gave us 4 independent lightcurves, and a total of 31 UV lightcurves which overlap in wavelength. Figures 3.11 and 3.12 show the 4 independent UV lightcurves along with the optical data taken from the ground with the WET.

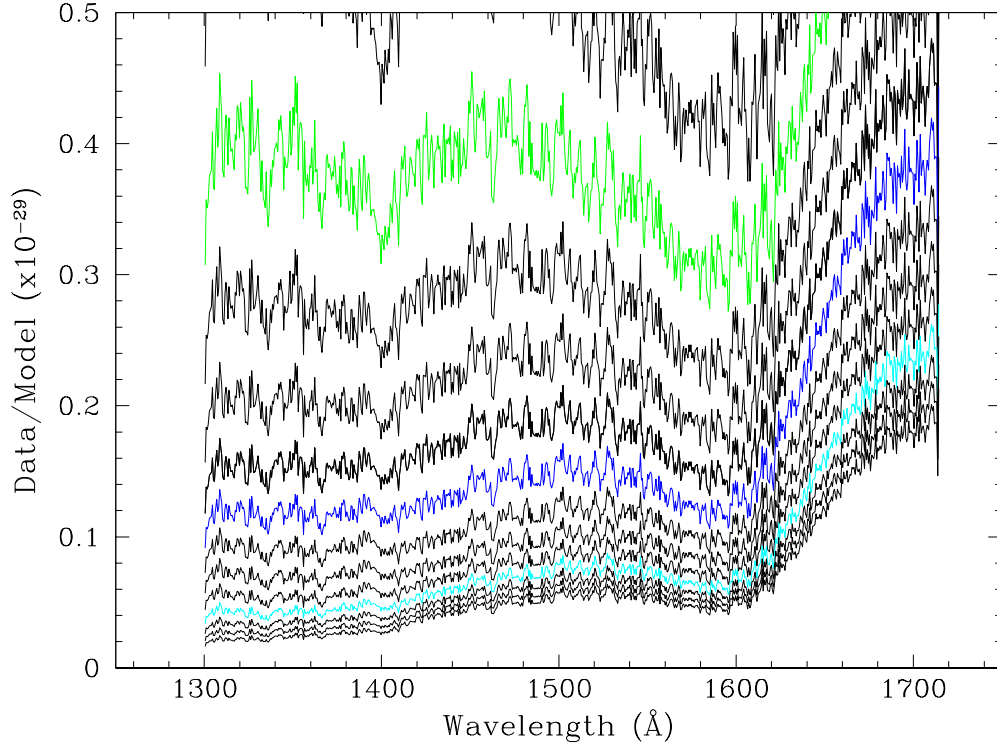


Figure 3.10: Observed BPM37093 HST spectrum divided by model spectra with various temperatures and $\log g = 8.75$. The temperatures of the models are in 250K increments. The green is the result using a 12000K model, the blue curve is the result using a 13000K model and the cyan curve is the result using a 14000K model. The ratios never become close to a straight line, unlike when we fit GD358's continuum with Koester's models.

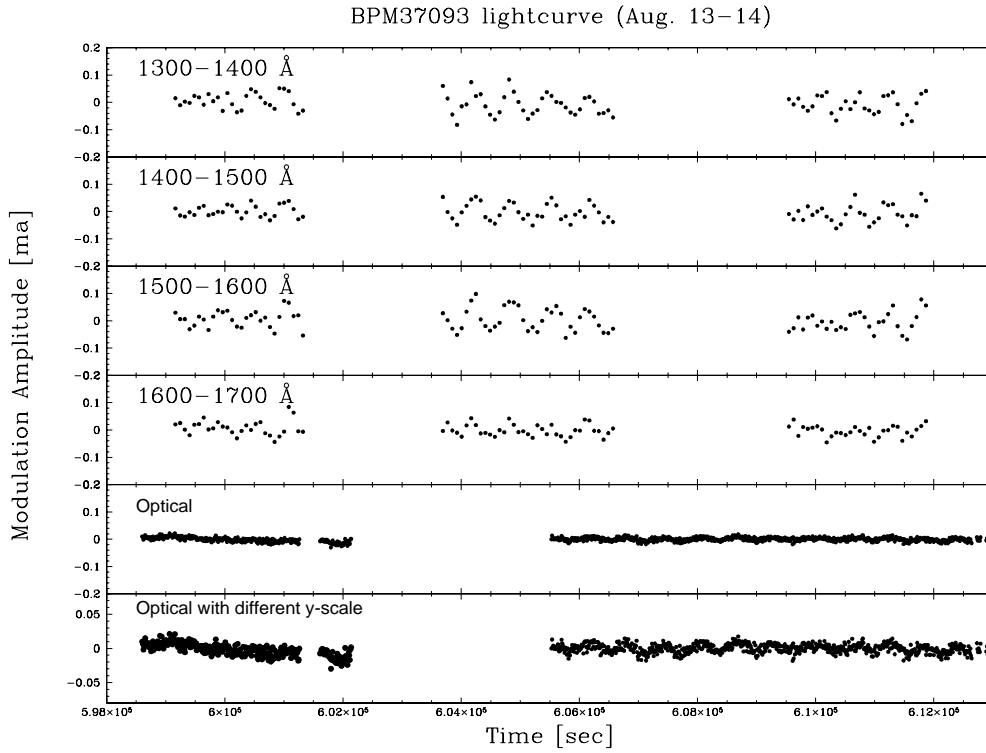


Figure 3.11: The lightcurves in the UV during the HST's first visit along with the obtained ground-based optical data. The vertical scale is the same for all panels. The amplitude is much higher in the UV than it is in the optical, which is exactly what the models in Figure 3.2 predicted. The density of points in the optical data is much higher than in the UV because the optical data were integrated for 10s, while the UV data were integrated for 80s.

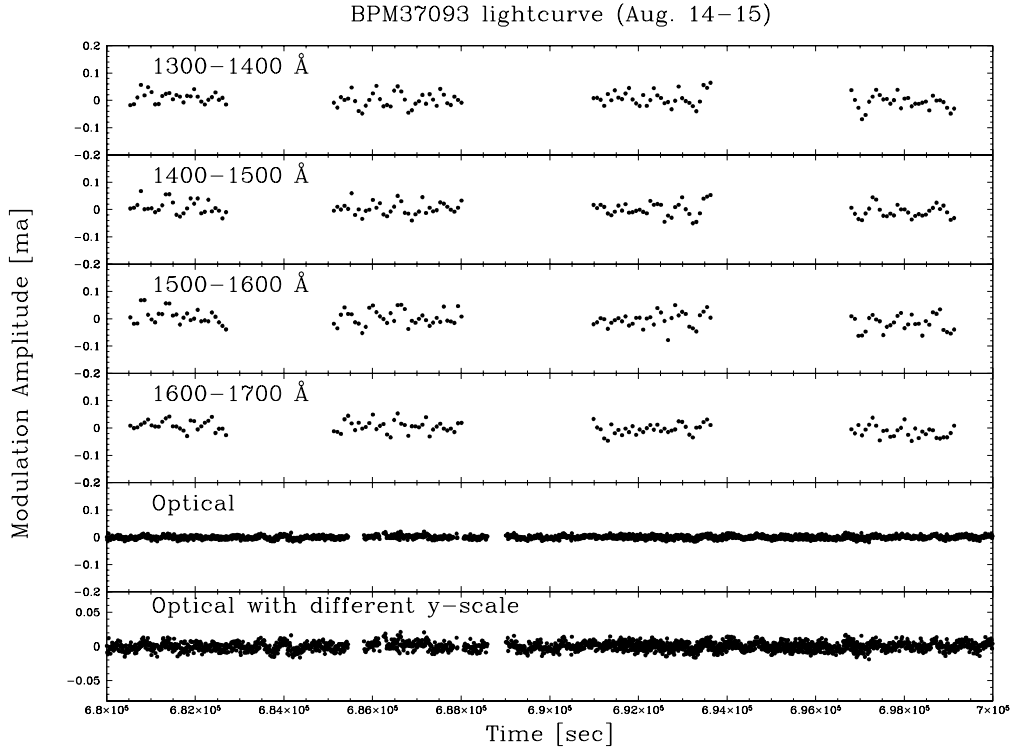


Figure 3.12: The lightcurves in the UV during the HST’s second visit along with the obtained ground-based optical data. The vertical scale is the same for all panels. The amplitude is much higher in the UV than it is in the optical, which is exactly what the models in Figure 3.2 predicted. The density of points in the optical data is much higher than in the UV because the optical data were integrated for 10s, while the UV data were integrated for 80s.

3.2.2 The Ground-Based Optical Data taken with the WET

Since the HST has a low-earth orbit, it cannot observe a star continuously, as is necessary to resolve all the pulsation modes present in pulsating white dwarf stars, unless the star is in the so called “continuous viewing zone”. BPM37093 is not in the continuous viewing zone, thus the UV data alone cannot accurately tell us the pulsation periods. We must supplement the HST data with more continuous data over a longer timebase. We also, of course, need the optical data to apply the limb darkening ℓ identification method.

Antonio Kanaan has observed BPM37093 for several seasons since its discovery as a DAV in 1991 (Kanaan et al. 1992), and noticed that BPM37093 shows amplitude modulations in time scale of days (Kanaan 1995). Unfortunately, STIS does not detect zeroth order data as the FOS did and it was therefore essential to obtain simultaneous ground-based optical data while the HST observed. Since we wanted to make sure we had as many observatories as possible observing BPM37093 around the time of the HST observations, we decided to use the WET for the task. The personnel at STScI were very cooperative in coordinating our observations. We notified them, after we knew all the optical telescope schedules on the ground, when the best time of HST observations would be, and they scheduled it within the time range we asked them.

Because of its position in the southern sky ($\alpha = 13h48m48s$, $\delta = -49^\circ49'00''$, for epoch 2000), the only telescopes which can observe BPM37093 are the ones in the Southern hemisphere. For the WET observations carried out in April, 1999 the following observatories participated: Mt John Observatory in New Zealand, Siding Spring Observatory in Australia, South African

Astronomical Observatory (SAAO) in South Africa, Observatório do Pico dos Dias (OPD) in Brazil, and Cerro Tololo Interamerican Astronomical Observatory (CTIO) in Chile. The journal of observations is given in Table 3.1, and the lightcurve obtained during the WET run is shown in Figures 3.13 and 3.14. As you can see, we were fortunate and obtained almost complete simultaneous coverage of the HST with the WET.

Telescope	Run	Date (UT)	Time(UT)	Length (s)
MJUO 1m	ap1999q1	1999 Apr 4	8:04:20	6950
SSO 40in	ap0899q1	1999 Apr 8	10:38:00	20130
SSO 40in	ap0899q2	1999 Apr 8	16:34:00	3620
SSO 40in	ap0899q3	1999 Apr 8	17:52:30	5460
SSO 40in	ap0999q1	1999 Apr 9	10:15:20	29000
CTIO 1.5m	tsm-0033	1999 Apr 10	2:10:00	26100
SSO 40in	ap1099q1	1999 Apr 10	9:04:40	36680
CTIO 1.5m	tsm-0035	1999 Apr 11	5:55:00	6620
SSO 40in	ap1199q1	1999 Apr 11	8:59:50	37110
SSO 40in	ap1299q1	1999 Apr 12	11:03:00	29900
CTIO 1.5m	tsm-0042	1999 Apr 13	0:43:00	31440
SSO 40in	ap1399q1	1999 Apr 13	9:35:00	10400
SSO 40in	ap1399q2	1999 Apr 13	12:29:00	25000
SSO 40in	ap1499q1	1999 Apr 14	9:14:00	36700
CTIO 1.5m	tsm-0044	1999 Apr 14	23:42:00	34560
CTIO 1.5m	tsm-0045	1999 Apr 16	0:08:30	32730
CTIO 1.5m	tsm-0046	1999 Apr 17	0:10:40	32100
MJUO 1m	ap1799q1	1999 Apr 17	9:34:30	7270
CTIO 1.5m	tsm-0047	1999 Apr 18	4:46:00	15640
MJUO 1m	ap1899q1	1999 Apr 18	7:30:00	7690
MJUO 1m	ap1899q2	1999 Apr 18	11:36:00	8310
MJUO 1m	ap1899q3	1999 Apr 18	14:04:30	14400
CTIO 1.5m	tsm-0048	1999 Apr 19	0:04:30	32330
MJUO 1m	ap1999q4	1999 Apr 19	15:05:50	10500
Itajuba (OPD) 1.6m	ro123	1999 Apr 20	1:23:40	18800

Table 3.1: Journal of observations for BPM37093 during the April 1999 WET run

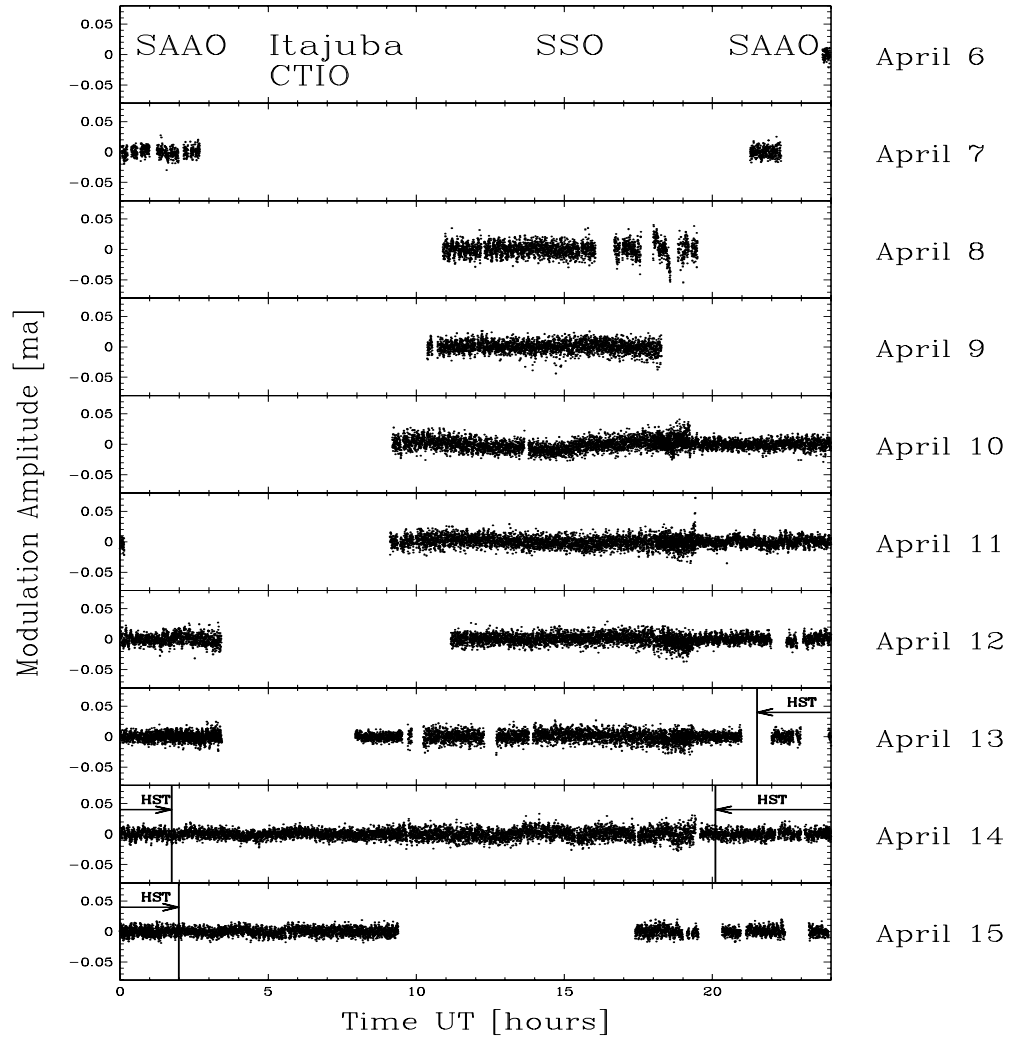


Figure 3.13: The lightcurve of optical data of BPM37093 gathered by the WET (Part 1). This figure shows the lightcurve from the first half of the WET run. We marked the time when the HST observations took place.

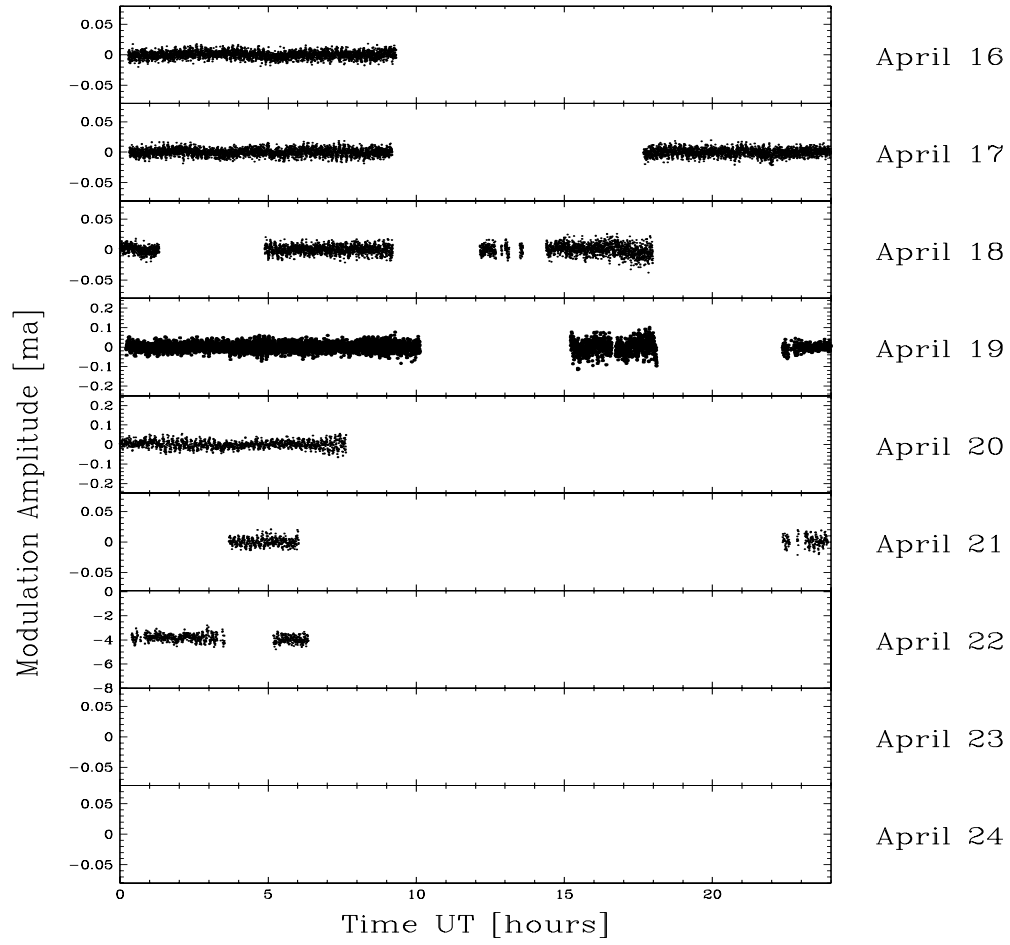


Figure 3.14: The lightcurve of optical data gathered by the WET (Part2). This figure shows the lightcurve from the second half of the WET run.

3.3 Fourier Transform

We show the Fourier transforms of 4 of the 31 UV lightcurves and the optical lightcurves in Figure 3.15. The 4 lightcurves producing the 4 UV Fourier transforms are independent in wavelength, i.e., there are no overlaps in the wavelengths of the lightcurves. The corresponding windows for each Fourier transforms are shown in Figure 3.16. In Figure 3.15, the top panel shows the Fourier transform of the lightcurve integrated from 1300 to 1400Å, the second panel that of the lightcurve integrated from 1400 to 1500Å, and so on. The theoretical calculation showed (Figure 3.2 to 3.6) the pulsation amplitudes should be larger in the UV compared to the optical for $\ell = 1, 2$ and 3 modes, and we indeed observe this (Figure 3.15). The low temporal resolution in the UV is due to the constraints from the instrument and the low-earth orbit of the HST, and the fact that we only observed for 7 orbits. On the other hand, the WET data resolved all the observed periodicities and allowed us to determine the periods quite accurately. Figure 3.17 shows the Fourier transform of the WET data from 0 to 4000 μ Hz. The peaks corresponding to the pulsations are confined to the 1500 to 2000 μ Hz range. It is clear that there are no significant peaks outside this region. In the second panel of Figure 3.18, we show only the 1500 to 2200 μ Hz region. Kanaan has previously observed substantial amplitude modulation in BPM37093 (Kanaan 1995, 1996, 1999). We also see significant amplitude modulation — Figure 3.18 shows our data taken by the WET in 1998 and 1999. Many modes observed in 1998 are not observed with significant amplitudes in 1999. We observed 8 modes in 1998 WET run, but we only observed 2 of them, the 633s and 548s (549s mode in 1999) modes, during the 1999 WET run. On the other hand, we also saw two modes, the 512s and 531s

modes, during the 1999 WET run which were not observed the previous year.

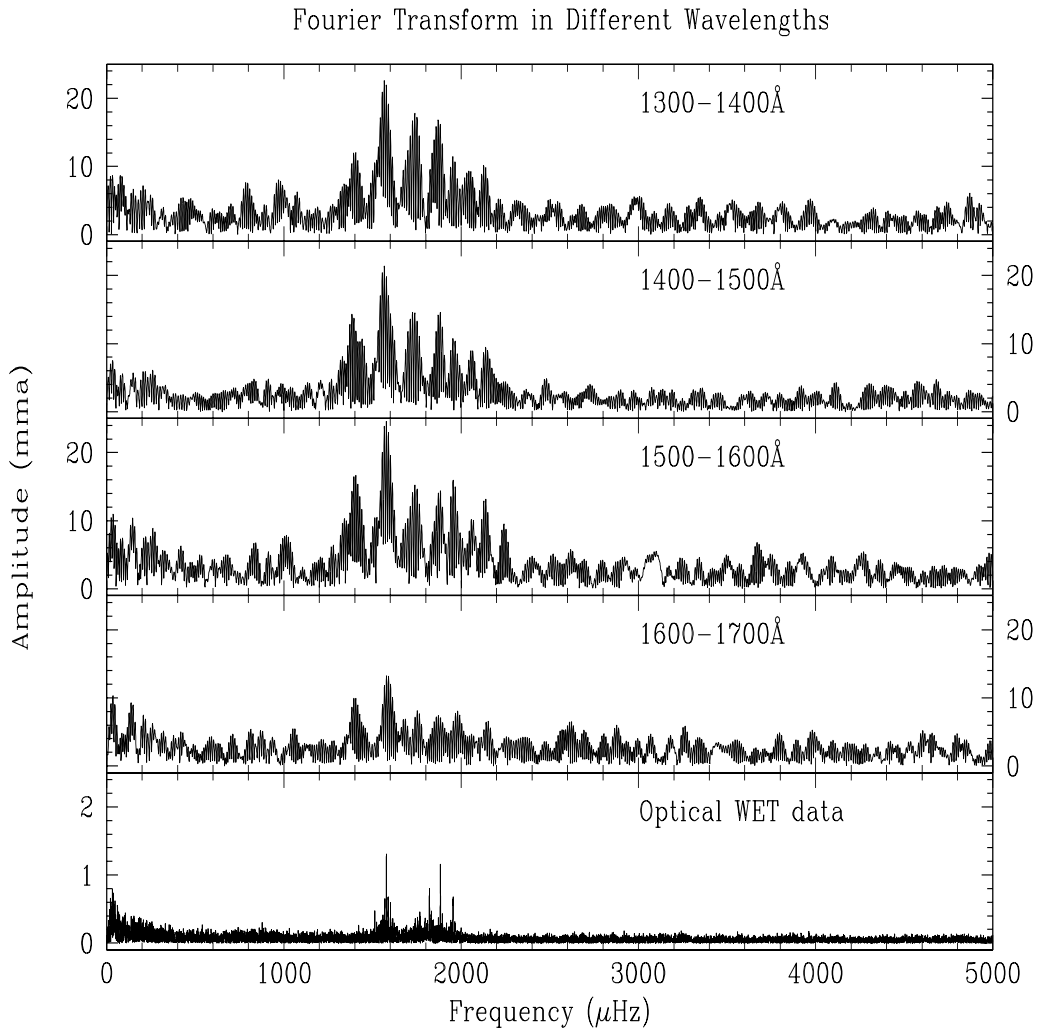


Figure 3.15: The Fourier transforms of the lightcurves in the UV and optical. All panels but the bottom have the same vertical scale. We had a total of 7 orbits of observations with the HST. Due to the low-earth orbit of the HST, we can only observe BPM37093 during half of the HST's 90 min orbit.

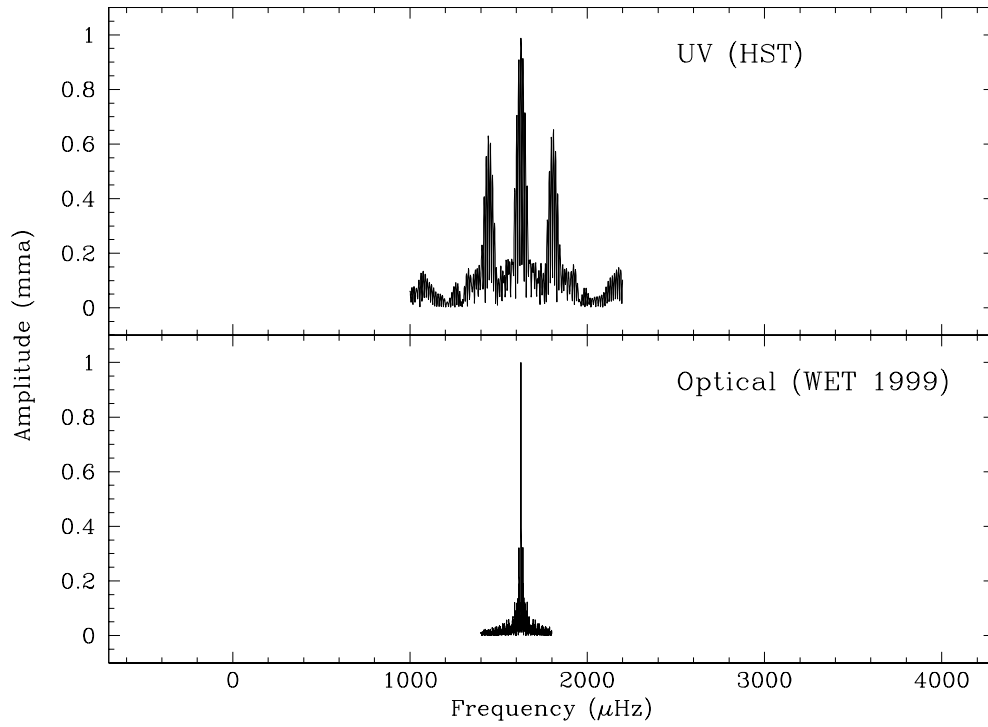


Figure 3.16: The WET window shows how superb a job we can do to determine the period of the modes in the optical compared to the data taken by the HST.

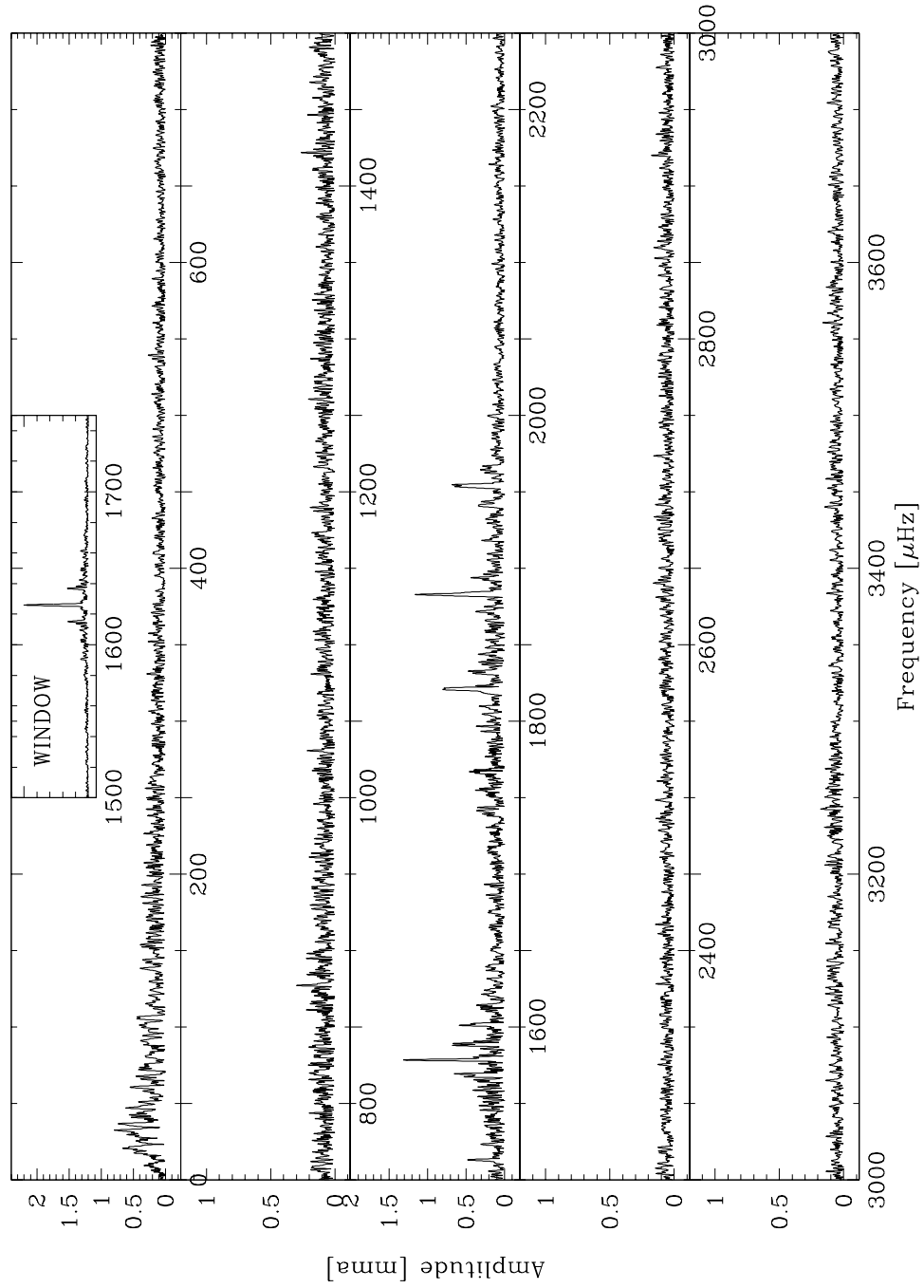


Figure 3.17: The Fourier transforms of the optical data taken with the WET. Pulsations are detected only in 1500 to 2000 μHz range.

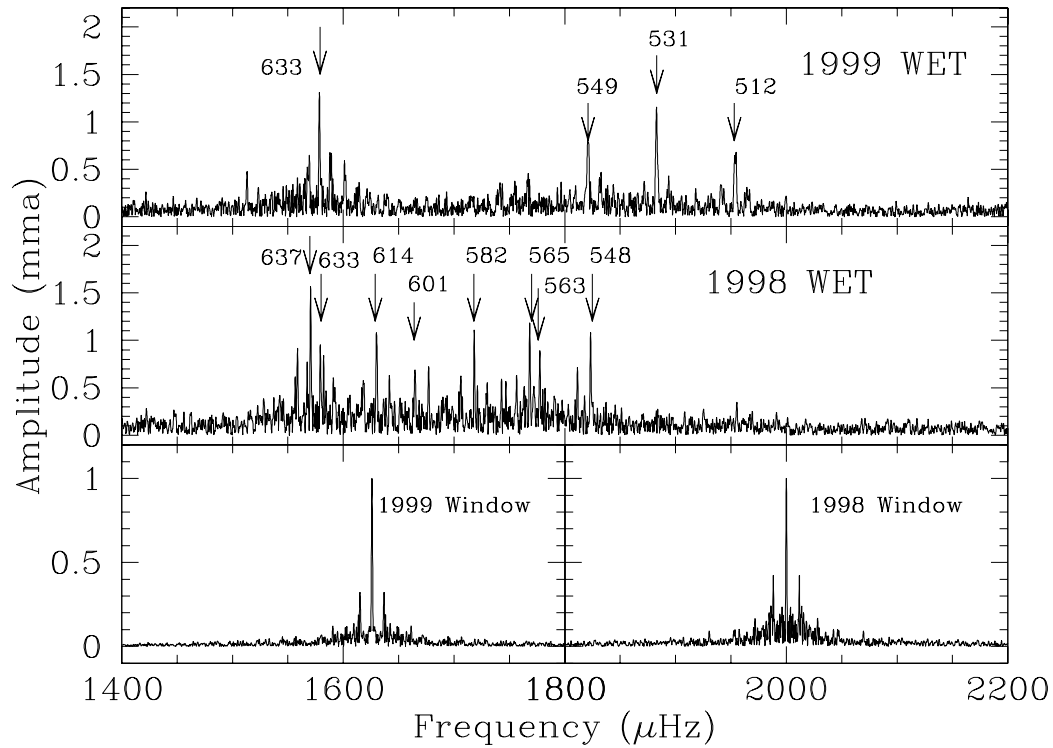


Figure 3.18: The Fourier transforms of the two WET data sets. The top panel shows the Fourier transform from the WET run in 1999, and the middle panel shows that from 1998. The bottom panel shows the windows corresponding to the 1998 and 1999 WET runs. Note how the amplitudes of the modes have changed from one year to another.

3.4 Amplitude Modulation

During the 1999 WET run (XCov17), we saw that BPM37093's pulsation amplitudes were changing on timescales of days. Figures 3.19 and 3.20 show the running Fourier transform of the optical WET data; the running windows are shown in Figure 3.21. Each panel is a Fourier transform of a 2-day lightcurve. The HST observations took place during the 7th and 8th days, and fortunately, the window of 7th and 8th days (labeled as Day7—8 in the figure) is the best among all the running windows. This was achieved thanks to the good weather in the Southern hemisphere and our plan of having the HST observation take place when there were the largest number of telescopes on the ground observing BPM37093. It looks as if the power is moving from the 512s mode to the longer period modes during our observations (Figure 3.19 and 3.20). The Fourier transforms in Figure 3.20 look much more like the previous WET data (shown in Figure 3.18) than do the Fourier transform shown in Figure 3.19.

In Figure 3.22, we show how the optical amplitudes of the 4 principal periodicities (633s, 531s, 549s, 512s) changed during the WET run. Assuming constant periods for the 4 modes, we measured the amplitudes from each 2-day lightcurve, simultaneously fitting the 4 modes with periods obtained from the total WET data sets. The first point comes from day 1 and 2 of our observations, the second point from day 2 and 3, and so on. The lightcurves are therefore not entirely independent of each other. The 549s mode which was barely present at the beginning of the run quickly grew quickly in amplitude and became the highest amplitude mode by the end of the WET run. We must caution that because of less intense coverage at the ends of the WET run (see Figure 3.13 and 3.14), the beginning and ending data points in Figure 3.22 are

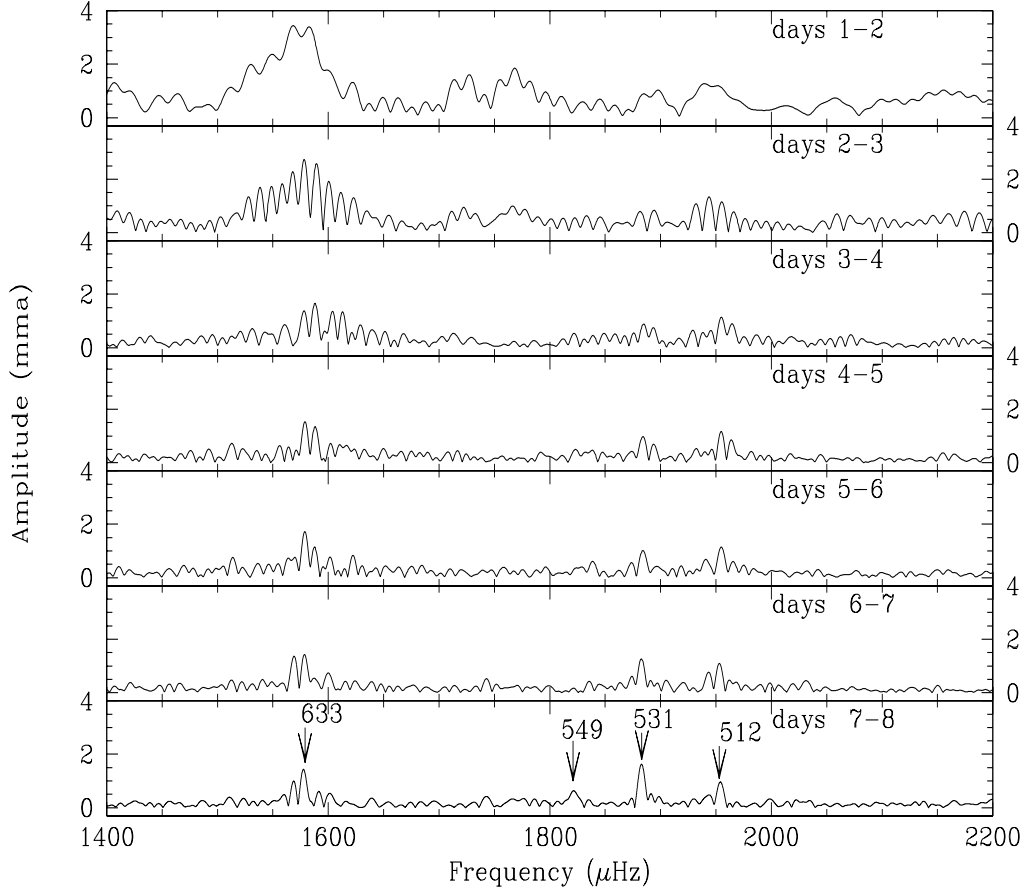


Figure 3.19: The running Fourier transforms of the 2-day optical BPM37093 lightcurves. Note the power spectrum changes during the WET run. Each panel is labeled by the days of the lightcurve used to produce the Fourier Transforms. For instance, Day 1-2 means data from 1st and 2nd day of the WET run were used to calculate the Fourier transform. Days 7-8 overlap with the HST observation. We labeled each observed mode with its measured periods.

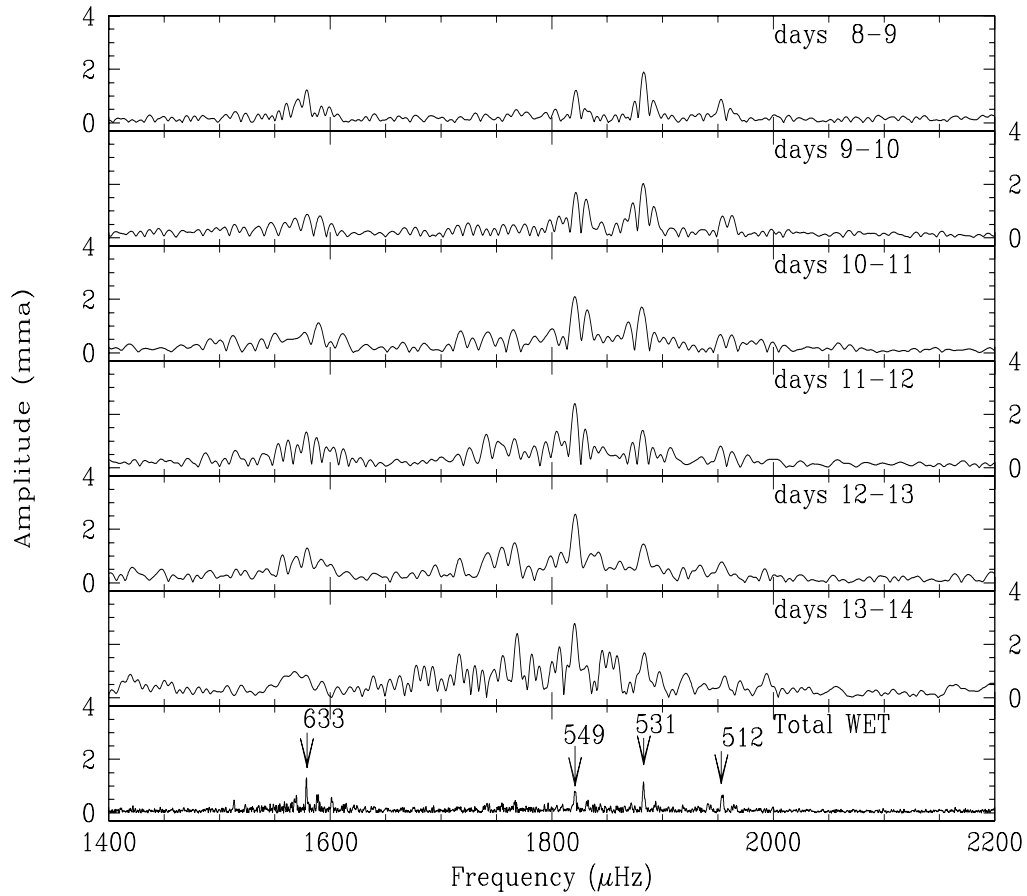


Figure 3.20: The running Fourier transform (part 2). Same as Figure 3.19. The Fourier transform of the total WET data set is shown at the bottom of the figure.

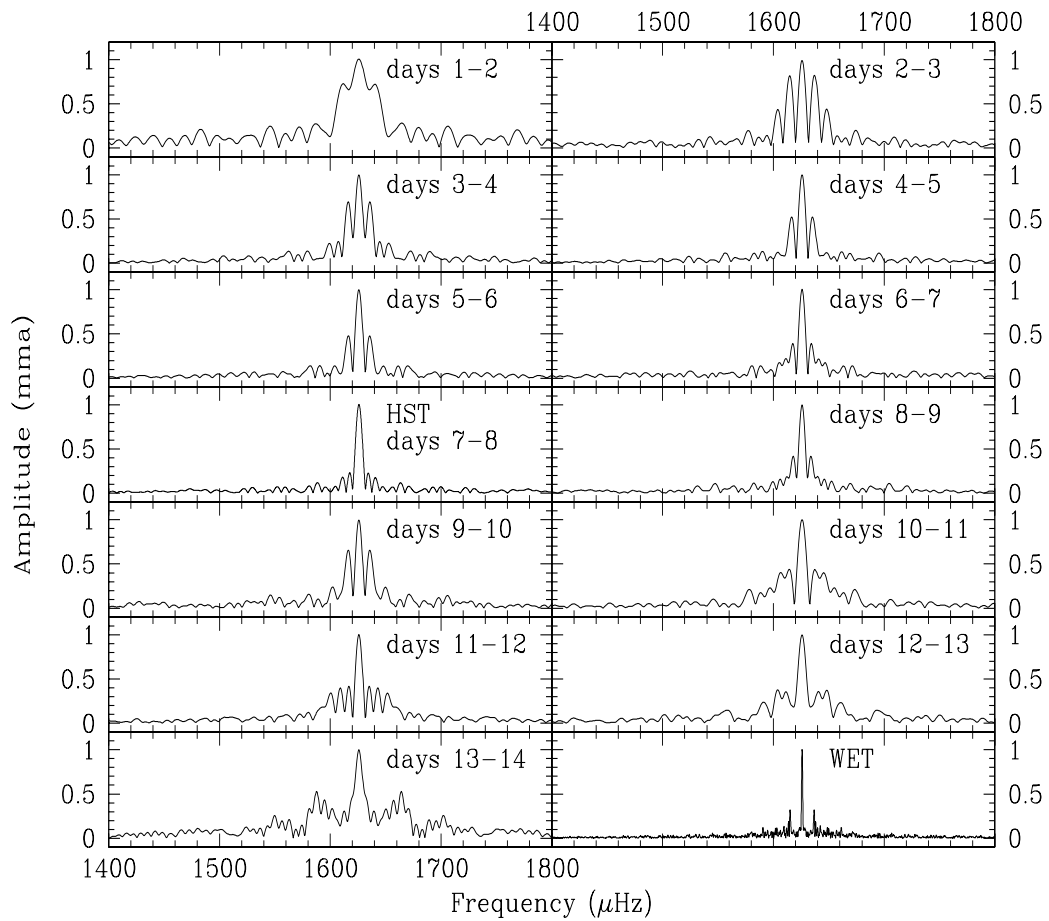


Figure 3.21: The window of the 2-day lightcurves for Figure 3.19 and 3.20. The best window is for the days 7-8. The HST observations also took place during this time.

less accurate than the others. We caution against using this plot to measure the precise amplitudes and instead use it simply to show that the amplitude modulations were occurring.

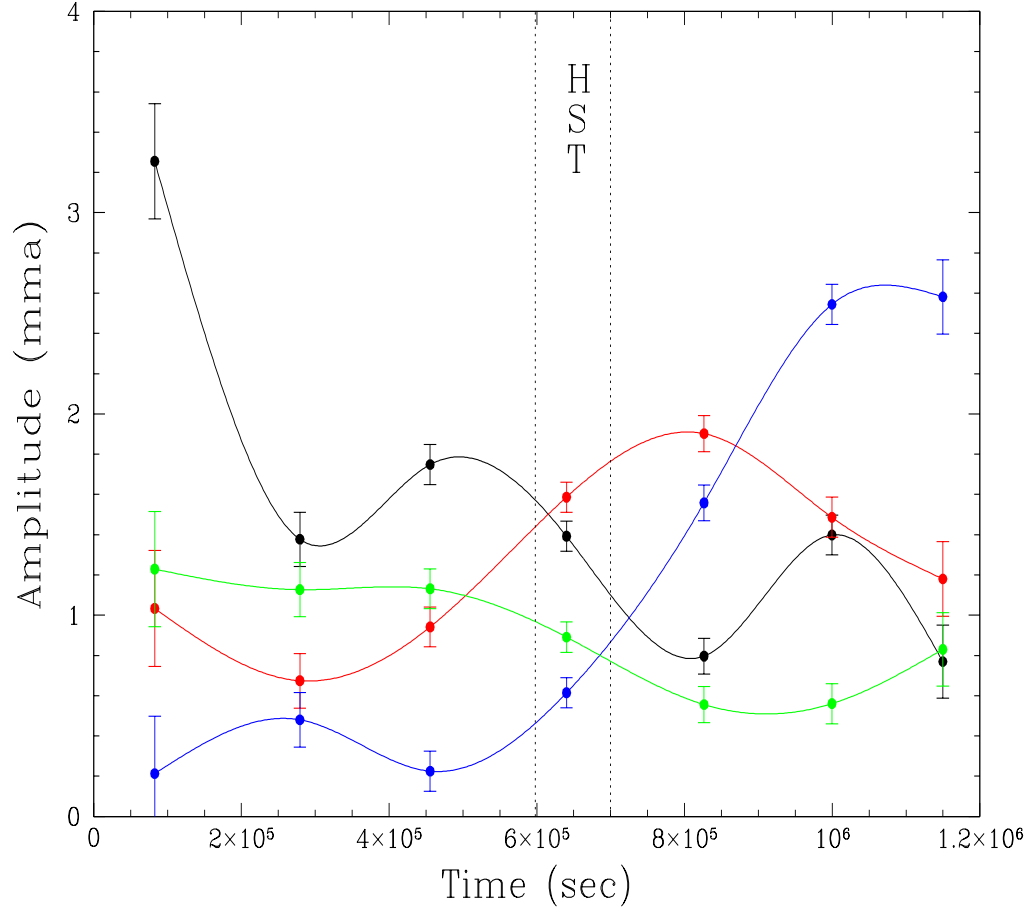


Figure 3.22: BPM37093's amplitude modulation as observed in the optical data taken by the WET. The black dots shows the 633s mode, the red dots shows the 531s mode, the green dots show 512s model and the blue dots show the 549s mode. The start of the first visit and the end of the second visit of the HST observation are shown by the vertical dotted lines.

3.5 Application of The Period Distribution Method to BPM37093

Figure 3.18 shows the main power region (1500–1900 μHz) of BPM37093 from both WET runs. In the 1998 data set (XCov16), we identified eight independent periodicities, as labeled by arrows and their periods in this figure. In 1999 (XCov17), we observed four periodicities, also labeled. Two of the four periodicities observed in XCov17, the 531s and 512s periodicities, were not present in XCov16.

As we discussed in the previous chapter, definitive mode identification using the period distribution method was only achieved when the Fourier transform clearly showed period spacing of successive k modes and the fine-structure splittings due to rotation helped verify the ℓ value of the modes. It is not always the case that we see all the component of fine-structure splitting. For PG1159-035 (see Winget et al. [1991] for the detail analysis), there were sets of triplets and quintuplets observed in the Fourier transform. By assuming the quintuplets are $\ell = 2$ modes and the triplets are $\ell = 1$ modes, they obtained period spacings for the two ℓ modes. When they compared the ratio of the $\ell = 2$ period spacing to the $\ell = 1$ period spacing, it matched the theoretical prediction. Furthermore, the size of the fine structure splittings of the two ℓ modes also matched the theoretical calculations. Therefore, they were able to not only use the period spacing but also the fine-structure splitting to confirm the mode identification.

The number of split modes and their spacings are both a function of ℓ (ex. GD358: Winget et al. 1994, and PG1159: Winget et al. 1990). But for BPM37093, the periodicities do not show such splittings, despite our data being

accurate enough to show them if the splittings were greater than $\approx 0.77\mu\text{Hz}$ (corresponding to rotation period of $\approx 7d$ and shorter).

We do, however, see two pairs of modes closely spaced in frequency. the 633s, 637s pair and the 563s, 565s pair. They are spaced too close to be successive k modes of the same ℓ , thus we conjecture that they may be two pairs of modes split by stellar rotation. Their splittings in frequency are $8.6 \pm 1.5\mu\text{Hz}$ (for the 633s, 637s pair) and $9.3 \pm 1.5\mu\text{Hz}$ (the 563s, 565s pair). They are the same within their error bars, as expected for fine structure splitting caused by uniform stellar rotation. The splitting implies the rotation period is on the order of days² and these are consistent with other white dwarf pulsators.

If we assume that these modes are $\ell = 2$, then we obtain a rotation rate of $P_{rot}/\Delta m = 1.12 \pm 0.10d$ from the 633s, 637s pair and $1.04 \pm 0.09d$ for the 565s, 563s pair. These rates are consistent with the rotation rates of other white dwarf stars. GD358's fine structure indicated a rotation rate from 0.89d to 1.6d, depending on the radial overtone mode, while PG1159-035 showed a rotation rate of $1.38 \pm 0.01d$. What is the effect of the total mass on the rotation rate? We can estimate the expected rotation rate for a $1.1M_{\odot}$ white dwarf star assuming conservation of angular momentum and the rotation rate of a $0.6M_{\odot}$ white dwarf star is 1d. It turns out to be about $0.8d^3$ — the rotation rate of BPM37093 is not expected to be significantly different from other white

²This is an assumption as we have no indication of what m mode we are seeing.

³We assumed simply that the rotation period P can be described by $P = 2\pi r/v$ where r is the radius of the star and v is the rotation velocity. The radius can be estimated from the observed surface gravity g ($g = GM_{\star}/r^2$ where G is the gravitational constant) and v from the angular momentum conservation ($M_1 r_1 v_1^2 = M_2 r_2 v_2^2$ where the values with subscript 1 stands for quantities for $1.1M_{\odot}$ star and subscript 2 stands for quantities for $0.6M_{\odot}$ star.). Using these relations, we get $P_2/P_1 = (M_1/M_2)^{5/4} \times (g_2/g_1)^{3/4} \sim 0.8$ with $P_2 = 1d$.

dwarf pulsators. If we assume these modes are $\ell = 1$, we obtain a rotation rate of $0.67 \pm 0.09\text{d}$ for the 633s, 637s pair and $0.62 \pm 0.05\text{d}$ for the 565s, 563s pair. As the m values for these modes cannot be determined unambiguously, these numbers are just a lower limit to the rotation rates we can derive under the additional $\ell = 2$ or $\ell = 1$ assumptions. If the m differences are larger than 1, the rotation rate will be slower than the above estimates. Thus, we find these pairs of modes are consistent with the assumptions that they are fine structure splitting due to rotation of $\ell = 2$ or $\ell = 1$ modes. The other explanation for the doublets are that they are of different ℓ values which just happen to have similar periods showing up in our Fourier transforms (we call this *accidental degeneracy*). Winget et al. (1991) observed PG1159-035 to show accidental degeneracy. There is nothing to dismiss this possibility, but it seems an incredible coincidence that we observed two doublets which shows similar splittings and be consistent with rotation rate observed in other white dwarf stars. Therefore, although we can not entirely dismiss the doublets consisting of two different ℓ modes, it is unlikely.

Montgomery & Winget (1999) used the observed periods in the XCov16 data and compared then with their models to estimate the crystallization mass fraction of BPM37093. They assumed six of the observed modes (633s, 614s, 601s, 582s, 565s, and 548s) were all $\ell = 2$ modes with different radial overtone values, resulting in a $\approx 17\text{s}$ average period spacing. One of the results they showed is that when using only modes with such a limited period range (from 500s to 700s) to estimate the average period spacing, one can expect an error on the order of $\sim 5\%$ from the asymptotic period spacing. This uncertainty is due to the effect of mode trapping which causes the period spacing between the

modes to deviate from uniform period spacing. Using then, 17 ± 1 s as the period spacing, they found the crystallization mass fraction to have a range of 0% to over 80% depending on the H layer mass and the total stellar mass assumed. For example, a $T_{\text{eff}} = 11800\text{K}$, $1.05M_{\odot}$ model [a mass close to Koester & Allard's (2000) mass estimate of $1.03 \pm 0.08M_{\odot}$, but hotter effective temperature than their $11520 \pm 110\text{K}$ estimate] gives the crystallization mass fraction of 0% for $\log M_{\text{H}}/M_{\star} = -5$ and a period spacing of 16s and 50% for the same H layer mass and an 18s period spacing. For thin H layer masses ($\log M_{\text{H}}/M_{\star}$ less than ≈ -6), the estimated crystallization mass fraction is 0% for 16–18s period spacing. For a $T_{\text{eff}} = 11800\text{K}$, $1.1M_{\odot}$ model [a mass and effective temperature close to Bergeron et al.'s estimates of (1995) $1.09 \pm 0.05M_{\odot}$ and $11730 \pm 740\text{K}$ ⁴], the crystallization mass fraction ranges from 0% for thin H layer masses ($\log M_{\text{H}}/M_{\star}$ less than ≈ -7) and 16–18s period spacing, to slightly over 80% for $\log M_{\text{H}}/M_{\star} = -5$ and 18s period spacing⁵. Since the average period spacing depends not only on the crystallization mass fraction, but also on other parameters such as the total mass, the H layer mass, and the effective temperatures, we cannot uniquely determine the crystallization mass fraction from the average period spacing alone. Montgomery & Winget (1999) show in more detail how the crystallization mass fraction is related to the total stellar mass, H layer mass, period spacing and effective temperature.

What happens if we assumed the modes are $\ell = 1$, though? Since

⁴Bergeron et al. (1995) do not show the errors explicitly, but Winget et al. (1997) used results from Bergeron et al. (1995) and Bragaglia, Renzini & Bergeron (1995) and obtained these uncertainties.

⁵See Figure 10(b) and 11(b) in Montgomery & Winget (1999) for the relation between the crystallization mass fraction, period spacing and the H layer mass for 1.05 and $1.1M_{\odot}$ models.

Montgomery & Winget (1999) presented their models only for $\ell = 2$ period spacings, we have to first estimate what the $\ell = 2$ period spacing would be in the case where the measured 17 ± 1 s spacing is the $\ell = 1$ average period spacing. In the asymptotic limit, the average g-mode period spacing as a function of ℓ is

$$\langle \Delta P_\ell \rangle \propto \frac{1}{\sqrt{\ell(\ell+1)}} \quad (3.1)$$

(Unno et al. 1989), where $\langle \Delta P_\ell \rangle$ is the average period spacing for modes of a given ℓ . We therefore expect the period spacing for $\ell = 2$ to be $1/\sqrt{3}$ times the $\ell = 1$ period spacing. So in our case, the period spacing for $\ell = 2$ becomes $\sim 10 \pm 1$ s if the $\ell = 1$ period spacing is 17s. Montgomery & Winget (1999) describe how the period spacing changes with the total mass, H layer mass, and effective temperature [equation (6) in their paper]. They derived the following fit from their numerical calculations on the average period spacing:

$$\langle \Delta P_\ell \rangle_{\ell=2} = 14.7 \bar{f} [1 + 0.54(h - 5)\bar{f}]^{0.24} \left(\frac{M_\star}{1.1M_\odot} \right)^{-1.7} \left(\frac{T_{\text{eff}}}{12000K} \right)^{-0.95} \quad (3.2)$$

where $\bar{f} \equiv \langle \Delta P_\ell \rangle / \langle \Delta P_\ell \rangle_0$ is the ratio of the asymptotic period spacing for a given crystallization mass fraction to that at zero crystallization and h is the hydrogen mass fraction given by $-\log(M_H/M_\star)$. The expression is thought to be valid in the effective temperature range of 11200K to 12800K and the mass range of $1.05M_\odot$ to $1.15M_\odot$. To determine the lowest possible mass that would give us a 10s $\ell = 2$ period spacing, we set the crystallized mass fraction to zero (hence $\bar{f} = 1$), h to the largest reasonable value of -5 (any greater and nuclear burning would occur in the compositionally pure H layer), and T_{eff} to

the largest acceptable value for BPM37093 of $\approx 12000\text{K}$. The mass then comes out to $1.38M_{\odot}$, i.e., to get an $\ell = 2$ period spacing of 10s, we need a $1.38M_{\odot}$ model, $\log M_H/M_{\star} = -5$, $T_{\text{eff}} = 12000\text{K}$ and 0% crystallization.⁶ Since the spectroscopic mass estimates by Koester and Bergeron indicate that BPM37093 is massive, but not as massive as $1.1M_{\odot}$ and beyond, it seems that if all the observed modes are of the same ℓ , they must be $\ell = 2$.

Kleinman et al. (1998) studied a DAV, G29-38, which exhibits large amplitude variations from year to year. Every year they observed G29-38 pulsating in modes with different periods and amplitudes. At any one year, there were not enough observed modes to apply period distribution method, but when they combined all observed modes spanning 10 yrs, they were able to uncover a set of normal modes which they could use to apply the period distribution method. As BPM37093 also shows amplitude modulations and does not show the same set of modes every year (as we saw in Figure 3.18), we will try Kleinman et al.'s approach of asteroseismology. The new modes we found in XCov 17 are consistent with this $\ell = 2$ interpretation. The 512s and 531s periodicities were not detected in XCov 16, but the spacing between these two modes is 19.51s, and that between the 549s and 531s modes is 18.10s. The differences between the average the period spacing ($17 \pm 1\text{s}$) we found in XCov 16 and these numbers are consistent with the effect of mode trapping (see for example Bradley 1996). Taking these new period spacings into account, the average period spacing changes only slightly to $\sim 17.5 \pm 1\text{s}$.

Kanaan (1999) used all the observed periodicities in BPM37093 (from its

⁶This mass is outside the valid range of Equation 3.2, but the point is that a mode with an $\ell = 2$ period spacing of 10s would require a significantly higher mass than $1.15M_{\odot}$.

period (s)	$\Delta P = P_{k+1} - P_k$ (s)	k
512	19	k_0
531	17, 18	$k_0 + 1$
548	15, 17	$k_0 + 2$
549	14, 16	$k_0 + 2$
563	19	$k_0 + 3$
565	17	$k_0 + 3$
582	19	$k_0 + 5$
601	13	$k_0 + 6$
614	19, 23	$k_0 + 7$
633		$k_0 + 8$
637		$k_0 + 8$

Table 3.2: Periods observed in 1998 and 1999 WET runs. The first column shows the period obtained from the Fourier transforms, the second the period spacing defined as $\Delta P = P_{k+1} - P_k$ and the third column shows k assuming we are seeing different k modes, but the same ℓ . The shortest observed mode is defined as k_0 . Except for the 548, 549s modes, the modes with the same k are the doublets we think are the same k but different m modes. We think the 548 and 549s modes are the same mode, but the periods are off due to either frequency modulation, or observational errors. If all modes are of the same ℓ , we have observed 8 consecutive overtone modes when we combine the observed modes from the two WET runs.

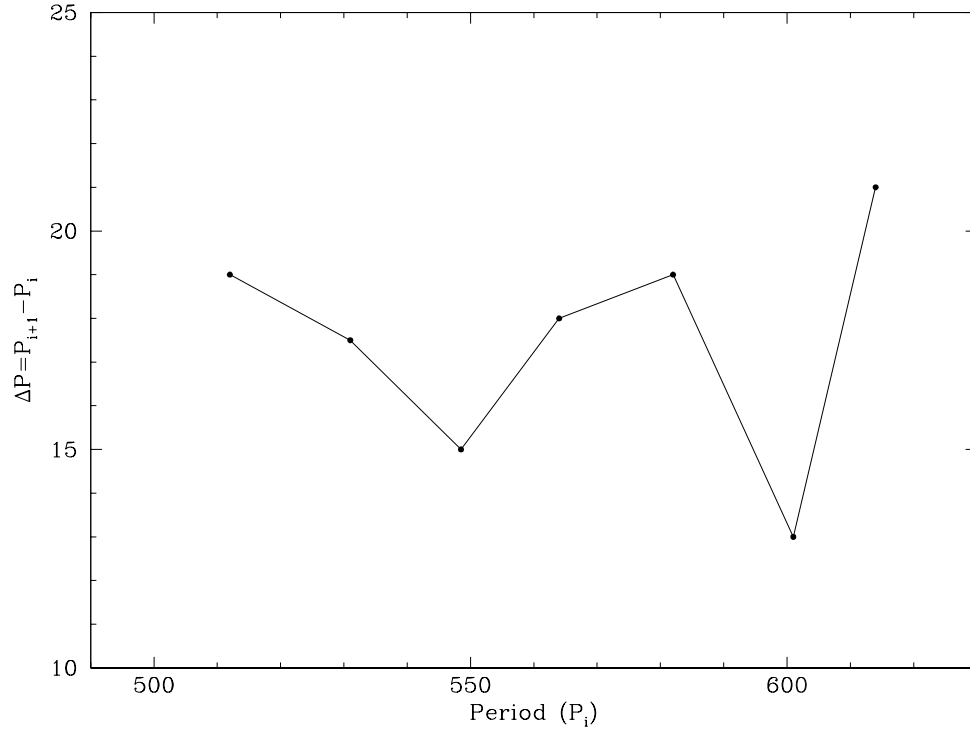


Figure 3.23: Period spacing diagram of BPM37093 using the observed periods from the 1998 and 1999 WET runs. The x-axis is the period of the mode P_i and the y-axis is the period spacing $\Delta P = P_{i+1} - P_i$. We assumed all modes are of the same ℓ . For the modes we saw doublets, we used the average of the two modes as P_i .

discovery in 1991 to the WET run in 1999) and determined a period spacing of $\sim 18 \pm 1$, consistent with our results. Just to be safe, we again used Equation 3.2 to estimate what mass would produce an $\ell = 1$ average period spacing of 19s. The answer is $1.3M_{\odot}$, again much more massive than all estimated BPM37093 masses. We can safely rule out the possibility of all modes being $\ell = 1$. The constant ≈ 18 s period spacing strongly suggest we are seeing a set of all $\ell = 2$ modes, rather than a random mixture of $\ell = 1$ and 2 modes, which would not show such uniform period spacing (see Figure 3.23 for the period spacing diagram and Table 3.2 for the list of periods observed in 1998 and 1999 WET runs).

Montgomery (1998) tried fitting the observed period spacing diagram with his model grid in search of a unique fit. If successful, this would provide us with a model with parameters such as the H layer mass, crystallization mass fraction, effective temperature, total stellar mass and absolute luminosity. He was unsuccessful, but discovered the models show that the crystallization mass fraction influences the observed trapping features just like the H layer mass does. He concluded that the only way to find a unique fit is to compare the observations with a very fine model grid in a systematic manner. Unfortunately, such a procedure requires enormous computer resources. Travis Metcalf, at UT, is developing such procedure that does not use so much CPU time and will be applying it to BPM37093 once it is ready.

In summary, our two WET observations along with previous data on BPM37093 indicate a period spacing of $\sim 17 - 19$ s if we assume all the modes are of the same ℓ . From this average period spacing, using mass estimates from Koester & Allard (2000), and Bergeron et al. (1995), it is likely that all the

observed periodicities are $\ell = 2$ modes. To have a period spacing of 17–19s for $\ell = 1$ modes, the total mass of a model star must be larger than $\approx 1.3M_{\odot}$. There are no observations supporting BPM37093 being this massive. Therefore, we believe our assumption of most, if not all, modes being $\ell = 2$ is quite reasonable. Using models from Montgomery & Winget (1999), the crystallization mass fraction is anywhere from 0% to 80% depending on the H layer mass and the total stellar mass. In general, thin H layer masses ($\log M_{\text{H}}/M_{\star} < -7$) favor 0% crystallization mass fraction while thick H layer masses ($\log M_{\text{H}}/M_{\star} = -5$) favor a non-zero crystallization mass fraction. As asteroseismological analysis of other DAVs (Clemens 1993; Kleinman 1995, 2000) favor thick H layer masses, it is likely that BPM37093 has a crystallized interior, but we need to wait for the final answer until we can constrain the H layer mass of BPM37093 better. Although as not crucial as the H layer mass, a better fit to the HST spectrum (Figure 3.9) which has a much better signal to noise than the IUE spectrum, might help constrain the total mass. There are about 20 modes detected from the two WET runs and the previous observations by Kanaan. Our attempt to apply the period distribution method via Kleinman et al’s (1998) approach of combining observed modes from different seasons instead of using observed modes from one season, has not allowed us to measure the H layer mass, although enough to constrain the crystallization mass fraction. As the pulsation modes we observed changed from year to year, we need to monitor this star every year to detect as many modes as possible. We need to identify more trapped modes, the key to measuring the H layer mass and the crystallization mass fraction, as well as to look for fine structure splitting which helps in ℓ identification.

3.6 Application of the Limb Darkening Method

3.6.1 Mode Identification using Amplitude Ratios

To compare the amplitudes in the UV with those in the optical, we need accurate measurements of the mode amplitudes in both wavelengths. If the amplitudes are changing over time, we must measure the amplitudes simultaneously in both wavelength bands to obtain reliable amplitude ratios for mode identification. For BPM37093, we measured the UV amplitudes from the four independent HST lightcurves and used the Days 7-8 WET lightcurve for the optical amplitudes.

The UV Phases vs. the Optical Phases

Before we study the amplitude ratios, we must first take a look at the phases in the UV and compare them with the optical. Since the light variations we see from g-modes are strictly a temperature effect, Robinson, Kepler, & Nather (1982) showed that the modes should have the same phases at all wavelengths, as long as nonadiabatic effects are not dominant. This has been observed true for GD358 (chapter 2), R548 (Robinson, Kepler & Nather 1982), PG1351+489, G226-29 and G185-32 (Kepler, et al. 2000). But Clemens, van Kerkwijk & Wu (2000) found small phase differences vs. wavelength from time-series spectroscopic data of the large amplitude DAV, G29-38, taken with the Keck telescope. They found in the continuum, the blue ($\sim 3800\text{\AA}$) photons arrived a few seconds (corresponding to up to a 2% phase shift depending on the period of the mode) earlier than the red ($\sim 6000\text{\AA}$) photons. There is no explanation for this observed phase shift at this time, although all the previous observations are not precise enough to detect this small a change so we do not know how

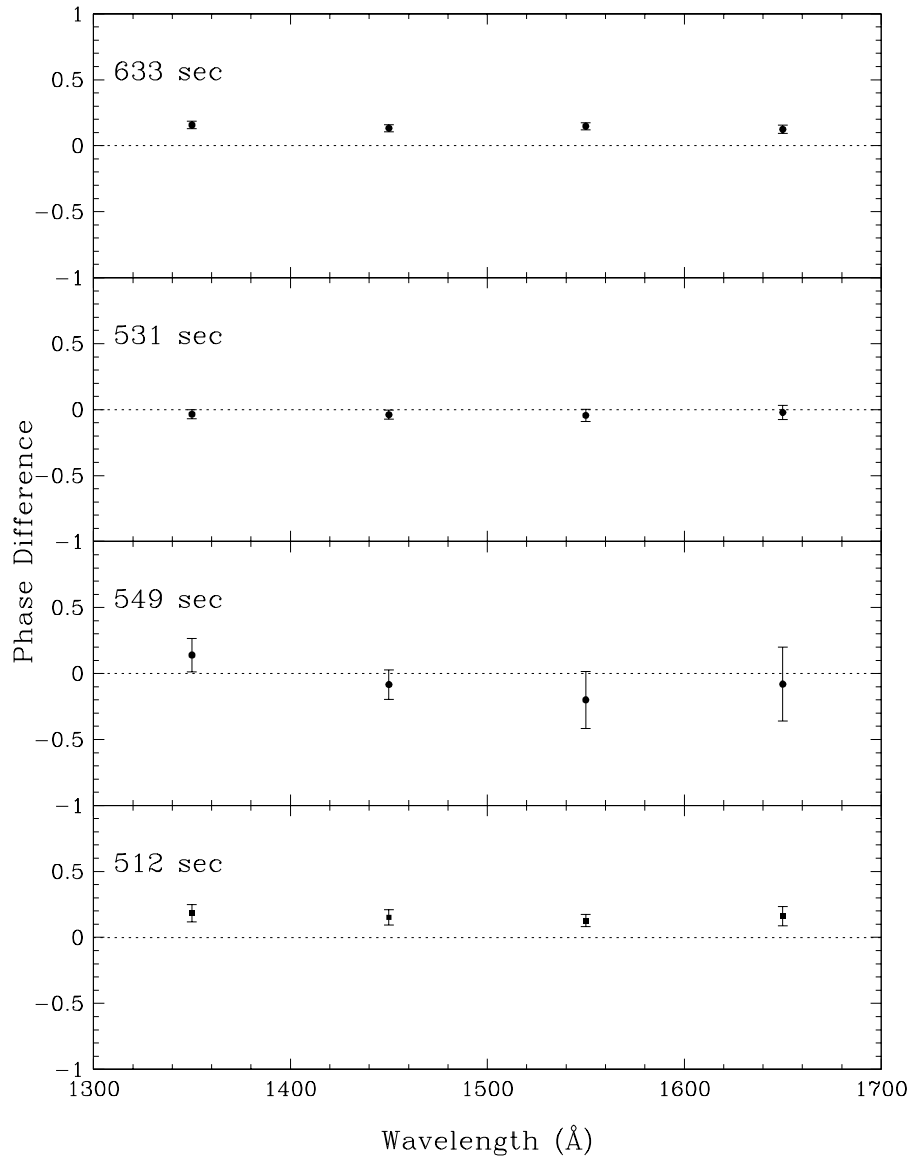


Figure 3.24: Mode phase as a function of wavelengths for BPM37093. When the phase difference is equal to zero, the UV is in phase with the optical data. When it is ± 0.5 , it means that the UV phase is out of phase ($\pm\pi$) with the optical. The phases of the 633s, 531s, and 549s periodicities are slightly offset from the optical phase.

universal this effect is.

In Figure 3.24, we show phases of the four observed BPM37093 periodicities in the UV compared to the phases estimated from the optical data taken around the HST observations (the Days 7-8 lightcurve). The uncertainties are estimated by a least squares fitting program which determines the mode phases and the amplitudes and is really only a lower limit; the true uncertainties can often be a factor of four (Kleinman 1995) or more (Montgomery & O'Donoghue 1999) higher. The UV phases of the three periodicities, the 633s, 531s and 512s modes, are actually slightly offset (e.g. $\sim 15\%$ for the 633s periodicity and $\sim 5\%$ for the 531s periodicity) from those of the optical. If these differences are real, perhaps, for this most massive DAV, nonadiabatic and/or nonlinear effects are important and are causing true phase shifts. The fact that all the UV phases for each mode are offset in the same direction (e.g. the 633s and 512s UV phases are all offset in positive direction, while the 531s mode's phases are all offset in negative direction) indicates that we cannot account for these offsets by the possible uncertainty underestimate of the least squares fitting program alone. If the true uncertainties were substantially larger than these plotted, the measurements would be scattered around the true phase. Instead, the UV phases show a systematic offsets from the optical phase for the three modes and hence there is a high probability that these are real phase shifts. The 549s periodicity's phases have much larger error bars and scatter compared to those of the other 3 periodicities, indicating we do not have good estimates of the UV phases or amplitudes. As we saw in Figure 3.22, the amplitude of the 549s periodicity was just starting to grow around the time of the HST observation: its amplitude is still the smallest among the 4 periodicities. A

successful mode identification with the data on the 549s periodicity is unlikely.

Amplitude Ratios and Mode Identification

In Figure 3.25, we compare a model calculation using $T_{\text{eff}} = 11500\text{K}$ and $\log g = 8.75$ model with the observed BPM37093 amplitude ratios. We can immediately see that none of the modes are $\ell = 3$. The 531s and 512s mode ratios are consistent with each other given their error bars while the 633s mode ratios appear significantly different. The curve of the 549s periodicity is very noisy as expected from the UV phases seen in Figure 3.24. Despite the poor quantitative fit between any of the observed amplitude ratio curves and the $\ell = 1$ or 2 theoretical curves, the theoretical curves do reproduce the qualitative shape of the observed 633s, 531s and 512s curves. If the models are wrong, they may not be far wrong. At any rate, we see that (1) we cannot use the theoretical models to directly assign the ℓ values with these data, (2) if the models are at least roughly correct, which we believe they are, none of the modes are $\ell = 3$ and (3) the 531s and 512s modes are likely to be of the same ℓ while the 633s mode is different. Since theoretical calculations tell us the $\ell = 1$ amplitude ratios are expected to be smaller than the $\ell = 2$ ratios, we can consistently assign the 512s and 531s modes $\ell = 1$ and the 633s mode, $\ell = 2$. These ℓ assignments neither change the conclusions from the period distribution method nor improve the crystallization mass fraction estimates since they came from the average period spacing which depends on the periods of many modes, not only on one or two modes.

Since Kepler et al. (2000) were able to assign ℓ values for other DAVs with more typical masses (e.g. $\approx 0.6M_{\odot}$) using similar models, we know these

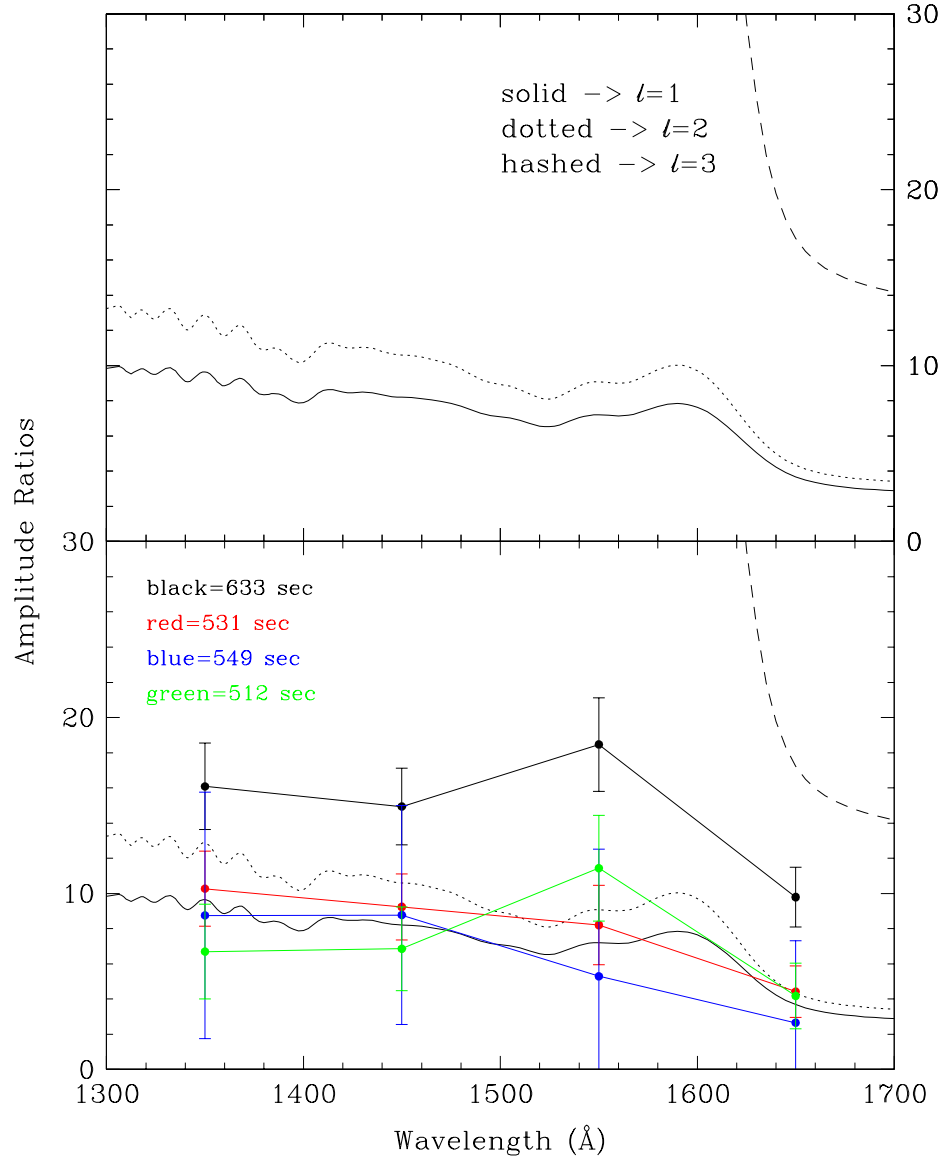


Figure 3.25: BPM37093's UV amplitudes normalized by the optical amplitude. The top panel shows the calculated amplitude ratio using $T_{eff} = 11500$ K and $\log g = 8.75$ model. The solid line is the model $\ell = 1$ mode, the dotted line is the model $\ell = 2$ mode, and hashed line is the model $\ell = 3$ mode. The bottom panel shows the observed data on the four primary periodicities. In this figure we only show the four independent data points.

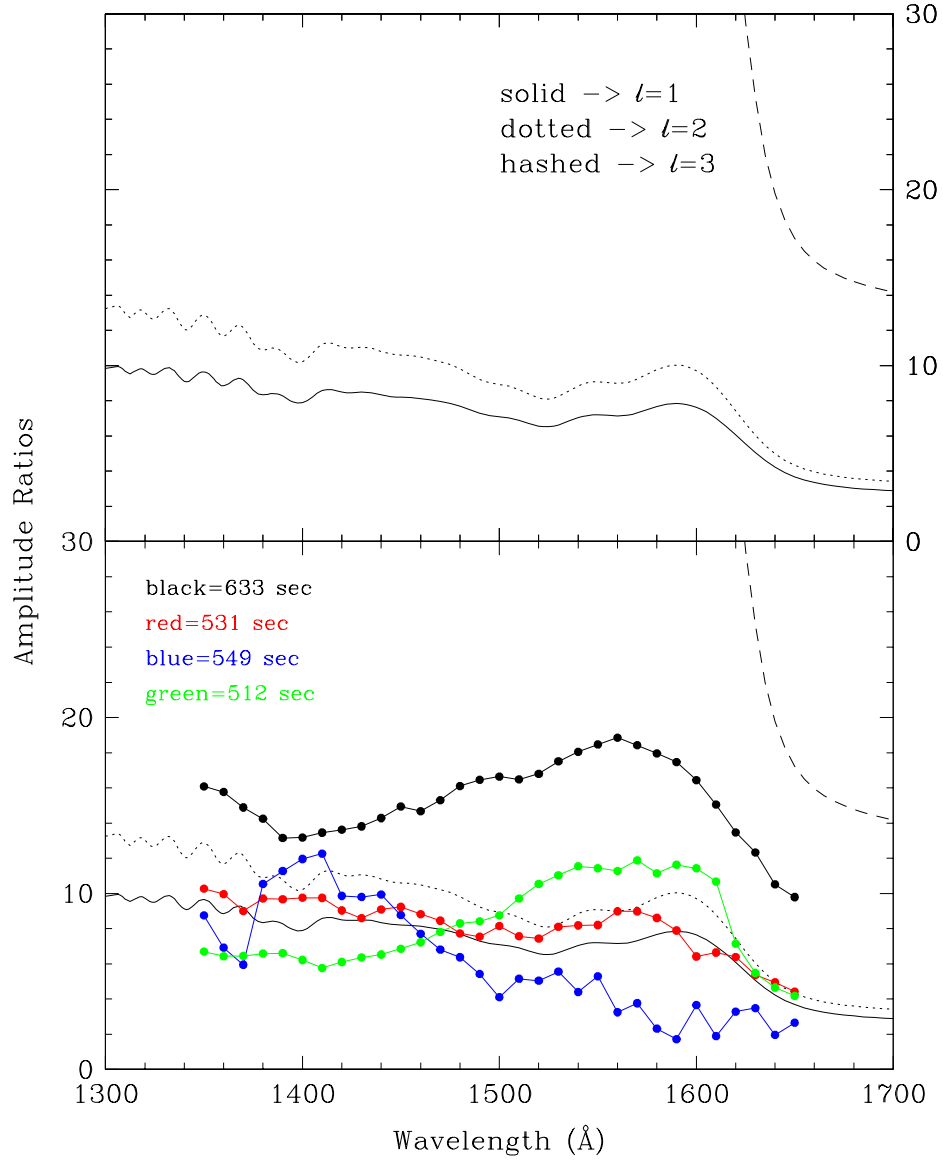


Figure 3.26: .

BPM37093's UV amplitudes normalized by the optical amplitude. The top panel shows the calculated amplitude ratio using model with $T_{eff} = 11500$ K and $\log g = 8.75$. The solid line is the model $\ell = 1$ mode, the dotted line is the model $\ell = 2$ mode, and hashed line is the model $\ell = 3$ mode. The bottom panel shows the observed data on the four primary periodicities similar to the previous figure, but in this figure we included amplitude ratios we obtained by using the running lightcurves. Only 4 among the 31 points shown are independent. This figure shows how well the models reproduce the shape of the observed chromatic amplitude ratio curves better than Figure 3.25.

models are reasonable for normal mass DAVs. Since BPM37093 is uniquely massive, we suspect the models could be failing because of missing physics under the extreme conditions (such as the opacity table not being quite adequate for high gravity condition) likely to be found in BPM37093. Koester has also recently found (Koester 2000, private communication) that the amplitude ratios for some models can change by including the effects of the pulsations themselves on the star's limb darkening⁷. Our models do not currently include this effect.

3.6.2 Mode Identification using the Fourier Transform Ratio

As we saw in the last chapter, the ratios of the UV to optical Fourier transforms can tell us whether all modes we observed in a star are of the same ℓ or not, but only if the amplitudes of the modes are similar to each other. If there is a mode that strongly dominates the Fourier transform, the ratio of the Fourier transforms will be heavily weighted by that mode.

Figure 3.27 shows the HST UV Fourier transform divided by our Days 7–8 optical Fourier transform. Again, we can immediately rule out $\ell = 3$ completely although the shape of the curves do not really agree with either the $\ell = 1$ or $\ell = 2$ calculations either. Our data are consistently higher than both the $\ell = 1$ and $\ell = 2$ theoretical curves, similar to the 633s mode amplitude ratio curve in Figure 3.26. Figure 3.30 shows the UV amplitudes themselves of

⁷Imagine the stellar surface divided into many patches of equal size. The flux from each patch is proportional to $T^4 \times h$ where T is the temperature and h is the limb darkening at each patch. The perturbation to the flux caused by pulsation at each patch is proportional to $4 \times T^3 \delta T \times h + T^4 \times \delta h$ where δT is the temperature perturbation and δh is the perturbation to the limb darkening. Currently the second term is ignored in our model calculations, but Koester found that they can make differences to some models.

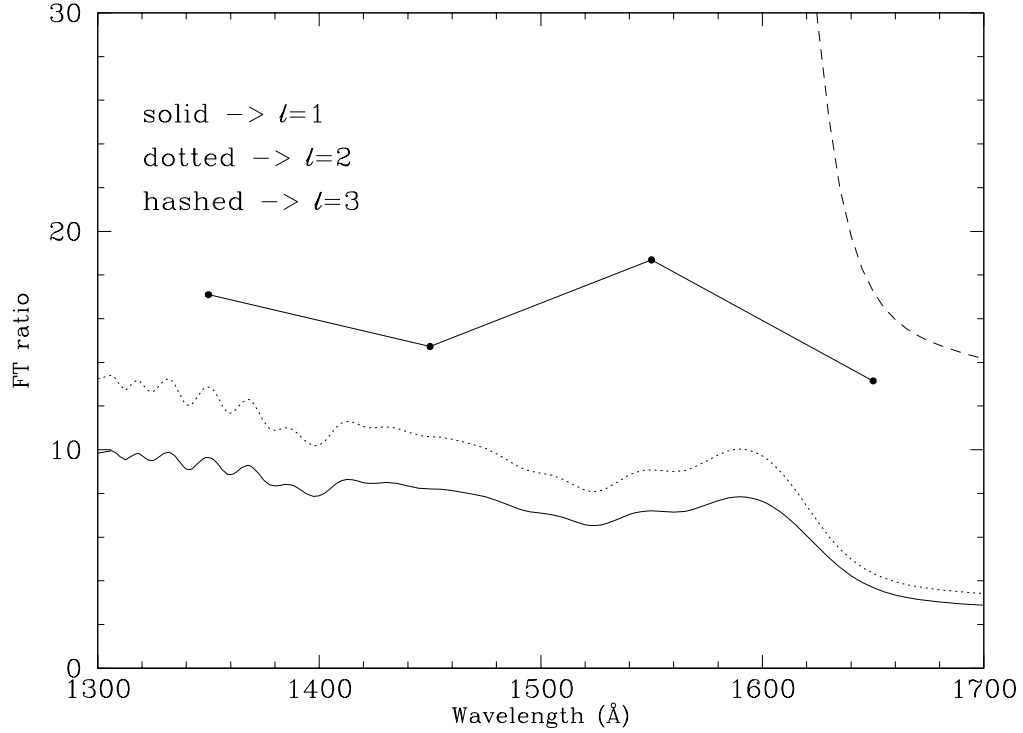


Figure 3.27: The Fourier transform ratios for BPM37093 (solid dots) along with the theoretical ratio using $T_{eff} = 11500\text{K}$ and $\log g = 8.75$ model calculated using Koester's model atmosphere. The solid line is a model $\ell = 1$ mode, the dotted line is a model $\ell = 2$ mode, and the hashed line, a model $\ell = 3$ mode.

the four observed modes. The 633s mode dominated very strongly in the UV although it had had a slightly smaller amplitude than the 531s mode did in the optical (see Figure 3.22) and therefore the Fourier transform ratios only reflect the nature of the 633s mode alone, as evidenced by the similarity of Figure 3.27 and Figure 3.29.

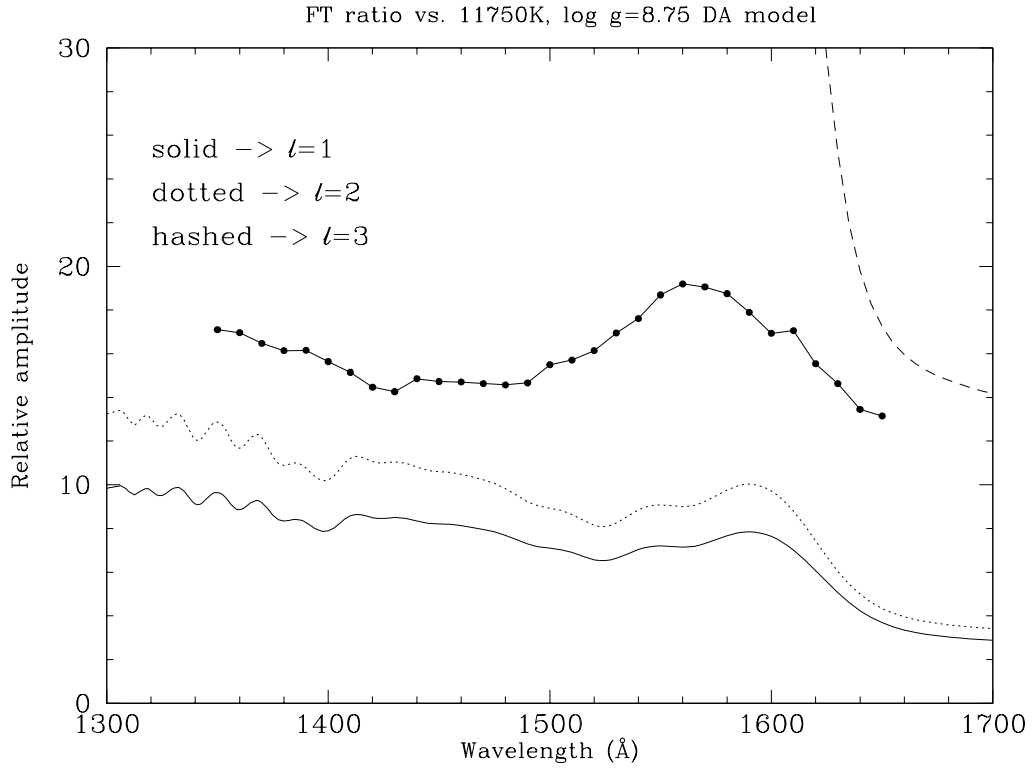


Figure 3.28: The Fourier transform ratios for BPM37093 (solid dots) along with the calculated ratio using $T_{eff} = 11500\text{K}$ and $\log g = 8.75$ model. Only 4 out of the 31 points are independent. (See Figure 3.27 for the 4 independent measurements.) The solid line is a model $\ell = 1$ mode, the dotted line is a model $\ell = 2$ mode, and the hashed line, a model $\ell = 3$ mode.

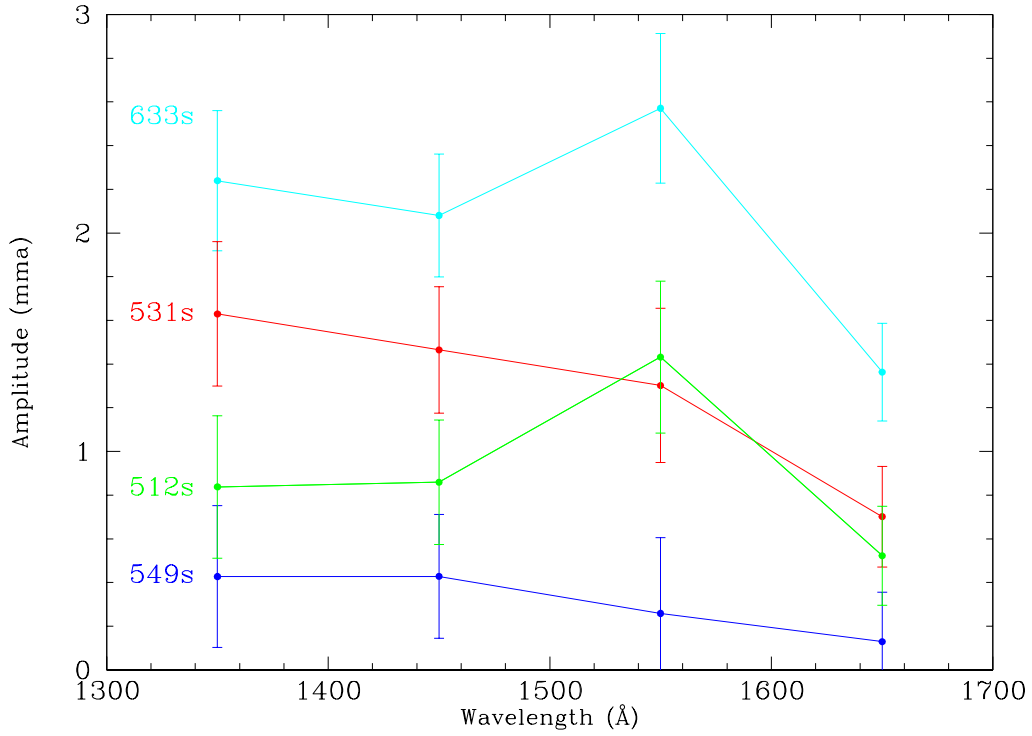


Figure 3.29: The amplitude of BPM37093's observed modes in the UV. The amplitudes were estimated using the 4 independent running lightcurves. The 633s mode's amplitude is in cyan, the 531s mode is in red, the 549s mode is in blue and the 512s mode is in green. In the optical, the 633s mode was slightly smaller than the 531s mode (see Figure 3.22), but in the UV, the 633s mode is actually dominant. Thus, the Fourier transform ratio (Figure 3.27) looks similar to the 633s amplitude ratio (Figure 3.32).

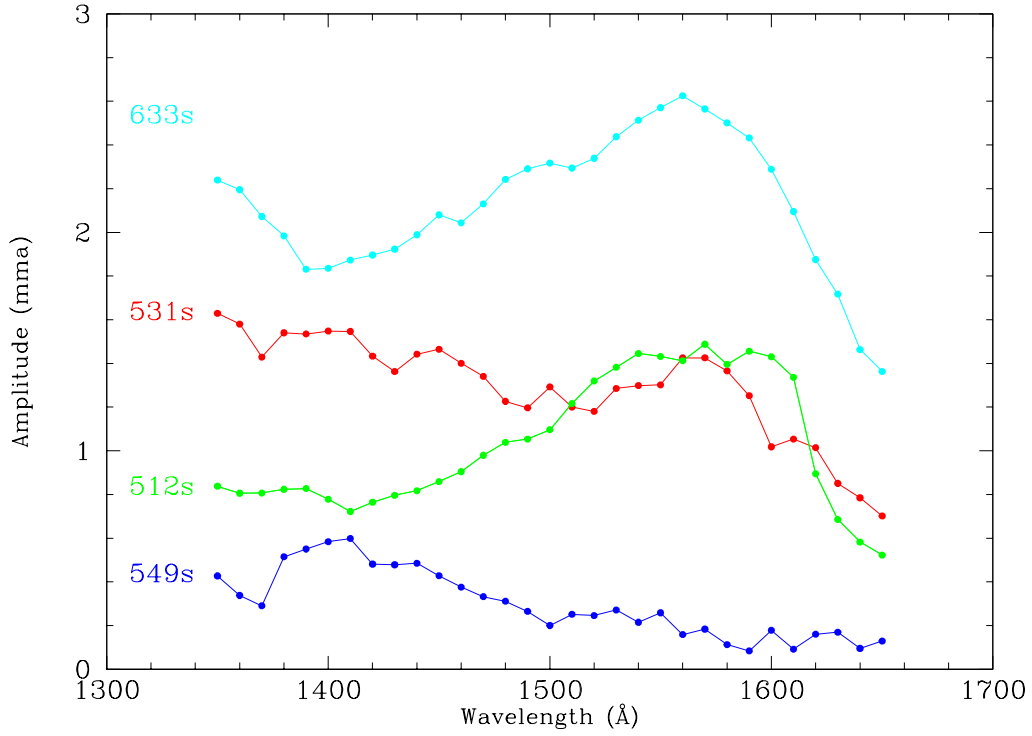


Figure 3.30: The amplitude of BPM37093's observed modes in the UV. The amplitudes were estimated using the 31 running lightcurves. Only 4 out of 31 measurements are independent (see Figure 3.29 to see the independent measurements only.). The 633s mode's amplitude is in cyan, the 531s mode is in red, the 549s mode is in blue and the 512s mode is in green.

3.6.3 Contamination Sources

We have discussed the differences between the models and the data both in the continuum spectrum and the amplitude ratios.

- (1) The model spectrum is a poor fit to the data between $\sim 1500\text{\AA}$ and 1750\AA .
- (2) The mode amplitude ratios rule out the possibility of $\ell = 3$ modes; although the observations' qualitative trends are reproduced by theoretical calculations, they do not quantitatively agree with either $\ell = 1$ or 2 model calculations.
- (3) We see small offsets in phases between the UV and the optical observations.

If we first assume the model calculations are correct, then what could be the source(s) of the disagreement between our observations and the models? We show in Figure 3.31 the BPM37093 UV spectrum (red curve), the $T_{\text{eff}} = 11500\text{K}$ and $\log g = 8.75$ model spectrum (green curve) and the residual spectrum (black curve) obtained by subtracting the model spectrum from the BPM37093 spectrum. Up to 1500\AA or so, the agreement between the data and model spectrum is good, but longward of that, there are disagreements between the two. Since there has been no report on any problem with flux calibrations for the instrument we used, STIS with the FUV–MAMA detector (Dowes 2000, private communication), we must consider the possibility that the differences between the model and the data spectrum is real and the data spectrum is possibly contaminated by another as yet unidentified source or sources in the 1500\AA to 1750\AA wavelength range. The contaminating source acts as a flux absorber between 1500\AA and 1650\AA , and adds excess flux between 1650\AA to 1750\AA . Optical spectrum analysis of BPM37093 by Bergeron et al. (1995) did not mention any unusual contamination, therefore the contaminating source

must have very little flux, if any, in the optical. The target acquisition image of BPM37093 taken by the HST does not show any companion. So we are left to deduce what the contaminating source might be from the residual spectrum alone, shown in Figure 3.31.

We have compared the wide range of sample spectra provided by STScI on the World Wide Web (WWW) to the residual spectrum⁸. We have ruled out all normal O, B, A, F, G, K, M type stars, DA, DO, DB white dwarf stars, sdO stars, planetary nebula nuclei, and elliptical and spiral galaxies. Nonstellar objects such as nebulae or quasars also seem difficult to fit to the residual spectrum. The remaining possibility is the interstellar medium (ISM) and dust surrounding the star. Since a nearby dust cloud is one of the possible explanations for the observed IR excess (Zuckerman & Becklin 1987) in G29-38 (see Zuckerman 1993 for review on possible cause of the IR excess; Kucher, Koresko & Brown 1998) it is not entirely unreasonable to consider the possibility of a dust cloud around another white dwarf pulsator. But both the ISM and dust are usually cool and show very little flux in the UV, making it hard to believe our problem arises from either the ISM or dust. We therefore believe that the differences between the model and data spectra are more likely to be due to the models, not to any object contamination. Koester believes these differences arise from the flux calibration (Koester 2000, private communication) of STIS (Dowes not withstanding) since he has seen scattered light in other wavelength ranges using STIS. STIS is a relatively new instrument (installed on the HST

⁸The WWW site (http://garnet.stsci.edu/STIS/ETC/stis_spec_etc.html) is an “Exposure Time Calculator” for HST observations using STIS. The calculator uses sample spectra to estimate the necessary exposure time required to achieve certain signal to noise ratios. The web site provides many different sample spectra from which the observers can choose.

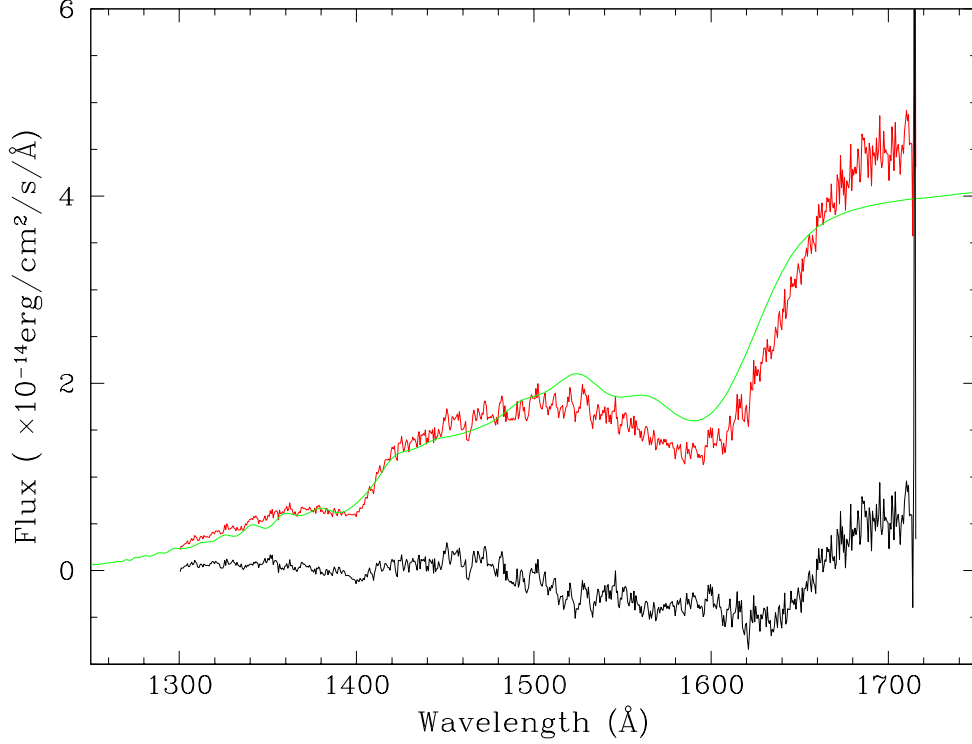


Figure 3.31: The observed, model and residual spectra of BPM37093. The observed spectrum is in red, the 11500K, $\log g = 8.75$ model spectrum is in green and the difference between the two $[(dataspectrum) - (modelspectrum)]$ is shown in black as the residual spectrum.

in 1997), and although no flux calibration problem has been yet reported, it is still early to conclusively decide against it⁹. We therefore have no reason to suspect the flux calibration problem over some problems in the models, but cannot rule either out.

The mismatch of the observed spectrum to the model spectrum means the observed amplitude ratios would be systematically different from the theoretical amplitude ratios. We expect the observed UV amplitudes in the range

⁹The FOS had flux calibration problems which were only partially resolved after decommissioning of the instrument (Kepler 2000).

we observe a depression of flux to have higher amplitudes than theoretically predicted, resulting in higher amplitude ratios. In the range where we observe excess flux, we expect to find lower amplitude ratios than predicted. These results explain why the humps around 1600\AA in the observed amplitude ratio curves are more pronounced than in the models, but cannot explain all the differences since the observed amplitude ratios disagree with the models even in the wavelength region (up to 1500\AA) where the observed and model spectra agree. As we discussed already, however, the agreement between the spectra is necessary but not sufficient to guarantee that the model adequately describes the amplitude ratios.

If a contamination source was affecting the phases, it would do so in the same manner regardless of the periods of the modes. Since both the size and the direction of the phase shifts are different from mode to mode, we further believe the phase shifts are intrinsic to the star.

3.6.4 Summary

We do not know how to explain the differences between the observed and model spectra in the wavelength range of 1500 to 1750\AA , but we suspect that it must be either the flux calibration, the models themselves, or both. We found phase offsets between the UV and the optical, making BPM37093 the second white dwarf pulsator to show such shifts. The cause of these phase shifts is unknown at this time, but perhaps BPM37093's high mass is causing some nonlinear and/or nonlinear effects unseen in most white dwarf pulsators.

Figure 3.32 combines Figures 3.26 and 3.27 to show all the observed amplitude ratios along with the Fourier transform ratios. Again, all ratios

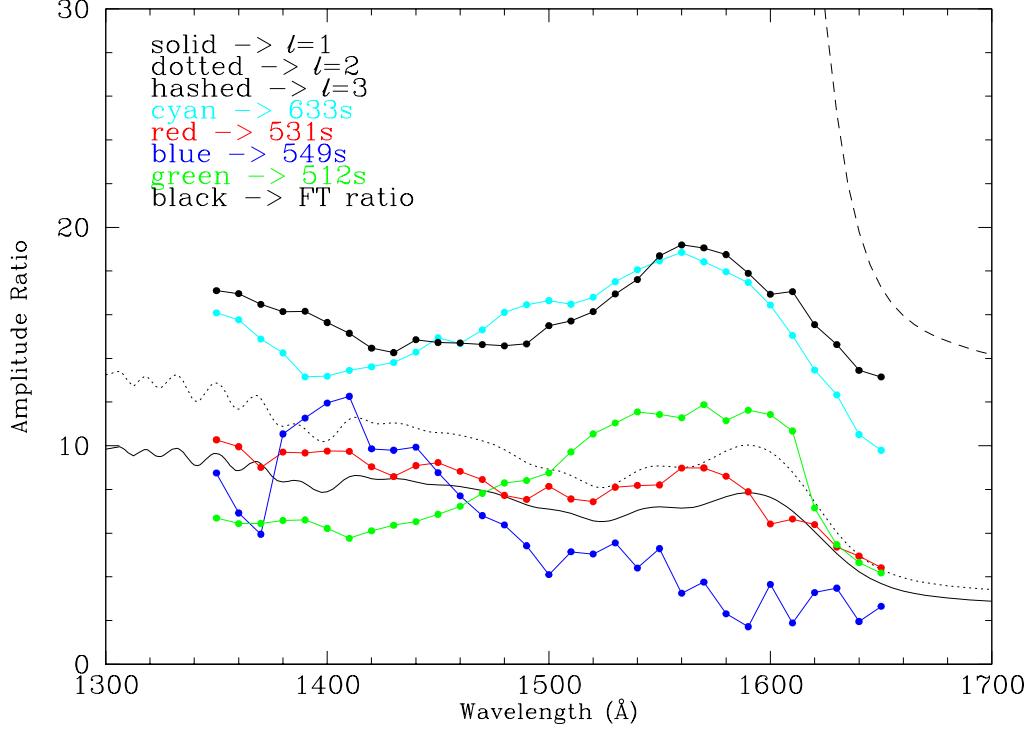


Figure 3.32: The UV to optical ratio of BPM37093 Fourier transforms (black) and the four observed pulsation modes' amplitudes ratios. The cyan curve shows the 633s mode, the red shows the 531s mode, the blue shows the 549s mode and the green shows the 512s mode. The model calculation are shown by the black lines (solid line for $\ell = 1$, dotted line for $\ell = 2$, and hashed line for $\ell = 3$ model).

exclude $\ell = 3$ completely, but neither the $\ell = 1$ or the $\ell = 2$ models fit very well either. We find evidence for assigning value $\ell = 1$ to the 512s and 531s and $\ell = 2$ to the 633s mode based on the curves' qualitative similarities and differences. To explain the model mismatches, we suspect the temperature derivatives of the local fluxes are not calculated correctly for such a high mass model as is expected from BPM37093 and/or the assumption that the pulsations do not affect limb darkening.

Chapter 4

Summary & Conclusions

4.1 Summary & Conclusions

We started this work to comprehensively examine the limb darkening method of mode identification in pulsating white dwarf stars. In particular, we chose two projects: 1) compare the mode identifications provided by the limb darkening method with those obtained by the more established (but more demanding) period distribution method and 2) use the limb darkening method to provide mode identifications for a star with rich scientific rewards (BPM37093 and the physics of crystallization) which could not be easily solved by the period distribution method. In short, the first project was a success in that the new mode identifications are consistent with the earlier values, but we discovered the required observational accuracy demanded by the limb darkening method is difficult to obtain and may make the method impractical for many of the white dwarf pulsators which show fast amplitude modulations. With BPM37093, we faced even greater barriers in that the observations could not definitively be fit by our current models of the limb darkening method. The results we did obtain are consistent with what we expect from the period distribution method, but again suffer from a lack of observational accuracy and probably, model incompleteness.

In the final analysis, the limb darkening method is an attractive and interesting method of mode identification, but it cannot yet replace or be used with confidence to complement the period distribution method of mode identification when there are too few modes for unique mode identification. It is difficult to obtain data of high enough quality, we need a WET-type observation in the optical and a simultaneous UV observations (i.e. a good number of orbits using the HST) without any amplitude, frequency or phase modulations, to apply the limb darkening method and it appears that the current white dwarf atmosphere models may not be complete enough to adequately predict the amplitude ratios vs. wavelength curves (chromatic amplitude ratios) needed by the limb darkening method. We must solve the latter problem before any significant further work can occur with the limb darkening method of mode identification for white dwarf pulsators.

4.1.1 GD358 & Its Drastic Amplitude Changes

We observed GD358 from the ground in June, July and August 1996. GD358 showed no signs of amplitude modulations in June and July, but in August, we observed the star's modes change drastically in amplitude. The pulsation amplitude for the 423s ($k = 8$) mode grew from less than 2mma at the start of the run to become the dominant mode at 164.8mma 27 hours later. When the 423s mode was observed at its largest amplitude, the usually dominant 700s ($k = 15$) and 770s ($k = 17$) modes did not have detectable amplitudes. The running Fourier transform (Figure 2.36) shows that their unresolved amplitudes are ~ 50 mma in suh-55 and become less than ~ 10 mma, buried in the noise, in an-0034. Increasing k increases the number of radial nodes in

the star, generally placing the higher k nodes in the star’s envelope since the envelope has a lower density compared to that of the core. The higher the k , therefore, the more a mode is concentrated in the envelope. GD358’s observed amplitude modulation suggests the structure of the outer part of the envelope may have changed rather suddenly, lowering the energy in the higher- k , more envelope-concentrated 700s and 770s modes and putting it into the lower- k , less envelope concentrated 423s mode. The pulse shape also changed during this time. When the 423s mode was large, the lightcurve was nearly sinusoidal (surprising since one normally expects such large amplitudes to cause nonlinearities in the lightcurve). The star’s more usual nonsinusoidal pulse shape (see Figure A.5) returned once the 423s mode’s amplitude died. This change may indicate that pulse shape nonlinearities are due to other modes being present in the star and not necessarily due to any nonlinear processes that are taking place inside the star. Perhaps, also the amplitude limiting mechanism is different for the 423s mode compared to that of the usually dominant 770s and 700s mode.

Was it a “star quake” that changed the structure of the envelope suddenly? Whatever it was, once it happened, the star slowly¹ went back to its previous state, presumably regaining the envelope structure it had before the “shake-up”. This strange behavior has made us realize how important it is to continually observe the known pulsators, even the ones we *think* we understand. Although we cannot explain the phenomena we observed, we must find out if it repeats itself, or if other pulsators show such similar changes. Fortunately,

¹The Fourier transform from April 1997 shows the familiar power spectrum. The timescale for returning to the familiar power spectrum has, therefore, an upper limit of 8 months.

the WET group at University of Texas at Austin has just such a plan for long term monitoring of white dwarf pulsators and we have a wealth of archive data we can eventually unearth and use to increase our observed timebase.

The limb darkening method gave us $\ell = 1$ or 2 for the 423s mode in GD358, and ruled out $\ell = 3$ completely. If it is $\ell = 1$, the two methods of mode identification are consistent, but if it is $\ell = 2$, they are not. We could not conclusively determine if the two mode identification methods give identical results due to the fast amplitude modulation discussed above. Although these drastic amplitude modulations were quite interesting, they made it difficult to conclusively determine the ℓ values of the modes using the limb darkening method. We hope to get a definitive answer on the precise consistency of the two methods from the new GD358 simultaneous HST and WET observations of May–June 2000.

4.1.2 BPM37093 Observations

We showed that the BPM37093 atmosphere models we use do a less than perfect job of matching the observed UV time averaged spectrum. This mismatch is one of the reasons why the model amplitude ratios do not describe the observed amplitude ratios very well. The other possible reason is that the models do not provide the accurate local temperature derivatives which are required to calculate the theoretical amplitude ratios. Also, the systematic differences between the UV and the optical phases we measured (Section 3.6) imply that there might be some as yet not understood nonlinear and/or nonadiabatic effects which are important for BPM37093 — reasonable given the star’s high mass. We must solve the discrepancies between the models and our observed

amplitude ratios as well as the model and observed time averaged spectra. Otherwise, we cannot definitively assign ℓ values to the observed modes using the limb darkening method.

For BPM37093, our application of the limb darkening method implies the existence of two different ℓ s ($\ell = 1$ and 2) in the star while the period distribution method tells us that the period spacing implies most, if not all, of the modes are $\ell = 2$. Combining these two conclusions, we are confident that most of the observed periods in BPM37093 are $\ell = 2$. BPM37093 is only the third known white dwarf pulsator, after PG1159–035 (Winget et al. 1991) and G29–38 (Clemens, van Kerkwijk, & Wu 2000), to show any $\ell = 2$ modes. Among the modes we observed, our best guess is the 633s mode is an $\ell = 2$ while the 512s and 531s modes appear to be $\ell = 1$ (See Figure 3.32).

We attempted to estimate the crystallization mass fraction of BPM37093 based on these mode identifications along with the average period spacing we obtained from our optical data. Such a measurement would be the first confirmation of the forty year old prediction of crystallization in white dwarf stars (Kirshnitz 1960; Abrisokov 1961; Salpeter 1961). We agree with the estimates by Montgomery & Winget (1999) that the crystallization mass fraction is somewhere between 0% and 80%, depending on the physical parameters such as the total stellar mass (M_\star) and the H layer mass (M_H) (See Table 4.1 for the expected crystallization mass fraction for given M_\star and M_H using the models in Montgomery & Winget 1999). Our ℓ -identification of three pulsation modes does not provide enough data to uniquely determine M_\star or M_H , nor therefore, the crystallization mass fraction. The limb darkening method is useful in that it can identify the ℓ -value of a mode in a star with only one pulsation mode,

but unless that mode is conveniently placed, it does not help much with the asteroseismological analysis. We must not only identify modes in the star, but we must usually (an exception might be a low period, $k = 1$ mode, in a hot DAV) identify a large number of modes. Without a number of identified modes, asteroseismology is not very rewarding. Normally, with enough modes identified, asteroseismology could give us the best M_{\star} and M_{H} directly. But since the crystallization mass fraction affects the period spacing of the modes similar to the way M_{\star} and M_{H} also do, the situation is more complicated. To improve our crystallization estimate, we need to increase the number of pulsation modes observed and identified, then do a more systematic comparison between the models and observations, since the number of parameters the models depend upon is quite large.

It would be great if we could get the HST and the WET to observe BPM37093 repeatedly every year to detect more pulsation modes and identify them, but, alas, this is not realistic. We can certainly increase the number of observed modes by observing from the ground, since the star appears to change its pulsation modes from year to year. The increased number of modes might eventually allow us to identify the modes by the period distribution method. Since the crystallization mass fraction depends strongly on many physical parameters of the star, we need a scheme to do a thorough multi-parameter fit to the observed periods. Travis Metcalfe at University of the Texas is developing a numerical method to do this — systematizing what was before a fairly subjective process. With more modes, and his algorithm, we hope to get tighter constraints on BPM37093's crystallization mass fraction.

The fact that no $\ell = 3$ mode was observed in BPM37093 also has an

important implication. White dwarf stars are observed to pulsate only in a narrow range of temperatures called the instability strip. The low temperature limit where we see the white dwarf stars pulsate is called the “red edge”, while the hot end is called the “blue edge”. People have often wondered if this was a true effect or simply an observational artifact (Winget 1981; Dolez & Vauclair 081; Dziembowski & Koester 1981). One way the red edge could be an artifact is if the pulsation energy goes into higher order ($\ell = 3$ and higher) modes as the pulsators approach the red edge of the instability strip. They may then have undetectable optical amplitudes due to the geometric cancellations effects described by Dziembowski (1977). But as we saw from the models, $\ell = 3$ modes can have much higher amplitudes in the UV compared to the optical and if they existed, they would have been easily detected in our data². BPM37093 is close to the observed red edge³ and has no identified $\ell = 3$ modes. Our observations, therefore, are one example that pulsation energy may not necessarily go into higher order modes, and the red edge is a true physical phenomenon, rather than just an observational selection effect.

4.1.3 Mode Identification Methods

We have noted that the period distribution method of mode identification is only as good as the number of modes we detect. If we cannot measure the period spacing and the fine structure splitting caused by stellar rotation, it is

²Recent work by Ising & Koester (2000) suggest that when nonlinear effects are taken into account, the $\ell = 3$ amplitude ratios might not have as strong a wavelength dependence as we see in Figure 4.2. This discussion assumes that the nonlinear effects are not important. Unfortunately, they have not calculated any models we can use to compare with our BPM37093 observations.

³The “edges” of the instability strip are mass dependent. For its mass, BPM37093’s effective temperature places it close to its red edge.

M_{\star}/M_{\odot}	$T_{\text{eff}}(\text{k})$	$\log M_{\text{H}}/M_{\star}$	Crystallization mass fraction %
1.05	11800	-5	0 – 80
1.05	11800	≤ -6	0
1.10	11800	-5	40 – 80
1.10	11800	≤ -7	0

Table 4.1: Estimated crystallization mass fraction and various physical parameters. The models which give these estimates come from Montgomery & Winget (1999). The observed average period spacing is 16 – 18s. Two different stellar mass models are listed here because there are two different spectroscopic mass estimates, Koester & Allard’s (1999) $1.03 \pm 0.08 M_{\odot}$ with $T_{\text{eff}} = 11520 \pm 110\text{K}$ and Bergeron et al.’s (1995) $1.09 \pm 0.05 M_{\odot}$ with $T_{\text{eff}} = 11730 \pm 740\text{K}$. For thin H layer models, the crystallization mass fraction is 0% while for thick H layer mass models, the core could be substantially crystallized.

very difficult to identify the modes. For stars with hundreds of observed modes, such as GD358 and PG1159–035, the period distribution method is a powerful method, but for stars without dozens of observed modes as most DAVs, it simply does not work. The limb darkening method can work for stars with a small number of pulsation modes because it relies on the wavelength dependence of each mode’s amplitudes rather than on the number of observed modes. It can therefore even identify the ℓ for a star with only a single pulsation mode. To successfully identify modes with this method, we must simultaneously measure the amplitudes of the modes very accurately in both the optical and the UV, or amplitudes in any two significantly different wavelengths. Therefore, if there are changes in pulsation amplitudes on time scales of hours or days, mode identification using the limb darkening method becomes very difficult to apply successfully. We must also have accurate models atmosphere for this method to work; if there are problems with the models, there may well be problems with the resulting identifications.

If the data and model spectra do not match well, there could be systematic could between the observed and predicted amplitude ratios. Even when the model spectrum fits the time averaged spectra, if the model does not accurately predict the local flux derivatives with respect to temperature at the wavelengths of interest (e.g. our models currently ignore the pulsations' effects on limb darkening and this can affect the local flux derivatives), the predicted amplitude ratios will not reproduce the observed ones. We think this latter requirement, along with possible errors in the HST STIS calibrations are possible explanations why the models we used were able to reproduce BPM37093's observed amplitude ratios qualitatively, but not quantitatively. The models must be able to describe the observations adequately. Without accurate model calculations, we cannot assign ℓ values. We need to further understand the observed discrepancies between our observations and the models so we can identify the ℓ modes definitively. Until then, at least for the cool DAVs, it is not clear that even with accurate UV and optical amplitudes, the current models are up to the task of applying the limb darkening method.

The limb darkening method currently is a sensitive way to a search for $\ell = 3$ modes in pulsating white dwarf stars, since $\ell = 3$ modes are expected to have much higher amplitudes in the UV relative to the optical compared to the $\ell = 1$ and 2 modes (see Figure 4.1 for an example of an amplitude ratio calculation for a DB model and Figure 4.2 for a DA model). The model differences between an $\ell = 3$ mode and $\ell = 1$ or $\ell = 2$ modes is also much greater than that between $\ell = 1$ and $\ell = 2$ modes and small inaccuracies in the models will not matter as much. We must caution that if results from Ising & Koester (2000) are applicable to all white dwarf pulsators, then it will be more

difficult to distinguish $\ell = 3$ from $\ell = 1$ and 2 (see earlier footnote on their work and Ising & Koester [2000]).

If a white dwarf pulsator's amplitudes remain stable for the duration of the observations (usually a couple of weeks), the combination of a ground-based optical campaign like the WET along with UV data from the HST⁴ can be the best way to successfully unlock the structure of the star. The limb darkening method requires amplitude measurements in both the UV and the optical⁵ and relies on the ground based data to measure accurate periods of the modes. The period distribution method can succeed (if the stars show the right combination of observable modes) with just WET data. The star's mode amplitudes must be stable for the duration of the observations (about a couple of weeks). Otherwise, the uncertainties in the observed amplitude ratios will become larger than the differences between the theoretical amplitude ratios of $\ell = 1$ and $\ell = 2$, hence making it impossible to determine the ℓ values conclusively. Combined WET and HST observations will naturally provide data necessary for both the period distribution and the limb darkening methods, thereby increasing the chances of identifying the modes and finding out the star's internal structure, regardless of how many modes we observe in the star. However, here, we were not able to conclusively prove that the two mode identification methods are consistent. Before we get more data to apply the limb darkening method, we should wait for the results of the May–June 2000 WET and HST simultaneous observations

⁴Currently, the only instrument capable of taking the UV data necessary to apply the limb darkening method is the HST.

⁵Amplitudes in any two well separated wavelengths will do for the limb darkening method, but because of very little flux in the IR, easy to arrange a continuous observation of pulsating white dwarf stars in the optical make using the UV and the optical to be the best choice for this method at this time.

for (hopefully) conclusive results.

4.1.4 Does the Limb Darkening Method Work?

Comparing our work and work done by others discussed in Section 2.1 gives us some insights as to the usability of the limb darkening method.

Discrepancies between models and observed spectrum

There are evidences suggesting our models are inaccurate. BPM37093's time averaged spectrum does not agree well with *any* of our current model spectrum. G29–38 Keck time series and time averaged spectra, both in the continuum and in the absorption lines, also showed discrepancies between observation and models.

Discrepancies between models and observed chromatic amplitudes

The observed chromatic amplitudes (in the rage of 6000\AA to 3800\AA) of the pulsation modes in G29–38 were steeper than the theoretical curves. We observed similar behavior in our GD358 data (Figure 2.52). The 423s mode's chromatic amplitude curve is steeper than either that of the $\ell = 1$ or $\ell = 2$ model curves. This is why the long wavelength range is a better fit with the $\ell = 1$ model while the short wavelength range is a better fit with the $\ell = 2$ model for the 423s mode. This was not the only reason our mode identification was indecisive, but it is interesting to note that a similar trend has been observed in at least one other star.

Ising & Koester (2000) found that including the effects of the pulsations on limb darkening resulted in large changes to some of the theoretical chromatic amplitude curves. Since we currently do not incorporate this effect in our models, we must apply their work in the future to the models used to compare

with the BPM37093 data to see if it can explain the discrepancies between the models and our observed amplitude ratios.

The limb darkening method requires that the models provide a good fit consistently across a broad wavelength region. But it has been shown to be quite difficult to fit the observed spectrum, both the continuum and the absorption lines, over such a large wavelength range with a single model (e.g. Provencal et al. [1996] derived an effective temperature of $27000 \pm 1000\text{K}$ for GD358 from UV spectroscopy while Beauchamp et al. [1999] used optical spectra to obtain a temperature of 24700K with a pure He atmosphere model and 24900K from an He atmosphere model with a trace amount hydrogen⁶). It will be important to solve this problem if we are to apply the limb darkening method to many more pulsators. Although I am not an expert on stellar atmosphere models, my impression is that the mixing length prescription of describing convection is perhaps the key to solving this problem. Every time new observations are made, new tweaks are made to the mixing length description to accommodate them. There is clearly something lacking in this process. Since we are now not only looking at the average spectra, but using the temperature derivatives of the spectra when we apply the limb darkening method, perhaps we need a better way to describe the convection zone than the multiply-tweaked mixing length theory. I believe we are hitting the limit of what we can achieve by using mixing length theory to describe convection.

According to Ising & Koester's (2000) work which is based on the work by Goldreich & Wu (1999) and Brickhill (1991), the convection zone is re-

⁶The amount of H included in the models are below the current detection limit.

sponsible for modulating the flux that comes from the layer beneath and then releasing it to the stellar surface, causing the white dwarf stars to pulsate. If nonlinear effects are the causes of the mismatch between the observed and theoretical chromatic amplitudes and in the chromatic phase shifts, by observing which modes in a given star are subject to nonlinear effects, we have a new opportunity to learn more about the processes in the convection zone. These processes may help us develop a better convection zone model.

Phase shifts

Phase differences between the optical and the UV (as well as within the optical in the case of the Keck data) were observed for two cool DAVs whose chromatic amplitudes were not adequately described by the models. Kepler et al. (2000) saw phase shifts in four modes in G185–32, but the other four observed modes did not show any phase shifts. They were able to identify ℓ -values for the modes with phase shifts without any problems. There is currently no explanation for these observed phase shifts.

CvKW also saw phase shifts in their data with the blue photons arriving earlier than the red photons. The phase shifts we observed in the BPM37093 data were different from mode to mode, but the phase shifts in G29–38 all had the same trend – the shorter wavelength photons arrived earlier. The models currently cannot reproduce these puzzling observations, but perhaps these phase shifts are indicators that nonlinear and/or nonadiabatic effects are in fact important for G29–38, and perhaps for the massive BPM37093 as well.

Could it be possible that the unexplained phase differences between the UV and the optical (Figure 3.24) observed for BPM37093 and the phase

shift observed in the optical continuum in G29–38 are indications that some nonlinear effects are indeed important? Since Kepler et al. (2000) were able to identify modes in other stars which had UV and optical phase shifts similar in size to those which we observed in BPM37093, whatever is causing the phase shifts does not necessarily affect the chromatic amplitudes as well. We must find out what causes the phase shifts and relate them to the observed discrepancies between the models and observations before we can always rely on the limb darkening method to identify ℓ -values in white dwarf stars.

New way to apply the limb darkening method

The limb darkening method can now be applied in a few different ways. One way is to use chromatic amplitudes by comparing pulsation amplitudes in the UV and optical data as we did in this work. We can also obtain high signal to noise, purely optical, time series spectra as we saw in CvKW. CvKW also found another diagnostic for determining ℓ values; the ratio of the observed velocity and flux amplitudes. Unfortunately, the linear adiabatic models have not been successful in describing all the observations so far, but hopefully these new state-of-the-art observations will spur the development of newer, better, models.

4.1.5 Asteroseismology with the limb darkening method

Although the limb darkening method seems to work for some stars, it still needs to be checked if it gives the same mode identifications as does the period spacing method before we can have confidence in the results we obtain from it. The fact that the models do not quantitatively agree with the observations for both the G29–38 and BPM37093 observations is quite troublesome. Are the

discrepancies only observed in cool DAV stars? Will any of the DBVs show such problems? Before we can fully rely on the limb darkening method, we must first confirm that it gives identical results with the period distribution method and we also must understand the cause of the mismatch between the observed and model chromatic amplitudes, as well as the chromatic phase shifts.

If a pulsator has many simultaneously excited pulsations and the accompanying fine structure splitting due to rotation as we saw in GD358 (Winget et al. 1994) that goes with it, we can use the period distribution method to identify the modes. For pulsators that have only small numbers of modes, or are without tell-tale structure of rotational splitting, the limb darkening method will be a powerful way to identify the modes. Having more than one method that are each independent of each other could prove immensely valuable. As an example, we saw in the BPM37093 observations that the period distribution method suggested most, if not all, the observed modes are $\ell = 2$. The limb darkening method agreed with the period distribution method and added information that there were both $\ell = 2$ (633s mode) and $\ell = 1$ (531s and 512s modes) present. Hopefully the BPM37093 observations and the G29–38 observations can help the theorists explain the causes of the problems and improve the models so that we can rely on the limb darkening method. Then the limb darkening method will be a very powerful tool for asteroseismology and will help us understand many more white dwarf pulsators' internal structure than the period distribution method alone.

4.2 The New Simultaneous HST & WET Observations of GD358 in May–June, 2000

Although we could not find out conclusively if the limb darkening method and the period distribution method are consistent in GD358, we expect to find a definitive answer very soon.

To identify the ℓ value of a mode, the size of the uncertainties for the amplitude ratios must be smaller than the difference between the expected $\ell = 1$ and $\ell = 2$ curves seen, for example, in Figures 4.1 and 4.2. Because of GD358's severe amplitude changes during our 1996 observations and our lack of truly simultaneous ground based observations, our data were not accurate enough for the task. We observed GD358 again with both the WET and the HST in May – June, 2000. The HST observed for 10 orbits this time which reduced the uncertainties of the UV amplitude determinations compared to those we present here with only 7 orbits. To show that we can achieve our goal of identifying the ℓ values of the modes, we estimated the size of the uncertainties expected for the amplitude ratios from these observations. δr , the uncertainty of the amplitude ratio $r(= A_{UV}/A_{opt})$ where A_{UV} and A_{opt} are the pulsation amplitudes in the UV and the optical respectively, can be expressed as:

$$\delta r = \frac{1}{A_{opt}^2} (A_{opt}^2 \delta A_{UV}^2 + A_{UV}^2 \delta A_{opt}^2)^{1/2} \quad (4.1)$$

where δA_{UV} is the uncertainty of the UV amplitude and δA_{opt} is the uncertainty of the optical amplitude. For the 770s mode of GD358 which is usually the most dominant mode, we estimate $A_{opt} = 20\text{mma}$ (Winget et al. 1994) and although Winget et al. do not list the uncertainties in their amplitude estimates, we can

estimate the 770s mode's uncertainty from our least squares fit of 2 weeks of optical data on GD358 in August 1996 to be $\delta A_{opt} = 0.56\text{mma}$. We estimate $\delta A_{UV} = 3.5\text{mma}$ from the 7-orbit HST observations of BPM37093 using the same instrumental setup as the upcoming GD358 HST observations. If the 770s mode's UV amplitude scales as expected from the theoretical calculations (Figure 4.1), then we expect $A_{UV} = 50\text{mma}$ at 1200\AA for $\ell = 1$. This results in $\delta r = 0.18$. Similarly, assuming that 770s mode's amplitude scales like the theoretical $\ell = 2$ mode, then $\delta r = 0.19$. These δr values are smaller than the differences between the theoretical $\ell = 1$ and $\ell = 2$ amplitude ratios, which is 0.4 at 1200\AA as seen in Figure 4.1, but only by a factor of two. We would need about three more orbits (for a total of 13) for a 3σ detection. The numbers we used are conservative because we expect both the optical and the UV amplitudes' uncertainties to be smaller due to the larger amount of data we gathered during these observations. This increased accuracy should make our results much better than estimated here, perhaps enabling a 3σ detection. We had the WET observing with a total of thirteen observatories instead of the three sites we had in August, 1996 and we had 10 HST orbits instead of the 7 we had for BPM37093, thereby enabling us to gather more data in both wavelength ranges.

We did a similar calculation for the originally planned 16-orbit HST observations of BPM37093. We found that $\delta r = 2.4$ assuming $A_{opt} = 1\text{mma}$, $A_{UV} = 6.2 \times A_{opt}$ (scaling with the theoretical $\ell = 1$ calculations at 1500\AA), $\delta A_{opt} = 0.1\text{mma}$ (the uncertainty achieved with the 2-day lightcurve during the 1999 WET run on BPM37093) and $\delta A_{UV} = 2.3$ [which we obtained by scaling δA_{UV} proportional to $1/(\text{number} - \text{of} - \text{orbits})^{1/2}$]. This δr is not good

Detection Level	Number of Orbits	δA_{opt}	Comments
1 σ	42	0.1	δA_{opt} from 2-day lightcurves
2 σ	330	0.1	δA_{opt} from 2-day lightcurves
1 σ	35	0.038	δA_{opt} from 14-day lightcurves
2 σ	148	0.038	δA_{opt} from 14-day lightcurves
1 σ	34	0.0	“perfect” optical data ($\delta A_{opt}=0$)
2 σ	77	0.0	“perfect” optical data ($\delta A_{opt}=0$)

Table 4.2: Assuming that the UV amplitude for BPM37093 scales from the optical amplitude (1mma) as theoretical calculations predict (Figure 4.2), we estimated the number of orbits necessary to achieve 1 and 2σ detection of a pulsation mode being $\ell = 1$ or 2 for three different cases of the optical uncertainties. It is evident that it will be unrealistic to achieve 2σ detection (it is impossible to get 77 orbits on the HST to observe one star), but a 1σ measurement is doable, though difficult.

enough. From the models, we need $\delta r < 1.6$ to distinguish between $\ell = 1$ and $\ell = 2$. Since BPM37093’s pulsation amplitudes are much smaller than GD358’s, it is harder to measure accurately the amplitudes and hence more difficult to identify the modes using the amplitude ratios. In order to identify (at a level of 1σ) the ℓ value of the observed modes, we would need to re-observe BPM37093 with its pulsation amplitudes stable for 42+ HST orbits. We would need 330 orbits for a 2σ detection! If we can reach an optical uncertainty $\delta A_{opt} = 0.038$ (achievable if the amplitudes are stable for the duration of a 14-day WET run), then we need 35 orbits to achieve a 1σ detection and 148 orbits for 2σ detection. If we use perfect optical data, $\delta A_{opt} = 0$, we would still need 34 orbits to obtain a 1σ detection and 77 orbits for a 2σ detection (see Table 4.2).

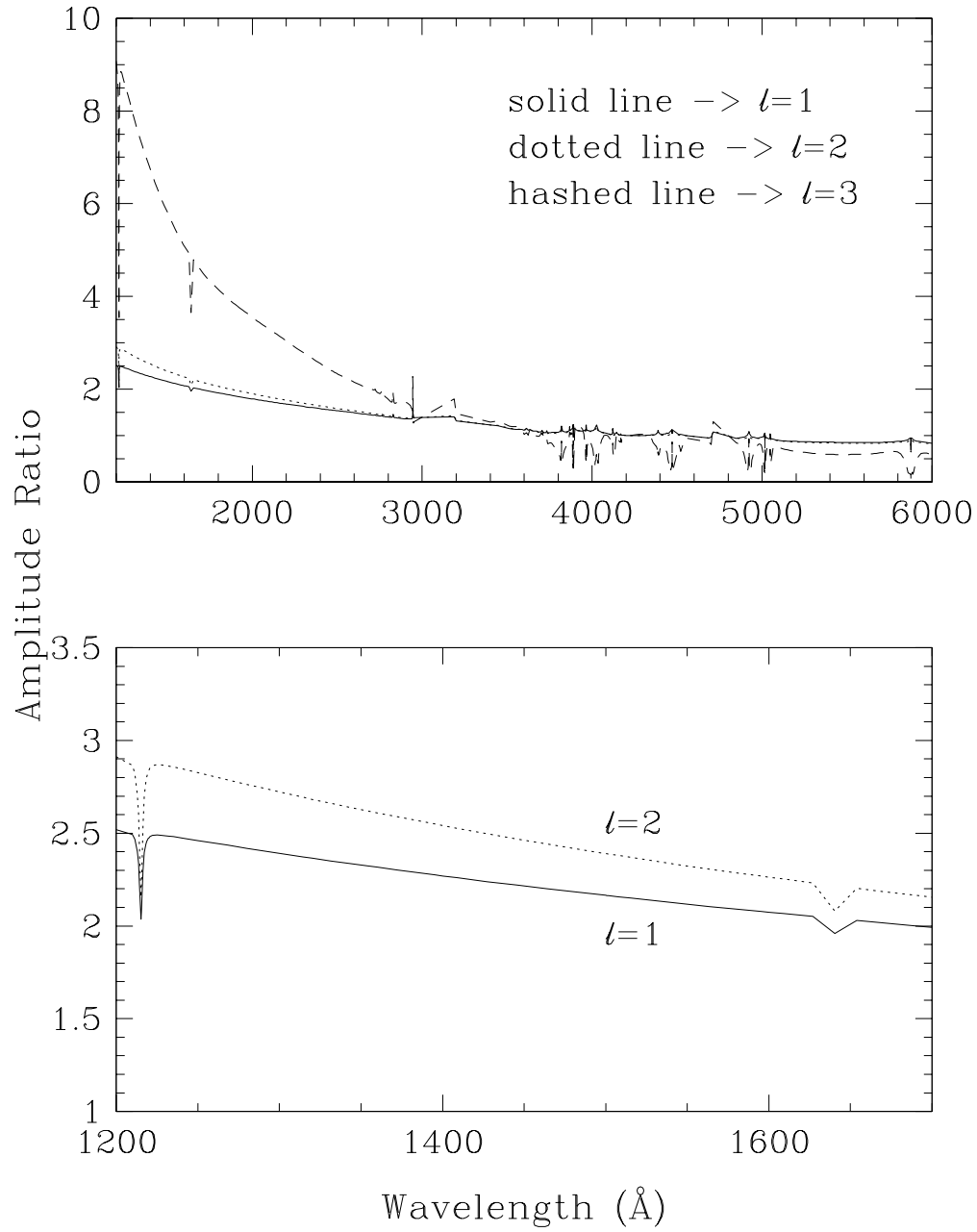


Figure 4.1: DB model calculations of the pulsation amplitude at each wavelength compared to that at 4200 Å. In order to distinguish between $\ell = 1$ and $\ell = 2$ using the wavelength dependences of the amplitude ratios, we must measure an amplitude ratio accurate significantly smaller than the differences between the $\ell = 1$ and $\ell = 2$ curves.

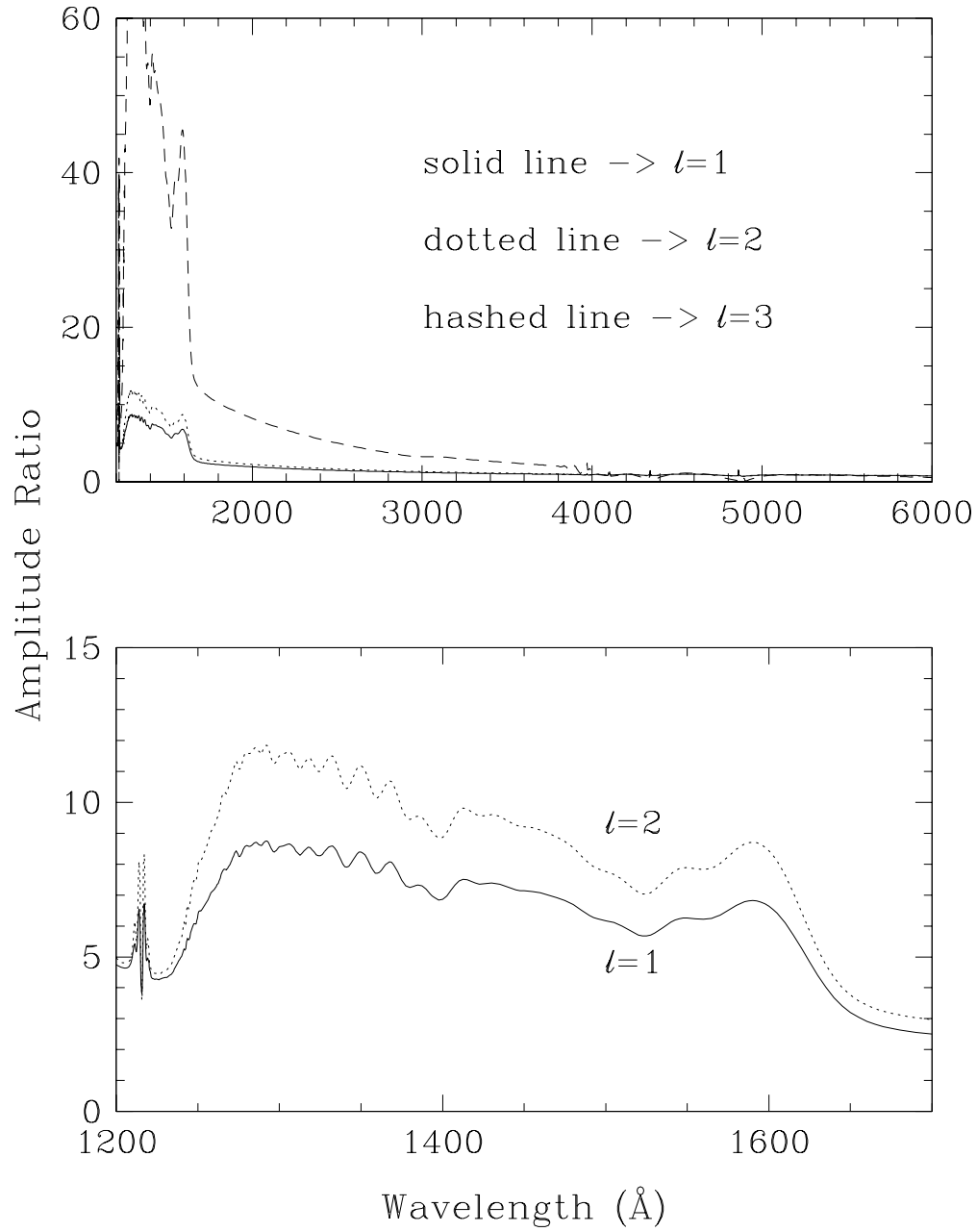


Figure 4.2: DA model calculations of the pulsation amplitude at each wavelength compared to that at 4200 Å. In order to distinguish between $\ell = 1$ and $\ell = 2$ using the wavelength dependences of the amplitude ratio, we must measure an amplitude ratio accurately significantly smaller than the differences between the $\ell = 1$ and $\ell = 2$ curves.

Appendix

Appendix A

Amplitude Changes in GD358

The amplitude changes we saw in the optical data in August 1996 are unprecedented in the observations of pulsating white dwarfs. No report has been made of such a large amplitude variation in such a short amount of time. Here we will describe what we found in our data.

A.1 Changes in the Dominant Mode

The lightcurves in the first and second panels of Figure A.1 look very different from each other. The Fourier transform of the lightcurve from the first panel is similar to that from the 1994 WET data where we identified over 100 individual pulsation modes, while the Fourier transform of the second panel is dominated by only a single periodicity (Figure A.2); this represents a complete change in the mode structure, as well as the period of the dominant mode, in about one day!

In the run an-0034, the 423s mode's amplitude is the highest we observed it. To check for additional pulsation power (perhaps lower amplitude pulsations dwarfed by the 423s mode power), we prewhitened the an-0034 lightcurve by the 423s mode. Prewhitening is to subtract a sinusoid with given amplitude, phase and period from the original lightcurve. The prewhitening

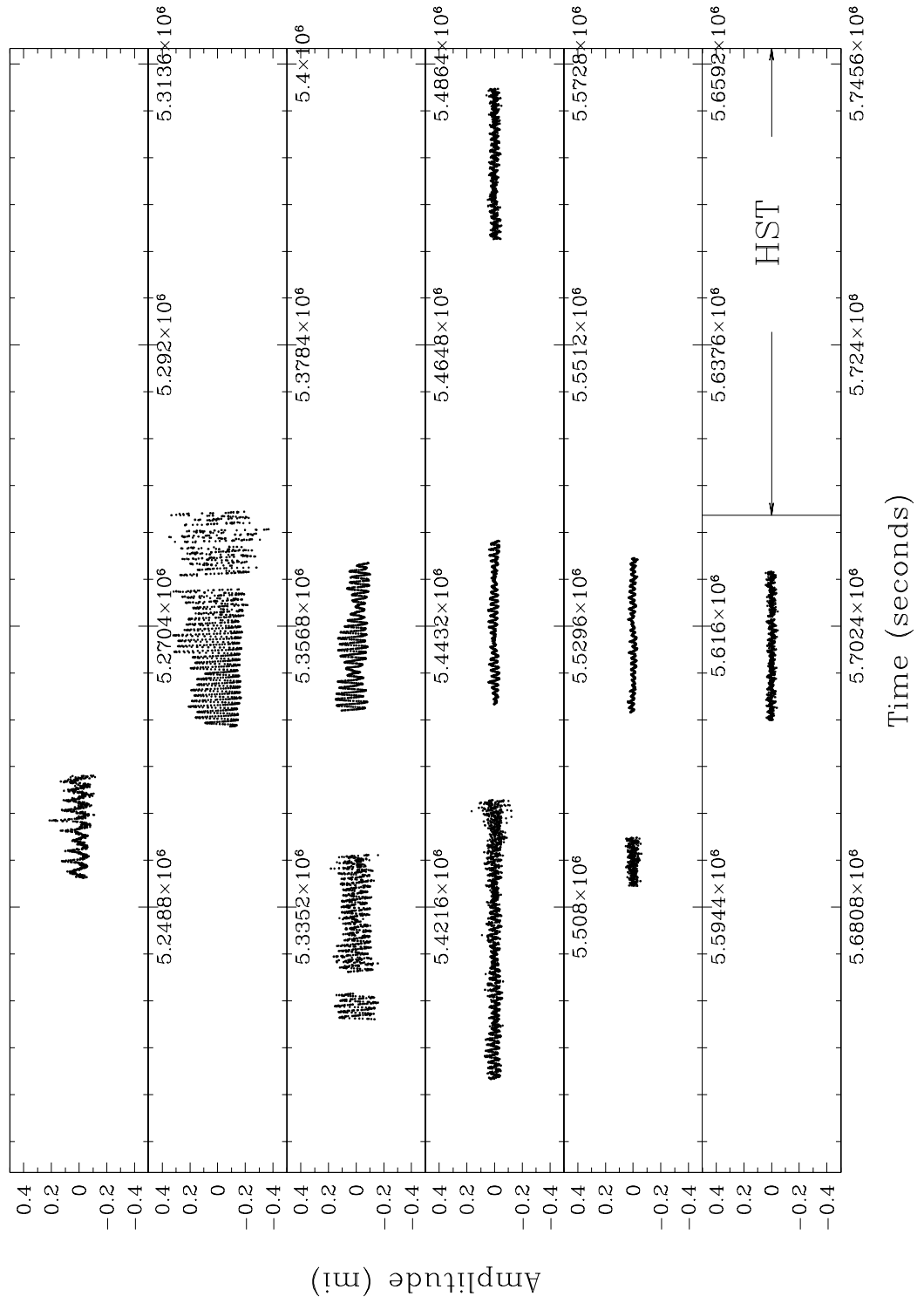


Figure A.1: First half of the ground-based optical lightcurve of GD358. Each panel is one day long.

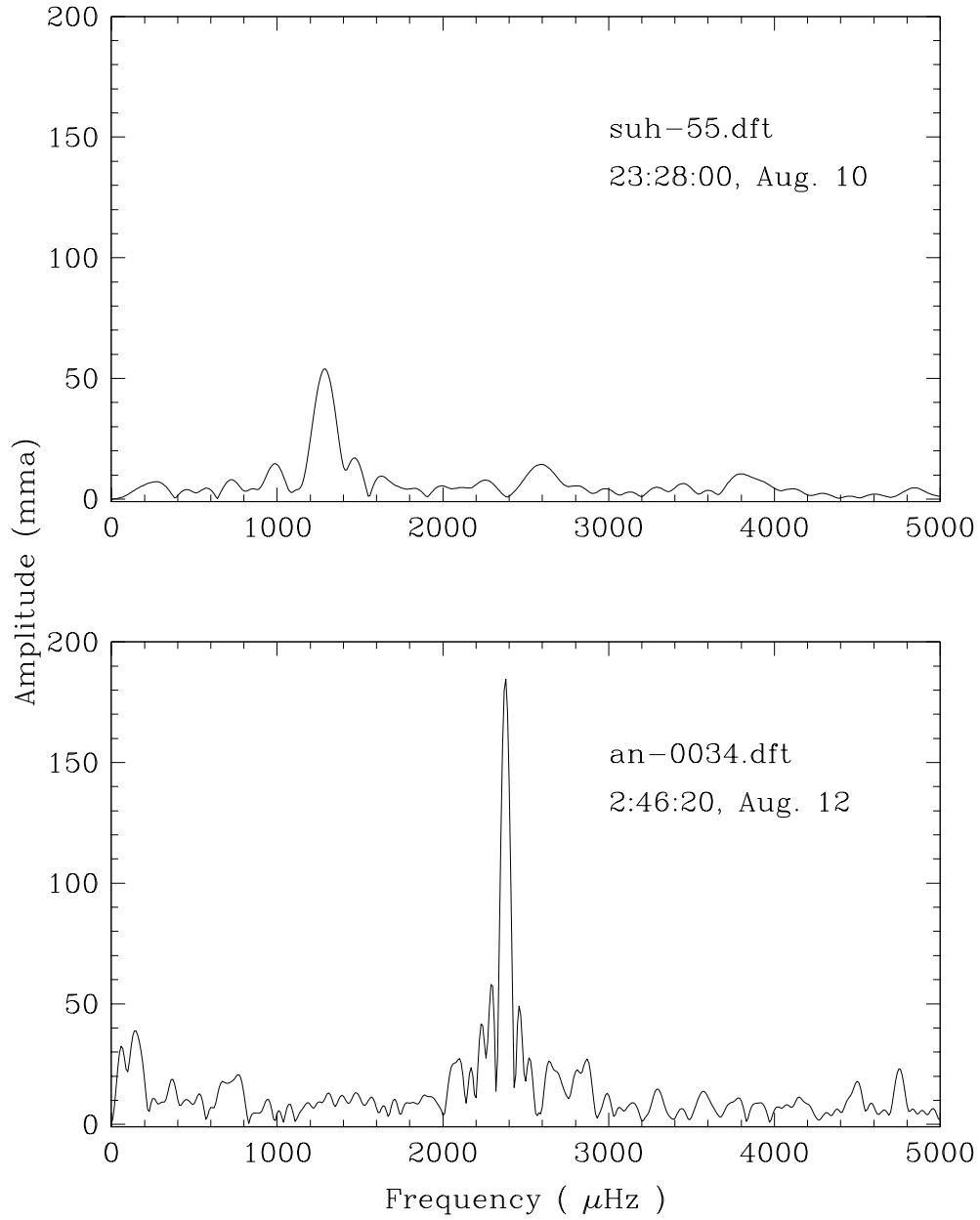


Figure A.2: Fourier transforms of GD358 observed one day apart. The top panel shows the Fourier transform of the data taken on the 1st day of the 3-site campaign (suh-55: taken in Poland with start time at 23:28:00 UT on August 10), and the bottom panel shows the data taken about one day later from McDonald (an-0034: taken with start time at 2:48:20 UT on August 12). The observed power has shifted completely and dramatically, both in frequency and amplitude.

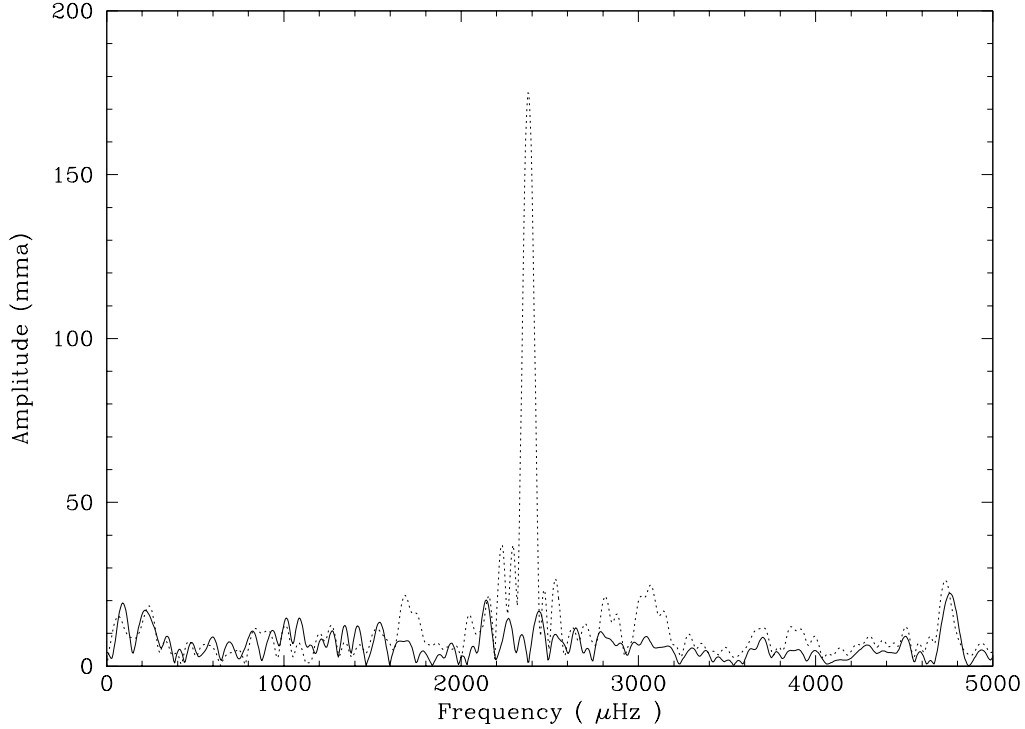


Figure A.3: Fourier transform of an-0034 before (dotted line) and after (solid line) it was prewhitened by the 423s mode. After prewhitening, there is little significant power left. The lightcurve was dominated by one mode, possible explanation for why the lightcurve looked so linear (sinusoidal) in Figure 2.33.

helps us look find smaller amplitude pulsations by eliminating the effect of the dominant pulsation mode. In Figure A.3, we show the Fourier transform of the an-0034 lightcurve both before and after the prewhitening. We see now that GD358 was indeed dominated entirely by a single mode at a different period from the dominant mode a day earlier.

A month after these observations (September, 1996) and in April of 1997, we obtained additional GD358 data. The September 1996 data were obtained by our French and Polish collaborators during a WET run on a different target, while the April 1997 data were obtained at McDonald Observatory by

us. The lightcurve and the power spectrum during these observations (Figure A.4) seem to have returned to the more or less normal state seen in the past (Figure 2.35 and similar to the first panel in Figure A.2) not the unusually high amplitude state it was in in August, 1996 (Figure A.2). Table A.1 shows the journal of observations for the September, 1996 and April, 1997 data.

We show the lightcurves of GD358 at three different times in Figure A.5. The middle panel shows the lightcurve when the amplitude of the 423s mode was at its largest. The lightcurve looks almost sinusoidal, reasonable since there was very little else but the single 423s mode in the power spectrum. The other two lightcurves, however, each containing several pulsation modes, are less sinusoidal. If the non-sinusoidal nature of a lightcurve comes from the fact that many modes are present simultaneously, then one would expect the shape of the lightcurve to be sinusoidal only when it is pulsating in a single mode. On the other hand, in the August 1996 sinusoidal lightcurve, the peak-to-peak light variation was about 30% of the star's average light in the optical. Such a large light variation is expected to introduce nonlinear effects into its lightcurve, even if the star is pulsating in a single mode, and causing the lightcurve to look nonsinusoidal. Thus, the nearly sinusoidal shape of our lightcurves (Figure A.5) is somewhat of a mystery.

After the 423s mode reached the highest amplitude run an-0034 data, the 464s mode started to grow and the 423s became smaller, but there was still very little sign of the usually dominant 770s mode (Figure 2.36 and 2.37). In the September 1997 data, the Fourier transform shows that GD358 is pulsating in periods close to what we are familiar with from the WET data, but the highest amplitude mode is the 810s mode ($k = 18$ according to Winget et al. 1994)

Telescope	Run	Date (UT)	Time(UT)	Length (s)
PdM 2m	gv-0480	1996 Sep 10	20:29:01	5670
Suhora 60cm	suh-62	1996 Sep 11	18:11:00	10790
PdM 2m	gv-0484	1996 Sep 14	21:22:02	2330
Suhora 60cm	suh-63	1996 Sep 18	18:45:00	15860
Suhora 60cm	suh-65	1996 Sep 19	18:06:20	13380
McD 2.1m	an-0061	1997 Apr 1	06:54:20	415
McD 2.1m	an-0066	1997 Apr 7	06:52:50	1763

Table A.1: Journal of Observation for September, 1996 and April, 1997. September, 1996 data were taken by our Whole Earth Telescope collaborators during a WET run whose target was not GD358. PdM stands for Pic du Midi in France, and Suhora is for Mt. Suhora in Poland. The 1997 data were all taken at McDonald Observatory in Texas.

and not the usual 770s mode (Figure A.4). It is not until the data taken in April 1997 when we observe the 770s mode as the highest amplitude mode in the Fourier transform. It is unfortunate that we do not have more data to fill in the gap between September, 1996 and April, 1997 to see how the amplitude changed. The time scale which it took the star to change from its normal multi-mode state to a single mode pulsator was very short, about one day. All we can do for the reverse transition, however, is set a lower limit of about one month. We wish we could explain what all these changes in pulsation amplitudes and the shape of the lightcurves. We have many theorists, but no theory to describe such changes at this time.

A.2 Amplitude Estimates of the 423s Mode During the HST Observation

Figure A.6 shows how the amplitude of the 423s mode changed with time during our optical observations. The line in this figure is a spline fit to the

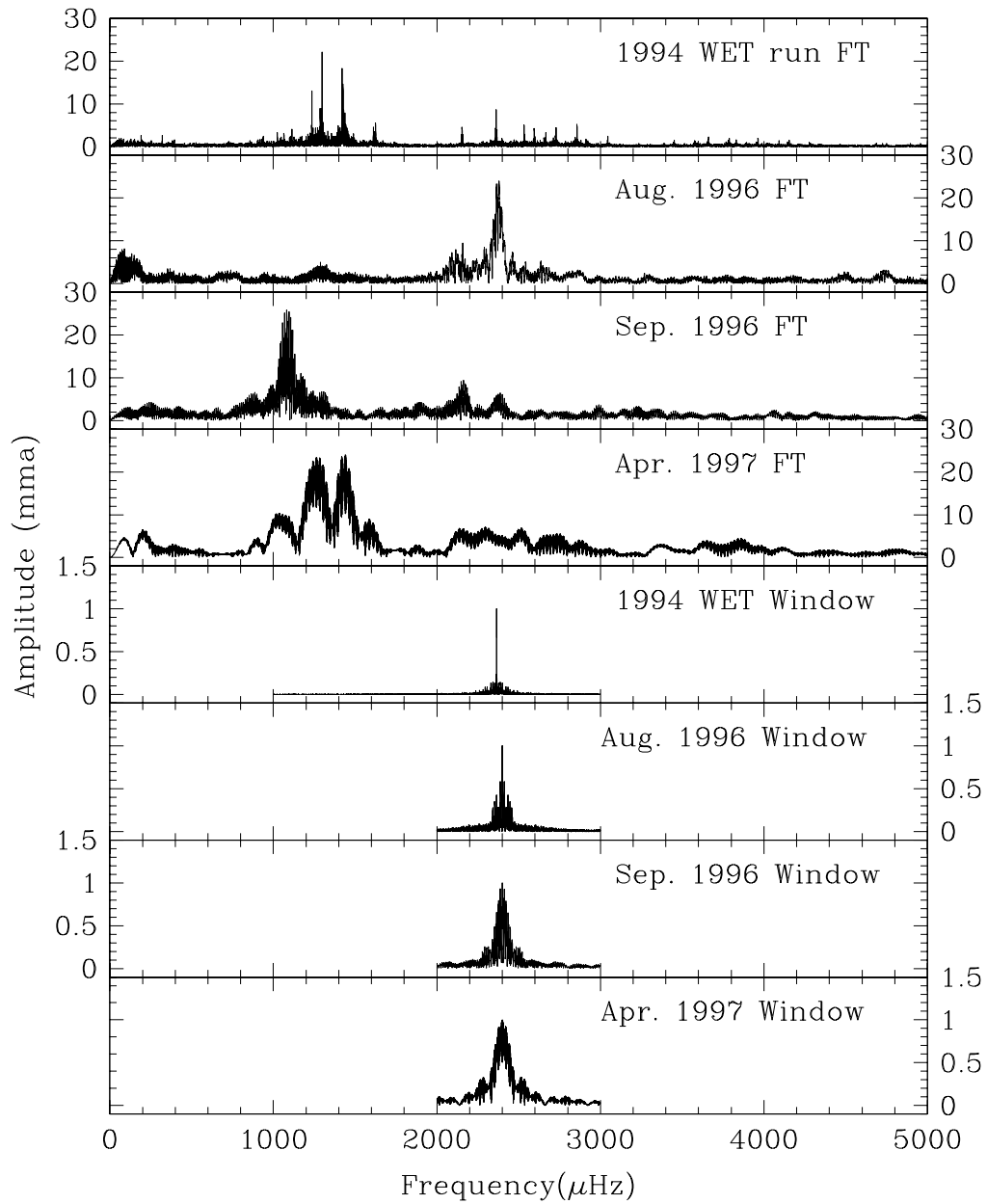


Figure A.4: GD358 Fourier transform at four different times along with their spectral windows. The 1994 and 1997 Fourier transforms look similar (within the observed frequency resolution, that is). The September 1996 data look similar as well to these two data sets, but the highest amplitude modes have shorter frequencies (longer period). Obviously, the August 1996 Fourier transform looks very different from the other Fourier transforms.

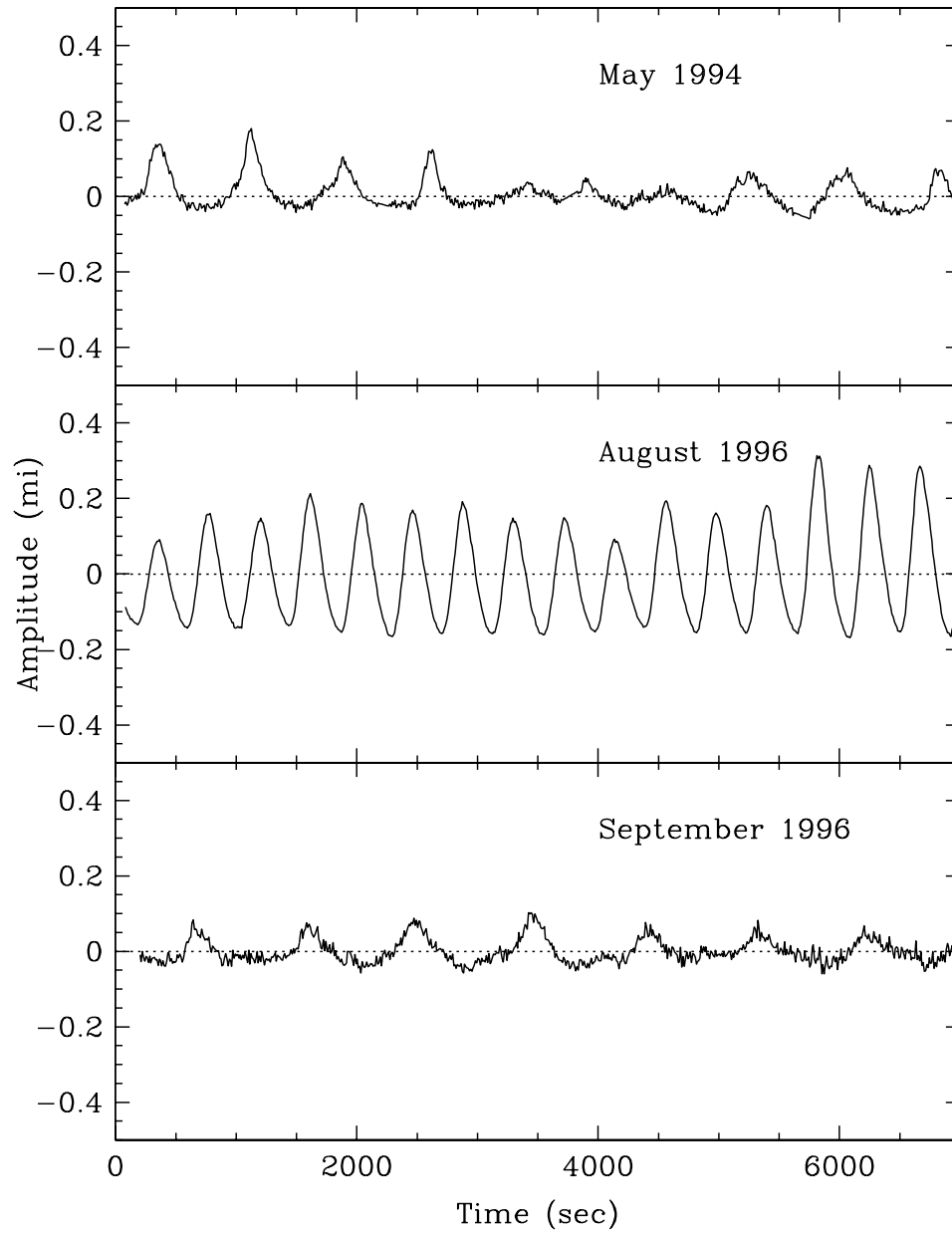


Figure A.5: GD358 lightcurves over time. The shape of the lightcurve was sinusoidal when the amplitude was highest. The 1994 and September 1996 data exhibit similar pulse shapes and their corresponding power spectra also look similar (Figure A.4).

data. Obviously, it would be very difficult to accurately determine the mode's amplitude during the time of the HST observations using these data. Figure A.7 shows the results of using various trials assumptions to determine the 423s mode UV/optical amplitude ratios. The triangles represent using the whole August 1996 optical data to determine the optical amplitude, simply using the amplitude in the Fourier transform of the entire data set. Because of the high amplitude observed on August 12, we ended up overestimating the optical amplitude during the HST observations and the UV to optical amplitude ratios are an underestimate. The solid and hollow squares show the results from using the optical amplitude determined by the spline fit at the beginning and the end of the HST observations, respectively. These values should give us a range of possible amplitude ratios if the spline fit to the measured amplitudes is an accurate description of what happened. The solid squares look as if they might favor $\ell = 3$ while the hollow squares match no theoretical models.

We used only the HST UV data (not the zeroth order data) to obtain the amplitude ratios represented by the solid circles. We took the ratios of the UV amplitudes to the reddest (2486Å) UV amplitude. This procedure, in effect, first normalizes the amplitudes at 2486Å. We then renormalized the curve by the model $\ell = 1$ amplitude ratio at 2486Å and multiplied the entire curve by this amount. The good agreement between the $\ell = 1$ model and the reddest solid circle, then is artificial and is a result of how we normalized the data. Although we could have calculated the model amplitude ratios normalized at 2486Å to compare with the observed amplitude ratios, we wanted to see all the amplitude ratios in the same figure so that we can easily compare them. The result, of course, is that no believable ℓ -identification can be made with

these methods. If the spline fit is a reasonable approximation to the optical amplitude, $\ell = 3$ might be the best assignment, but we excluded $\ell = 3$ based on the amplitude ratios using the UV and the zeroth order data. The $\ell = 1/\ell = 2$ argument using the UV data alone is artificial and cannot be used to conclude anything. It is interesting, however, to see the familiar $\ell = 2$ match in the blue and $\ell = 1$ in the red, as we saw earlier in Figure 2.51.

From Figure A.6, we clearly can see how the amplitude ratios are dependent on our choice of what amplitude we compare the UV amplitude with. This again illustrates how important it is to get accurate measurements of the optical amplitudes in order to apply the limb darkening method. We will attempt to do this again with the simultaneous HST and WET observations obtained in May/June 2000.

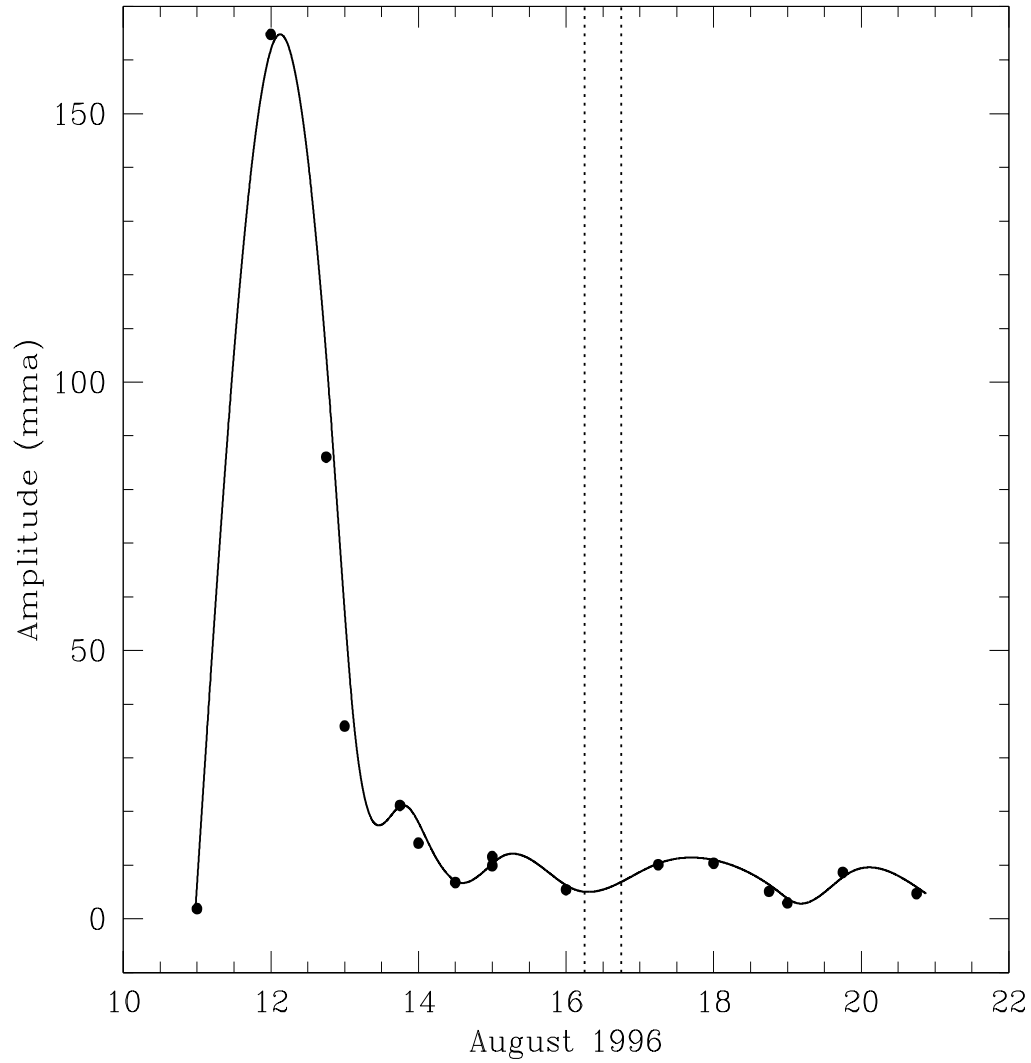


Figure A.6: The amplitude modulation of G358 423s mode observed in the optical in August, 1996. The timescale of this change is surprisingly short. We have never observed such a fast amplitude modulation in any of the pulsating white dwarfs. The dotted lines represent the time interval in which we took our HST UV data.

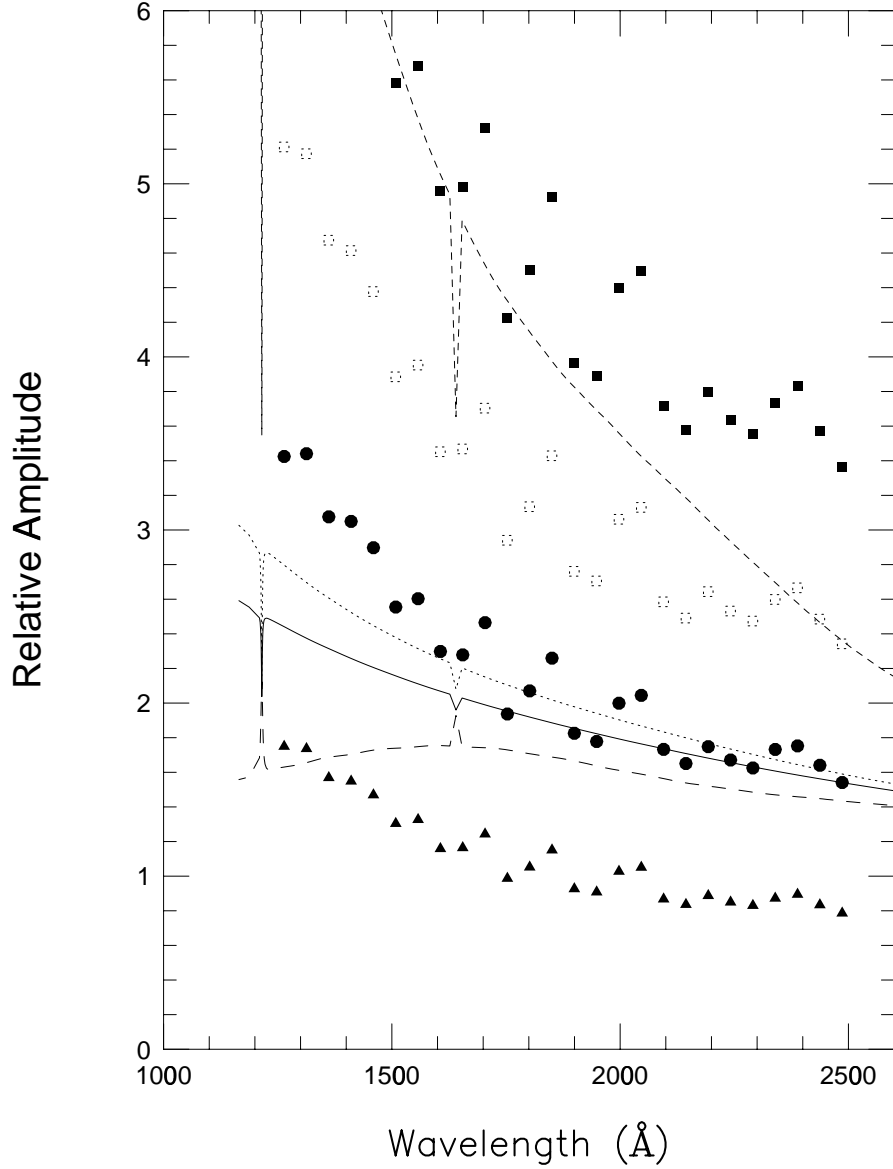


Figure A.7: The 423s mode amplitude ratio using different normalizations. The lines are Koester's DB model with $T_{\text{eff}} = 25000\text{K}$ and $\log g = 8.0$ normalized at 5500\AA . The solid line is $\ell = 1$, the dotted line is $\ell = 2$, the short dashed line is $\ell = 3$, and the long dashed line is $\ell = 4$. The solid circles used the reddest UV amplitude to compare with the other UV amplitudes. It was forced to have the reddest circle match the theoretical $\ell = 1$ curve. The triangles used the whole August 1996 optical data to estimate the optical amplitude assuming the amplitude was constant during the observation. The solid and hollow squares estimated the optical amplitude with a spline fit at the beginning and the end of the HST observations, respectively.

Bibliography

- [1] Abrisokov, A. 1961, Soviet Phys.–JETP, 12, 1254
- [2] Allard, N., & Koester, D. 1992, A&A, 258, 464
- [3] Beauchamp, A., 1996, in Hydrogen Deficient Stars, Astron. Soc. of Pacific Conf. Series, ed. Jefferys & Heber, 96, 295
- [4] Bergeron, P. et al. 1995, ApJ, 258, 449
- [5] Bradley, P.A. 1993 Phd Thesis, University of Texas at Austin
- [6] Bradley, P.A. & Winget, D.E. 1994, 430, 850
- [7] Bradley, P.A. 1996, ApJ, 468, 350
- [8] Bragaglia, A., Renzini, A., & Bergeron, P. 1995, ApJ, 443 735
- [9] Brickhill, A.J. 1991, MNRAS, 251, 673
- [10] Clemens, J.C., van Kerkwijk, M.H., & Wu, Y. 2000, MNRAS, 314, 220
- [11] Dolez, N. & Vauclair, G. 1981, A&A, 102, 375
- [12] Dowes, R. 2000, private communication
- [13] Dziembowski, W. 1977, Acta Astron., 27, 203
- [14] Dziembowski, W. & Koester, D. 1981, A&A, 97, 16

- [15] Eracleous, M. & Horne, K. 1996, ApJ, 471, 427
- [16] Finley, D.S., Koester, D., & Barsi, G. 1997, ApJ, 488, 375
- [17] Fontain, G., Brassard, P., Bergeron, P. & Wesemael, F., 1996, 469, 320
- [18] Goldreich, P. & Wu, Y. 1999, ApJ, 511, 904
- [19] Harrington, R.S., et al. 1985, AJ, 90, 123
- [20] Ising & Koester, D. 2000, 12th European Workshop on White Dwarf Stars,
in press
- [21] Kucher, M.J., Koresko, D. & Brown, M.E. 1998, ApJ, 508, L81
- [22] Jefferies, R.D. 1997, MNRAS, 288, 585
- [23] Kanaan, A. et al. 1992, ApJ, 390, L89
- [24] Kanaan, A. 1996, PhD Thesis, University of Texas at Austin
- [25] Kanaan, A. 1999, Balt. Astron., 8, 87
- [26] Kawaler, S.D., & Bradley, P.A. 1994, ApJ, 415, 428
- [27] Koester, D., et al. 1998, A&A, 338, 612
- [28] Kepler, S.O., Robinson, E.L., & Nather, R.E. 1983, ApJ, 271, 744
- [29] Kepler, S.O. 1984, PhD Thesis, University of Texas at Austin
- [30] Kepler, S.O. 1984, ApJ, 278, 754
- [31] Kepler, S.O., Robinson, E.L., & Nather, R.E. 1995, Balt. Astr., 4, 302

- [32] Kepler, S.O. & Bradley, P.A., 1995, *Balt. Astr.*, 4, 166
- [33] Kepler, S.O. 1997, *Proceeding of "A Half Century of Stellar Pulsation Interpretation"*. (eds) P.A. Bradley & J.A. Guzik, 140
- [34] Kepler, S.O., Robinson, E.L., Koester, D., Clemens, J.C., & Nather, R.E. 1999, *Balt. Astron.*, 9, 59
- [35] Kepler, S.O., et al. 2000, 539, 379
- [36] Kleinman, S.J., et al. 1998, *ApJ*, 495, 424
- [37] Koester, D., Weidemann, V., & Vauclair, G. 1983, *A&A*, 123, L11
- [38] Koester, D. et al. 1985, *A&A*, 149, 423
- [39] Koester, D. 1999, private communication
- [40] Koester, D., & Allard, N. 1999, *Balt. Astron.*, 8, 119
- [41] Koester, D. 2000a, private communication
- [42] Kirshnitz, D.A. 1960, *Soviet Phys.—JETP*, 11 365
- [43] Leggett, S.J., Ruiz, M.T. & Bergeron, P. 1998, *ApJ*, 497, 294
- [44] Liebert, J., et al. 1986, *ApJ*, 309, 241
- [45] Liebert, J., Dahn, C.C., Monet, D.G., 1988, *ApJ*, 332, 891
- [46] McCook, G.P., & Sion, E.M. 1999, *ApJS*, 121, 1
- [47] Mestel, L., 1952, *MNRAS*, 112,
- [48] McGraw, J.T. 1979, *ApJ*, 229, 203

- [49] Montgomery, M.H. 1999, the 11th European Workshop on White Dwarfs, ASP Conf Series Vol. 169, (eds) Solheim & Meistas, 133
- [50] Montgomery, M.H. 1994, Master's Thesis, University of Texas at Austin
- [51] Montgomery, M.H. 1998, PhD Thesis, University of Texas at Austin
- [52] Montgomery, M.H. & Winget, D.E. 1999, ApJ, 526, 976
- [53] Montgomery, M.H. & O'Donoghue, D. 1999, Delta Scuti Star Newsletter, 13, 28
- [54] Nather, R.E., et al. 1990, ApJ, 361,309
- [55] Nather, R.E. 1995, Balt. Astron, 4, 321
- [56] Nitta, A., et al. 1999, 11th European Workshop on White Dwarfs, ASP Conf Series Vol. 169, (eds) Solheim & Meistas, 144
- [57] Ozwalt, T.D., Smith, J.A., Wood, M.A. & Hentzen, P. 1996, Nather, 382, 692
- [58] Pilachowski, C.A. & Milkey, R.W. 1987, PASP, 99 839
- [59] Provencal, J.L., Shipman, H.L., P. Thejil, & Vennes, S. 2000, ApJ, submitted
- [60] Reimers, & Koester, D. 1994, A & A, 295, 451
- [61] Robinson, E.L. 1979, Proceedings of the Fourth Annual Workshop on Novae, Dwarf Novae and Other Cataclysmic Variable, 343
- [62] Robinson, E.L., Kepler, S.O., Nather, R.E. 1982, ApJ, 259, 219

- [63] Robinson E.L., et al. 1995, ApJ, 438, 908
- [64] Romanshin, W., & Angel, J.R.P. 1980, ApJ, 235, 992
- [65] Salpeter, E. 1961, ApJ, 134, 669
- [66] Thejl, P., Vennes, S., & Shipman, H.L. 1991, ApJ, 370, 355
- [67] Unno, W., Osaki, Y., Ando, H., Saio, H., & Shibahashi, H. 1989, Nonradial Oscillaion of Stars(Tokyo:Univ.Tokyo Press)
- [68] van Altena, Lee, and Hoffleit 1995, The General Catalogue of Trigonometric Stellar Parallaxi (4th edition), Yale University Observatory
- [69] van Kerkwijk, M.H., Clemens, J.C., & Wu, Y. 2000, MNRAS, 314, 209
- [70] Weidemann, V. & Koester, D. 1983, A& A, 121, 77
- [71] Weidemann, V. 1990, **ARAA**, 28, 103
- [72] Welsh, W.F., et. al. 1998, ApJ, 509, 118
- [73] Winget, D.E., Van Horn, H.M, & Hansen, C.J. 1981, ApJ, 245 L33
- [74] Winget, D.E. 1981, PhD Thesis, University of Rochester
- [75] Winget, D.E. et al. 1981, ApJ, 251, L65
- [76] Winget, D.E., Robinson, E.L., Nather, R.E., & Fontaine, G. 1982, ApJ, 262, L11
- [77] Winget D.E. 1986, proceeding of the 19th IAU General Assembly, 221
- [78] Winget, D.E., et al. 1991, ApJ, 378,326

- [79] Winget, D.E. et al. 1994, ApJ, 430, 839
- [80] Winget, D.E. 1998, Journal of Phys.: Condens. Matter, 10, 11247
- [81] Winget, D.E. et al. 1997, ApJ, 487, L191
- [82] Wu, Yanqin 1999, ApJ,
- [83] York, et al. 2000, AJ submitted
- [84] Zuckerman, B. & Becklin, E.E. 1987, Nature, 330, 138

Vita

Atsuko Nitta was born on August 21, 1966, in Tokyo, Japan, as the daughter of Isamu and Michiko Nitta. After graduating from Toho Girls' High school in 1985, she entered Ochanomizu University. She majored in physics and received a B.S. in March 1990. After graduation, she continued her studies in physics at the graduate school of Ochanomizu University. She received an Ishizaka Foundation Scholarship in 1991 and came to the Physics department at University of Texas at Austin. In the spring of 1993, while she was a physics student, she met Don Winget and Ed Nather and started working with the Whole Earth Telescope group. She transferred to the Astronomy department in 1994, and earned her M.A. in astronomy in 1996.

Permanent address: 72 Silver Fox Trail, Mayhill, NM 88339

This dissertation was typeset with \LaTeX^\dagger by the author.

[†] \LaTeX is a document preparation system developed by Leslie Lamport as a special version of Donald Knuth's \TeX Program.